BRNO UNIVERSITY OF TECHNOLOGY
VYSOKÉ UČENÍ TECHNICKÉ V BRNĚ

FACULTY OF MECHANICAL ENGINEERING
FAKULTA STROJNÍHO INŽENÝRSTVÍ

ENERGY INSTITUTE
ENERGETICKÝ ÚSTAV

REDUCED-ORDER MODEL OF SWIRLING FLOW
REDUKOVANÝ MODEL VÍROVÉHO PROUDĚNÍ

DOCTORAL THESIS
DIZERTAČNÍ PRÁCE

AUTHOR — Ing. ONDŘEJ URBAN
AUTOR PRÁCE

SUPERVISOR — doc. Ing. PAVEL RUDOLF, Ph.D.
ŠKOLITEL

BRNO 2022

Abstract

This doctoral thesis is aimed at studying the vortex rope phenomenon. For this purpose, a new swirl generator capable of regulating the swirl intensity was designed. The behavior of the vortex rope was studied both numerically and experimentally. Scale-resolving numerical simulations were employed, visualization methods based on volume rendering were proposed, and different vortex criteria were tested. Several flow field decomposition methods were studied. Finally, methods for extracting quasiperiodic patterns were proposed. These methods enabled the construction of a reduced-order model for a range of operating conditions.

Key words

vortex rope, CFD, swirl generator, dynamic decomposition, reduced-order model

Rozšířený abstrakt

Předmětem práce je studium vírového copu. Nejprve je podán přehled výsledků z dostupných publikovaných prací. Je zmíněn vztah mezi vírovým copem vznikajícím ve vodních turbínách, zejména Francisových, a jevem zvaným rozpad víru. Jsou uvedeny experimentální a numerické studie zabývající se podobou vírového copu a jím způsobenými tlakovými pulzacemi. Nakonec jsou zmíněny metody, které byly navrženy pro zmírnění těchto tlakových pulzací až úplné zamezení vzniku vírového copu.

Základní výzkum vírového copu je možno provádět místo modelů vodních turbín na jednodušších vírových generátorech. V práci jsou uvedeny v minulosti navržené vírové generátory. Ukazuje se, že jsou buď poměrně složité, nebo tak jednoduché, že neumožňují měnit míru vytvořeného zavíření. Proto byl navržen nový vírový generátor, který je konstrukčně jednoduchý (bez pohyblivých částí), ale umožňuje měnit míru zavíření. Principem je použití dvou vstupů – axiálního a tangenciálního. Poměr průtoků přivedených jednotlivými vstupy určuje míru zavíření.

Proudění v nově navrženém vírovém generátoru bylo studováno jak numericky, tak experimentálně. Numerické studie jsou založené na hybridním modelu turbulence stress-blended eddy simulation (SBES), který v oblasti difuzoru, kde je proudění nestacionární a vzniká zde vírový cop, používá simulaci velkých vírů (LES), která zachycuje i část kaskády turbulentních vírů do rozměrů daných velikostí buněk sítě. Pozorované chování vírového copu bylo srovnáno se záznamy z vysokorychlostní kamery. Pro validaci výsledků CFD bylo provedeno srovnání rychlostních polí s měřeními optickou metodou PIV.

Protože výsledkem LES simulace jsou pole obsahující velké množství vírových struktur, bylo třeba se zabývat metodami identifikace těchto vírů (tzv. vírovými kritérii) a metodami počítačové vizualizace proudění. Vedle běžně používaných vírových kritérií byly testovány i méně běžné metody, které jsou výpočetně náročnější, zato mají propracovanější definice založené na zajímavých myšlenkách. Pro vizualizaci výsledků simulací pak byly navrženy metody založené na objemovém renderování. V práci je ukázáno, že objemové rendery obecně přinášejí více informací než konvenční vizualizace vírových struktur pomocí izoploch.

Dále byla provedena numerická studie různých metod pro potlačení vírového copu. Nejprve bylo testováno vstřikování vody skrz dno náboje, kde se ukázalo, že může dojít naopak k zesílení tlakových pulzací vlivem rozrotovaného vstřikovaného proudu vody. Proto byly testovány i další možnosti – odsávání ve spodní části difuzoru a kombinace vstřikování a odsávání. Kromě těchto aktivních metod jsou uvedeny i výsledky provedené studie zabývající se pasivními metodami – vestavbami v difuzoru.

Poslední část je zaměřená na tvorbu redukovaného modelu tlakového pole umožňujícího extrapolaci výsledků z výpočtů pro různé provozní body neomezeně v čase a současně i interpolaci mezi provozními body. Nejprve jsou studovány různé metody dekompozice dat. Základní myšlenkou redukovaného modelu je identifikace významných prostorových módů (tvarů kmitu) a k nim příslušejících časových funkcí. K tomu byla použita metoda vlastní ortogonální dekompozice, kdy na základě simulace s proměnnými okrajovými podmínkami bylo stanoveno 11 významných prostorových módů pro popis tlakových polí napříč zvoleným provozním pásmem. K nim poté byly s použitím výsledků CFD simulací pro tři zvolené provozní body stanoveny časové funkce pro tyto body. Tyto časové funkce, přesněji diskrétní řady hodnot těchto funkcí, byly proloženy pomocí funkcí popisujících kvaziperiodické kmitání (harmonické kmitání s do jisté míry v čase proměnlivou frekvencí a amplitudou). Parametry regresních funkcí byly stanoveny pomocí strojového učení. Bylo potřeba navrhnout metodiku získání dostatečně přesné počáteční podmínky, aby k následné optimalizaci bylo možné použít rychlé algoritmy založené na gradientním sestupu. Získané parametry byly nakonec interpolovány v závislosti na provozním bodu. Nakonec byl proveden základní rozbor výsledků.

Bibliographic citation

URBAN, O. *Reduced-order model of swirling flow*. Brno, 2022. Doctoral thesis. Brno University of Technology. Supervisor doc. Ing. Pavel Rudolf, Ph.D.

Declaration

I honestly declare that I have written this thesis *Reduced-order model of swirling flow* myself under the professional guidance of my supervisor.

_____

Ing. Ondřej Urban

Acknowledgements

Here, I would like to thank all those who helped me finish this work. First of all, my thanks go to my supervisor, doc. Ing. Pavel Rudolf, Ph.D., for the possibility of working on this thesis full-time at the department and his professional guidance.

I am grateful to my undergraduate students who joined the project this thesis is about and worked out their bachelor's theses under my supervision. Their interest motivated me to start learning things I had not originally planned to do, for example programming in Python. Without them, this thesis would be much poorer.

I express my deepest appreciation to prof. Ing. František Pochylý, CSc. He is the most enthusiastic and optimistic person at the department, the author of many clever ideas that led to patents, so I am extremely grateful for the opportunity to cooperate with him and learn from him.

The experiments could be done only thanks to my colleagues from the laboratory and Ing. David Štefan, Ph.D., who performed the construction design of the swirl generator studied within this work and supervised the PIV measurements performed by prof. Ing. Václav Uruba, CSc. and Ing. Pavel Procházka, Ph.D.

Finally, I would like to thank all other staff and Ph.D. students, especially my office mate Lucka, who read the manuscript of this thesis and got me aware of many errors.

This thesis was worked out within the following research projects:

GA17-01088S – 3D Instability of a Shear Layer in Adverse Pressure Gradient
Goals: design of a swirl generator, LES simulations, experimental measurements

CZ.02.1.01/0.0/0.0/16_026/0008392 – Computer Simulations for Effective Low-Emission Energy Engineering
Goals: developing a reduced-order model of swirling flow

TH04020045 – Suppression of Negative Effects of Inflow Recirculation in High-Capacity Cooling Pumps
Goals: developing installations preventing recirculation

Contents

Introduction and goals of the thesis

Water turbines are machines designed specifically for given operating conditions. When operating in off-design conditions, the flow is often strongly unsteady and exhibits onset and propagation of pressure pulsations, noise, and vibrations that can negatively affect the lifetime of exposed parts. Such dangerous phenomena often lead to a restriction of the turbine operating range. Let us focus on the draft tube of reaction water turbines, where a helical structure called the vortex rope emerges in a certain range of operating conditions, typically in part load, i.e. when the flow rate is below the design value. The vortex rope is observed when swirl is admitted into the draft tube, and its interaction with the draft tube elbow was found to be the source of significant pressure pulsations. This is a problem specifically in Francis turbines due to their fixed blades. In contrast, Kaplan turbines feature adjustable blades that allow for reduction of the swirl at the runner outlet/draft tube inlet in off-design conditions by changing their pitch angle.

Meanwhile, people are striving to increase the share of renewable energy in the energy mix. This goal can be accomplished by solar and wind power plants. Their output is strongly affected by the weather and therefore very unstable. To ensure stability of the electrical grid, sufficient backup capable of on-demand connection to the grid, output power adjustments, and disconnection from the grid is needed. Water turbines are its key part as they can provide the mentioned actions most rapidly. Naturally, reaching the widest possible operating range has recently become one of the most important demands on new or refurbished machines. This leads to the need for mitigation of the dynamic load caused by unsteady vortical structures.

The presented facts motivate research of the vortex rope phenomenon. A review of published works is given in the following two chapters. The goal of this thesis is to contribute to this research and, in particular, to extend the work that has been done at the department. The following milestones were pursued.

- *Design of a new swirl generator allowing control of swirl intensity while being inexpensive and easy to manufacture (i.e. no moving parts, bearings, etc.).*

It will be shown in the review that the vortex rope research was performed using either model turbines or complicated swirl generators, or very simple 3D-printed swirl generators with fixed blades and thus a fixed swirl intensity. The middle ground stated above is clearly missing. Model turbines are essential for the design of real turbines; however, simpler devices are sufficient for general research.

- *Performing CFD simulations of flow in the proposed swirl generator, validating them against the results of PIV measurements, and studying the behavior of the vortex rope and its dependence on operating conditions.*

CFD simulations have become a common part of the hydraulic machinery design process. Therefore, RANS simulations with the RSM turbulence model will be used in the design phase since their performance in cases with the vortex rope was found to be good in previous work carried out at the department. The final design will be simulated again with the SBES turbulence model. This model uses an LES formulation of the eddy viscosity in the regions of unsteady flow, except boundary layers. This should provide more precise results, which will be studied in detail.

- *Finding suitable vortex identification methods and proposing visualization techniques leveraging the content of the CFD data.*

The present case is 3D, while the paper this work is printed on or the screen it is viewed on are 2D. The consequence of this dimension mismatch is that the data cannot be fully restored from visualizations. For 2D cases, scalar data are usually visualized by colors, vector data by arrows. With the knowledge of the color transfer function and scaling of the arrows, it is possible to fully restore the original data from their visualizations. For 3D data displayed in 2D, this is not possible. Since the present case features a highly swirling flow with a vortex rope accompanied by many turbulent eddies as small as the mesh cell size, it is desirable to find both a suitable method for identification of these vortices and a visualization method that well tackles the dimension mismatch issue. It will be shown that visualizations based on isosurfaces, which are still the most common method, can even be misleading. A method based on volume rendering that outperforms visualizations of the vortex rope based on isosurfaces will be presented and used throughout this work.

- *Conceptual study of several passive and active flow control methods for mitigating the vortex rope.*

Several different methods for mitigating the vortex rope will be studied by means of CFD simulations; some of them will also be tested experimentally within an ongoing research project. Visualizations of the CFD data will be performed to qualitatively assess the impact of the methods on the flow field.

- *Reduced-order modelling of the present flow with a vortex rope.*

Different decomposition techniques will be studied and applied, especially the most popular one, the proper orthogonal decomposition (POD), and recently proposed spectral orthogonal decomposition (SPOD), which is a method enabling to reach a balance between optimal model order reduction and spectral purity of modes. Recent development of machine learning methods has manifested itself also in this field. They enable discovering patterns in the data and finding models for them. Based on observations of vortex rope behavior, methods aimed at extracting quasiperiodic patterns will be sought.

1 Vortex rope in water turbines

The origin of the vortex rope in water turbines can be traced to the shape of the runner blades. The blade shape is designed to work optimally at the design point, often denoted as BEP (Best Efficiency Point). With the change of operating point, the velocity distribution at the blade inlet and outlet changes as well. This leads to the existence of the efficiency peak and to the need for geometry adjustments to maintain high efficiency for a wide range of operating points. This is the reason why axial Kaplan turbines are constructed with adjustable blades. It should be noted that axial turbines with fixed blades, so-called propeller turbines, have also found their place on the market. However, in turbines with fixed blades, most notably radial Francis turbines, the loss in efficiency in off-design conditions is also accompanied by the emergence of unsteady vortical structures that cause pressure pulsations, noise, and vibrations. Their impact on the machine may be dangerous, leading to restrictions in the operating range of the machine.

The vortex rope is one of these phenomena. Its origin can be found in the mentioned different velocity profiles at the blade outlet in off-design conditions. In the middle of Fig. 1.1, a typical velocity triangle of a Francis turbine in BEP is depicted. It features only a small tangential component of the absolute velocity v_u, which allows reaching higher draft tube opening angles without boundary layer separation. As the flow rate decreases (Fig. 1.1 left), the tangential component increases, which is given by the fixed value of the β_2 angle and the runner circumferential speed u (the first is given by the blade shape – at least in its vicinity – and the latter is given by the constant utility frequency maintained in the electrical grid). The direction of the vector $\boldsymbol{v}_u$ matches the direction of the vector $\boldsymbol{u}$, i.e. water rotates in the same direction as the runner. If the flow rate is increased above BEP, the tangential component also increases. The difference is that the direction of its vector is opposite to the direction of the circumferential speed vector.

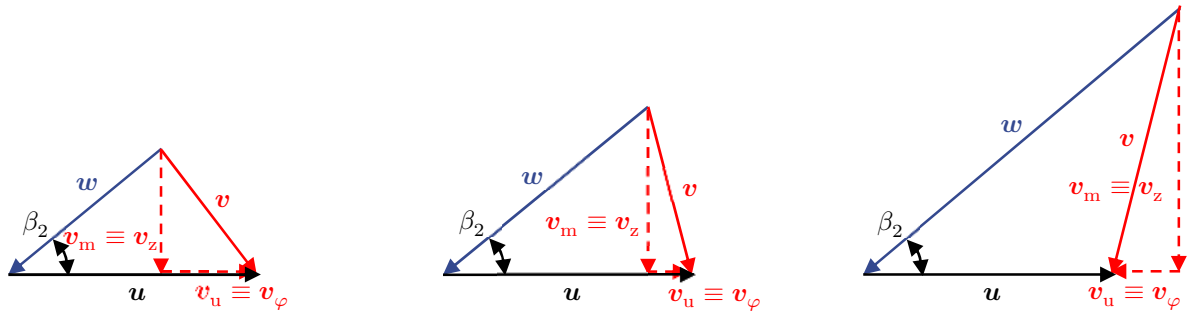

Fig. 1.1: *Velocity triangles at a Francis turbine runner outlet. Left: part load, middle: BEP, right: overload.*

Now let us look at the part load regime. In this regime, a helical vortical structure, the so-called vortex rope, is commonly observed. The vortex rope is often related to vortex breakdown[1, 2]. Comprehensive reviews of studies of this phenomenon were carried out by Escudier[3], Lucca-Negro[4], and Hall[5]. For a review written in Czech, see the bachelor's thesis by Lunda[6]. Several types of vortex breakdown are distinguished; however, only two of them are observed in turbulent flows with high Reynolds numbers – the bubble type and the spiral type. Vortex breakdown can be viewed as a flow type change. At the inlet, swirling flow is present. The axial velocity at the axis gradually decreases up to a stagnation point. This effect can be caused by viscous forces and can be further magnified by an increase in the cross section of the pipe. Indeed, Hall[7] showed that

decreasing the axial velocity away from the axis leads to an even greater decrease at the axis. Downstream of the stagnation point, we can distinguish a region of decelerated flow or even backflow extending along the axis and a region of swirling flow along its circumference. These two zones are separated by a shear layer with significant velocity gradients. In bubble vortex breakdown, the stagnation point is followed by a recirculation bubble. In spiral vortex breakdown, the straight vortex filament present in the upstream flow abruptly bends and continues further downstream in a characteristic helical shape. The rotation of the vortex about its center line goes hand in hand with the velocity deceleration at the axis and acceleration in the outer zone. Vortex breakdown in general lacks a generally-accepted theoretical description. So far, three theories have been elaborated.

In the first theory, vortex breakdown is related to the wave propagation theory. Squire[8] and Benjamin[9] showed that for an axially symmetric vortex, there exists a critical point beyond which waves propagate only downstream. Such a flow is referred to as supercritical. If the flow is subcritical, the waves can also propagate upstream. According to the Squire's theory, vortex breakdown is caused by a concentration of perturbations that cannot propagate upstream. Benjamin, on the other hand, considers vortex breakdown to be a transition between supercritical and subcritical flow, analogously to the hydraulic jump, for example. In water turbines, his theory was successfully exploited by Resiga et al.[10] to explain a sudden drop in efficiency observed in a specific Francis turbine model.

The second approach is similar to the description of boundary layer separation. The flow at the inlet can be described by quasi-cylindrical equations. It was found that the solution of these equations fails to converge at the vortex breakdown onset point. Similarly, the boundary layer equations fail to converge at the point of separation. Furthermore, it was shown that at this point the flow undergoes a transition from supercritical to subcritical state, which is in agreement with the previous theory[11]. The drawback of this description is that it provides no information on what is happening further downstream.

In the last approach, vortex breakdown is considered to be a flow instability. It is based on extensive knowledge of flow stability analysis. As an example with application to the vortex rope in a Francis turbine model, the work of Pasche et al.[12] can be mentioned. They performed a stability analysis of the mean flow and found out that one of the unstable modes corresponds to the vortex rope.

Although all of these theories led to reasonable results, there are also disputes and limitations for all of them. It can therefore be stated that vortex breakdown can not be explained exclusively by any of them.

Let's return to the vortex rope. Nishi described its onset in his papers[13, 14] as follows.

- With increasing swirl, water loses its axial velocity until a stagnation point is reached at some point on the axis, followed by a dead water or reverse flow region.
- Between the central dead water or reverse flow region and the outer swirling flow, a shear layer with concentrated vorticity may exist. Vortex filaments are of spiral shape and may roll up into a single vortex, the vortex rope.
- If the swirl is increased further on, the pitch of the spiral vortex rope increases. It was observed that the center line of the vortex rope is approximately perpendicular to the streamlines of the outer swirling flow. The sense of the spiral shape of the vortex rope is therefore opposite to the sense of rotation of the outer swirling flow.

Foroutan and Yavuzkurt[15] related the onset of the vortex rope to the Kelvin–Helmholtz instability of the mentioned shear layer.

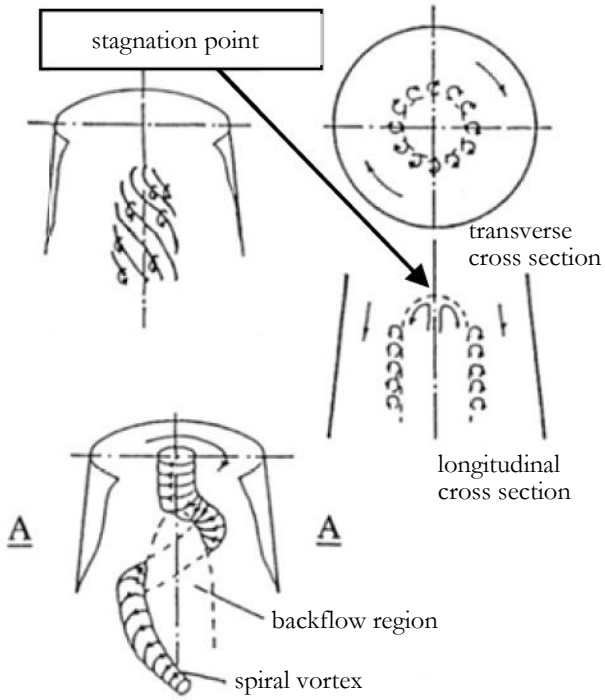

Fig. 1.2: *A sketch by Nishi*[13] *illustrating the onset of the vortex rope (edited).*

1.1 Vortex rope regimes

Nishi in his works[13, 16] distinguishes four regimes of the draft tube flow based on the form of vortical structures. They are illustrated in Fig. 1.3 (left).

Regime I: The vortex rope is almost straight. In the straight part of the draft tube (upstream of the elbow), no backflow region is observed.

Regime II: The vortex rope is unstable: it takes various forms irregularly.

Regime III: A single vortex rope with a stable shape is observed. The stagnation point is found near the diffuser inlet.

Regime IV: Twin (and sometimes even triple) vortex ropes are observed. The stagnation point reaches the runner hub tip.

In another paper[17], Nishi works with a modified draft tube shape, where the goal was to decrease the amplitude of pressure pulsations caused by the dynamics of the vortex rope in the elbow. The idea was to reach as high pressure increase as possible already in the straight conical part, leading to a higher opening angle. The opening angle of the original draft tube was 9°, while the modified draft tube had 15°. In this new draft tube, the author found a region where regimes III and IV alternate – see Fig. 1.3 (right).

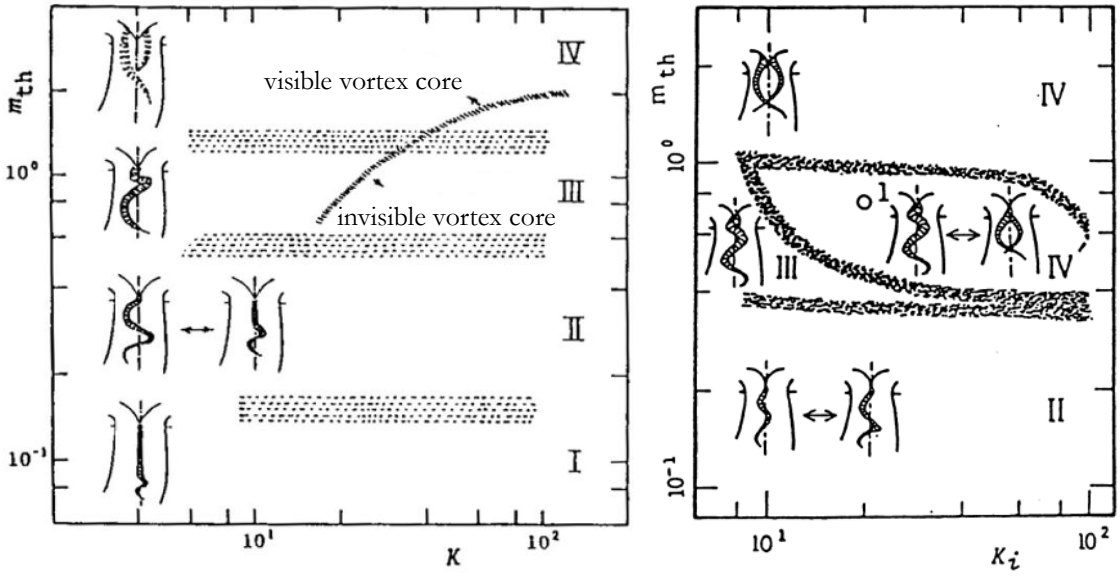

Fig. 1.3: *Sketches of vortex rope regimes by Nishi[16, 17] (edited). Parametr m is related to the opening of the guide vanes so that with growing m, the swirl at the draft tube inlet grows. K stands for the cavitation number.*

In his dissertation[18], Jacob observed the shape of the vortex rope in two different Francis turbine models. Fig. 1.4 (left) documents the frequency spectra of pressure pulsations in the turbine with a lower specific speed, working with the optimal head and different flow rates. We can observe features that are common to Nishi's descriptions: as the flow rate decreases, a single vortex rope appears at first and later it breaks. The sketches of Nishi, however, feature in the final phase more coherent twin vortex ropes.

The frequency spectra feature a dominant peak. Other peaks correspond to its superharmonics. The most dominant frequency, which is the frequency of the vortex rope precessing motion, corresponds approximately to a quarter of the rotational frequency of the runner. Studies of the vortex

rope precession frequency were started by the work of Rheingans[19], who found the mentioned ratio to be $1/3{,}6$. As more experiments were conducted later on, newer works state a range of $0{,}2$ to $0{,}4$[1]. In the series of the frequency spectra, it is evident that the peak amplitude of the pressure pulsations was reached when the flow rate was half the optimal. As the flow rate was further decreased, the pressure pulsations decreased rapidly. This is connected to the breaking of the highly coherent vortex rope into a complicated structure made up primarily of smaller, less coherent vortices. The figure also depicts a smaller coherent structure under the hub tip, reminiscing one of the twin vortex ropes in Nishi's sketches.

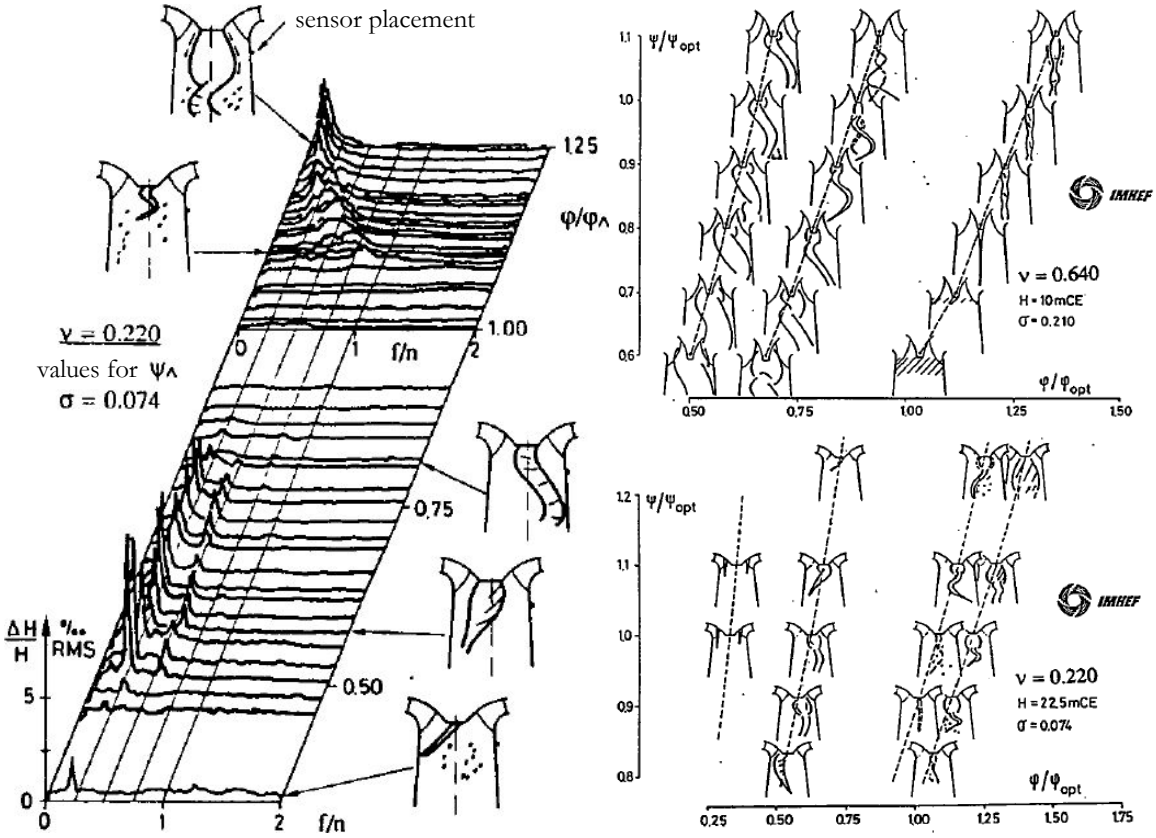

$$\varphi = \frac{Q}{2\pi^2 R^3 n}, \qquad \psi = \frac{Y}{2\pi^2 R^2 n^2}, \qquad \nu = \varphi^{\frac{1}{2}}\psi^{\frac{3}{4}}$$

Fig. 1.4: *Sketch of vortex rope regimes by Jacob*[18] *(edited). The hat index denotes BEP. H denotes head, σ denotes the cavitation number.*

In the right part of Fig. 1.4, results from the same model with different heads as well as from the model with a higher specific speed are presented. In the second model at the optimal head, when the flow rate was decreased below BEP, thin twin vortex ropes were observed first, followed by a single distinct vortex rope.

In his dissertation[20], Skoták also investigated vortical structures in the draft tube of a Francis turbine model. Experiments were conducted for three different openings of the guide vanes, for which operating points with different unit speed values were measured. The author presents the hill chart of the turbine divided into different zones based on the observed vortex rope regimes and on the swirl number values. The swirl number was computed from velocity profiles measured

by laser Doppler anemometry (LDA). As can be seen in Fig. 1.5, the contours of the swirl number correspond well to the borders of the zones with different vortex rope regimes. It shall be noted that the borders are not meant to be sharp; there exist transition zones around them, where the shape of the vortex rope was changing irregularly. In addition, hysteresis was observed. As the flow rate decreases below BEP, the vortex rope becomes larger until it breaks, in agreement with the previously mentioned works, into twin vortex ropes. In a certain deep part load zone, even triple vortex ropes were observed. Regimes denoted 1a+ and 1b+ with a single vortex rope differ in its pitch and precession frequency (both are higher in type b). A distinct transition between these regimes was observed.

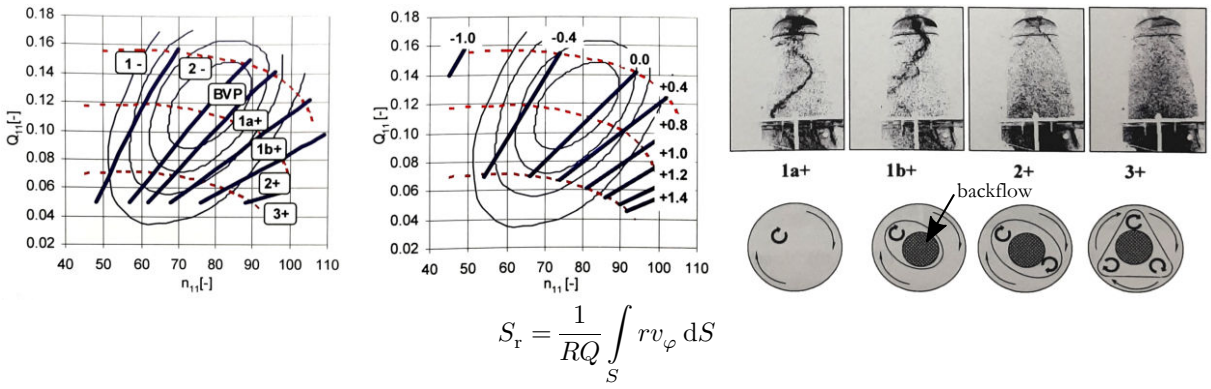

$$S_\mathrm{r} = \frac{1}{RQ}\int_S rv_\varphi \,\mathrm{d}S$$

Fig. 1.5: *Hill chart of a model turbine with marked zones of different vortex rope regimes (left) and zones of different values of the swirl number (right, the definition is stated below) and pictures of vortical structures observed in part load conditions by Skoták*[20] *(edited). The number denotes the number of coherent spiral structures observed, the + sign denotes rotation in the same sense as the runner, and the – sign stands for the opposite sense. BVP is an abbreviation for the Czech translation of vortexless zone.*

A similar division of the hill chart into different zones based on the vortex rope regimes and the swirl number values was presented by Wahl[21]. In addition to that, he also investigated the regime with twin vortex ropes more closely, resulting in data exhibiting a decrease in the amplitude of pressure pulsations and an increase in their frequency compared to the regime with a single vortex rope. Later, a similar behavior was also recorded in the prototype. The relation between the shape of the vortex rope and the value of the swirl number was also described by Cassidy and Falvey[22].

The swirl number was used for the description of different parameters characterizing the flow in a Francis turbine draft tube also by Favrel et al.[23] They showed that the precession frequency as well as the eigenfrequency of the whole hydraulic system can advantageously be considered as a function of the swirl number only instead of the unit speed and the unit discharge. Cala et al.[24] examined the dependence of the Strouhal number based on the precession frequency of the spiral vortical structure present in a swirling combustor on the Reynolds number for two different swirl numbers. It turned out that the Strouhal number differed between the cases with the different swirl numbers but was almost unaffected by the Reynolds number.

Cheng et al.[25] pointed out that the swirl number is not suitable when it comes to quantification of the vortex rope strength. From their observations depicted in Fig. 1.6, it is evident that the vortex rope becomes stronger as the flow rate decreases below BEP. The largest vortex rope and the strongest pressure pulsations were observed at 88% of the optimal unit discharge. With a further decrease, the amplitude of pressure pulsations decreased, and the vortex rope was no longer visible. At 50% of the optimal unit discharge, no signs of the existence of the vortex rope could be detected even in the frequency spectra of pressure measurements – they had the character of broadband noise. When looking at the dependence of two different swirl number definitions on

the unit discharge, it is evident that they do not reflect the disappearance of the vortex rope. One swirl number continues growing; the second decreases only slowly. Therefore, the authors introduce a new quantity denoted V_s that is based on observations of the mean axial velocity profiles $v_z = f(r)$. At first, function $G(r)$ is defined as follows:

$$G(r) = \frac{\frac{\mathrm{d}v_z}{\mathrm{d}r}\frac{\mathrm{d}^2 v_z}{\mathrm{d}r^2}}{\int_0^R \frac{\mathrm{d}^2 v_z}{\mathrm{d}r^2}\,\mathrm{d}r} \tag{1.1}$$

If the axial derivative of the radial velocity can be neglected, then the radial derivative of the axial velocity corresponds to a negative circumferential vorticity Ω_φ. Namely

$$\Omega_\varphi = \frac{\mathrm{d}v_r}{\mathrm{d}z} - \frac{\mathrm{d}v_z}{\mathrm{d}r} \tag{1.2}$$

Therefore, high values of $G(r)$ mean that both the circumferential vorticity and its radial derivative are significant. The parameter V_s is defined as the integral of the absolute value of this function along the radius

$$V_s = \int_0^R |G(r)|\,\mathrm{d}r \tag{1.3}$$

It should be noted that the authors worked with experimentally measured velocity profiles that do not include the boundary layer. The results in Fig. 1.6 are consequently computed with an upper limit of only $0{,}9R$. It can be seen that V_s reaches its local maximum at the same point where the largest vortex rope and the strongest pressure pulsations were observed. The authors investigated its values also along the length of the draft tube and found out that they also correspond to the characteristics of the vortex rope: the values first increased and then fell down as the vortex rope dissipated downstream.

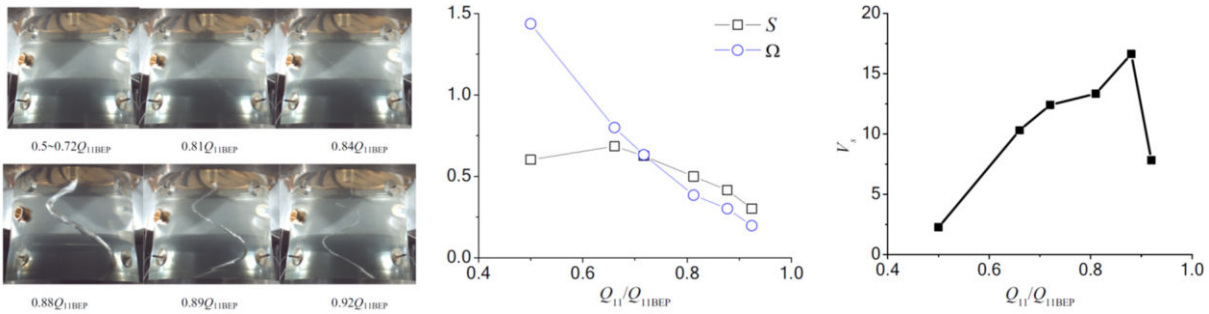

$$S = \frac{1}{R}\frac{\int_0^R r^2 v_\varphi v_z\,\mathrm{d}r}{\int_0^R r\,{v_z}^2\mathrm{d}r}, \qquad \Omega = D\frac{\int_S r v_\varphi v_z\,\mathrm{d}S}{Q^2}$$

Fig. 1.6: *Observations of the vortex rope and values of two different definitions of the swirl number and the parameter V_s for different values of the unit discharge by Cheng et al.*[25].

Houde et al. [26] investigated vortical structures in a propeller turbine. The unit speed was fixed on a value slightly higher than optimal. As the flow rate was decreased below BEP, a thin cavitating vortex emerged and grew with further decreases until it broke into a more complex structure, similarly to the previously mentioned Francis turbine cases. No, single, and twin spiral vortices appeared irregularly under the hub tip.

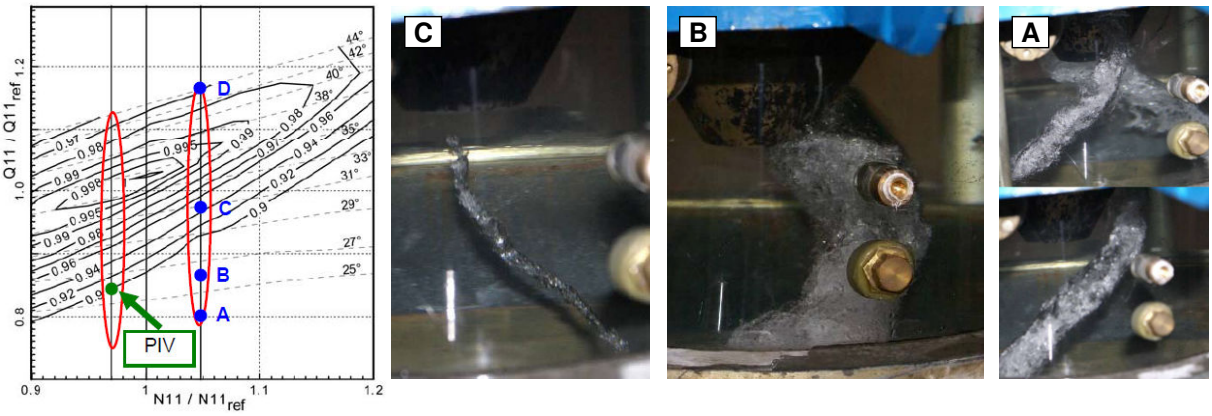

Fig. 1.7: *Hill chart and photographs of vortical structures observed in the draft tube of a propeller turbine by Houde et al.*[26] *(edited).*

1.2 CFD simulations

Studying the vortex rope by means of computational fluid dynamics (CFD) dates back to the 1990s[27, 28]. The works from that time focus on the applicability of a popular two-equation turbulence model, the k–ε standard model. Skoták[20] states that in commercial solver Fluent version 5.7, this model predicts no vortex rope. Better results were achieved with newer version 6.1 in which a new formulation was implemented. In the same version using the RNG k–ε model, Zhang et al. successfully simulated the vortex rope and its mitigation by axial water jet injection[29]. Ruprecht et al.[30] used their custom solver and found out that the standard formulation of this model needs to be modified. Their modified formulation (the modifications were not specified) led to, in authors' words, excellent agreement of the vortex rope precession frequency with experimental measurements. However, the dissipation further downstream was overestimated. To this point, Dörfler[27] states that this model needs to be modified so that it considers the stabilizing effect of the curvature of streamlines.

Due to the issues of two-equation models, the use of which is motivated by their lower computational cost, more advanced turbulence models were tested as well. They were found to reliably capture the shape and motion of the vortex rope. These models comprise the anisotropic Reynolds stress equation model (RSM) and scale-resolving models. Ruprecht[31] developed a custom model that belongs to the category of very large eddy simulation (VLES), which bridges detailed but costly large eddy simulation (LES) and models based on Reynolds-averaged governing equations. He successfully tested it on cases of flow in water turbines, including a draft tube with a vortex rope.

In his work[20], Skoták tested the RSM model as well and states that the results are very satisfactory in terms of predicting the onset and behavior of the vortex rope. He also performed a simulation using the LES model. It shall be noted that the presented mesh apparently does not satisfy the strict requirements on proper simulations using this model. Nevertheless, the shape and motion of the vortex rope were predicted well. The last simulation presented in the work of Skoták assumes

an inviscid fluid to tackle the mentioned overestimation of the vortex rope dissipation further downstream.

Jošt and Lipej[28] build on Skoták's work. They used commercial solver CFX version 11. On a given case and three different meshes, they test the ability of the SST–SAS turbulence model to predict the amplitude of pressure pulsations at different operating points. In the results depicted in Fig. 1.8, it is evident that the mesh played a significant role in the point with the strongest pressure pulsations, otherwise the values are similar. Excluding the point with the lowest flow rate, the CFD simulations always underestimated the amplitude compared to the experimental measurements.

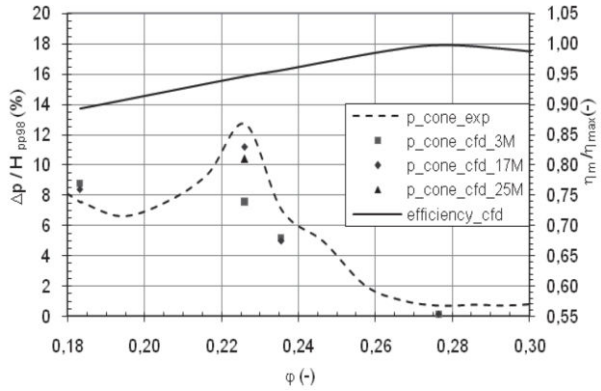

Fig. 1.8: *Dependence of the pressure pulsations amplitude (98% peak-to-peak) and efficiency coefficient on the discharge coefficient by Jošt and Lipej[28] (edited).*

In the following part of their work, the authors compare SAS–SST, ω–RSM and LES turbulence models. In the first two cases, the whole turbine is modelled, while in the case of LES, only the draft tube with an unsteady inlet boundary condition extracted from the SAS–SST simulation results was considered. The predicted shape of the vortex rope was very similar in all three cases. The frequencies and amplitudes of pressure pulsations were again underestimated compared to experimental measurements.

With the goal of collecting experimental data for verification of CFD simulations, the FLINDT (FLow INvestigation in a Francis Draft Tube) project was established. Measurements were carried out on a high specific speed Francis turbine model[32]. Ciocan et al. [33] performed CFD simulations in commercial software CFX version 5.6 using the standard k–ε turbulence model. In their paper, they present a comparison of different numerical results with experimental results: the frequency of the vortex rope precession, evolution of pressure pulsations, velocity profiles in the draft tube, vorticity field in a given cross section, and the vortex rope center line. Conditions without cavitation were assumed, with the simulations domain comprising the runner and the draft tube without the spiral case and the guide vanes. Significantly lower vorticity magnitude values from the simulations compared to the experimental measurements were noted. This was attributed to the coarseness of the mesh, leading to significant numerical diffusion. In other cases, the numerical results agreed well with the experimental measurements.

Vu et al.[34] build on the same data. In their paper, they study, among others, the effect of inlet boundary conditions. Profiles of velocity and turbulence kinetic energy were available from experiments, while mixing length needs to be determined. The authors recommend 0,5% of the runner outlet diameter.

Another interesting study based on FLINDT data was carried out by Foroutan and Yavuzkurt[35]. In commercial solver Fluent version 13.0, they performed transient simulations of the draft tube flow only. At the inlet, they first prescribe a steady boundary condition obtained by averaging the experimental measurements. It turned out that the two-equation models k–ε and SST k–ω did not predict unsteady flow at all, unlike what was achieved later with the DES (Detached Eddy Simulation) model. The authors also examined the evolution of turbulence kinetic energy along a selected cross section in the draft tube and found out that all the models predicted significantly lower values near the axis compared with the experimental measurements. For this reason, they used an unsteady inlet boundary condition where fluctuations were generated using the method of Mathey et al.[36] This led to an increase in the turbulence kinetic energy values near the axis, so the difference was decreased to 9%. What also deserves attention is the impact of the boundary condidion on the shape of the vortex rope. The authors first tried to visualize it with an isosurface of static pressure, but the vortex rope was hardly distinguishable among the structures generated at the inlet boundary condition. To this point, they state that a pressure decrease can also be caused by unsteady straining and viscous effects. Therefore, they resorted to the Δ-criterion, which better highlighted the vortex rope; see Fig. 1.9. The fidelity of this boundary condition is, however, arguable. Although the turbulence kinetic energy profile was improved, the pressure field is disputable. The isocontour in the figure suggests that for cavitation numbers low enough, the whole inlet should be cavitating together with the vortex rope. In the presented experiments, however, only the vortex rope was cavitating (see the pictures in the cited paper).

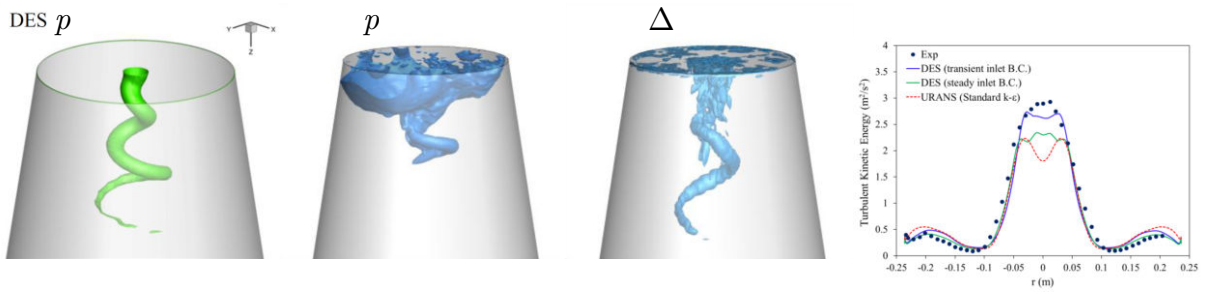

Fig. 1.9: *Left: vortex rope from a DES simulation with a steady inlet boundary condition visualized as a static pressure isosurface, middle: vortex rope from a DES simulation with an unsteady inlet boundary condition visualized as a static pressure isosurface (left) and a Δ-criterion isosurface (right), right: turbulence kinetic energy profiles in a transverse draft tube cross section. Pictures by Foroutan and Yavuzkurt*[35].

Susan-Resiga et al.[10] studied the velocity profiles at the draft tube inlet. They showed that it is possible to express them as the sum of three vortex models: rigid body rotation, a Batchelor vortex with a large radius and a positive axial velocity rotating in the opposite sense to the turbine runner, and a Batchelor vortex with a small radius rand a negative axial velocity rotating in the same sense as the turbine runner. The parameters in the equations that describe these vortices are smooth functions of the flow rate. The resultant profiles were later used by other authors in their numerical studies. Rajan and Cimbala[37] belong to them. They simulated the vortex rope with the DES turbulence model in commercial solver Fluent. In Fig. 1.10, their visualizations of the vortex rope using isosurfaces of different quantities are presented. It turns out that the static pressure isosurface captures only a part of the whole structure. It can be fully captured by quantities derived for the purpose of vortex identification. With one of them, the Q-criterion, the authors visualized the vortex rope in four different operating points; see Fig. 1.11. It can be observed that with decreasing flow rate, the vortex rope becomes longer, its opening angle increases, and pressure in its core

decreases, leading to stronger pressure pulsations. It should be noted that the lowest flow rate corresponds to 91% of the BEP value, meaning that the covered operating range is rather narrow.

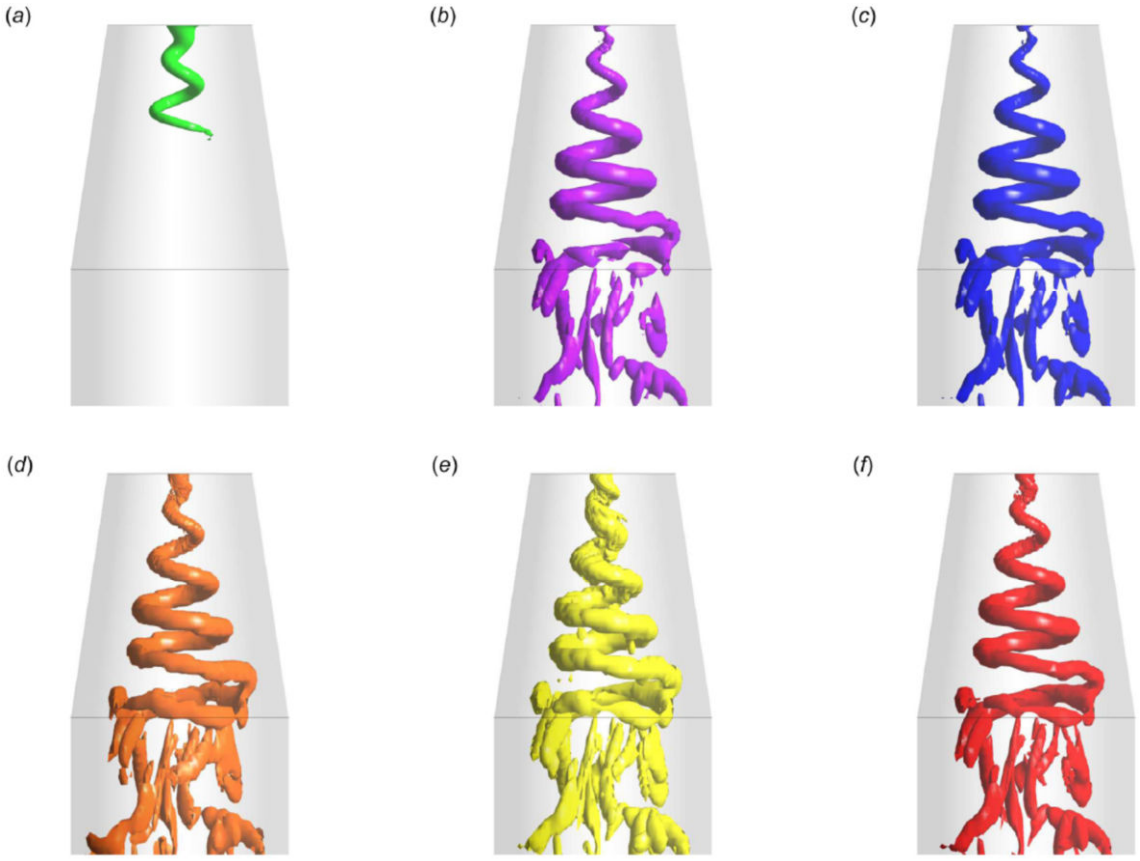

Fig. 1.10: *Visualizations of the vortex rope by Rajan and Cimbala*[37] *using isosurfaces of various quantities: (a) static pressure, (b)* λ_2*-criterion, (c)* Q*-criterion, (d) real eigen helicity, (e)* Δ*-criterion, (f) swirling strength.*

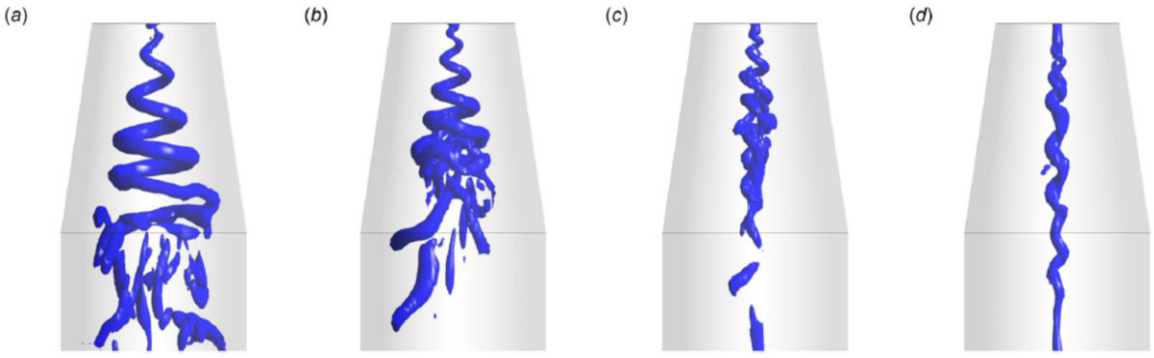

Fig. 1.11: *Visualizations of the vortex rope by Rajan and Cimbala*[37] *using* Q*-criterion isosurfaces for various operating points given by the values of flow coefficient* φ *(the same definition as in Fig. 1.4): (a)* 0,34*, (b)* 0,35*, (c)* 0,36*, (d)* 0,37 *(BEP).*

Another project that led to a large amount of data from experiments with a Francis turbine is called Francis-99. It builds on a previous project called Turbine-99[38] where a Kaplan turbine was studied.

In the case of the Francis-99 project, flow in a low specific speed Francis turbine model was investigated (prototype is installed in the power plant in Tokke, Norway). The data are published on the project website[39].

From the point of view of vortex rope studies, interesting results come from the second workshop within this project, which was aimed at CFD simulations of transient phenomena. Minakov et al.[40] simulated turbine startup in commercial solver Fluent using a hybrid turbulence model based on k–ω SST and delayed detached eddy simulation (DDES) models. The domain was discretized into a polyhedral grid without boundary layer refinements. This is justified by the fact that only the vortex rope was of interest. A further simplification resided in omitting the spiral case and the guide vanes. As a velocity boundary condition at the runner inlet, the profiles from the experimental measurements were prescribed. The flow in the runner was modelled in a rotating frame of reference. The results are presented in Fig. 1.12. It turns out that in deep part load (the flow rate in the first snapshot is approximately 10% of the BEP flow rate), there exists a huge long vortical structure in the draft tube. This vortex causes significant pressure pulsations. As the flow rate is increased, the structure becomes less compact until, close to BEP, a smaller spiral vortex rope with a lower pitch and a high opening angle emerges. Finally, in BEP, a long straight vortex starting from the hub tip was observed.

The same authors present in a different paper the results of testing the ability of turbulence models to predict the vortex rope behavior in part load. It was found out that the k–ω SST model is too dissipative, while the RSM model predicts a vortex rope of the same rough shape as more detailed DES and LES simulations. It cannot capture the tendency of the vortex rope to break into two intertwined structures, which is a matter of finer scales (see Fig. 1.13).

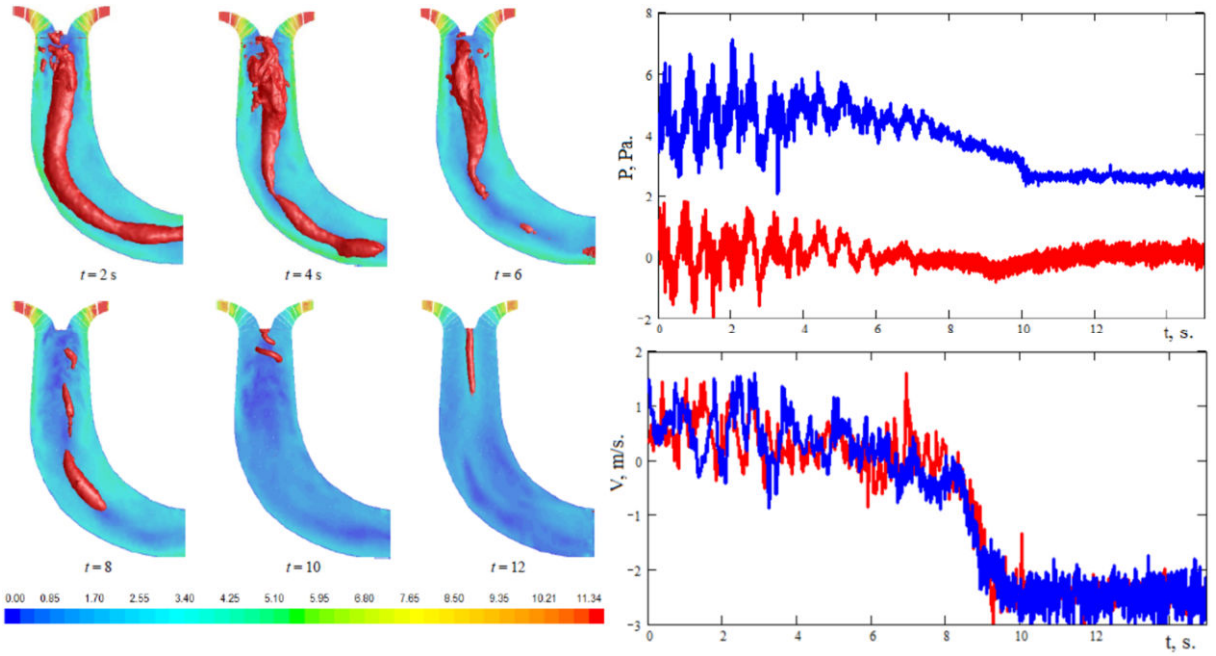

Fig. 1.12: *Left: visualizations of the vortex rope using a static pressure isosurface and a longitudinal slice of the velocity magnitude field by Minakov et al.[40] from the second workshop of the Francis-99 project. Right: static pressure evolution in time at a point at the draft tube wall (top) and axial velocity evolution in time at a point near the draft tube axis (bottom). Red: experimental measurements, blue: CFD simulation.*

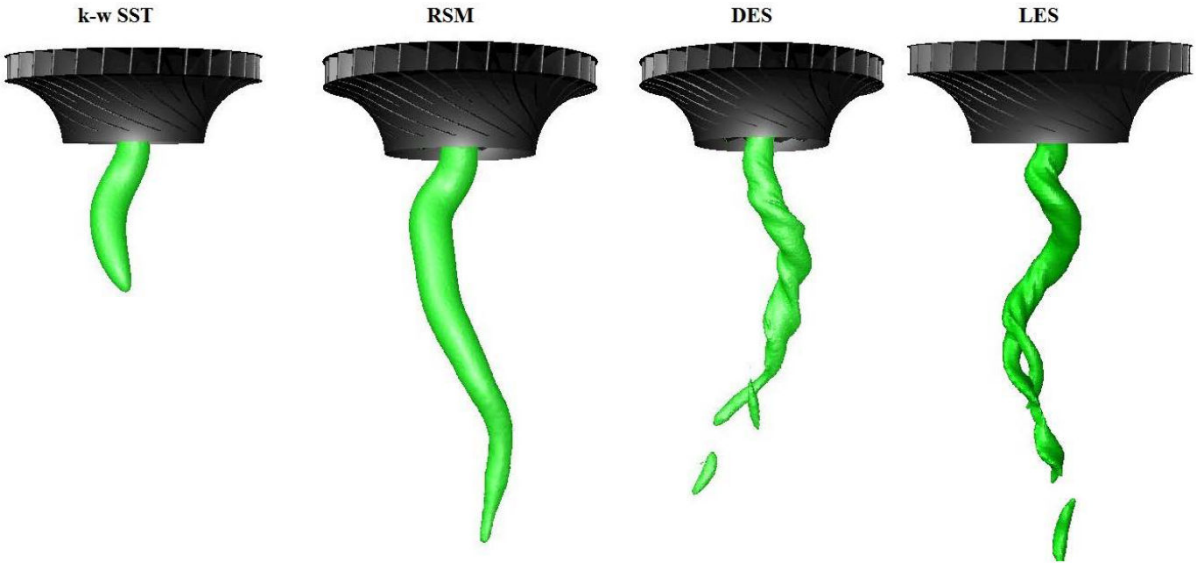

Fig. 1.13: *Vortex rope visualizations from the second Francis-99 workshop by Minakov et al.*[41] *Different turbulence models are compared.*

Cheng et al.[42] performed a similar test in commercial solver CFX with the same result. They concentrated on the VLES model. It bridges scale-resolving LES simulations and models based on Reynolds averaging. They point out that with the first (coarsest) mesh, the pressure in the vortex rope core was above the vapor pressure, which is in contrast with the experiments in which cavitation was observed. As they refined the mesh, the pressure in the vortex rope core decreased. It required a mesh with 10 million cells to arrive at a pressure value lower than the vapor pressure. Simultaneously, the pressure isosurfaces visualizing the vortex rope get longer as the mesh is refined; see Fig. 1.14. To this point, Dörfler[27] recommends the vortex rope core to be resolved by at least 20 grid cells, otherwise the velocity gradient and the pressure drop are underpredicted.

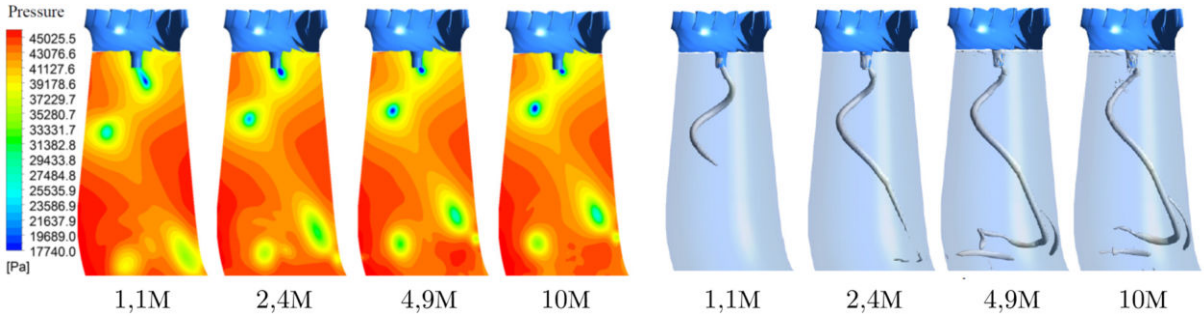

Fig. 1.14: *Pictures illustrating the effect of grid refinement on VLES simulation results by Cheng et al.*[42] *Left: longitudinal slices through the static pressure field, right: isosurfaces of the* λ_2*-criterion.*

In Stuttgart High Performance Computing Center, very detailed simulations of the flow in water turbines are performed. Krappel and Riedelbauch[43] tested the k–ω SST model and the hybrid SAS–SST model with different discretization schemes on different grids in commercial solver CFX version 17.0. The finest grid contained 300 million cells. The first mentioned model led to overestimated hydraulic losses and premature detachment of the boundary layer from the draft tube

wall. Regarding the hybrid model, the authors point out that it is necessary to avoid extensive dissipation that may be caused by the grid size and the convective term discretization.

Junginger and Riedelbauch[44] simulated flow in a propeller turbine in full load using the scale adaptive simulation (SAS) and the stress-blended eddy simulation (SBES) turbulence models. The results indicate that SAS resolves significantly fewer eddies compared to SBES. Moreover, SBES correctly predicted all important integral parameters (in the range of the uncertainty of experimental measurements) on the finest two grids (50 and 100 million cells).

To conclude this section, it should be noted that all the works presented herein assumed single-phase flow. In reality, cavitation often occurs. It is known that cavitation can significantly affect flow, including the vortex rope shape. However, cavitating flow modelling is beyond the scope of this work.

1.3 Pressure pulsations induced by vortex rope

Manifestations of flow in the draft tube are directly related to the vortex rope regimes treated in the previous sections. For many phenomena, there is no clear explanation. The situation is also complicated by the incomparability of model tests with the prototype unit. For studies of pressure pulsations, the eigenfrequency of the hydraulic system is important. It is often incomparable due to different mounting, materials, replacement of the penstock by a pressure tank, and other factors. Unreachability of the complete dynamic similarity also plays its role. Oftentimes, the Froude number of the model significantly differs from the prototype. It is defined as $\mathrm{Fr} = \sqrt{H/L}$, where H denotes the turbine head and L denotes a characteristic dimension.

Best described in the literature are pulsations that occur in the regime with a single regular vortex rope. Nishi[14] divides the pulsations at the vortex rope precession frequency into synchronous and asynchronous parts. The synchronous part is characterized by the fact that the phase is the same throughout the whole circumference. On the other hand, the asynchronous part exhibits a phase shift that often corresponds to the angle between the pressure transducers. It follows that the asynchronous part is a consequence of the vortex rope precessing motion. The synchronous pressure pulsations propagate throughout the systém; they are associated with fluctuations in the output power and sometimes also with axial vibrations. Radial vibrations are, however, caused by asynchronous pressure pulsations[27].

It was found out that the synchronous component strongly depends on the cavitation number. Nishi[46] describes the emergence of strong synchronous pressure pulsations as a resonance condition where the frequency of the pulsations (corresponding to the vortex rope precession frequency) coincides with the eigenfrequency of the hydraulic system. In practice, this happens only when the vortex core is filled with a gas, e.g. due to cavitation or dissolved gas, leading to higher compliance. Without the presence of gas, the eigenfrequency of the system is typically significantly higher than the vortex rope precession frequency. This effect is modelled by a quantity called cavitation compliance, introduced by Brennen[47] and later elaborated for water turbines by Dörfler[48]. Nishi also found out that strong synchronous pressure pulsations at the vortex rope precession frequency can occur only in elbow draft tubes, not in straight ones. The origin shall therefore be sought in the effect of the vortex rope dynamics on the flow in the draft tube elbow. A case of such a flow was studied numerically and experimentally by Skoták[20]. The dependence of the pressure pulsations amplitude in both elbow and straight draft tubes on the cavitation number is depicted in Fig. 1.15. Stuparu and Resiga[49] found out that synchronous pressure pulsations can also occur in

a straight draft tube, but, compared to elbow draft tubes, at a lower frequency than the vortex rope precession frequency. They found a connection of these pulsations with changes of the vortex rope shape in time.

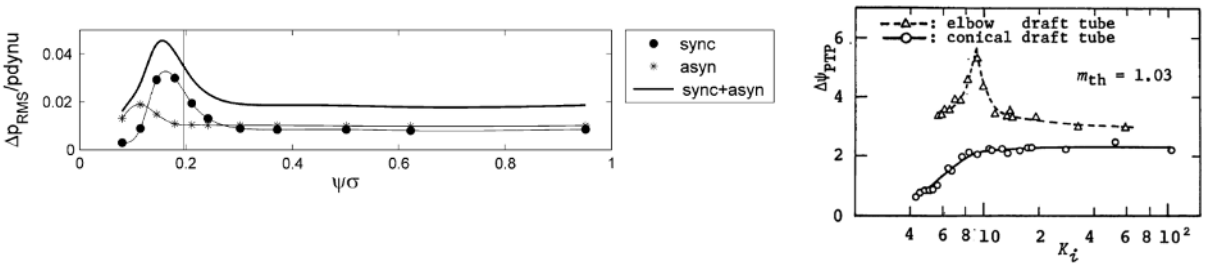

Fig. 1.15: *Dependence of the synchronous and asynchronous pressure pulsations amplitude on the cavitation number by Dörfler*[27] *(left) and comparison of the pressure pulsations amplitude in straight and elbow draft tube by Nishi*[46] *(right).*

In upper part load, with the flow rate in the range from 70% to 85% of the BEP flow rate, pressure pulsations with a significant peak at a frequency higher than the runner rotational frequency (Nicolet[45] reports from 2 to 4 times higher) were observed. This peak is accompanied by other peaks, with the differences between them corresponding to the precession frequency of the vortex rope. Koutník et al.[50] observed that the pulsations at the base frequency are synchronous, while pulsations at the neighboring peak frequencies are asynchronous. Experimental studies suggest that the pulsations are caused by the rotation of the vortex rope about its center line. The key factor is that its cross section is elliptical[45, 50, 51]. A mathematical model based on the Lagrangian description of continuum, describing the motion of the elliptical vortex rope and the condition of its emergence, was also derived[52]. A comprehensive study of these pulsations has recently been published by Dörfler[53]. He states that the pulsations are caused by instability of the second eigenmode of a system with a cavitating vortex rope. A positive fact is that although the manifestations in models were very intensive, no such problems were encountered in prototypes. Nicolet[45] explains it as a consequence of the Froude number mismatch. Dörfler[27] presents a case supporting this theory, namely a turbine with a horizontal draft tube, where the manifestations in a model and in the prototype agreed.

Another type of pressure pulsations is those connected with the transition between vortex rope regimes (see section 1.1). It concerns the range from 80% to 90% of the BEP flow rate, mostly in high specific speed turbines[54]. Abrupt changes in pressure may be observed, even in the prototype[27].

Platonov et al.[55] draw attention to a phenomenon not yet well studied: the formation of a vortex ring. It can be encountered in a narrow operating range where the vortex rope is long and thin. It is manifested by the vortex filament twisting into a loop, leading to an intersection followed by the detachment of the vortex ring and spiral vortex reconnection. The detached vortex ring often travels to the draft tube wall, leading to abrupt pressure changes upon impact. The authors were the first to observe this phenomenon in a model turbine. Previously, this phenomenon was studied in swirl generators by Skripkin et al.[56] and Štefan et al.[57]

1.4 Measures for vortex rope mitigation

Fins in the draft tube

Suitable fins in the draft tube may effectively mitigate the synchronous pressure pulsations and their resonance amplification. Their effect on asynchronous pressure pulsations is less pronounced[27]. The aim of fins is to reduce the swirl, so they are attached perpendicularly to the draft tube wall. Characteristic dimensions are their height and length.

Nishi[58] studied the effects of fins of two types. An important finding is that the fins may lead to even worse pulsations in certain circumstances. It is also necessary to take into account their lifetime if the fins are exposed to cavitation. Another finding is that the vortex rope precession frequency increases with the height of the fins. The mechanism of fins resides in affecting the hydraulic system eigenfrequency as well as the source of the resonance itself, which is the oscillation of the pressure recovery coefficient at the vortex rope precession frequency. If the fins lead to a reduction in cavitation, the hydraulic system eigenfrequency increases, and the resonance is therefore delayed. Without this effect, the system gets closer to the resonance point, which is caused, as was mentioned, by the increased vortex rope precession frequency.

An unwanted effect of fins is vortices forming at their tip. In their core, cavitation is typically present, leading to erosion as they approach the draft tube wall. One of the protection methods is air admission through a small hole on the back side of the fins, exploiting the lower pressure in the wake[27, 59]. Fins with the possibility of air admission were thoroughly numerically studied by Kim et al.[60]. Air admission was not assumed in the calculations. The results show that the efficiency drop is between 0.5 and 1%. A positive effect is that the amplitude of pressure pulsations was reduced by 41% in the most severe case.

Runner cone extension

The principle of this measure is that it fills the stagnant and backflow regions at the draft tube axis. Thanks to this, the vortex rope forms farther downstream, leading to less intense pressure pulsations[61], or instead of a single vortex rope, twin vortex ropes rotate around the extended cone[27]. Gogstad mentions in his contribution[61] the results of Vekve's dissertation[62], where different cone extensions were studied. The longest of them, with a length of 0.41 times the runner outlet diameter, was also applied in the prototype unit (Litjfossen power plant in Norway), leading to an efficiency drop of 0.5% and a decrease in the amplitude of pressure pulsations between 30 and 40%. Vekve states that wider extensions lead to a decreased adverse pressure gradient thanks to a smaller cross section and consequently prevent vortex rope formation.

Admission or injection of air

This measure is based on changing the dynamical properties of the system and affecting the flow by admitting air into the draft tube. It is poorly-effective in horizontal turbines as the air moves upwards due to buoyancy and therefore does not affect the vortex rope[27]. In the past, air admission inlets were located on the draft tube walls[63], while in the present time air admission through a hollow shaft and the runner cone is preferred[64]. Daskiran et al.[65] published an interesting work regarding this topic. They propose utilization of a pump turbine for wastewater aeration. The concentration of dissolved oxygen must be within 1–2% for aerobic bacteria to dissolve pollutants. The authors used LES simulations to find out that for aeration, inlets at the draft tube walls are

more effective, while for diminishing pressure pulsations, air admission through the runner cone performs better. Namely, without aeration, the amplitude of pressure pulsations at the studied operating point was 12.4% of the turbine head. With air admission through the runner cone, it was decreased to 3.8%, while with air admission through the draft tube wall, it was reduced to 5.8% with continuous admission and to 7% when intermitent admission was used.

Chirkov et al. [66] performed a numerical simulation of air injection (neglecting air compressibility) into the draft tube through the runner cone. It turned out that with a flow rate of only 0.1% of the water flow rate, the amplitude of pressure pulsations decreased several times, and at 0.4% of the water flow rate, the pressure pulsations were practically suppressed. The authors observed a reduction in cavitation and an effect of air bubbles on the flow.

Unterluggauer et al.[67] present a numerical study of air injection upstream of the runner. The aim was to increase the life expectancy of the runner that was subject, among others, to the dynamical load caused by vortex shedding at the trailing edge. This method of air injection led to a sheet of air enclosing the blades, reducing the load, but had no effect on the vortex rope in the draft tube. The reason is that the highest air concentrations were found at the crown. Therefore, the authors recommend combining with the mentioned injection through the runner cone. Platonov et al.[55] went even further by injecting air into the spiral case of a model turbine. From high speed camera recordings, it is apparent that the air was dispersed throughout the whole draft tube and did not prevent the emergence of cavitating vortical structures. Nevertheless, in part load, the amplitude of pressure pulsations was noticeably reduced. In contrast, it was higher near BEP. Air injection may worsen the situations even in part load, as observed by Muntean[68] or Koutník[69] in Štěchovice pumped-storage power plant.

Water jet injection

Resiga et al.[70] introduced a technique based on injecting water into the draft tube through the runner cone. The effect resides in the acceleration of the flow in the stagnant region at the draft tube axis. This leads at first to changes in the vortex rope shape and its precession frequency. When the jet flow rate is high enough, the vortical structure is completely suppressed. The water injected into the draft tube is taken from the spiral case, so it must be counted as a volumetric loss. However, one of the water jet injection effects is an increase in efficiency, so with a suitable design, an overall efficiency drop can be avoided[71]. This solution was later modified so that water is taken from the diffuser outlet. Tests were carried out on a swirl generator[2]. The flow rate necessary to suppress the vortex rope was found to be 12% of the swirl generator flow rate. The pressure difference between the diffuser outlet and the injection point provided 10% of the swirl generator flow rate, meaning that the rest needed to be provided by a pump, in this case by an ejector[72].

Water jet injection into the draft tube later gained interest among other researchers. Altimemy et al.[73] carried out LES simulations of water jet injection both through the runner cone and the draft tube walls. The first method was shown to be more effective. Its application in practice is hindered by the need for a water circuit in the vicinity of the turbine electric generator since there is a risk of water leakage that could eventually lead to dangerous situations. The effect of water jet injection through the runner cone for different flow rates is presented in Fig. 1.16.

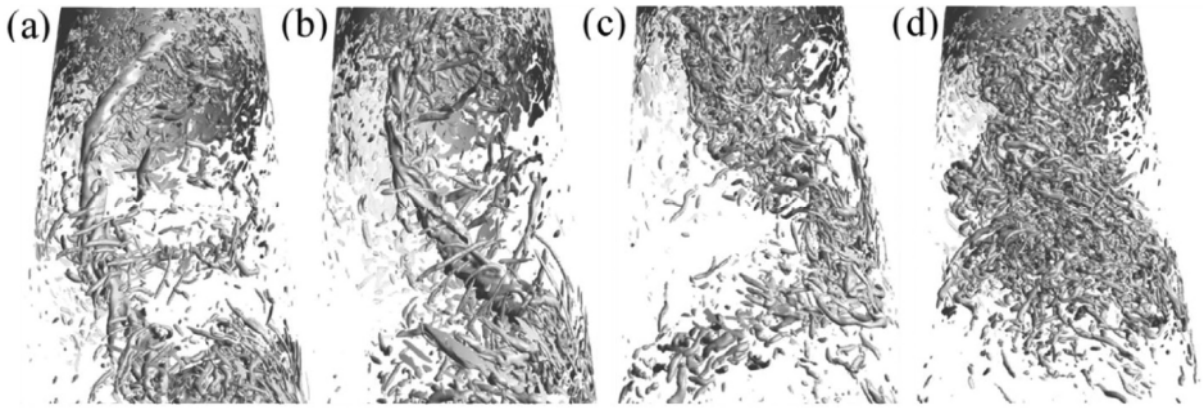

Fig. 1.16: *Isosurfaces of the Q-criterion during water jet injection through the runner cone by Altimemy et al.*[73] *The flow rate is a)* 0%, *b)* 2%, *c)* 4%, *and d)* 6% *of the turbine flow rate.*

Other measures

Blommaert et al.[74] proposed a device generating counterpulses to pressure pulsations observed in a model Francis turbine. The device effectively suppressed pulsations at the vortex rope precession frequency but amplified pulsations at its superharmonics.

Feng et al.[75] carried out numerical simulations of several passive measures. These included a runner cone extension, damping gates, and flow deflectors. The calculations were performed in commercial solver CFX version 14.0 with k–ω SST turbulence model. The results in Fig. 1.17 show that the runner cone extension has little effect, damping gates lead to a smaller vortex rope with a higher precession frequency and a decreased pressure pulsations amplitude, and finally flow deflectors even have a slightly better effect. When using such installations, dynamic load and cavitation effects must be taken into account[20].

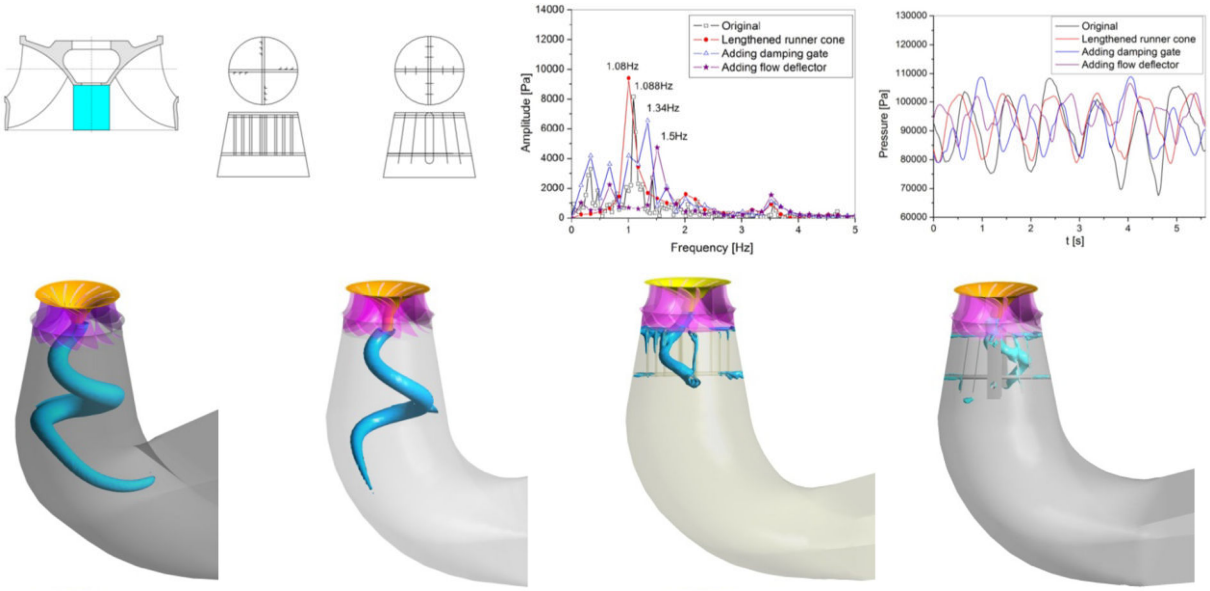

Fig. 1.17: *Tested installations (top left), resultant evolutions of pressure in a selected point and their frequency spectra (top right), and visualizations of the vortex rope (bottom) by Feng et al.*[75]

2 Studies of vortex rope in swirl generators

Model turbines are essential if the aim is to get a solid notion of the real prototype behavior. For general research of the vortex rope without relation to a specific case, the question arises whether it is meaningful to invest in a model turbine in its whole complexity. General research of vortex breakdown was conducted in simple swirl generators with tangential inlet, axial outlet, and guide vanes to control the swirl intensity. With such a device, despite all the inherent simplifications and even with air as a fluid, Cassidy and Falvey[22] were remarkably successful in predicting the pressure pulsations amplitude of a real turbine in part load. They exploited dimensionless similarity criteria. Nishi[14] conducted measurements of a model turbine, from which he later removed the runner. He found out that even without the runner, characteristic features of the draft tube flow can be reproduced, e.g. the vortex rope precession or resonance amplification of pressure pulsations. These findings motivate the use of simple swirl generators instead of model turbines if possible.

Swirl generator designed at UPT in Timisoara

Resiga et al.[76] pointed out that in vortex generators without an impeller, the flow entering the diffuser has different characteristics compared to turbines. From Bernoulli's equation, if dissipation is neglected (i.e. an inviscid fluid is assumed), it follows that the total pressure is constant along streamlines. In swirl generators with fixed blades and a single inlet, all streamlines that pass through the inlet (where the total pressure is constant if the velocity profile is uniform) continue throughout the domain to the outlet. Therefore, the total pressure is constant everywhere. This does not correspond to turbines, where streamlines passing through the inlet end on the runner blades. Downstream of the runner, the total pressure varies across the cross section, namely it is lower at the axis or hub and higher at the outer walls.

For the above-mentioned reasons, the authors designed an axial swirl generator where the liquid flows at first along fixed blades, creating a free vortex, and then passes through a runner with an outlet profile corresponding to that in actual turbines. Namely, velocity profiles measured in the FLINDT project were the design goal. The shape of the blades corresponds to turbine blades at the hub, leading to a lower total pressure at the outlet, and to pump blades at the tip, leading to an increased total pressure. As a result, the desired total pressure profile is achieved, and the runner can rotate freely without braking. However, that would provide only a single operating point, so a magnetorheological brake[77] that can be used to lower the rotational speed was included. This leads to various conditions at the runner outlet and thus different forms of the vortex rope[78].

The generator from Timisoara was later improved by Skripkin et al[79]. The modification concerns the method of runner speed control, which is realized by means of magnetic coupling between the runner and a ring outside of the generator driven by an external electric motor; see Fig. 2.2.

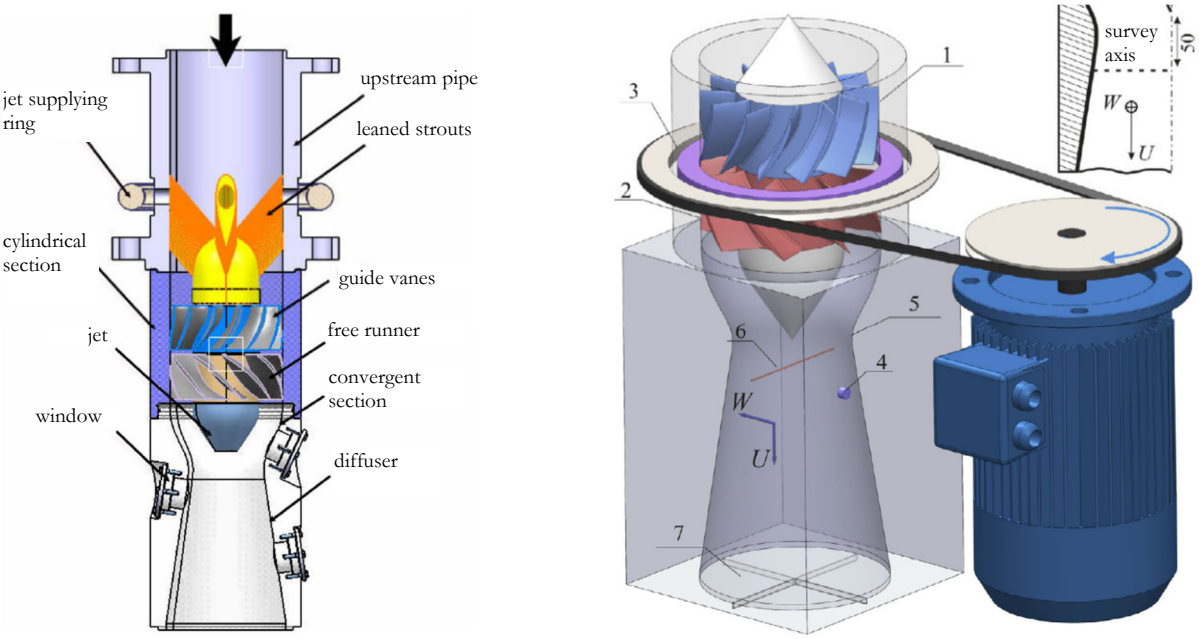

Fig. 2.1: *Swirl generator by Resiga et al.*[78] *(left) and Skripkin et al.*[79] *(right) (edited).*

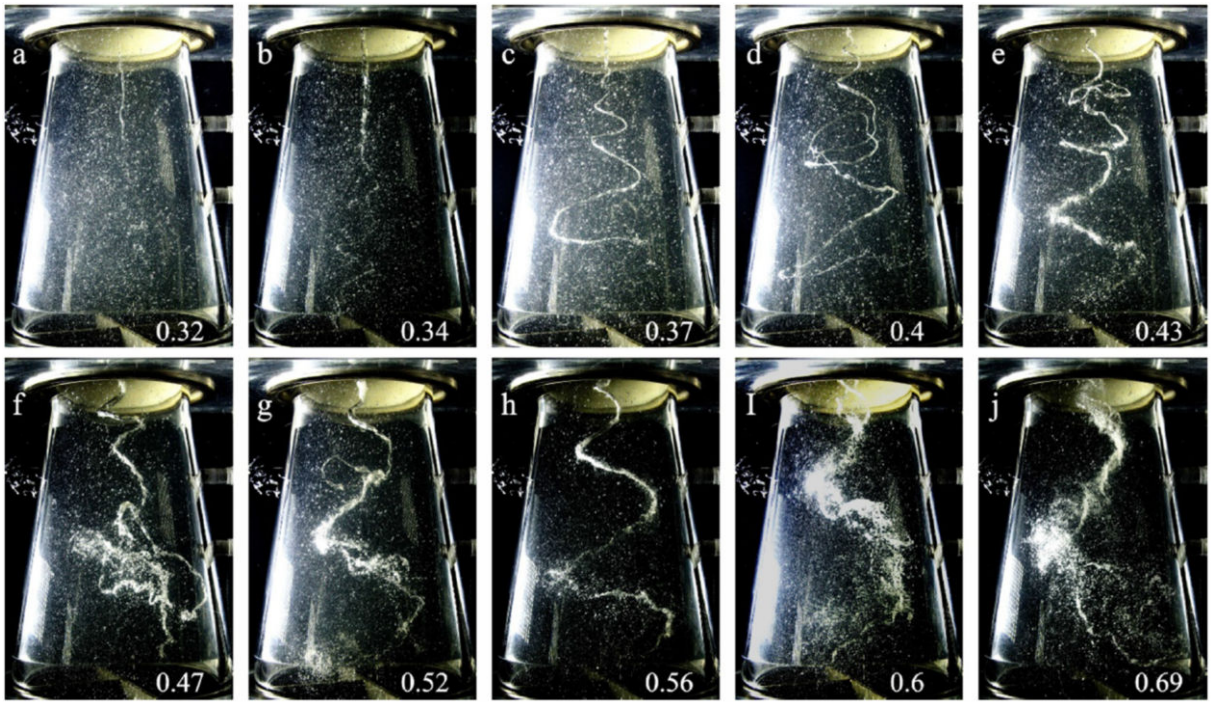

$$S = \frac{1}{R}\frac{\int_0^R r^2 v_\varphi v_z \,\mathrm{d}r}{\int_0^R r\, {v_z}^2 \mathrm{d}r}$$

Fig. 2.2: *Different forms of vortex rope for different swirl numbers in the generator of Skripkin et al.*[79]

Swirl generators designed at BUT in Brno

Rudolf[80], followed later by Štefan[81], aimed at maximal design simplicity and designed axial swirl generators with fixed blades. The disadvantage is the impossibility of changing the swirl number, so only one vortex rope regime is observed. It is still possible to adjust the flow rate and pressure, allowing studying the shape and behavior of the vortex rope for different cavitation numbers. The geometries and results of CFD simulations are presented in Fig. 2.3. It is evident that in the generator with a higher blade curvature, and thus a higher swirl number, a larger vortex rope with a higher pitch is observed, which is in accordance with the vortex rope observations in model turbines described in the previous chapter. For the generator with the higher swirl number, extensive experimental investigations were carried out. Among others, it was found out that synchronous pressure pulsations at a frequency lower than the vortex rope precession frequency are present, which is in agreement with the previously mentioned finding by Stuparu and Resiga.[49] These pulsations were found to be related to the vortex rope shape instability.

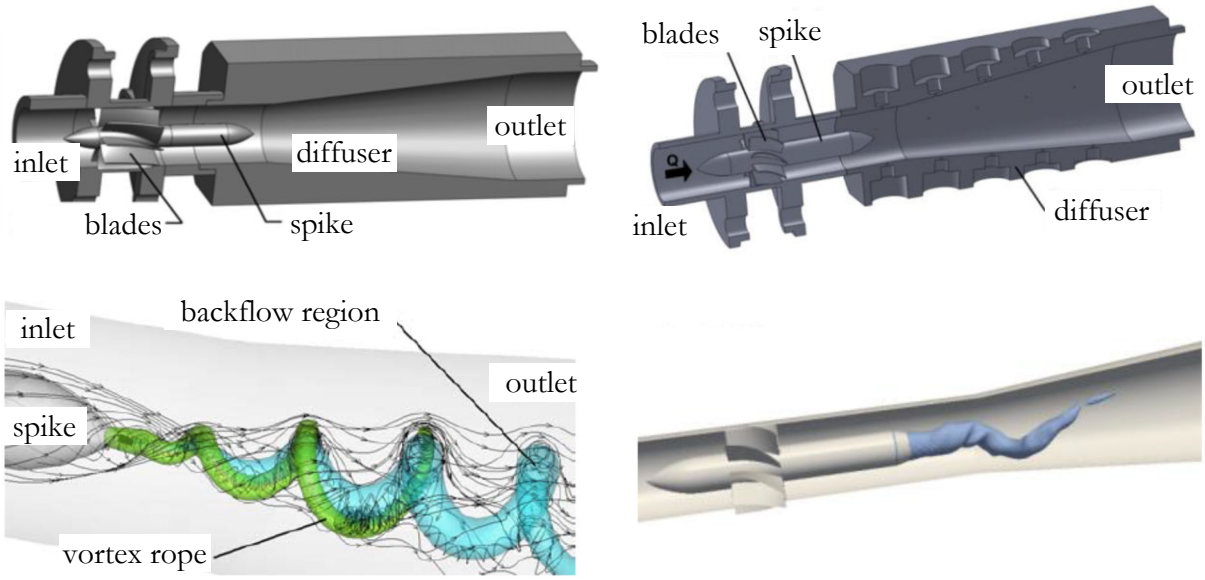

Fig. 2.3: *Swirl generators designed at BUT in Brno and results of CFD simulations, where the vortex rope is visualized using a pressure isosurface (edited)* [81, 82].

3 Design of a new swirl generator

The swirl generators described in the previous chapter can all be considered extreme cases. The generators of Resiga and Skripkin aim at flow matching that in actual water turbines, which is paid for by the design complexity. Rudolf and Štefan used very simple devices manufactured by 3D printing. The cost is the impossibility to change the swirl number. The first goal of this work is to design a new swirl generator in between these cases. The primary requirement is the ability to operate in a wide range of swirl numbers while still being easy to manufacture and relatively cheap, i.e. without moving parts, bearings, etc.

If fixed blades lead to a fixed swirl number and a runner is to be avoided for design complexity and financial cost, then the swirl at the diffuser inlet needs to be generated another way. The idea used here is to include a second inlet pipe ended by a spiral case generating the tangential velocity. Having two inlets allows setting a wide range of swirl numbers. The resultant flow coming to the diffuser is given by mixing the two inlet flows – the first is purely axial (further on referenced simply as the axial inlet), the second has a tangential component generated by the spiral case (further on referenced simply as the tangential inlet). It follows that increasing the ratio of the tangential to axial inlet flow rates increases the swirl number. A drawback of this method is the nonuniformity and unsteadiness of the resultant flow. The mixing of two different flows is typically accompanied by vortices as a consequence of the Kelvin–Helmholtz instability. Insertion of a ring with fixed guide vanes is considered for future work.

In the central part of the generator, a placement of a hub has been intended. This part should play the role of the turbine runner cone – at its tip, the vortex rope is expected to form. During the design phase, different shapes of the hub were tested. The first successful design that led to desired results is presented in Fig. 3.1. In this case, the downstream part of the hub resembles the turbine runner cone. It is positioned so that the flow passage resembles the flow passage of a turbine runner, excluding the blades. As it was later decided on the possibility of measurements of velocity profiles upstream of the diffuser inlet, a straight section between the spiral casing and the diffuser needed to be included. This led to the final design, where the hub and diffuser inlet shape are inspired by the generator of Resiga. A sketch of the new swirl generator with all dimensions and the coordinate system used throughout this work is presented in Fig. 3.2.

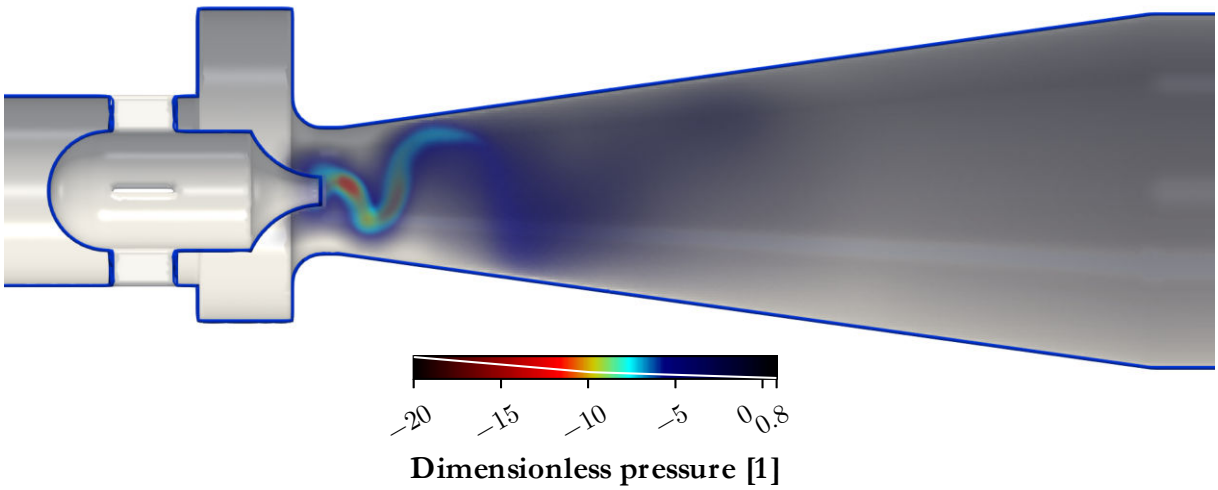

Fig. 3.1: *A slice through the first successfull version of the new swirl generator design including a volume render of the dimensionless pressure field from a CFD simulation with RSM turbulence model. Tangential to axial flow rate ratio is approximately 70:30.*

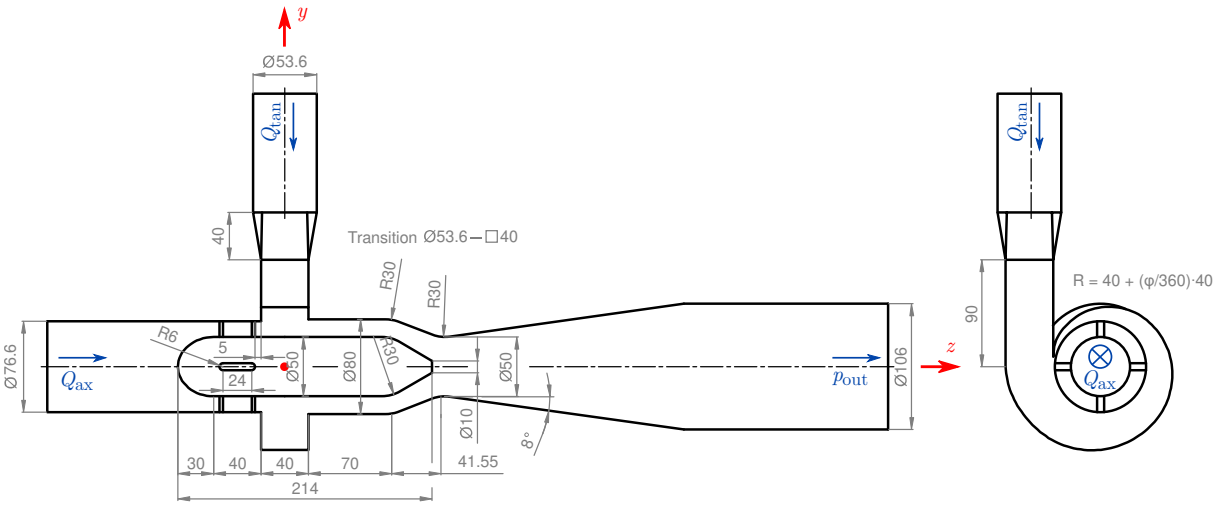

Fig. 3.2: *A sketch of the new swirl generator.*

The final construction design is rendered in Fig. 3.3. Plastic tubes available in the department laboratory were used for both the inlets and the outlet and connected to an existing hydraulic circuit. The diffuser was made of plexiglass and needed to be properly polished with respect to the planned PIV measurements. The spiral case was made from two blocks with a milled flow passage.

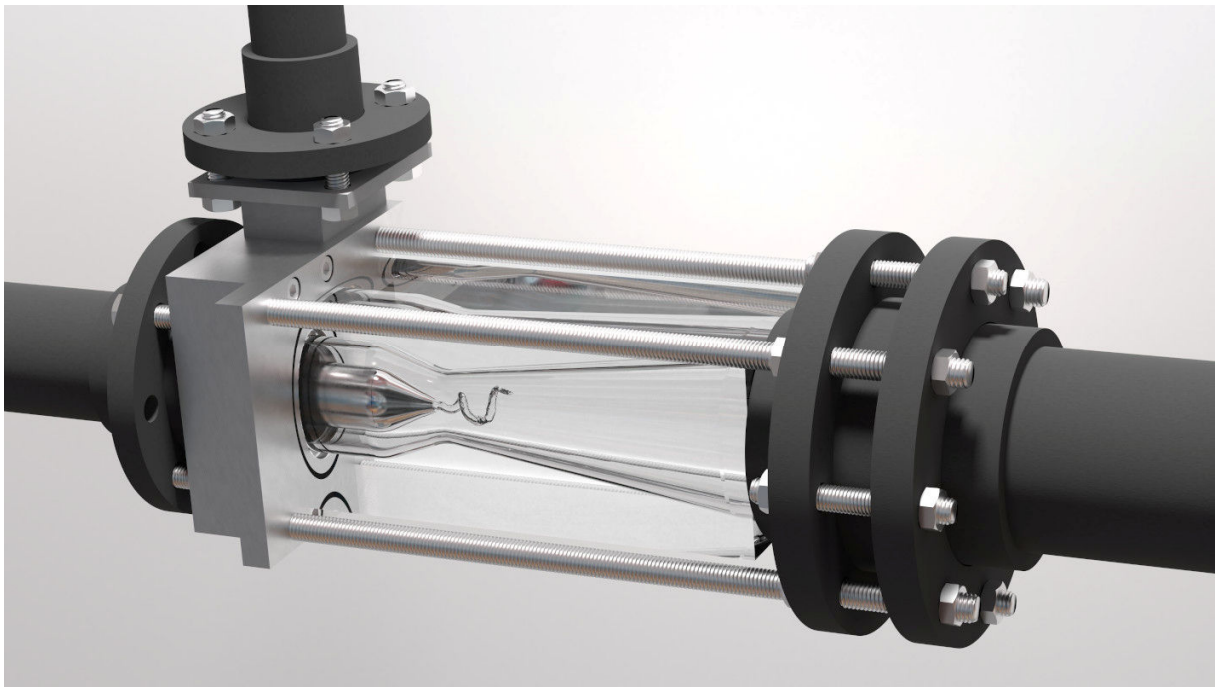

Fig. 3.3: *A render of the final construction design with a vortex rope predicted by a CFD simulation with SBES turbulence model.*

4 CFD simulations

4.1 List of conducted CFD simulations

The conducted CFD simulations comprise both modelling based on the unsteady Reynolds-averaged Navier–Stokes (URANS) equation and scale-resolving simulations. The URANS computations were carried out during the design phase of the swirl generator, while the scale-resolving calculations were performed afterwards to gain more precise results. The SBES turbulence model was chosen based on the results of Junginger[44]. The simulations were performed with commercial software Fluent version 18.1.

The material properties are common for all the simulations and are listed in the table below. They correspond to water at atmospheric pressure and room temperature.

Tab. 4.1: *Material setup of Fluent.*

Materials		
Cell material:	Water (liquid)	
Properties:	**Density [kg/m³]**	**Dynamic viscosity [Pa·s]**
	998.2	0.001003

For each simulation, an abbreviation will be used. The first element is an abbreviation of the turbulence model (e.g. RSM, SBES), the second distinguishes between fixed and transient boundary conditions (F for fixed, T for transient). For fixed boundary conditions, the last three elements represent the total flow rate in liters per second and the percentage of the total flow rate at the tangential inlet and the axial inlet, respectively. For transient boundary conditions, there is only a single number to distinguish among the simulations as the boundary conditions are not so easy to express. The following table summarizes all the simulations and provides the necessary information about their setup.

Tab. 4.2: *List of CFD simulations.*

URANS simulations					
Abbreviation	**Boundary conditions**				Δt **[s]**
	Inlets		**Wall**	**Outlet**	
RSM-F-10-40-60	$Q_{(\mathrm{ax})} = 6\,\mathrm{l/s}$ $Q_{(\tan)} = 4\,\mathrm{l/s}$	D_h = pipe diameter $I = 5\%$	No slip	$p = 0$ Pa $D_\mathrm{h} = 0.106$ m $I = 10\%$	10^{-4}
RSM-F-10-50-50	$Q_{(\mathrm{ax})} = 5\,\mathrm{l/s}$ $Q_{(\tan)} = 5\,\mathrm{l/s}$	D_h = pipe diameter $I = 5\%$			
RSM-F-10-60-40	$Q_{(\mathrm{ax})} = 4\,\mathrm{l/s}$ $Q_{(\tan)} = 6\,\mathrm{l/s}$	D_h = pipe diameter $I = 5\%$			$5 \cdot 10^{-5}$
RSM-F-5-70-30	$Q_{(\mathrm{ax})} = 1.5\,\mathrm{l/s}$ $Q_{(\tan)} = 3.5\,\mathrm{l/s}$	D_h = pipe diameter $I = 5\%$			$3.\bar{3} \cdot 10^{-4}$
RSM-F-10-70-30	$Q_{(\mathrm{ax})} = 3\,\mathrm{l/s}$ $Q_{(\tan)} = 7\,\mathrm{l/s}$	D_h = pipe diameter $I = 5\%$			$3.\bar{3} \cdot 10^{-5}$
RSM-T-1	$Q_{\mathrm{m(ax)}} = 4.5 - 10t$ kg/s $Q_{\mathrm{m(tan)}} = 5.5 + 10t$ kg/s	D_h = pipe diameter $I = 5\%$			10^{-3}

Turbulence modelling	
Reynolds stress equation model, quadratic pressure-strain, non-equilibrium wall functions	
Solution methods and solver settings	
Pressure-velocity coupling	PISO
Gradient	Least squares cell-based
Pressure	PRESTO!
Momentum	QUICK
Transient formulation	Second order implicit
Turbulent kinetic energy	Second order upwind
Turbulent dissipation	Second order upwind
Reynolds stresses	Second order upwind
Iterations/time-step	20

Scale-resolving simulations

Abbreviation	**Boundary conditions**				Δt **[s]**
	Inlets		**Wall**	**Outlet**	
SBES-F-5-50-50	$Q_{(\mathrm{ax})} = 2.5$ l/s $Q_{(\tan)} = 2.5$ l/s	D_h = pipe diameter $I = 5\%$	No slip	$p = 0$ Pa $D_\mathrm{h} = 0.106$ m $I = 10\%$	10^{-5}
SBES-F-10-50-50	$Q_{(\mathrm{ax})} = 5$ l/s $Q_{(\tan)} = 5$ l/s	D_h = pipe diameter $I = 5\%$			$5 \cdot 10^{-6}$
SBES-F-5-60-40	$Q_{(\mathrm{ax})} = 2$ l/s $Q_{(\tan)} = 3$ l/s	D_h = pipe diameter $I = 5\%$			10^{-5}
SBES-F-5-70-30	$Q_{(\mathrm{ax})} = 1.5$ l/s $Q_{(\tan)} = 3.5$ l/s	D_h = pipe diameter $I = 5\%$			
SBES-T-1	$Q_{\mathrm{m(ax)}} = 3 - \frac{2}{1.1} t$ kg/s $Q_{\mathrm{m(tan)}} = 2 + \frac{2}{1.1} t$ kg/s	D_h = pipe diameter $I = 5\%$			
SBES-T-2	$Q_{\mathrm{m(ax)}} = 4 - \frac{0.5}{1.1} t$ kg/s $Q_{\mathrm{m(tan)}} = 1 + \frac{0.5}{1.1} t$ kg/s	D_h = pipe diameter $I = 5\%$			$8 \cdot 10^{-5}$
Turbulence modelling					
k–ω SST, Stress-Blended Eddy Simulation, WALE subgrid-scale model					
Solution methods and solver settings					
Pressure-velocity coupling	PISO				
Gradient	Least squares cell-based				
Pressure	PRESTO!				
Momentum	Bounded central differencing				
Transient formulation	Second order implicit				
Turbulent kinetic energy	Second order upwind				
Turbulent dissipation	Second order upwind				
Iterations/time-step	10 (15 for SBES-T-2)				

To get a notion of the simulated operating conditions, a swirl number was computed and plotted for each of the calculations. For fixed boundary conditions, the swirl number was averaged in time. For transient ones, the swirl number was computed as a function of time. In the literature, there are different definitions of parameters that quantify the level of swirl. The swirl number used herein is defined as the ratio of the axial flux of the tangential momentum to the axial flux of the axial momentum. This definition comes from a work by Chigier and Beér[83] and was later modified by Sheen et al.[84] as follows

$$\mathrm{Sr} = \frac{1}{R}\frac{\int_S r|v_\varphi v_z|\,\mathrm{d}S}{\int_S {v_z}^2\mathrm{d}S} \tag{4.1}$$

where S is a selected circular cross section, R its radius, v_φ tangential velocity and v_z axial velocity. In this case, two cross sections, namely $z = 127$ mm and $z = 160$ mm, were used.

The results are depicted in Fig. 4.1. It can be seen that the flow rate at the tangential inlet must reach almost 20% of the total flow rate to get swirl at the inlet of the diffuser. The swirl number then grows proportionally to the percentage of the total flow rate at the tangential inlet until it eventually flattens out. This is given by the mixing process of the two streams. If the energy of either of them drops below a certain level, the resultant flow in the diffuser is dominated by the other one. Therefore, the present generator is capable of reaching swirl numbers in the range from zero to one. A further increase could be achieved if the flow direction at the axial inlet was reversed. However, this option is not the subject of this work and is left as an idea for future work.

For transient simulations, the swirl number is affected by the rate of change of the boundary conditions. Its values tend to be slightly lower for the simulations where the boundary conditions change faster.

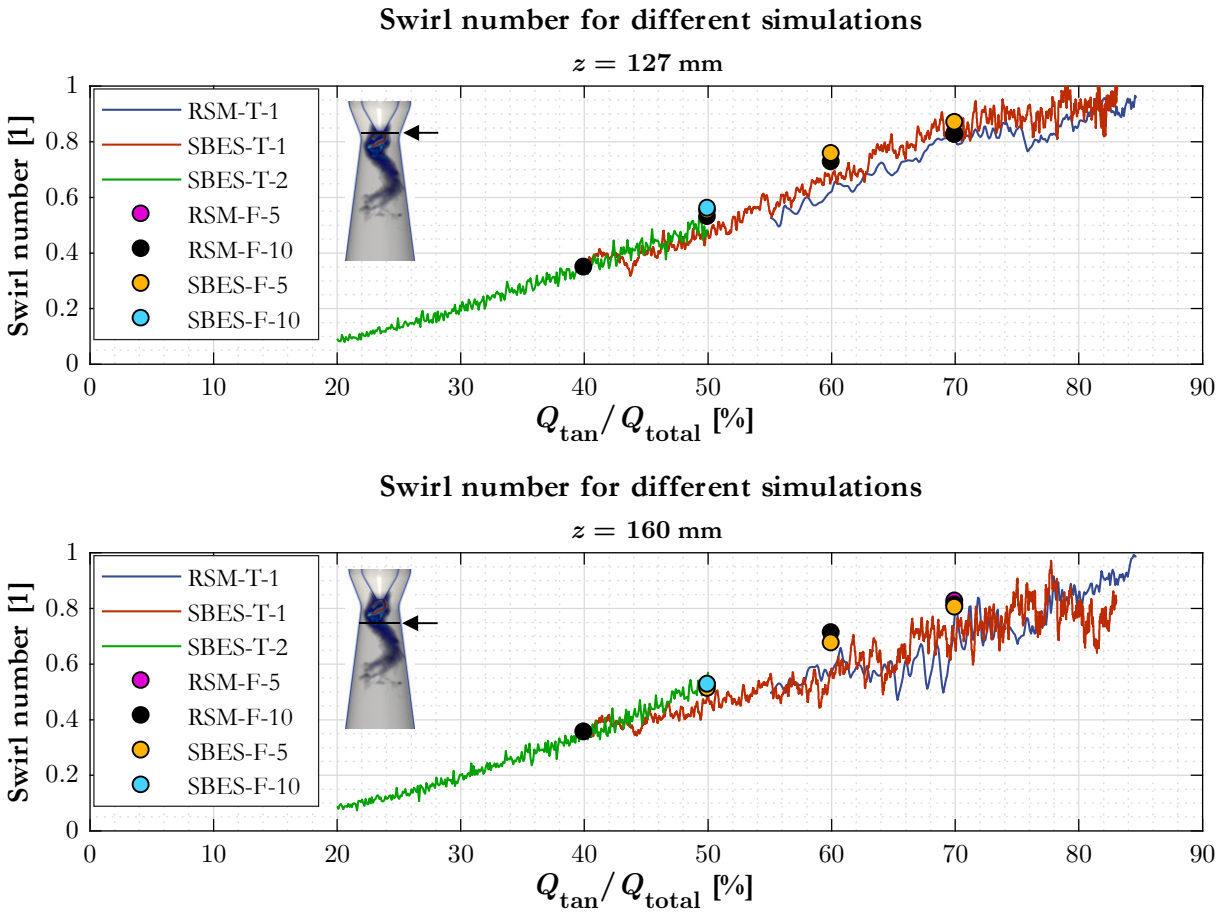

Fig. 4.1: *Swirl number dependency on the flow rates ratio.*

4.2 Methodology of CFD data postprocessing

At the end of CFD calculations, we end up with a large amount of spatio-temporal data. To leverage their content, it is necessary to convert them into meaningful representations that can be processed and understood by the human brain, i.e. to visualize them. This is not a problem in 2D cases, where the data values can easily be coded e.g. by color and plotted on a screen or printed on a paper. Once the case is 3D, we face the problem of how to convert them into 2D representations. This drop in dimension means that the process is irreversible, meaning that it is not possible to obtain all the data back from the resultant visualizations and a portion of the information is inevitably lost. This section describes what is in this work visualized and how, in order to get a good notion of the vortex rope dynamics and other flow features. The results presented here have already been published in a journal paper[85] and the bachelor's theses of Častulíková[86] and Kurková[87].

4.2.1 Data visualization techniques

Once the data for visualization are obtained, the first step is data modification. One can define and compute new variables from the existing ones, restrict the domain of interest by clipping, or interpolate the data to a different grid or data points. New objects can also be generated. These include streamlines and streamsurfaces or streamtubes, vortex lines and vortex tubes, particles and their trajectories, streaklines, and material lines or surfaces. The second step is the generation of objects that will be rendered in the next step. 3D scalar fields can be displayed on a series of 2D slices. One can also extract isosurfaces. Streamlines and other line objects can be visualized as tubes. Various glyphs can be used to visualize particles, vectors, or even tensors[88]. The data values on these objects can be coded by their color, transparency, material properties, textures, or dimensions. For an example with application to a vortex rope case, see a paper by Sadlo[89], where quantities related to vorticity transport were visualized on pathlines using variable radius, segmentation, and different colors. The final step is to render the scene and display the result. Scalar fields can be rendered directly by volume rendering. It is based on a fictitious light particle moving through the data field. Physically-based phenomena, such as emission, scattering, and absorption, can be considered[90]. Their parameters are given by the data values, i.e. we map the data values to a parameter (e.g. the emission strength) using a defined transfer function. In the end, we obtain a 2D field to be displayed on the screen. The development of this technique is driven particularly by medicine with applications to computed tomography (CT) or magnetic resonance imaging (MRI) data[91]. The art of volume rendering resides in the selection of the emission, scattering, and absorption parameters, where it is advisable to make unimportant parts of the data domain completely transparent and find such settings for the rest that provide the best notion of how the scalar values are distributed in the 3D space. For surface rendering, there exist a variety of methods ranging from simple targeted at speed to photorealistic, developed primarily for computer-generated imagery (CGI) with applications including movies and video games.

Visualizations in published CFD studies of the vortex rope often rely on simple techniques. The vortex rope itself is visualized usually as an isosurface of a suitable quantity, most often static pressure. Sometimes, a vortex identification method is used, e.g. the Q-criterion, the λ_2-criterion, or the swirling strength, to name the most popular. These criteria are described in section 4.2.4. Recall the already mentioned work of Rajan and Cimbala[37], who compared the static pressure and the mentioned vortex identification methods on a case with the vortex rope corresponding to the FLINDT project. They used a suitably selected isosurface and found out that visualizations based

on static pressure capture only the upper part of the vortex rope, while the vortex criteria capture the whole structure and its disintegration into smaller vortices downstream.

To the author's knowledge, volume rendering is used only seldom in the field of hydraulic machinery. Considering its advantages over dominantly used isosurfaces and its availability in software, it seems to the author as an oversight, especially with regard to the growing numbers of detailed simulations (scale-resolving turbulence models, LES) that capture a rich spectrum of structures (recall e.g. Fig. 1.16). Visualizations with only a single isosurface are similar to a map with only a single elevation contour line. It is possible to determine where a peak might be located in the terrain, but no information is given on its elevation and shape. Similarly, visualizations using only a single isosurface provide no information on what the field looks like both inside and outside of it. A well-made volume render can, in contrast, provide a good notion of the whole visualized scalar field. An example with a vortex rope is given in Fig. 4.2. The dimensionless pressure $\hat{p}$ field is visualized (see section 4.2.3 for definition). We can see that the isosurface of $\hat{p} = -10$ reveals twin spiral structures under the hub tip, but it suggests nothing about the large structure that can be revealed if $\hat{p} = -4$ is used. On the contrary, the isosurface of $\hat{p} = -4$ suggests nothing about the twin spiral structures as they are completely inside the revealed large structure. One possibility is to combine these two isosurfaces in a single picture using transparency. Nevertheless, volume rendering is superior to any number of isosurfaces. It provides a smooth representation of the spatial distribution of $\hat{p} < -2$ thanks to a suitable opacity transfer function. The region of higher values is completely transparent since it is not of interest.

A drawback of volume rendering that should be mentioned is that it is slow on unstructured grids. This is usually overcome by interpolating the data to a structured grid. One issue is with significant local refinements as the structured grid has all cells of the same size. Another issue arises if curved boundaries need to be captured. After the interpolation to a structured grid, they become jagged. Considering that the mentioned issues are not relevant in this work, volume rendering was chosen as the primary method of scalar fields visualization.

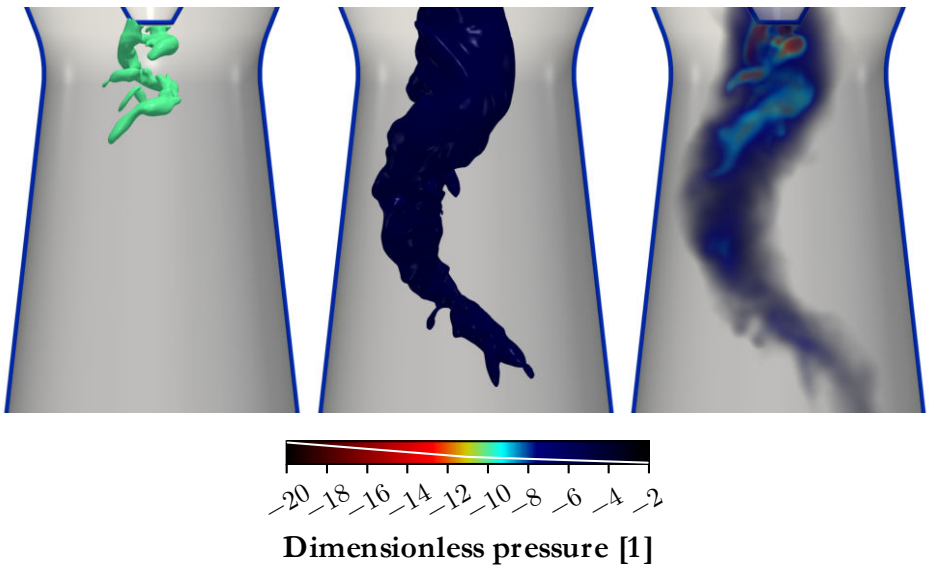

Fig. 4.2: *Comparison of vortex rope visualizations using dimensionless pressure $\hat{p}$. Left: isosurface of $\hat{p} = -10$, middle: isosurface of $\hat{p} = -4$, right: volume render. The white line represents the opacity transfer function of the volume render.*

4.2.2 Software

The visualizations presented in this work were created in ParaView and Blender (both are open source tools). ParaView is a software for data analysis and visualization built on VTK (Visualization ToolKit)[92] and was employed for the prerendering operations (generating 3D surface objects, such as tubes for streamlines, isosurfaces, etc., and generating series of images for volume rendering in Blender) and, in some cases, also for the final rendering. Finite-time Lyapunov exponents, residual vorticity, and $\boldsymbol{M}_Z$-criterion were computed using custom Python programmable filters. Blender is a 3D creation suite that offers tools for the entire pipeline from modelling to rendering, animation, and video editing. Its Cycles renderer offers more control over lighting and material effects and well combines multiple overlapping volume renders. It was used for rendering of the objects generated in ParaView in some cases. The 3D surface objects were exported from ParaView in X3D format. Importing them into Blender and setting up for rendering is straightforward, with many guides publicly available. On the other hand, volume rendering of data fields in Blender is more complicated. A brief guide through this procedure is therefore given in appendix A.

4.2.3 Dimensionless quantities

For comparability of results among different cases, quantities are often nondimensionalized, i.e. scaled relative to a reference value. In this work, velocity and pressure are nondimensionalized. The reference value of velocity is the mean velocity in the throat

$$\hat{\boldsymbol{v}} = \frac{\boldsymbol{v}}{v_{\mathrm{ref}}}, \qquad v_{\mathrm{ref}} = \frac{Q_{\mathrm{total}}}{S_{\mathrm{throat}}} = \frac{4Q_{\mathrm{total}}}{\pi {d_{\mathrm{throat}}}^2} \tag{4.2}$$

where $d_{\mathrm{throat}} = 50$ mm (see Fig. 3.2), and the reference value of pressure is the dynamic pressure exerted by the reference velocity

$$\hat{p} = \frac{p}{p_{\mathrm{ref}}} = \frac{p}{\frac{1}{2}\rho {v_{\mathrm{ref}}}^2} = \frac{p\pi^2 {d_{\mathrm{throat}}}^4}{8\rho {Q_{\mathrm{total}}}^2} \tag{4.3}$$

4.2.4 Vortex identification

The central task of vortex rope visualizations is to identify the vortex rope itself. The simplest way is to exploit the fact that static pressure decreases towards the vortex rope core. This approach is especially suitable for quick explorations as the static pressure is readily available from CFD. Another way is to use various vortex identification methods. Although the intuitive notion of a vortex as a portion of fluid rotating around a common axis (vortex core) is clear, there is no widely accepted rigorous definition capable of clearly distinguishing the vortices among other possible flow structures. Kolář[93] presented a review of the most popular vortex identification methods and summarized the requirements on vortex definitions: objectivity (independence of the reference frame motion), validity for compressible and variable-density flows, and ability to determine the local intensity of swirling motion and the swirl orientation, among others. The problem resides in the

inability of the methods to meet all the requirements and in the arguability of some of them. In the following, some of these methods will be described.

Static pressure

To maintain swirling motion, a centripetal force must act on the particles, which requires a centrifugal pressure gradient. A vortex can therefore be identified in certain cases as a region of decreased static pressure, but generally, there is no guarantee that a given region of low static pressure is actually a vortex. For instance, a vortex can be part of a larger structure, and its effects on the static pressure field may be hardly identifiable if the influence of the larger structure on this field is much greater. As an example, imagine a small vortex in an elbow, where the pressure gradient caused by the elbow is much greater than the pressure gradient caused by the vortex. The vortex will in this case manifest itself as a small disturbance to the static pressure field; there may even be no local minimum in its core. Fortunately, this is not the case of the present swirl generator, so the vortex rope can be identified as a region of low static pressure.

The static pressure may not change sharply enough to clearly distinguish between individual vortices in the energy cascade. Renders of static pressure fields often look like blurred images. For that reason, many criteria were developed to provide a sharp border for the clear identification of individual vortices. A review of these criteria and their applications in hydraulic machinery was published by Zhang et al.[94]

Q-criterion

One of the most popular ones is the Q-criterion by Hunt et al.[95] It is based on the decomposition of the velocity gradient into symmetric and skew-symmetric parts

$$\nabla \boldsymbol{v} = \frac{1}{2}[\nabla \boldsymbol{v} + (\nabla \boldsymbol{v})^{\mathrm{T}}] + \frac{1}{2}[\nabla \boldsymbol{v} - (\nabla \boldsymbol{v})^{\mathrm{T}}] = \boldsymbol{S} + \boldsymbol{R} \tag{4.4}$$

The Q-criterion is then defined as follows

$$Q = \frac{1}{2}(\|\boldsymbol{R}\|^2 - \|\boldsymbol{S}\|^2) \tag{4.5}$$

where $\|\cdot\|$ denotes the Frobenius norm. This criterion is Galilean invariant but not objective[96]. Its meaning can be deduced from the meanings of $\boldsymbol{R}$ and $\boldsymbol{S}$. The first mentioned is related to the rotation of elementary particles as its components are proportional to the components of the vorticity vector, while the second is related to their deformation. Vortices are naturally connected with vorticity, a quantity defined as the curl of flow velocity

$$\boldsymbol{\Omega} = \nabla \times \boldsymbol{v} \tag{4.6}$$

It is a measure of the local spinning motion (rotation of the elementary particles), precisely twice its angular velocity. However, this motion can also be caused by purely shearing flows, as is the case of boundary layers. The vortices are therefore defined as regions with high positive values of Q, i.e. where rotation dominates over deformation. This effectively excludes the boundary layer since there is high vorticity but also high deformation.

Δ-criterion

This criterion by Chong et al.[97] is based on considerations regarding the velocity gradient tensor and its eigenvalues. The eigenvalue problem reads

$$(\nabla \boldsymbol{v})\boldsymbol{e}_i = \lambda_i \boldsymbol{e}_i \tag{4.7}$$

where $\boldsymbol{e}_i$ is the i-th eigenvector, assumed to have unit magnitude, and λ_i is the i-th eigenvalue. This equation can be rearranged to $(\nabla \boldsymbol{v} - \lambda_i \boldsymbol{I})\boldsymbol{e}_i = 0$. A nontrivial solution to this equation exists if and only if $\det(\nabla \boldsymbol{v} - \lambda_i \boldsymbol{I}) = 0$. After expressing the determinant, we arrive at the characteristic polynomial

$$-\lambda^3 + I_1\lambda^2 - I_2\lambda + I_3 = 0 \tag{4.8}$$

where the coefficients I_i are invariant, i.e they do not depend on the reference frame origin and orientation. They are given by

$$I_1 = \frac{\partial v_\mathrm{x}}{\partial x} + \frac{\partial v_\mathrm{y}}{\partial y} + \frac{\partial v_\mathrm{z}}{\partial z} = \lambda_1 + \lambda_2 + \lambda_3 \tag{4.9}$$

$$\begin{aligned} I_2 = \frac{\partial v_\mathrm{x}}{\partial x}\frac{\partial v_\mathrm{y}}{\partial y} + \frac{\partial v_\mathrm{x}}{\partial x}\frac{\partial v_\mathrm{z}}{\partial z} + \frac{\partial v_\mathrm{y}}{\partial y}\frac{\partial v_\mathrm{z}}{\partial z} - \frac{\partial v_\mathrm{x}}{\partial z}\frac{\partial v_\mathrm{z}}{\partial x} - \frac{\partial v_\mathrm{y}}{\partial z}\frac{\partial v_\mathrm{z}}{\partial y} - \frac{\partial v_\mathrm{x}}{\partial y}\frac{\partial v_\mathrm{y}}{\partial x} \\ = \lambda_1\lambda_2 + \lambda_1\lambda_3 + \lambda_2\lambda_3 = Q \end{aligned} \tag{4.10}$$

$$\begin{aligned} I_3 = \frac{\partial v_\mathrm{x}}{\partial x}\frac{\partial v_\mathrm{y}}{\partial y}\frac{\partial v_\mathrm{z}}{\partial z} + \frac{\partial v_\mathrm{x}}{\partial y}\frac{\partial v_\mathrm{y}}{\partial z}\frac{\partial v_\mathrm{z}}{\partial x} + \frac{\partial v_\mathrm{x}}{\partial z}\frac{\partial v_\mathrm{y}}{\partial x}\frac{\partial v_\mathrm{z}}{\partial y} - \frac{\partial v_\mathrm{x}}{\partial z}\frac{\partial v_\mathrm{y}}{\partial y}\frac{\partial v_\mathrm{z}}{\partial x} - \frac{\partial v_\mathrm{x}}{\partial x}\frac{\partial v_\mathrm{y}}{\partial z}\frac{\partial v_\mathrm{z}}{\partial y} \\ - \frac{\partial v_\mathrm{x}}{\partial y}\frac{\partial v_\mathrm{y}}{\partial x}\frac{\partial v_\mathrm{z}}{\partial z} = \lambda_1\lambda_2\lambda_3 = R \end{aligned} \tag{4.11}$$

The second invariant precisely corresponds to the aforementioned Q-criterion. The Δ-criterion is based on the observation that in vortices two of the eigenvalues are complex. An example of this situation, a pure helical vortex, is given in Fig. 4.3.

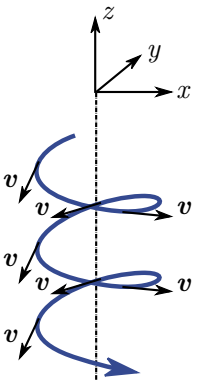

$\boldsymbol{v} = \boldsymbol{\omega} \times \boldsymbol{r}$
$v_\mathrm{x} = -\omega y$
$v_\mathrm{y} = \omega x$
$v_\mathrm{z} = K$

K is an arbitrary constant

$$\nabla \boldsymbol{v} = \begin{bmatrix} 0 & -\omega & 0 \\ \omega & 0 & 0 \\ 0 & 0 & 0 \end{bmatrix}$$

$$\det(\nabla \boldsymbol{v} - \lambda_i \boldsymbol{I}) = \det\left(\begin{bmatrix} -\lambda_i & -\omega & 0 \\ \omega & -\lambda_i & 0 \\ 0 & 0 & -\lambda_i \end{bmatrix}\right)$$
$$= -{\lambda_i}^3 - \omega^2\lambda_i = \lambda_i(-{\lambda_i}^2 - \omega^2) = 0$$

$$\lambda_1 = 0,\ \lambda_2 = \mathrm{i}\omega,\ \lambda_3 = -\mathrm{i}\omega$$

Fig. 4.3: *Velocity gradient eigenvalues for a helical vortex.*

If an incompressible fluid is assumed, then $I_1 = 0$ (from the continuity equation) and the characteristic equation reduces to

$$-\lambda^3 - I_2\lambda + I_3 = 0 \tag{4.12}$$

The discriminant of this cubic equation is

$$D = -4{I_2}^3 - 27{I_3}^2 \tag{4.13}$$

It can be shown that if the discriminant is negative, two eigenvalues are complex. The Δ-criterion is in fact this discriminant divided by $27 \cdot 4$

$$\Delta = \left(\frac{Q}{3}\right)^3 + \left(\frac{R}{2}\right)^2 \tag{4.14}$$

With this definition, vortices are regions where $\Delta > 0$. It is evident that the Δ-criterion is less strict than the Q-criterion. Negative values of Q are permitted if the absolute value of R is sufficiently large. A drawback of this criterion is that the maximal values of Δ are often very large as the maximal values of Q are often already large and in the definition of Δ, they are rised to the power of three. If the value of Δ is to be taken as a measure of the swirl intensity, it is difficult to perform volume rendering of this quantity due to its enormous range of values and their distribution. A possible solution is to render a sufficiently large odd root of it instead.

Swirling strength

The swirling strength of Zhou et al.[98] is based on the same idea as the Δ-criterion. The difference is that the eigenvalues of the velocity gradient tensor are directly computed, and their imaginary part is taken as a measure of the swirl intensity. Let $\lambda_1 \in \mathbb{R}$, $\lambda_2 = a + \mathrm{i}b$, $\lambda_3 = a - \mathrm{i}b$. Then vortices are regions where $b > 0$. Unlike the Δ-criterion, b values were found to lie within a reasonable range; therefore, this criterion will be preferred over the Δ-criterion in this work.

λ_2-criterion

Another popular vortex criterion, the λ_2-criterion of Jeong and Hussain[99], is based on different considerations. It is known that the swirling motion itself leads to a local pressure minimum at the vortex axis. We can take the gradient of the Navier–Stokes equation assuming an incompressible fluid and no external forces

$$\nabla\left(\frac{\partial \boldsymbol{v}}{\partial t} + (\boldsymbol{v}\cdot\nabla)\boldsymbol{v} - \nu\Delta\boldsymbol{v}\right) = -\frac{1}{\rho}\nabla(\nabla p) \tag{4.15}$$

If the Hessian matrix $\nabla(\nabla p)$ has two positive eigenvalues, then there exists a plane in which p reaches its local minimum at the point of interest. As the next step, the velocity gradient is decomposed into the symmetric part $\boldsymbol{S}$ and the antisymmetric part $\boldsymbol{R}$. Some of the terms on the left-hand side vanish as they correspond to the vorticity transport equation. We then arrive at the following form

$$\frac{\mathrm{D}\boldsymbol{S}}{\mathrm{D}t} + \boldsymbol{S}^2 + \boldsymbol{R}^2 - \ \nu\Delta\boldsymbol{S} = -\frac{1}{\rho}\nabla(\nabla p) \tag{4.16}$$

As was mentioned, the local pressure minimum does not necessarily guarantee the existence of a vortex, and vice versa. For this reason, the contribution of the material derivative of $\boldsymbol{S}$ and the viscous term to the Hessian matrix is discarded, and the λ_2-criterion requires two eigenvalues of $\boldsymbol{S}^2 + \boldsymbol{R}^2$ to be negative. The eigenvalues are usually sorted in ascending order, and a vortex is defined as the region where λ_2 is negative. The absolute value of this eigenvalue can serve as a measure of the local swirl intensity.

Residual vorticity

A more elaborate vortex criterion was proposed by Kolář[93]. It tackles the already mentioned drawback of vorticity, i.e. admitting nonzero values not only for purely rotating flows but also for purely shearing flows. The proposed method is based on a triple decomposition of the velocity gradient into the so-called effective shear, residual strain, and residual rotation parts. The last part leads to the residual vorticity, i.e. a portion of the original vorticity related only to shearless motion. A bottleneck of this method is the effective shear extraction procedure. First, the decomposition of the velocity gradient tensor is defined as follows

$$\nabla\boldsymbol{v} = \nabla\boldsymbol{v}_{\mathrm{shear}} + \nabla\boldsymbol{v}_{\mathrm{residual}} \tag{4.17}$$

$$\nabla\boldsymbol{v}_{\mathrm{residual}} = \boldsymbol{\Upsilon}, \qquad \Upsilon_{ij} = \left(\operatorname{sgn}\frac{\partial v_i}{\partial x_j}\right)\min\left(\left|\frac{\partial v_i}{\partial x_j}\right|, \left|\frac{\partial v_j}{\partial x_i}\right|\right) \tag{4.18}$$

The shear tensor is by definition purely asymmetric, and this procedure is proposed so that this property is satisfied. The results, however, depend on the choice of the frame of reference. We seek the frame in which the Frobenius norm of the residual tensor is minimized. The shear part in this so-called best reference frame (BRF) is denoted as the effective shear. Kolář also derived a relation between $\|\nabla\boldsymbol{v}\|$ and $\|\nabla\boldsymbol{v}_{\mathrm{residual}}\|$

$$\|\nabla\boldsymbol{v}_{\mathrm{residual}}\|^2 + 4(|S_{12}R_{12}| + |S_{23}R_{23}| + |S_{31}R_{31}|) = \|\nabla\boldsymbol{v}\|^2 \tag{4.19}$$

Considering the fact that $\|\nabla\boldsymbol{v}\|$ is frame-independent, the BRF is defined as the frame where $|S_{12}R_{12}| + |S_{23}R_{23}| + |S_{31}R_{31}|$ is maximized. The computation of the residual vorticity therefore involves time-consuming optimization. Once the BRF is found, the residual tensor is computed and then the residual vorticity is extracted from its antisymmetric part and returned back to the original frame. As this criterion is currently not available in both Ansys and ParaView softwares (probably due to the long-lasting calculations), a custom Python programmable filter for ParaView was created. The following algorithm was adopted.

1) Compute the velocity gradient tensor and its symmetric part $\boldsymbol{S}$ and antisymmetric part $\boldsymbol{R}$ in the original reference frame.
2) Prepare a grid of coordinate systems given by the angles of rotation applied to the original coordinate system. The range that is needed to explore is $\alpha \in \langle 0; \pi)$, $\beta \in \langle 0; \pi)$, $\gamma \in \langle 0; \frac{\pi}{2})$. Uniform sampling with steps $\Delta\alpha = \Delta\beta = \Delta\gamma$ is used. This grid will be used to

find the initial point from which the local optimum will be approached by an iterative algorithm.

3) Compute the symmetric and antisymmetric parts of the velocity gradient tensor for all coordinate frames from the grid. The rotation matrix is given by

$$\boldsymbol{Q} = \begin{bmatrix} \cos\alpha\cos\beta & \cos\alpha\sin\beta\sin\gamma - \sin\alpha\cos\gamma & \cos\alpha\sin\beta\cos\gamma + \sin\alpha\sin\gamma \\ \sin\alpha\cos\beta & \sin\alpha\sin\beta\sin\gamma + \cos\alpha\cos\gamma & \sin\alpha\sin\beta\cos\gamma - \cos\alpha\sin\gamma \\ -\sin\beta & \cos\beta\sin\gamma & \cos\beta\cos\gamma \end{bmatrix} \tag{4.20}$$

and the velocity gradient parts in the rotated reference frame can be computed as follows

$$\boldsymbol{S}_{\mathrm{RRF}} = \boldsymbol{Q}\boldsymbol{S}\boldsymbol{Q}^{\mathrm{T}}, \boldsymbol{R}_{\mathrm{RRF}} = \boldsymbol{Q}\boldsymbol{R}\boldsymbol{Q}^{\mathrm{T}} \tag{4.21}$$

Compute the functional that is to be maximized (second term in (4.19)).

4) Find the coordinate system from the grid where the functional is maximal. This will be the starting point for the following iterative procedure. The coordinate system is given by angles $(\alpha_0, \beta_0, \gamma_0)$.
5) Compute the gradient of the functional.
6) Move in the direction of the gradient by a given step. In this case, the initial step was chosen to be the half step size of the grid, i.e. $\frac{\Delta\alpha}{2}$. Compute the functional value at this point.
7) If the functional value improved, compute its gradient and move in its direction by the same step. If the functional value did not improve, return back to the initial point and move in the direction of the gradient by half the original step size. Continue until the chosen stop criteria are met.
8) In the best reference frame, compute the velocity gradient tensor

$$\nabla\boldsymbol{v}_{\mathrm{BRF}} = \boldsymbol{Q}_{\mathrm{BRF}}\nabla\boldsymbol{v}\boldsymbol{Q}_{\mathrm{BRF}}^{\mathrm{T}} \tag{4.22}$$

and then its residual part using (4.18). Compute the antisymmetric part

$$\boldsymbol{R}_{\mathrm{residual_{BRF}}} = \frac{1}{2}\left(\nabla\boldsymbol{v}_{\mathrm{residual_{BRF}}} - \nabla\boldsymbol{v}_{\mathrm{residual_{BRF}}}^{\mathrm{T}}\right) \tag{4.23}$$

and extract the residual vorticity

$$\boldsymbol{\Omega}_{\mathrm{residual_{BRF}}} = 2\left[R_{\mathrm{residual_{BRF}}_{32}} \quad R_{\mathrm{residual_{BRF}}_{13}} \quad R_{\mathrm{residual_{BRF}}_{21}}\right]^{\mathrm{T}} \tag{4.24}$$

Finally, return the residual vorticity back to the original reference frame

$$\boldsymbol{\Omega}_{\mathrm{residual}} = \boldsymbol{Q}_{\mathrm{BRF}}^{\mathrm{T}}\boldsymbol{\Omega}_{\mathrm{residual_{BRF}}} \tag{4.25}$$

An advantage of vorticity-based criteria is that the vorticity also determines the swirl orientation. Axial vorticity can be used to determine the sense of rotation of the vortex rope. A modified residual vorticity is for this purpose proposed as follows

$$\widetilde{\Omega}_{\mathrm{residual}} = \|\boldsymbol{\Omega}_{\mathrm{residual}}\| \operatorname{sgn} \Omega_{\mathrm{residual_z}} \tag{4.26}$$

This is a scalar quantity, and its field can therefore be visualized by volume rendering. The sign of this quantity corresponds to the sign of the axial residual vorticity and distinguishes between clockwise and anticlockwise rotation of the respective elementary particle around the axis parallel to the diffuser axis. Its magnitude corresponds to the residual vorticity magnitude and serves as a measure of the swirl intensity.

Visualizations of the vortex rope by volume rendering of the introduced quantities are presented in Fig. 4.4. Snapshots from simulation SBES-T-1 were used. The color bar range was determined with the goal of reaching maximal similarity of the representations. The opacity transfer function represented by the white line is of the same shape for all cases to ensure comparability of the scaling. Two snapshots with different swirl numbers are depicted to also assess the dependence of each variable on the operating point.

Static pressure turns out to be highly sensitive to the swirl number (decreasing rapidly with increasing swirl number). For the case with the higher swirl number, it gives qualitatively different results compared to the other quantities. It highlights a whole spiraling structure rather than individual vortices. Together, the results show that the flow in the diffuser in this case exhibits a large spiral structure (highlighted by the static pressure) which consists of twin spiraling vortices under the hub tip and many smaller vortices downstream (highlighted by the other quantities). The values of the Q-criterion and λ_2-criterion scale rapidly, resulting in less-pronounced weaker vortices compared to the swirling strength or vorticity fields. The triple decomposition attributes around 40% of the total vorticity in the vortex rope to shearing motion and leads to an interesting result where even smaller vortices are clearly distinguishable. Together with a clear physical meaning and the ability to determine the swirl orientation, this is the reason why the (modified) residual vorticity is the vortex identification method of choice in this work. Overall, all the vortex identification methods highlighted structures of practically the same shape but with a different scaling of the values quantifying their strength.

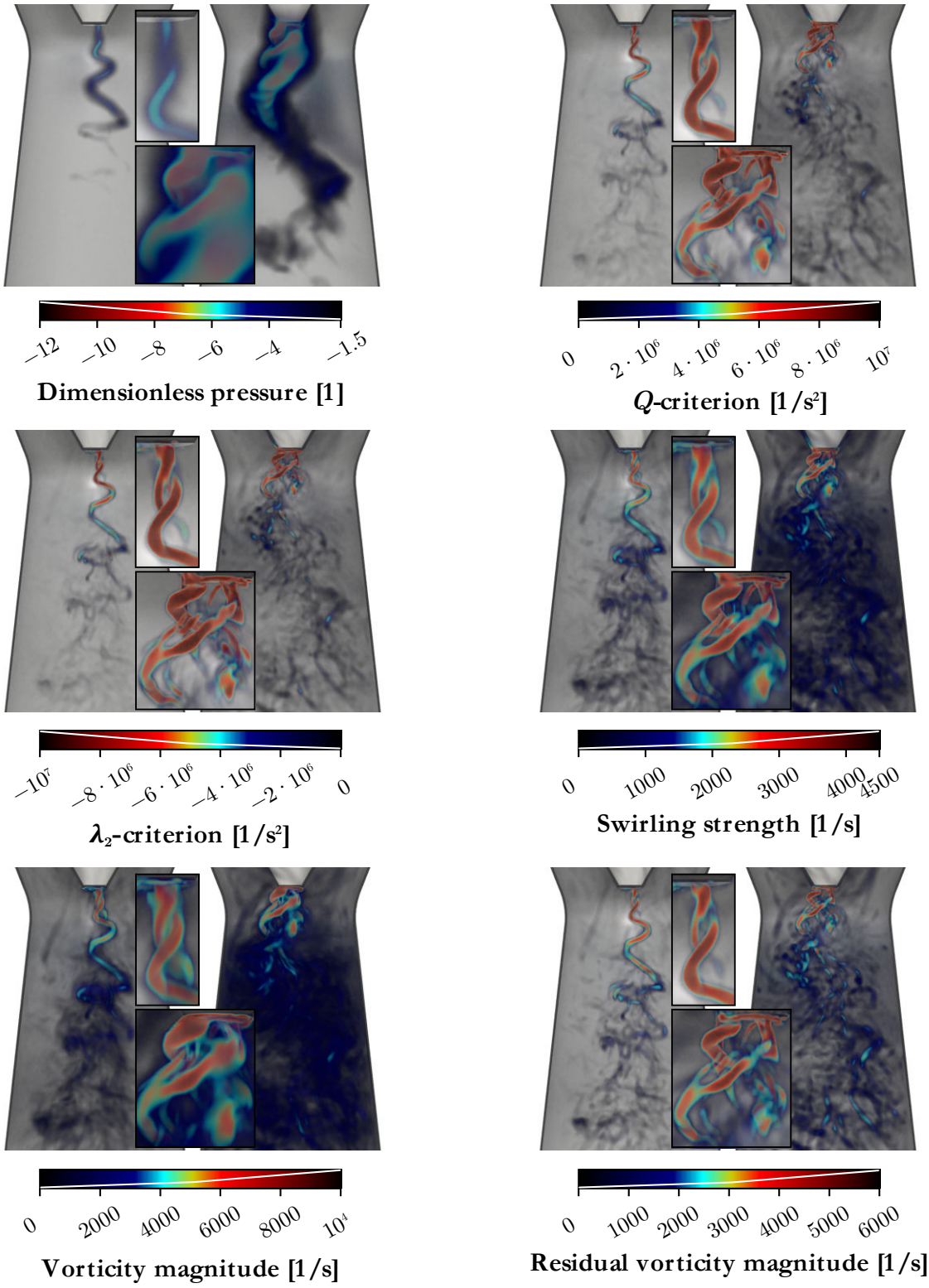

Fig. 4.4: *Volume renders of some variables for visualization of the vortex rope. Left: a snapshot with* $\mathrm{Sr} \cong 0.45$*, right: a snapshot with* $\mathrm{Sr} \cong 0.85$ *(evaluated in a plane close under the hub tip). Boundary layers are removed from the vorticity (not residual vorticity) field to make the vortex rope visible. Rendered in Blender.*

M_Z-criterion

The vortex identification methods presented so far have a common drawback: they are only Galilean invariant, i.e. their results do not depend on translation of the reference frame but do depend on its rotation. There is usually no single natural choice of a reference frame, which leads to the need for an objective (independent of the frame motion) definition of a vortex[96].

Haller[100] showed that the deviation of the vorticity from its spatial mean is objective. In our case, the spatial mean in the diffuser turns out to be negligible, and so can be omitted. The same principle can be applied to the residual vorticity. Haller[96] also proposed another objective vortex definition, which is based on Lagrangian considerations. It should be noted that this criterion is applicable only to an incompressible fluid. Assume an elementary particle located in point $\boldsymbol{x}_0$ in time 0. After infinitesimally small time $\mathrm{d}t$, the new position is

$$\boldsymbol{x}(\boldsymbol{x}_0, \mathrm{d}t) = \boldsymbol{x}_0 + \boldsymbol{v}(\boldsymbol{x}_0, 0)\mathrm{d}t \tag{4.27}$$

Now assume a particle located in point $\boldsymbol{x}_0 + \boldsymbol{\xi}$ in time 0. We can analogously write

$$\boldsymbol{x}(\boldsymbol{x}_0 + \boldsymbol{\xi}, \mathrm{d}t) = \boldsymbol{x}_0 + \boldsymbol{\xi} + \boldsymbol{v}(\boldsymbol{x}_0 + \boldsymbol{\xi}, 0)\mathrm{d}t \tag{4.28}$$

Subtracting these equations leads to

$$\boldsymbol{x}(\boldsymbol{x}_0 + \boldsymbol{\xi}, \mathrm{d}t) - \boldsymbol{x}(\boldsymbol{x}_0, \mathrm{d}t) = \boldsymbol{\xi} + [\boldsymbol{v}(\boldsymbol{x}_0 + \boldsymbol{\xi}, 0) - \boldsymbol{v}(\boldsymbol{x}_0, 0)]\mathrm{d}t \tag{4.29}$$

The left-hand side can be written as $\boldsymbol{\xi} + \mathrm{d}\boldsymbol{\xi}$. For an infinitesimally small $\boldsymbol{\xi}$, the terms in the bracket on the right-hand side become $\nabla\boldsymbol{v}(\boldsymbol{x}_0, 0)\boldsymbol{\xi}$. With these assumptions, we obtain

$$\frac{\mathrm{d}\boldsymbol{\xi}}{\mathrm{d}t} = \nabla\boldsymbol{v}(\boldsymbol{x}_0, 0)\boldsymbol{\xi} \tag{4.30}$$

Next, the so-called Lyapunov function is defined as

$$\mathcal{V} = \frac{1}{2}\frac{\mathrm{d}\|\boldsymbol{\xi}\|^2}{\mathrm{d}t} = \frac{1}{2}\frac{\mathrm{d}(\boldsymbol{\xi}^{\mathrm{T}}\boldsymbol{\xi})}{\mathrm{d}t} = \frac{1}{2}\left(\frac{\mathrm{d}\boldsymbol{\xi}^{\mathrm{T}}}{\mathrm{d}t}\boldsymbol{\xi} + \boldsymbol{\xi}^{\mathrm{T}}\frac{\mathrm{d}\boldsymbol{\xi}}{\mathrm{d}t}\right) = \boldsymbol{\xi}^{\mathrm{T}}\boldsymbol{S}\boldsymbol{\xi} \tag{4.31}$$

In the last step, (4.30) was plugged into the equation and the velocity gradient decomposition (4.4) was exploited. This equation determines how the squared particle distance $\|\boldsymbol{\xi}\|^2$ evolves in time, i.e. if the neighboring particles tend to get closer (e.g. in a confusor), farther (e.g. in a diffuser) or stay in the same distance (e.g. flow in a straight pipe). It is no surprise that the strain-rate tensor $\boldsymbol{S}$ is the determining factor. For an incompressible fluid, it has zero trace, i.e. the sum of the main diagonal elements is zero. As a result, at least one of its eigenvalues is positive and at least one is negative (excluding the case where all the eigenvalues are zero as the sum of the eigenvalues of a matrix is equal to its trace). The fact that $\boldsymbol{S}$ is symmetric also means that its eigenvalues are real. Moreover, if the eigenvalues are distinct, then the eigenvectors are orthogonal to each other. Therefore, two of the eigenvalues, denoted as s_i ($i = 1, 2, 3$), have the same sign and the last one has the opposite sign. They are ordered as follows

$$\operatorname{sgn} s_1 = \operatorname{sgn} s_2 \neq \operatorname{sgn} s_3\,, \qquad |s_1| \geq |s_2| \tag{4.32}$$

Next, vectors $\boldsymbol{\xi}$ for which the Lyapunov function $\mathcal{V}$ is zero are sought, i.e. the distance of the particle given by $\boldsymbol{\xi}$ does not change at least for infinitesimally small time. The vectors $\boldsymbol{\xi}$ are expressed in the basis of unit eigenvectors $\boldsymbol{e}_i$ corresponding to the eigenvalues s_i. The coordinates are denoted as η_i.

$$\boldsymbol{\xi} = \eta_1 \boldsymbol{e}_1 + \eta_2 \boldsymbol{e}_2 + \eta_3 \boldsymbol{e}_3 \tag{4.33}$$

Plugging this into the right-hand side of (4.31) and setting equal to zero leads to

$$(\eta_1 \boldsymbol{e}_1^{\mathrm{T}} + \eta_2 \boldsymbol{e}_2^{\mathrm{T}} + \eta_3 \boldsymbol{e}_3^{\mathrm{T}}) \boldsymbol{S} (\eta_1 \boldsymbol{e}_1 + \eta_2 \boldsymbol{e}_2 + \eta_3 \boldsymbol{e}_3) = 0 \tag{4.34}$$

After algebraic manipulation utilizing $\boldsymbol{S}\boldsymbol{e}_i = s_i \boldsymbol{e}_i$, $\boldsymbol{e}_i^{\mathrm{T}} \boldsymbol{e}_i = 1$, $\boldsymbol{e}_i^{\mathrm{T}} \boldsymbol{e}_j = 0$ for $i \neq j$, and $s_1 + s_2 + s_3 = 0$, we arrive at

$${\eta_3}^2 = -{\eta_1}^2 \frac{s_1}{s_3} + {\eta_2}^2 \left(1 + \frac{s_1}{s_3}\right) \tag{4.35}$$

This is the equation of an elliptic cone in coordinates η_1, η_2, η_3. From the eigenvalues ordering (4.32) and their zero sum, it follows that $\frac{s_1}{s_3} \in (-1; -0.5)$ if the eigenvalues are distinct. Haller denotes this cone by the letter Z. The theory continues by defining the strain acceleration tensor as

$$\boldsymbol{M} = \frac{\mathrm{D}\boldsymbol{S}}{\mathrm{D}t} + (\nabla \boldsymbol{v})^{\mathrm{T}} \boldsymbol{S} + \boldsymbol{S} \nabla \boldsymbol{v} \tag{4.36}$$

Matrix $\boldsymbol{M}$ is also symmetric. Its trace is (assuming the Frobenius norm) $\operatorname{tr}(\boldsymbol{M}) = 2\|\boldsymbol{S}\|^2 \geq 0$. The positive trace means that at least one element of the main diagonal is positive. It follows that $\boldsymbol{M}$ is either positive-definite, positive semi-definite, or indefinite. Taking the time derivative of the Lyapunov function $\mathcal{V}$ and utilizing (4.30) leads to

$$\frac{\mathrm{d}\mathcal{V}}{\mathrm{d}t} = \frac{1}{2} \frac{\mathrm{d}^2 \|\boldsymbol{\xi}\|^2}{\mathrm{d}t^2} = \boldsymbol{\xi}^{\mathrm{T}} (\nabla \boldsymbol{v})^{\mathrm{T}} \boldsymbol{S} \boldsymbol{\xi} + \boldsymbol{\xi}^{\mathrm{T}} \frac{\mathrm{D}\boldsymbol{S}}{\mathrm{D}t} \boldsymbol{\xi} + \boldsymbol{\xi}^{\mathrm{T}} \boldsymbol{S} \nabla \boldsymbol{v} \boldsymbol{\xi} = \boldsymbol{\xi}^{\mathrm{T}} \boldsymbol{M} \boldsymbol{\xi} \tag{4.37}$$

Recall that we are interested in vectors $\boldsymbol{\xi}$ for which $\mathcal{V} = 0$, i.e. the first temporal derivative of the squared particle distance $\|\boldsymbol{\xi}\|^2$ is zero. This second derivative then determines whether the distance between the particles is in its local minimum (positive values), maximum (negative values), or saddle (zero). These facts provide a notion of how the trajectories of the neighboring particles look like. For example, if $\boldsymbol{M}$ is positive-definite on Z, i.e for each $\boldsymbol{\xi}$ from Z (satisfying (4.35) assuming the form (4.33)), then this second derivative is always positive, meaning that every neighboring particle with zero temporal derivative of its distance is in its locally closest point to the particle of interest. This leads to the saddle flow topology. On the other hand, if $\boldsymbol{M}$ is indefinite, we arrive at an elliptic vortex. These situations are sketched in Fig. 4.5.

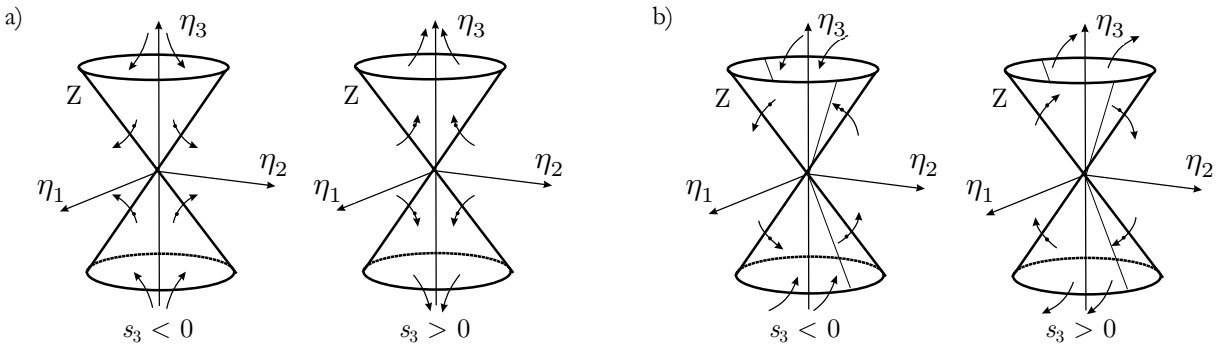

Fig. 4.5: *Trajectories for a) positive-definite $\boldsymbol{M}$ and b) indefinite $\boldsymbol{M}$ sketched by Haller[96] (edited). The particle of interest is in the origin, and trajectories of the neighboring particles are relative to this particle. The elliptic cone in the coordinate system of the strain-rate tensor eigenvectors is alsco depicted.*

Based on this concept, Haller partitions the flow domain into three parts: the hyperbolic domain ($\boldsymbol{M}$ is positive-definite on Z), the elliptic domain ($\boldsymbol{M}$ is indefinite on Z), and the parabolic domain (union of all the boundaries separating the hyperbolic and elliptic domains). A vortex is then defined as a set of trajectories that remain in the elliptic domain. For rigorous justifications, see the original paper. The only thing needed is to find a way to determine whether $\boldsymbol{M}$ is indefinite on Z at a given point. Remind that if $\boldsymbol{\xi}^{\mathrm{T}}\boldsymbol{M}\boldsymbol{\xi}$ is always positive, then $\boldsymbol{M}$ is positive-definite, while if it is sometimes negative, $\boldsymbol{M}$ is indefinite. We therefore seek the minimum of $\boldsymbol{\xi}^{\mathrm{T}}\boldsymbol{M}\boldsymbol{\xi}$ for $\boldsymbol{\xi} = \boldsymbol{\xi}|_{\mathrm{Z}} = \boldsymbol{E}\boldsymbol{\eta}|_{\mathrm{Z}}$, where $\boldsymbol{E} = [\boldsymbol{e}_1 \quad \boldsymbol{e}_2 \quad \boldsymbol{e}_3]$ and $\boldsymbol{\eta} = [\eta_1 \quad \eta_2 \quad \eta_3]^{\mathrm{T}}$. Vectors $\boldsymbol{\xi}$ from the elliptic cone Z can be expressed using the parametric equation of an ellipse dependent on the η_3-coordinate and central angle α (as each slice of the elliptic cone perpendicular to η_3-axis is actually an ellipse). Function $m(\alpha, \eta_3)$ is then defined as

$$m(\alpha, \eta_3) = (\boldsymbol{\xi}^{\mathrm{T}}\boldsymbol{M}\boldsymbol{\xi})|_{\mathrm{Z}} = (\boldsymbol{\eta}^{\mathrm{T}}\boldsymbol{E}^{\mathrm{T}}\boldsymbol{M}\boldsymbol{E}\boldsymbol{\eta})|_{\mathrm{Z}} \tag{4.38}$$

If $\min m(\alpha, \eta_3) < 0$, then $\boldsymbol{M}$ is indefinite on the elliptic cone Z. The following expression comes from the parametric equation of the ellipse for $\eta_3 = \sqrt{a(1-a)}$, $a = -\frac{s_1}{s_3}$. The key fact is that the sign of the minimum does not depend on η_3; therefore, a suitable value could be chosen. For further simplification, $\widehat{\boldsymbol{M}} = \boldsymbol{E}^{\mathrm{T}}\boldsymbol{M}\boldsymbol{E}$. Function $m(\alpha)$ can after these considerations be written as

$$\begin{aligned} m(\alpha) = {} & (1-a)\widehat{M}_{11}\cos^2\alpha + a\widehat{M}_{22}\sin^2\alpha + a(1-a)\widehat{M}_{33} \\ & + \sqrt{a(1-a)}\Big(2\sqrt{1-a}\widehat{M}_{13}\cos\alpha + 2\sqrt{a}\widehat{M}_{23}\sin\alpha \\ & + \widehat{M}_{12}\sin 2\alpha\Big) \end{aligned} \tag{4.39}$$

Testing whether the minimum is negative requires a suitable numerical method. Unfortunately, as Haller pointed out, this criterion requires many numerical operations including second-order spatial differentiation and computation of particle trajectories, leading to numerical errors that consequently incorrectly disqualify a significant portion of particles from being contained in a vortex. For this reason, a relaxed definition is used: a trajectory is contained in a vortex, if the ratio of the time spent in the elliptic zone to the integration time is above a selected threshold. This criterion is referred to as the $\boldsymbol{M}_{\mathrm{Z}}$-criterion.

To summarize, the following procedure needs to be carried out.

1) Compute the minimum of $m(\alpha)$ at all grid points for each snapshot from the whole integration time to determine if the point belongs to the elliptic domain.
2) Compute trajectories of particles starting in the initial time for each grid point (very expensive).
3) For each trajectory, determine the percentage of time spent in the elliptic zone. If the value is above a selected threshold, then the starting point is contained in a vortex in the initial time.

As this criterion is also not available in both Ansys and ParaView softwares, a custom procedure using available ParaView tools and custom Python programmable filters was created.

The $\boldsymbol{M}_{\mathrm{Z}}$-criterion by definition gives no information about the intensity of swirling motion. For this reason, combining with the residual vorticity is suggested in this work. From the computational domain, only those data points (particles) that satisfy the $\boldsymbol{M}_{\mathrm{Z}}$-criterion are extracted. These points are then colored according to the residual vorticity and rendered by volume rendering (Fig. 4.6). At first, one needs to choose an appropriate integration time. For each case given by the swirl number, there is a longitudinal slice of an area under the hub tip with the vortex rope, colored by $\boldsymbol{M}_{\mathrm{Z}}$, for three different integration times T. Generally, as T grows, more particles get into the hyperbolic zone, leading to their $\boldsymbol{M}_{\mathrm{Z}}$-value decay. For the case with the lower swirl number, we can observe that particles starting from the vortex rope core remain in the elliptic zone for long times, whereas particles starting from its surroundings spend considerable portion of time in the hyperbolic zone. There is a sharp gradient of $\boldsymbol{M}_{\mathrm{Z}}$ values that clearly highlights the vortex core edge. For the case with the higher swirl number, the situation is more complicated as there are many smaller vortices concentrated in the large spiral structure. Together with shorter time scales, this increases the uncertainty of the results. Volume renders with the threshold of $\boldsymbol{M}_{\mathrm{Z}} > 0.99$ contain the vortex rope in the first case, but miss many structures with high residual vorticity, especially the twin spiral vortices under the hub tip in the second case. A lower threshold of $\boldsymbol{M}_{\mathrm{Z}} > 0.9$ is fulfilled by substantially more particles in the second case, leading to much more structures visible in the volume render. In the first case, the change is less significant.

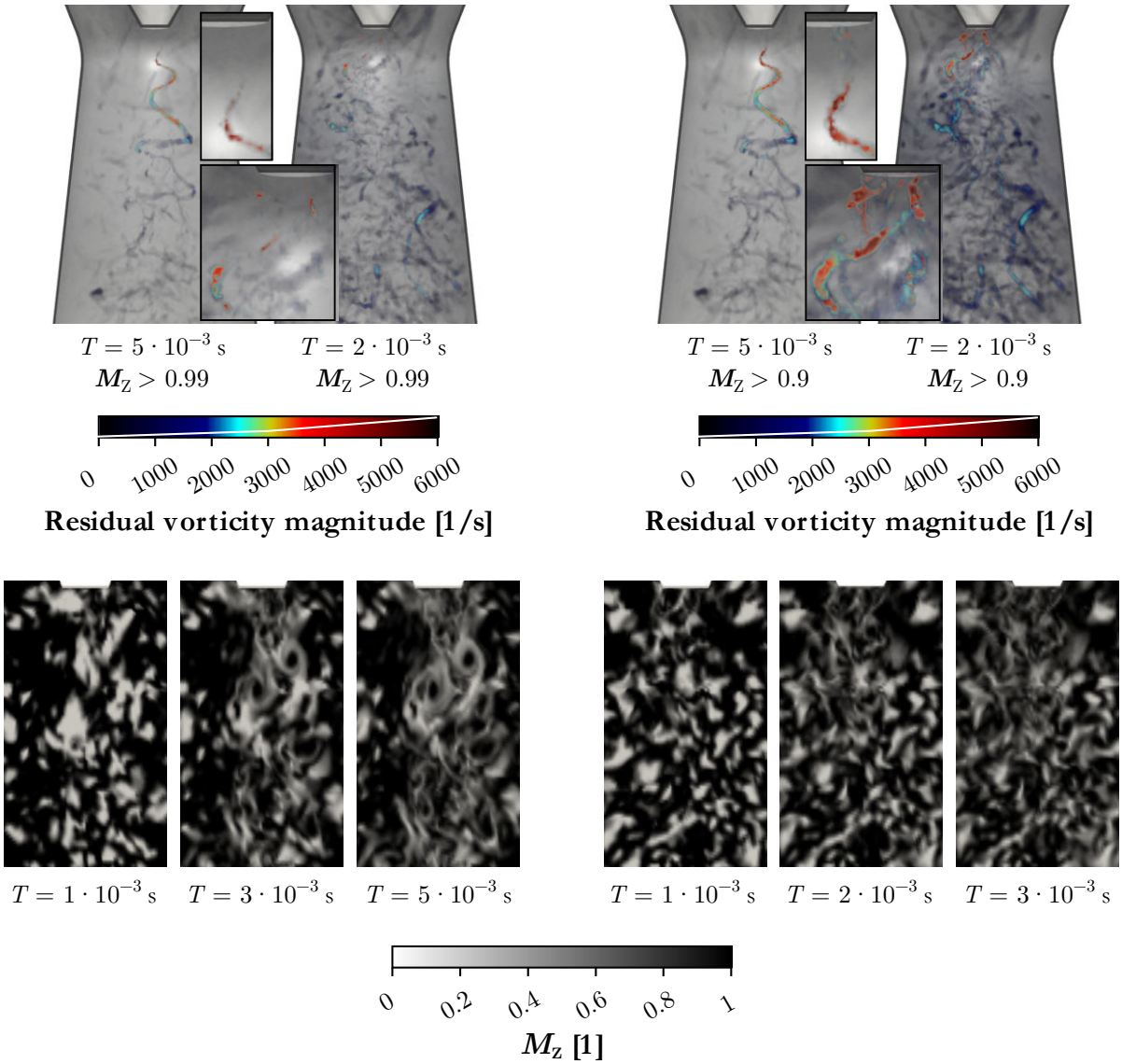

Fig. 4.6: *Top: volume renders of the* M_Z*-criterion combined with the residual vorticity for two thresholds. Rendered in Blender. Bottom: longitudinal slices of the* M_Z*-criterion field (area under the hub tip) for different integration times. The snapshots are the same as in Fig. 4.4 (*$\mathrm{Sr} \cong 0.45$ *and* 0.85*).*

Although the M_Z-criterion is appealing by its definition and properties, it was found unsuitable for the present vortex rope visualizations due to the numerical difficulties. Nevertheless, it can still be used for flow field topology studies together with the so-called finite-time Lyapunov exponent.

4.2.5 Finite-time Lyapunov exponent

The finite-time Lyapunov exponent (FTLE) is an objective (independent of the reference frame) Lagrangian quantity connected with Lagrangian coherent structures (see the work of Haller[101] for a comprehensive review). Its applications comprise e.g. studies of general turbulence[102], flow over an airfoil[103], motion of animals[104, 105], and oceanic eddies[106]. The FTLE is a measure of the separation of neighboring particles in time, i.e. the local maximizing curves (ridges) of the FTLE field

indicate either locally maximal stretching or locally maximal shear[102]. When integrating forward in time, high values of FTLE signalize repelling structures. Similarly, backward integration leads to attracting structures. Details on the procedure can be found in the work of Shadden et al.[107] Consider a function that for each initial position $\boldsymbol{x}_0$ of a particle, initial time t_0, and final time t returns the position $\boldsymbol{x}$ of the particle in the final time t. This so-called flow map can be written as

$$\varphi_{t_0}^{t}(\boldsymbol{x}_0) = \boldsymbol{x}(t_0, \boldsymbol{x}_0, t) \tag{4.40}$$

Now take two initial positions: $\boldsymbol{x}_0$ and $\boldsymbol{x}_0 + \mathrm{d}\boldsymbol{x}$. Flow map $\varphi_{t_0}^{t}(\boldsymbol{x}_0 + \mathrm{d}\boldsymbol{x})$ can be expressed using the Taylor series. Assuming infinitesimally small $\mathrm{d}\boldsymbol{x}$, the higher-order terms vanish and we obtain

$$\varphi_{t_0}^{t}(\boldsymbol{x}_0 + \mathrm{d}\boldsymbol{x}) - \varphi_{t_0}^{t}(\boldsymbol{x}_0) = \Delta\boldsymbol{x} = \nabla\varphi_{t_0}^{t}(\boldsymbol{x}_0)\mathrm{d}\boldsymbol{x} \tag{4.41}$$

This equation is in fact the same as equation (4.30) used in the definition of the $\boldsymbol{M}_{\mathrm{Z}}$-criterion. It represents the distance $\Delta\boldsymbol{x}$ in time t between particles seeded in points $\boldsymbol{x}_0$ and $\boldsymbol{x}_0 + \mathrm{d}\boldsymbol{x}$ in time t_0. Such $\mathrm{d}\boldsymbol{x}$ is sought that maximizes the Euclidean norm of $\Delta\boldsymbol{x}$

$$\|\Delta\boldsymbol{x}\| = \sqrt{\mathrm{d}\boldsymbol{x} \cdot \left[\left(\nabla\varphi_{t_0}^{t}(\boldsymbol{x}_0)\right)^{\mathrm{T}} \nabla\varphi_{t_0}^{t}(\boldsymbol{x}_0)\mathrm{d}\boldsymbol{x}\right]} = \sqrt{\mathrm{d}\boldsymbol{x} \cdot (\boldsymbol{D}\mathrm{d}\boldsymbol{x})} \tag{4.42}$$

where $\boldsymbol{D}$ is the so-called Cauchy–Green deformation tensor. Assume the standard eigenvalue problem $\boldsymbol{D}\boldsymbol{e}_i = \lambda_i \boldsymbol{e}_i$ where $\boldsymbol{e}_i$ is an eigenvector and λ_i an eigenvalue. As $\boldsymbol{D}$ is by construction symmetric and positive-definite, its eigenvalues are positive real numbers and its eigenvectors are orthogonal. Then, $\|\Delta\boldsymbol{x}\|$ is maximized if the direction of $\mathrm{d}\boldsymbol{x}$ corresponds to the direction of the eigenvector $\boldsymbol{e}_i = \boldsymbol{e}_{\max}$ with the largest eigenvalue, i.e. $\lambda_{\max} = \max \lambda_i$. Assuming unit eigenvectors as usual, we can rewrite equation (4.42) using $\mathrm{d}\boldsymbol{x}_{\max} = \boldsymbol{e}_{\max}\|\mathrm{d}\boldsymbol{x}_{\max}\|$ and $\boldsymbol{D}\mathrm{d}\boldsymbol{x}_{\max} = \lambda_{\max}\boldsymbol{e}_{\max}\|\mathrm{d}\boldsymbol{x}_{\max}\|$ as follows

$$\|\Delta\boldsymbol{x}_{\max}\| = \sqrt{\lambda_{\max}}\|\mathrm{d}\boldsymbol{x}_{\max}\| = \|\mathrm{d}\boldsymbol{x}_{\max}\| \exp(\sigma|t - t_0|) \tag{4.43}$$

where the finite-time Lyapunov exponent σ is given by

$$\sigma = \frac{1}{|t - t_0|} \ln \sqrt{\lambda_{\max}} \tag{4.44}$$

The flow map can be considered in both positive and negative time, justifying the absolute values of the time difference in the previous equations.

To its advantage FTLE was found to be relatively insensitive to imperfect velocity data[108]. Its principal disadvantage, however, is the cost associated with the computation of particle trajectories for each seed point in the domain in order to compute the flow map. The distribution of the seed points needs to be fine enough to reach the desired level of details, leading to a high number of trajectory computations for each time instant. To this point, efficient methods for computing a sequence of FTLE fields in time were proposed[109]. The Eulerian representation of the FTLE is then obtained by spatial interpolation.

The FTLE computation procedure comprises the following steps.

1) Choose a grid of seed points for which FTLE is to be computed.
2) Using a particle tracer, compute the position of particles in time t seeded at the grid points from the previous step in time t_0. This corresponds to the flow map $\varphi_{t_0}^{t}(\boldsymbol{x}_0)$.
3) Compute the gradient of the flow map. Then compute the Cauchy–Green deformation tensor and find its eigenvalues.
4) Find the largest eigenvalue and compute FTLE.

As FTLE is also not available in both Ansys and ParaView softwares, a custom procedure using available ParaView tools and custom Python programmable filters was created.

FTLE fields are usually rich in fine structures, making visualization challenging in 3D. In this work, a visualization method based on volume rendering is proposed. The results also depend on the chosen integration time. As time increases, the structures become sharper and clearer[102]. In Fig. 4.7, visualizations of the FTLE fields in a longitudinal slice and in the whole diffuser are presented. In the longitudinal slice, we can observe significant FTLE ridges surrounding the vortex core and a local minimum of FTLE in its center. This indicates a solid-body-like rotation. In the pictures of the whole diffuser, an isosurface of the Q-criterion is added to complement the volume renders of the FTLE fields. It fits well into the visible FTLE structures and enables us to see their relation to the vortex rope core. The opacity transfer function makes the regions of lower FTLE values completely transparent and increases sharply at the end of the range to better highlight the most significant structures.

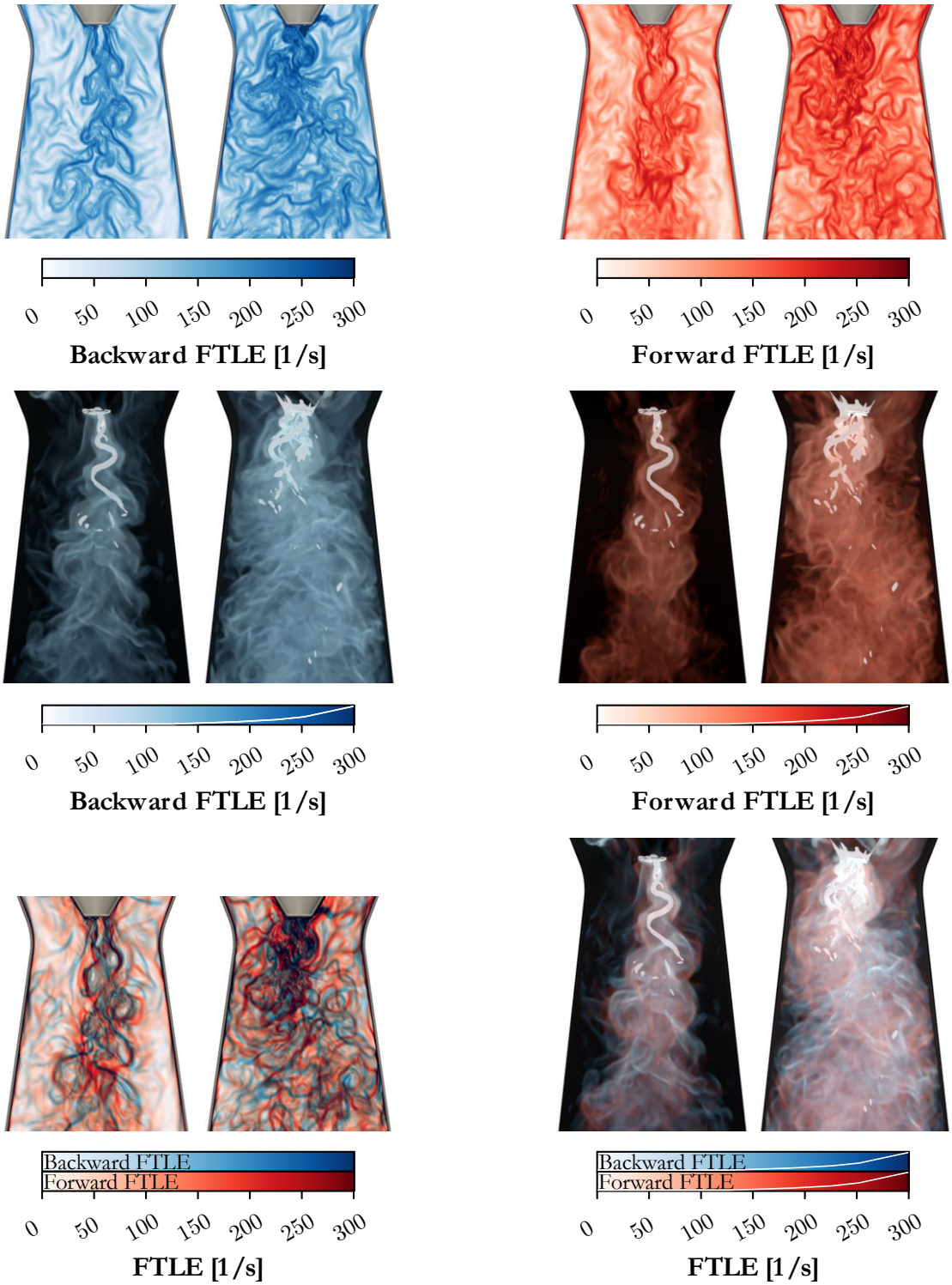

Fig. 4.7: *Top: Finite-time Lyapunov exponent (FTLE) fields in a longitudinal slice. Middle: volume renders of the same FTLE fields with removed boundary layers at the outer walls. Isosurface of the Q-criterion for the value of* $3 \cdot 10^6$ *is included and rendered as glowing white for enhanced visibility. Bottom: combinations of each pair in a single picture. The snapshots are the same as in the previous figures (*$\mathrm{Sr} \cong 0.45$ *and* 0.85*).*

4.3 Mesh convergence testing for scale-resolving simulations

Grid scaling testing was conducted according to the guidelines of Journal of Fluids Engineering by Celik et al.[110] Three meshes were created, all of them are uniformly scaled except the boundary layers at the walls, where it is necessary to reach wall y^+ below five. The grids consist of 2.8 million, 7 million, and 15.6 million cells, respectively.

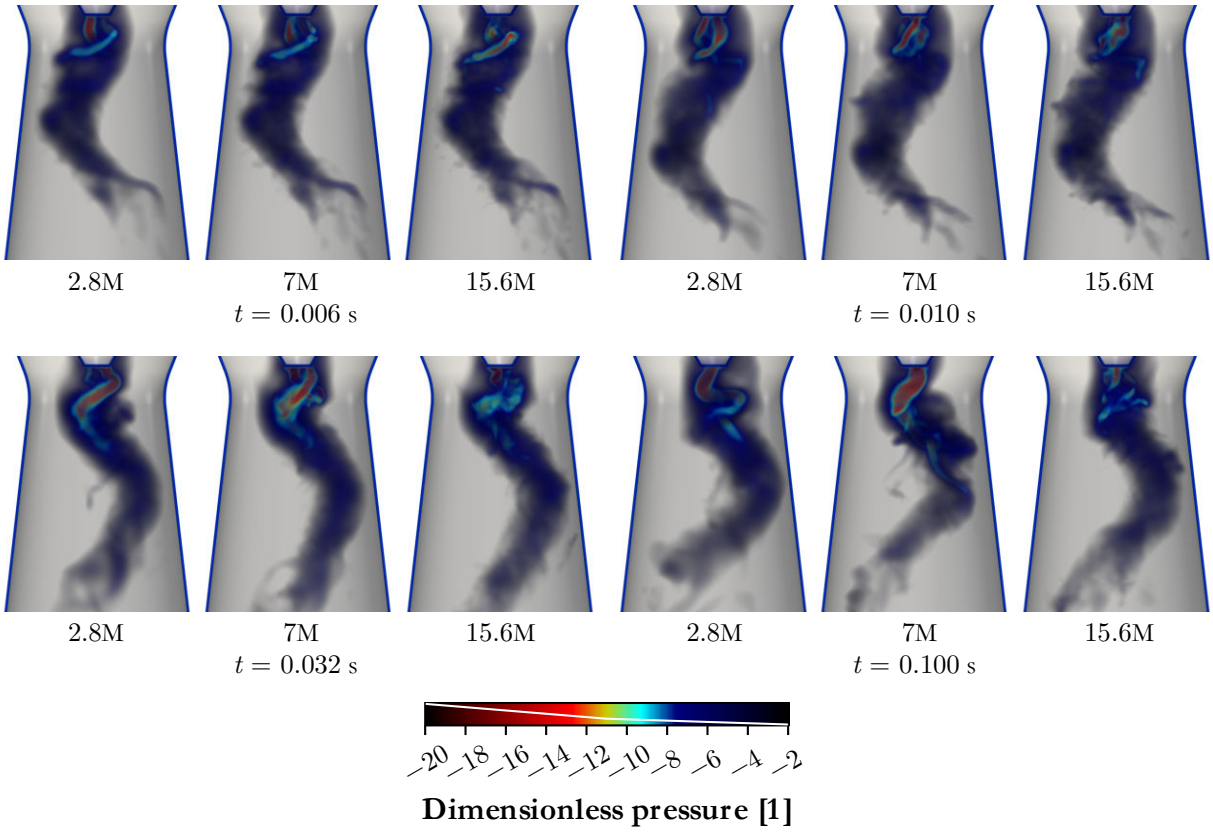

Fig. 4.8: *Dimensionless pressure fields on three different grids with the same initial condition.*

For the testing simulation, fixed boundary conditions with 70% of the total flow rate coming through the tangential inlet, where the total flow rate is 5 l/s, were chosen. The first simulation was carried out on the finest mesh, and when initial transitions faded out, the current state was saved for interpolation on the coarser grids. All three simulations therefore have the same initial conditions, which allows direct comparison of their results. For this purpose, volume rendering visualizations of the dimensionless pressure field are presented in Fig. 4.8. Four snapshots are documented. The first from a time shortly after the beginning of the simulations illustrates the same initial conditions. The time was chosen so that the initial transients already faded out. These are caused by the fact that the solution from the finest grid is not exactly valid on the coarser grids after interpolation. In the second, one can observe different behavior of the vortical structures under the hub tip, in red color. Three distinct helical structures can be seen on the second mesh, which is not the case for the other two. However, these triple vortex ropes survived only for a moment of time. In the third snapshot, the situation becomes quite similar for all the meshes. The evolution of these structures eventually turns out to be different for each mesh. The last snapshot,

which also corresponds to the last time step of the simulation, demonstrates this. Nevertheless, the motion of the vortex rope tail agrees very well among the simulations. It is evident that in all the pictures, the phase of the vortex rope tail matches. The different behavior of the smaller vortical structures can be attributed both to the resolution of the grid and, consequently, to its ability to capture small scales as well as to the inherent unpredictability of turbulent structures.

To assess the scale-resolving ability of the grids, visualizations of a vortex criterion can be used. In Fig. 4.9, volume renders of the modified residual vorticity for the three grids are presented. The rendered snapshot is that from the time shortly after the beginning of the simulation. As the fineness of the grid increases, smaller and smaller vortices are captured. This illustrates the ability of the SBES turbulence model to reflect the grid size. Indeed, SBES is based on the blending of URANS with LES by taking the eddy viscosity as a weighted average of the RANS and LES eddy viscosities

$$\mu_{\mathrm{t}}^{\mathrm{SBES}} = f_{\mathrm{s}}\mu_{\mathrm{t}}^{\mathrm{RANS}} + (1 - f_{\mathrm{s}})\mu_{\mathrm{t}}^{\mathrm{LES}} \tag{4.45}$$

where f_{s} is the shielding function and μ_{t} is the eddy dynamic viscosity. As can be seen, the shielding function controls the blending of RANS and LES closures. It was proposed with respect to a list of requirements, some of them being preventing the boundary layers from being solved by LES (otherwise, much finer meshes are needed) and quick switching to LES after their detachment. Unfortunately, its definition is proprietary. For more information, see the work of Menter, the author of this model[111]. The LES eddy viscosity was modelled using WALE (Wall-Adapting Local Eddy viscosity model). Unlike the RANS eddy viscosity, the LES eddy viscosity is directly affected by the grid size as it is a function of $\Delta = \sqrt[3]{V}$, where V is the cell volume. Its values are typically lower than in the RANS case for the same grid, allowing the scale-resolving ability. The reason is that only the effect of the smallest scales is taken into account. Therefore, the grid should be fine enough for correct results; namely, the smallest resolved vortices should fall into the so-called inertial subrange.

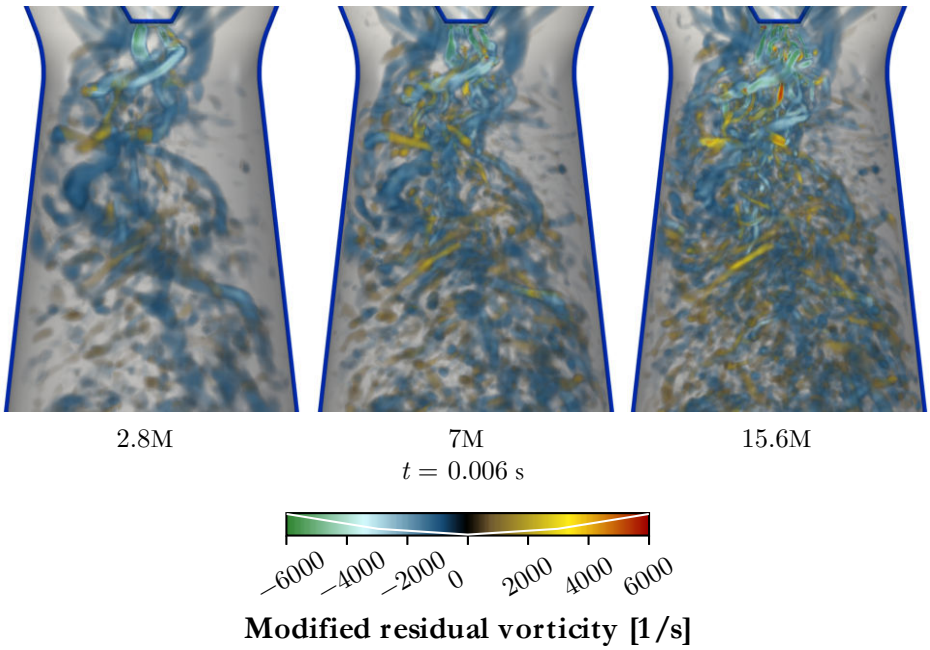

Fig. 4.9: *A volume render of the modified residual vorticity for the three grids. Different levels of detail are clearly visible.*

In all three present cases, the whole diffuser (except the boundary layers by the definition of f_s) was solved as LES, i.e. $f_s = 0$. However, the 2.8M grid seems too coarse, and also the switching from RANS to LES was completed only after a long simulation time. In the remaining two cases, the LES regime covered a wider area starting from the spiral case. The tests conducted showed that the 7M grid falls around the minimal requirements for good LES.

In Fig. 4.10, the static pressure evolution in time from two different probes is presented. The first probe is located right under the hub tip, where the dynamics are dominated by the mentioned irregular vortical structures forming single, most of the time double, and sometimes even triple helix. The temporal evolutions are different among the three meshes in terms of immediate values. The second probe is located farther downstream, where the dynamics are dominated by the passings of the precessing vortex core, characterized by a significant pressure decrease. It is evident that the occurrence of this effect, and thereby also the precession frequency, matches in all the simulations. It can also be observed that the simulation time range covers slightly more than two revolutions of the vortex rope.

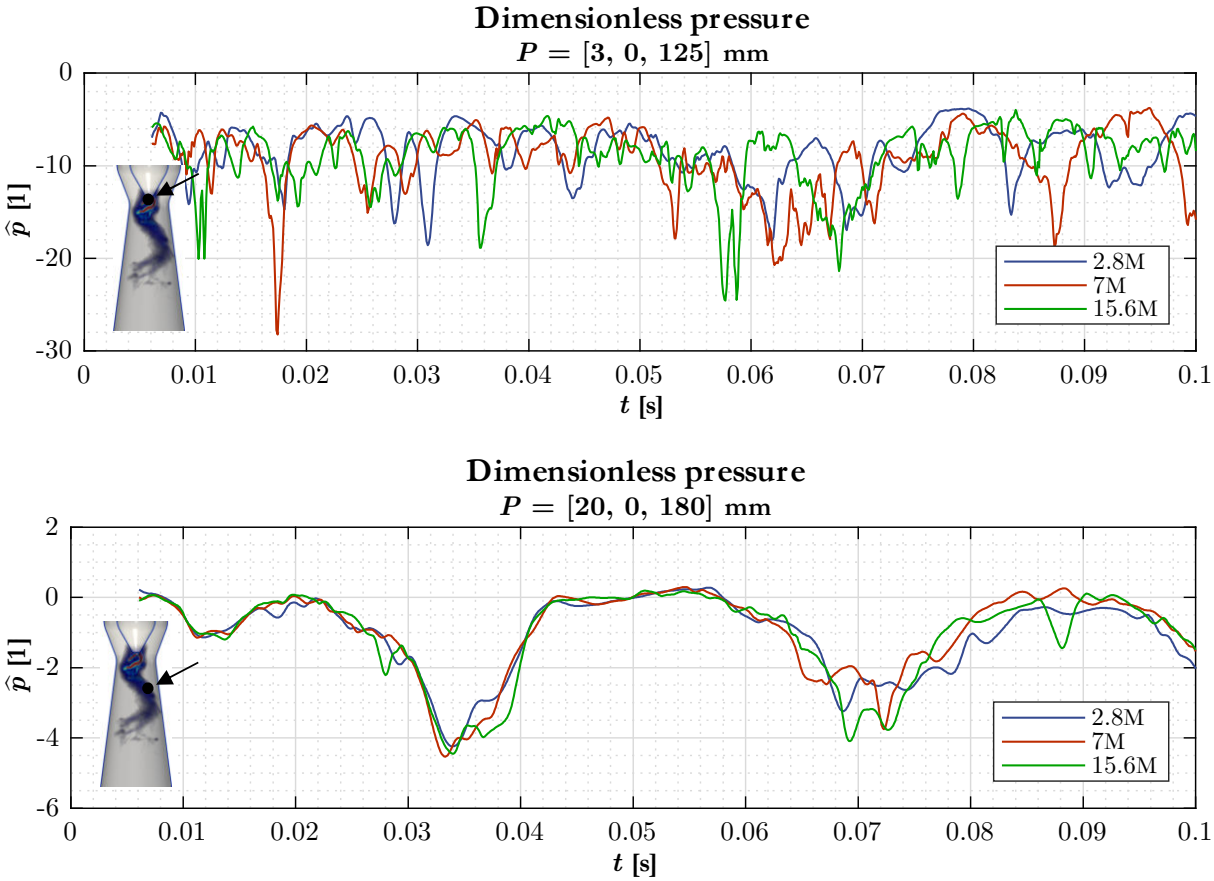

Fig. 4.10: *Evolution of static pressure in time for the probes depicted in the charts.*

For further investigation, the pressure recovery coefficient c_p was chosen in order to include also an integral quantity. The pressure recovery coefficient is defined using the Einstein summation convention as follows

$$c_\mathrm{p} = \frac{\int_{S_1 \cup S_2} p v_j n_j \mathrm{d}S}{-\int_{S_1} \rho \frac{v_i v_i}{2} v_j n_j \mathrm{d}S} \tag{4.46}$$

where S_1 is the inlet to the conical section of the diffuser, S_2 outlet of the diffuser, and n_j outer unit normal vector. The temporal evolution of this parameter is plotted in Fig. 4.11. It is evident that the trend (i.e. the low-frequency dynamics) matches reasonably. The average values and their grid convergence indices as defined in the mentioned paper by Celik et al. are reported in Tab. 4.3. The convergence is oscillatory and GCIs (Grid Convergence Index) are 1.07% for the finest mesh and 2.16% for the middle mesh. The apparent order of accuracy is 3.04.

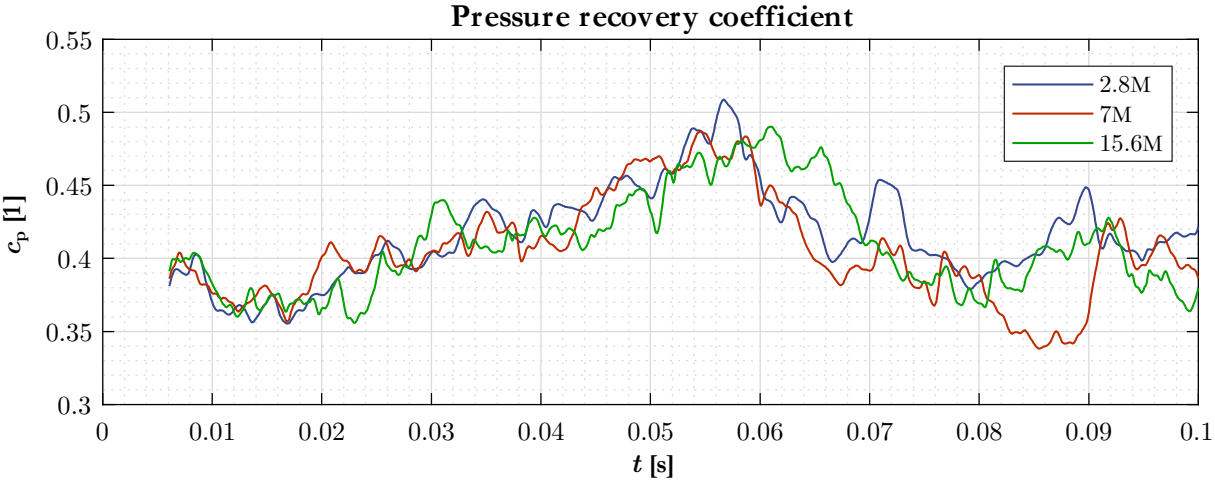

Fig. 4.11: *Pressure recovery coefficient evolution in time.*

Tab. 4.3: *Mesh dependency of the averaged pressure recovery coefficient.*

Mesh	$\overline{c_\mathrm{p}}$	GCI_{21}	GCI_{32}
15.6M	0.4099	1.07%	
7M	0.4056		2.16%
2.8M	0.4162		

Based on the presented results, it is concluded that the immediate values of various parameters may differ among the meshes, but their trends and statistics are satisfactorily close. Taking into account also the requirements on storage and computing power, the middle mesh (with 7 million elements) was found to be optimal for further work. The mesh is described in more detail in the next section.

4.4 Final mesh for scale-resolving simulations

The water domain was created in DesignModeler version 18.1. Two pairs of inlets were created. The first pair is relatively close to the generator itself, much less than often recommended 10 times the pipe diameter to get proper profiles of velocity and turbulence variables. This pair of inlets was used for simulations with transient boundary conditions. It is assumed that the influence of this incorrectness on the flow coming to the diffuser is negligible compared to the effects that are included: the transition from circular to square shape at the tangential inlet, passing along the hub at the axial inlet, and the mixing process of the two flows. Nevertheless, for the simulations with fixed boundary conditions, straight sections 10 diameters long were included so that the second pair of inlets is far enough from the generator to get more realistic profiles. The strategy consists of two steps. First, the simulation is run in steady mode to get the velocity profiles at the first pair of inlets. After that, the straight sections are discarded, and the obtained profiles are prescribed at the first pair of inlets to reduce the computational cost for the transient phase. The outlet is three diameters away from the diffuser. It balances the effect of the constant pressure boundary condition on the flow in the diffuser and the extra computational cost associated with a longer domain.

The domain was decomposed with respect to the intended mesh generation in Meshing version 18.1. The aim was to get a mostly hexahedral mesh that is preferably conformal and avoids bad quality regions.

At the walls, a thin layer was cut out to get better control over the mesh in the boundary layer, which is usually very thin in turbulent flows. Straight pipes were meshed as it is quite common – a square with slightly rounded edges was created in the center, and the rest was cut diagonally into four parts. The most difficult parts are those around the hub, in the spiral case, and the diffuser inlet. In what follows, they will be described in more detail.

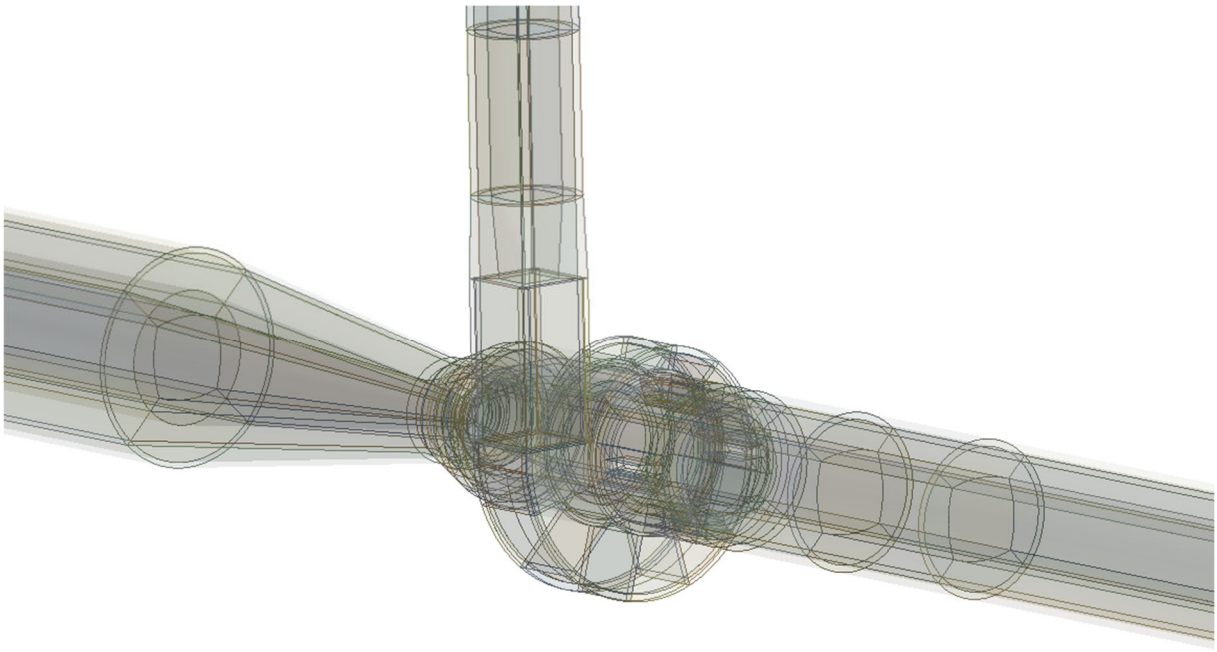

Fig. 4.12: *A view of the decomposed domain.*

Fig. 4.13 shows the decomposition and mesh at the upstream part of the hub. In the presented longitudinal cross section, an unstructured part meshed by the "Hexa Dominant" method is visible. It allows reducing the number of cells in the radial direction along its length, thus keeping the cell size in the narrow part along the hub similar to the inlet pipe. The price is a small amount of wedge cells and cells of a lower quality. A nonconformal interface can be seen in both views. It was found to be better than possible conformal options. Since the space for a conformal transition is limited, the results were poor. This change in the number of cells along the circumference leads to a better aspect ratio of the cells in the space between the hub and the outer walls (see the transverse cross section in Fig. 4.15, where it is apparent that the shape of cells is close to cubic).

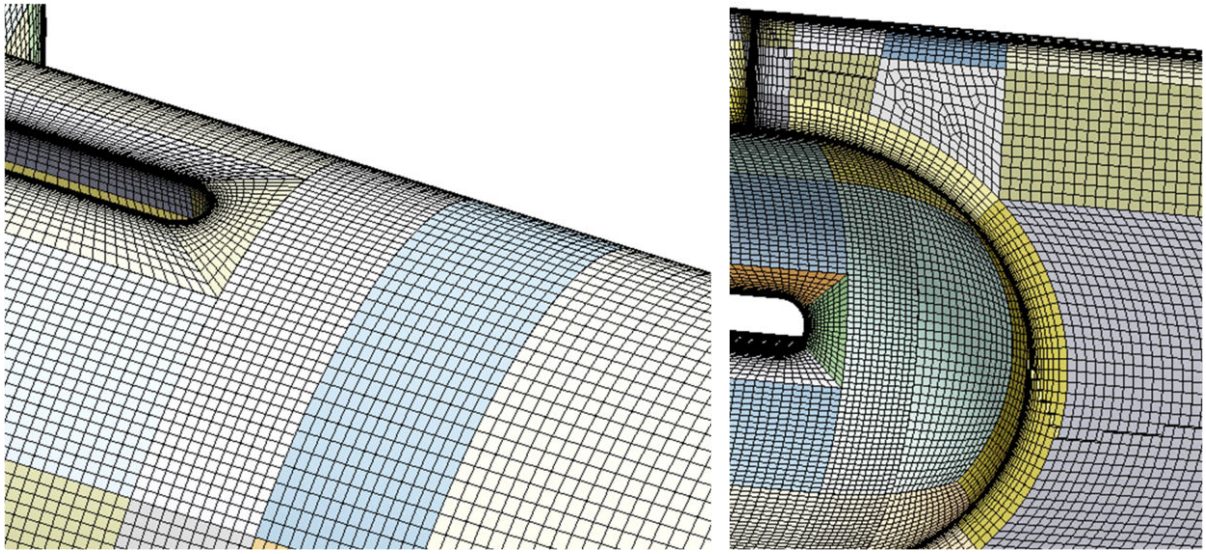

Fig. 4.13: *The mesh at the upstream part of the hub.*

In Fig. 4.14, the mesh at the hub fins is captured. The domain was cut circumferentially each 30 degrees, and the parts that contain a fin were further decomposed as depicted. The situation turned out to be a bit complicated by the fact that the fin width is constant, thus spanning a gradually bigger part of the 30-degree part when moving towards the axis. It led to somewhat stretched cells on the inner side to avoid sharp jumps in cell size or highly skewed cells.

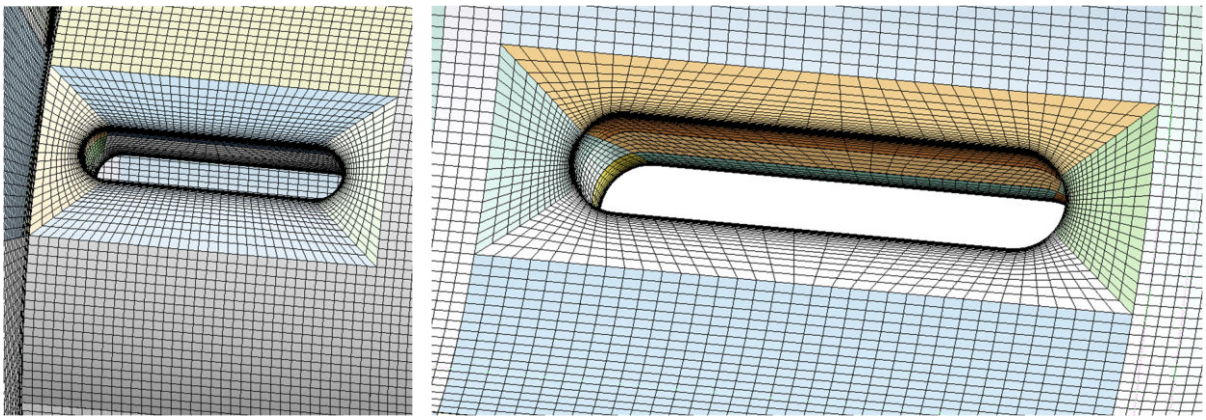

Fig. 4.14: *Mesh at the hub fins. Left: an outer view, right: an inner view (from the hub space).*

As we proceed further downstream, the mixing part follows. It is the place where the tangential and axial inflow meet. The challenges here are the change of diameter from 76.6 to 80 mm and the sharp corners around which the boundary layer mesh needs to be bent. The latter was addressed by small square parts with an unstructured mesh. A drawback is that the Courant number may be high in the small cells that are farther from the wall. Fortunately, it is not a problem for the used solver with an implicit temporal discretization method.

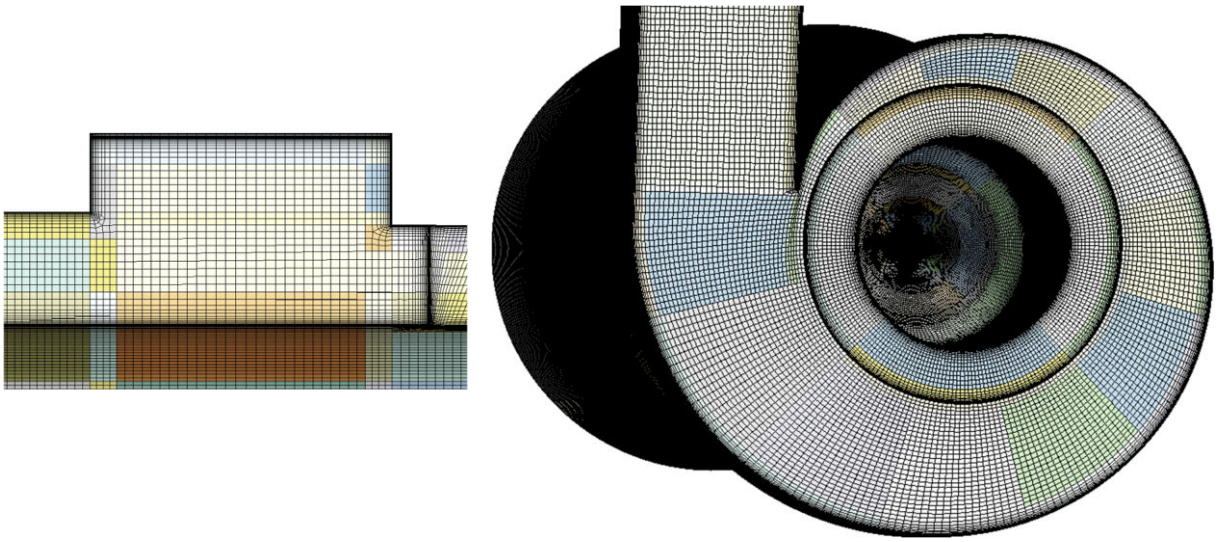

Fig. 4.15: *Mesh of the mixing part and spiral case.*

The spiral case was, in agreement with the previous part, also cut circumferentially each 30 degrees. The number of cells along its radius should gradually decrease along the circumference to avoid too small cells at the tongue. One approach could be an unstructured conformal mesh. However, in this case, a nonconformal mesh was preferred. The advantage is the cells aligned with the flow passage with minimal skewness. The price is obviously the presence of nonconformal interfaces.

The last nonconformal interface is in the place where the circular cross section of the tangential inlet pipe changes to the square shape of the spiral case. Thanks to it, optimal meshes can be used in both parts. A conformal transition would be too complicated here.

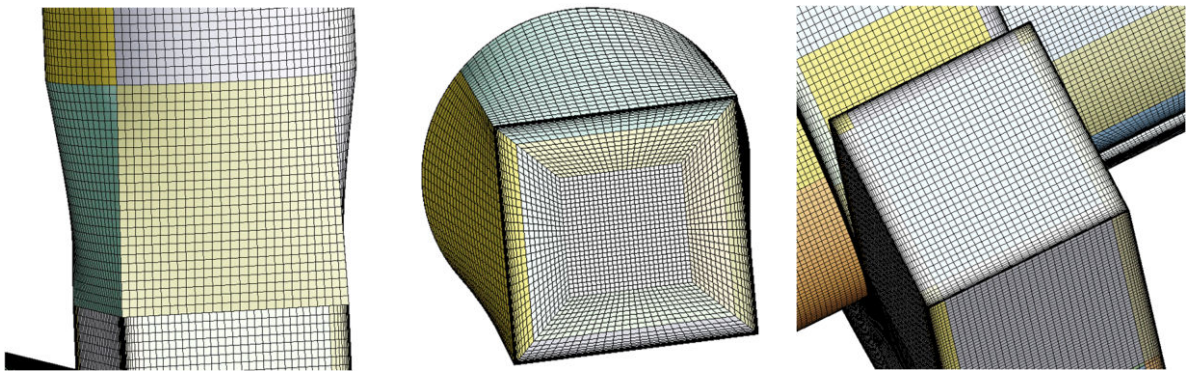

Fig. 4.16: *Mesh of the transition part.*

The diffuser inlet is also challenging. The distance between the hub and the outer wall gradually increases, so to avoid larger cells in the diffuser, a decomposition was created. The opposite is actually desirable – since the diffuser is the zone of interest, a bit finer mesh was the goal. The decomposition allowed for a fully conformal grid. The "Hexa Dominant" method was used again, leading to a small number of cells with a higher skewness. Most of the cells are well aligned, so the result is considered satisfactory.

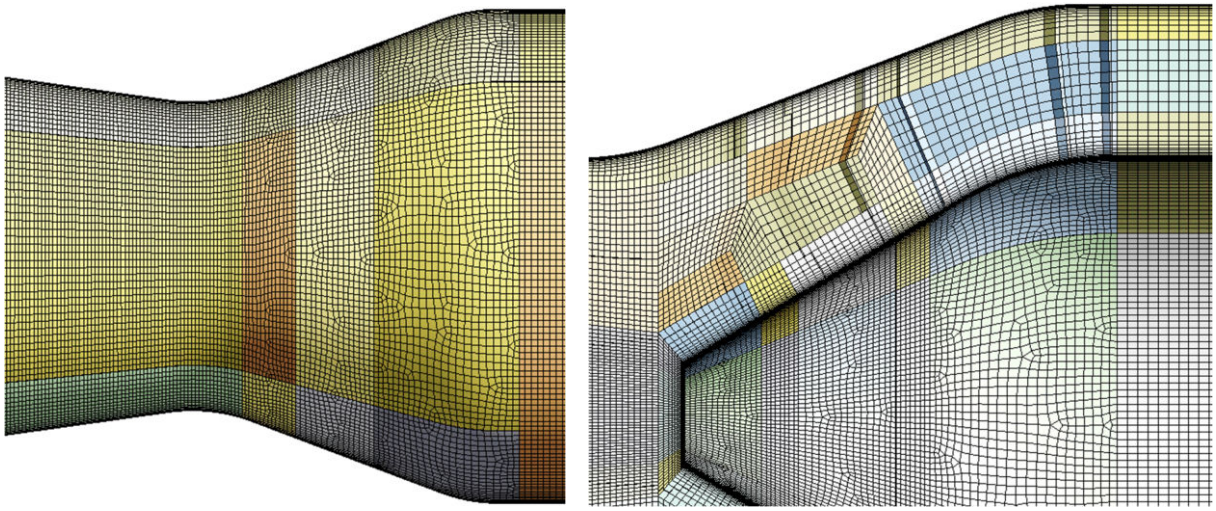

Fig. 4.17: *Mesh at the diffuser inlet.*

In the diffuser, as the part of interest, a structured grid was created for each subpart. A challenging part is the hub tip, where the cells are compressed as the transverse cross section of the central part of the decomposition gradually gets smaller towards it. Some refinement is actually desirable to resolve the vortex rope well. On the other hand, too small cells would lead to excessive Courant numbers and thus the need for a very small time step. In fact, the smaller the hub tip is, the more compressed the cells are if the present decomposition is used (see Fig. 4.18). In this case, the results are as desired. For smaller hub tips, however, a different decomposition should be used. The size of the cells increases in the downstream direction together with the diffuser transverse cross section area. In this case, the cells at the diffuser outlet are comparable in size with those in the straight part upstream of the diffuser inlet.

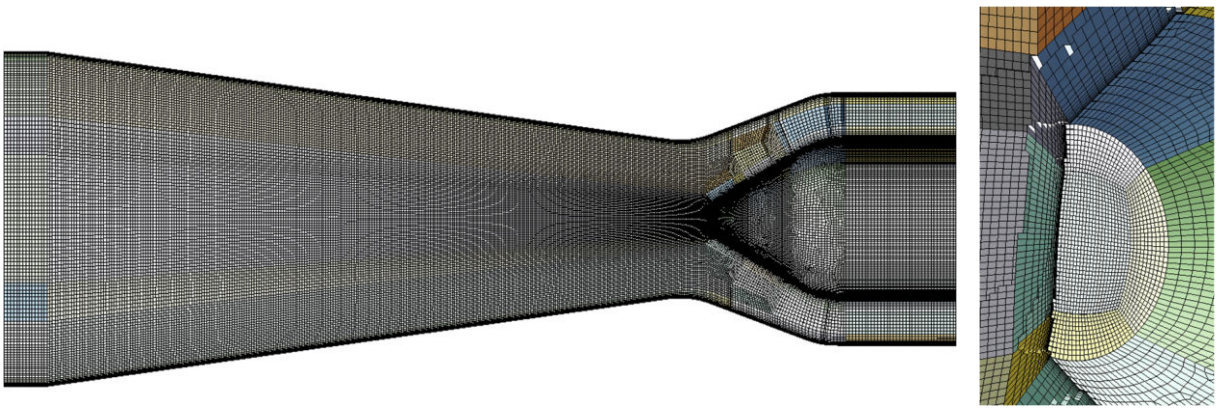

Fig. 4.18: *Mesh of the diffuser.*

For mesh quality evaluation, there are several metrics in Meshing, from which skewness was chosen. For this metric, the following guidance is provided in the software documentation: 0–0.25 Excellent, 0.25–0.5 Good, 0.5–0.75 Fair, 0.75–0.9 Poor, and 0.9–1 Bad. The bar chart in Fig. 4.19 shows that the vast majority of cells fall into the excellent range. Only a small number of cells are evaluated as poor.

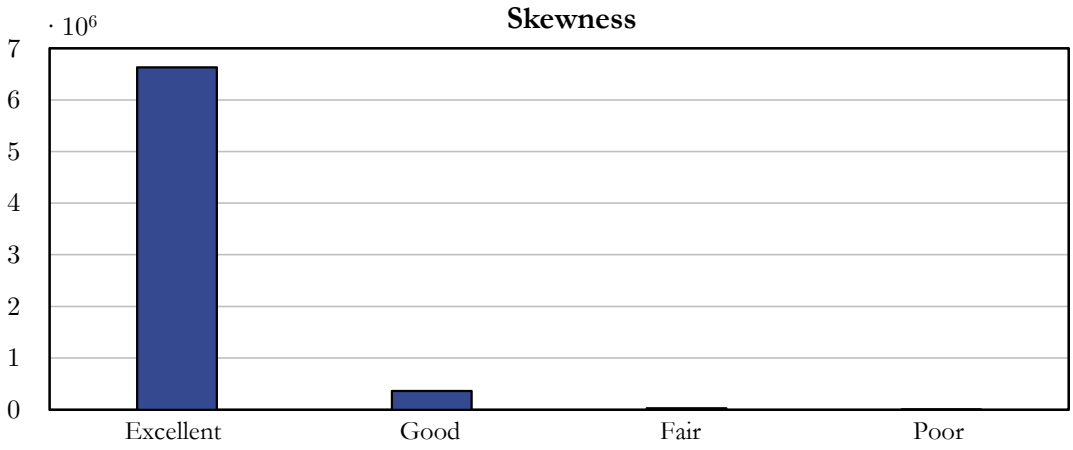

Fig. 4.19: *Bar chart of the skewness.*

In total, the mesh consists of 7,017,707 cells out of which 2,753,841 belong to the diffuser part, which is the zone the data were collected from. The mesh needed to be checked during the calculations that it is fine enough for the LES mode and that the wall y^+ is below 5 (optimally below 1). In Fig. 4.20, visualizations of the shielding function (isosurface for the value of $f_s = 0.5$) and wall y^+ are presented. The first reveals that the LES mode was used from the spiral case on. The second confirms that sufficient values of wall y^+ were attained. Although this is only a single snapshot from simulation SBES-F-5-50-50, the outcomes were the same for all the SBES simulations.

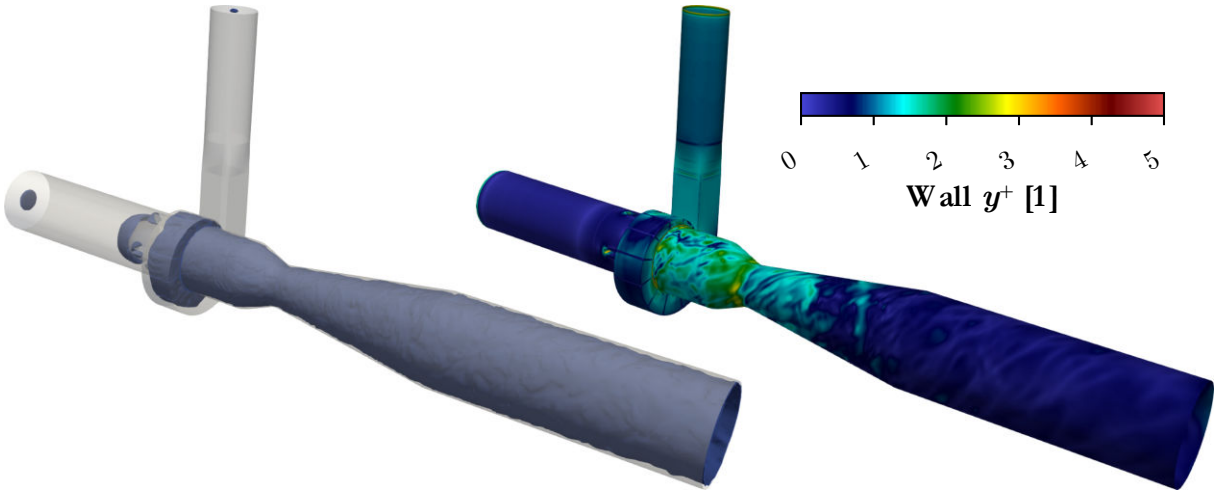

Fig. 4.20: *Left: isosurface of the SBES shielding function f_s for the value of 0.5, right: contours of wall y^+. A snapshot from simulation SBES-F-5-50-50 is visualized. In other SBES simulations, the results were similar.*

4.5 Comparison of CFD results with PIV measurements

The new swirl generator designed in this work was the subject of PIV measurements carried out in cooperation with Institute of Thermomechanics of the Czech Academy of Sciences as part of a research project. Only a brief description of the test circuit and equipment will be given in what follows. The main purpose of this work is to compare the measurements with the results of CFD simulations to find out whether CFD can reasonably predict the flow and consequently whether it is worth studying the results more in detail.

The PIV measurements were performed for two planes: a longitudinal plane passing through the diffuser axis and a transverse plane perpendicular to the axis located where the diameter is 70 mm. In this work, only the longitudinal plane measurements are used since positioning and measurement uncertainties are lower than those of the transverse plane measurements. The measurements were conducted in stereo regime, i.e. photographs from two cameras (NanoSense MkIII with Nikon lenses) were used to obtain all three velocity components. The recording length was 3.272 s with a frequency of 500 Hz. The New Wave Research Pegasus-PIV laser was used as the light source. Silver-coated borosilicate glass particles of spherical shape with a diameter of 10 μm were dispersed in the water. Tracing these particles in the photographs is the way of determining velocity vectors. For positioning calibration, a multilevel calibration target was used.

The hydraulic circuit in which the swirl generator was installed consists of two parts. The first part comprises a pump, stainless steel pipes, and a water tank. The circuit is closed by the second part made of plastic pipes. These plastic pipes allow easy adjusting with respect to the desired application. In this case, the plastic part comprises a T-junction to divide the flow into two branches for the two inlets of the generator. The hydraulic circuit, as well as the PIV cameras and swirl generator with the calibration target inserted in the diffuser, are depicted in Fig. 4.21. The pump is not visible since it is placed in the basement.

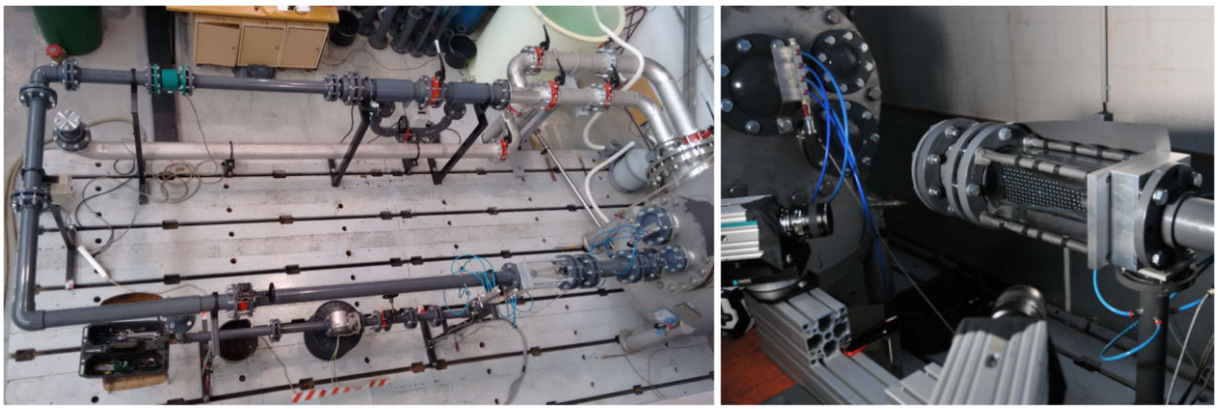

Fig. 4.21: *Left: overall view on the upper part of the hydraulic circuit, right: a view on the cameras and the multilevel calibration target placed inside the diffuser. Photographs credit: David Štefan.*

For comparison of the CFD results with the PIV measurements, three outcomes will be used: mean velocity fields, mean turbulence kinetic energy field, and discrete Fourier transform of axial velocity. Given the irregular nature of the observed flow, only statistical quantities can be directly compared. The velocity fields are assumed in the dimensionless form defined in section 4.2.3. The turbulence kinetic energy is also nondimensionalized. The reference value is the specific kinetic energy computed from the mean velocity in the throat

$$\hat{k} = \frac{\|\boldsymbol{v}'\|^2}{{v_{\mathrm{ref}}}^2} = \frac{\|\boldsymbol{v}'\|^2 \pi^2 {d_{\mathrm{throat}}}^4}{16 {Q_{\mathrm{total}}}^2} \tag{4.47}$$

It is noted that in this case, this kinetic energy is not associated only with eddies in turbulent flow as the true turbulence kinetic energy should be. It is actually associated with resolved unsteadiness; therefore, it would be nonzero also for unsteady laminar flows. Despite this fact, the term turbulence kinetic energy is often also used in this context in the literature. The discrete Fourier transform of axial velocity is used to compare the dynamics. A structured rectangular grid of 21×21 points was created over the PIV domain. Then, the data from both PIV and CFD were interpolated onto this grid and the discrete Fourier transform was computed for each point. Instead of comparing all the spectra, a weighted average of them was computed. To introduce it, it is first needed to define the weight. For each point, the temporal series of the axial velocity values is taken and its mean is subtracted. The absolute values of the resultant fluctuation values are computed, and the 2% of the largest values are discarded. The weight is then the largest of the remaining values. It is intended to be a measure of the amplitude of the fluctuations. The weighted average is then computed as usual

$$\overline{v}_{\mathrm{z}}(f) = \frac{\sum_{i=1}^{N} v_{\mathrm{z}}(f)_i w_i}{\sum_{i=1}^{N} w_i} \tag{4.48}$$

where i is the index of the grid point (total number of points is N), $v_{\mathrm{z}}(f)$ is the result of the discrete Fourier transform (amplitude of the v_{z} component with frequency f), and w_i is the weight.

There are two operating points for which both PIV data and data from CFD simulations with the SBES and RSM turbulence models are available. The first has a flow rates ratio of 50:50 and a total flow rate of 10 l/s, the second 70:30 and 5 l/s. When comparing the PIV measurements with the CFD results, one thing should be kept in mind. It originates from the fact that PIV results are available only for a plane. The actual measured plane is given by the accuracy of the placement of the calibration target and the calibration itself. In our case, the plane should pass through the diffuser axis. Any discrepancy obviously means that different velocity fields are measured. Moreover, it will be shown in Fig. 4.29 that the velocity profiles at the diffuser inlet predicted by the simulations with the SBES turbulence model are not axisymmetric. Consequently, the velocity fields also depend on the orientation of the longitudinal plane. Looking at the mean velocity fields presented in figures 4.22 and 4.23, the results of PIV and CFD SBES are very similar except for discrepancies that can be explained by the mentioned positional inaccuracies. Different radial velocity fields in the upper part indicate that the measured plane could have a certain offset. Leaving aside these discrepancies, it can be stated that in the first case, the mean velocity fields are well predicted by the SBES simulations and slightly worse by the RSM simulation. In the second case, there are noticeable differences in the axial velocity fields. The results of RSM are in this case closer to PIV than SBES. Namely, SBES predicts sharper velocity decay towards the axis and stronger backflow. The other two velocity components are similar.

The turbulence kinetic energy is in both cases also well predicted by the SBES simulations. The RSM simulation resulted in lower values, which is expected as this turbulence model does not resolve any eddies. In the first case, the contour shapes are well predicted. In the second case, the area of higher values is narrower and extends farther downstream compared to PIV and SBES.

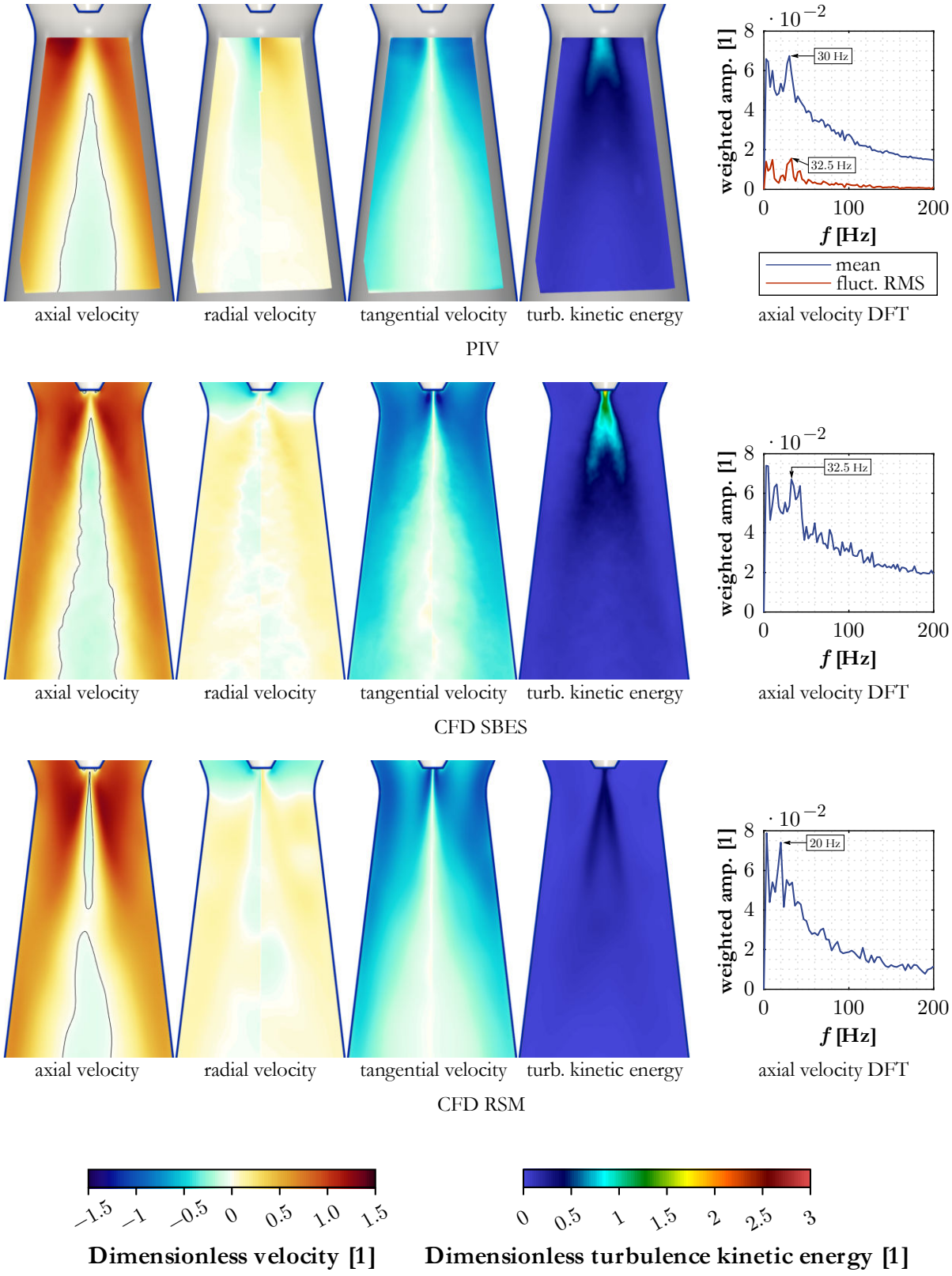

Fig. 4.22: *Results of PIV measurements and CFD simulations with the SBES and RSM turbulence models. Operating point with a flow rates ratio of 50:50 and a total flow rate of* 10 *l/s. The black line in the axial velocity field is the contour of zero value.*

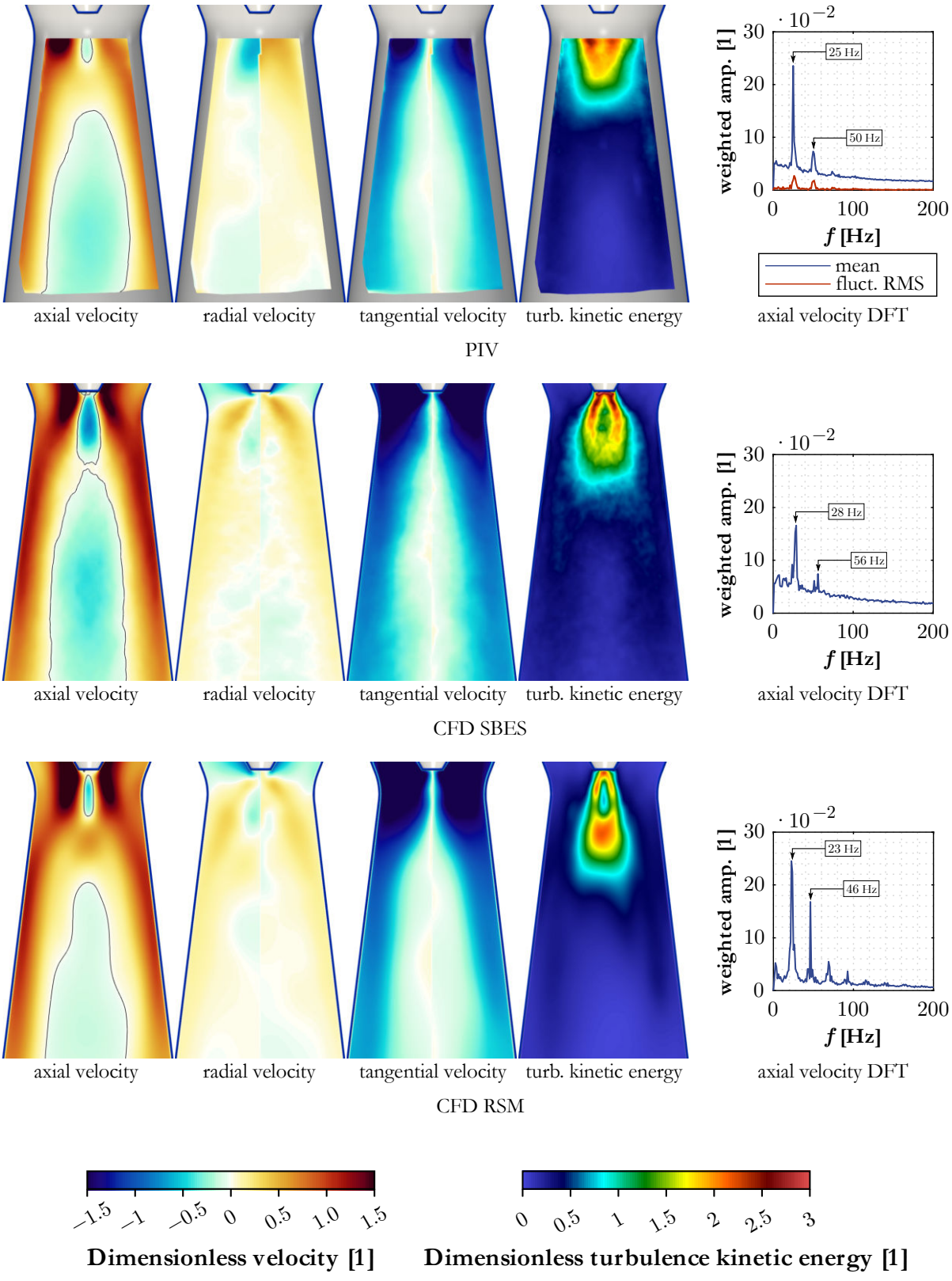

Fig. 4.23: *Results of PIV measurements and CFD simulations with the SBES and RSM turbulence models. Operating point with a flow rates ratio of 70:30 and a total flow rate of* 5 *l/s. The black line in the axial velocity field is the contour of zero value.*

The discrete Fourier spectra of the PIV measurements and SBES simulations are also similar. In the first case, there are two low-frequency peaks and then the most dominant peak around 30 Hz. It is noted that the spectra largely depend on the time interval covered by the data. PIV covers in both cases more than 3 seconds, which is much more than both CFD simulations. For this reason, the PIV data were split into several parts that cover the same time as the SBES simulations. The obtained spectra for each part were averaged, and the RMS value of the fluctuations was computed. The averaging led to a smoother evolution of the amplitude observed for higher frequencies. The only significant discrepancy between the PIV and SBES spectra is that the SBES spectrum has a second peak close to the most dominant one. However, this second peak is present in the fluctuation part of the PIV spectra. It is therefore possible that this is caused by the irregularity of the flow, and the second peak in the SBES spectrum is only a matter of the particular time interval covered by the simulation. The RSM spectrum misses the dominant frequency, but the decay of the amplitudes towards higher frequencies is well predicted.

In the second case, the results exhibit a dominant frequency and also its multiples (superharmonics) with decaying amplitude. At first glance, one can notice a significantly lower amplitude in the case of the SBES simulation. This is caused by the fact that the dominant frequency predicted by the SBES simulation is different from the frequency measured by PIV and is not periodic for the given time interval. Consequently, the PIV spectrum features one frequency with a high amplitude, whereas the SBES spectrum features two neighboring frequencies (in the discrete Fourier series) with amplitudes that are relatively high but noticeably lower than the PIV peak. This effect is usually called spectral leakage. Since RSM does not resolve eddies, the peaks are more pronounced. The amplitude of the dominant frequency is in agreement with PIV, but the superharmonics are overestimated. The dominant frequencies differ: the PIV value (25 Hz) is overpredicted by SBES (28 Hz) and underpredicted by RSM (23 Hz). It turns out that the prediction of the vortex rope precession frequency is complicated with regard to the complex velocity distribution at the inlet of the diffuser given by mixing of the two inflows that needs to be well resolved.

As the last point, results of CFD simulations with the SBES turbulence model are compared in Fig. 4.24 with high speed camera recordings to assess whether the vortex rope shape and behavior are well predicted by the simulations. For both operating points, the behavior of the vortex rope is similar and it is possible to find matching situations. In the first case, a thin vortex rope is observed. It is shown in the middle picture that the vortex filament may twist and form a vortex ring. The right picture illustrates that the filament may also break into two intertwined vortices, which happens most often right under the hub tip. In the second case, we observe a complex behavior of the vortical structures under the hub tip. The three pictures illustrate that the number of vortices changes over time. We can observe either a single vortex or mostly twin vortex ropes, which may also break into a larger number of smaller vortices. It is noted that the high speed camera recordings were in this case performed for the total flow rate of 10 l/s, whereas both CFD and PIV are for 5 l/s. Due to the mismatch in the Reynolds number, the results are not fully comparable (leaving aside the presence of a gas phase in the experiments). On the other hand, the swirl number is the same (see Fig. 4.1), so similar shapes of the vortex rope can be expected, which is confirmed by the present results. More pictures from CFD simulations with fixed boundary conditions and experiments can be found in appendix B.

Overall, it is concluded that the results of the simulations are worth further study, which is the subject of the following section. More on the vortex rope behavior is given in section 4.6.5.

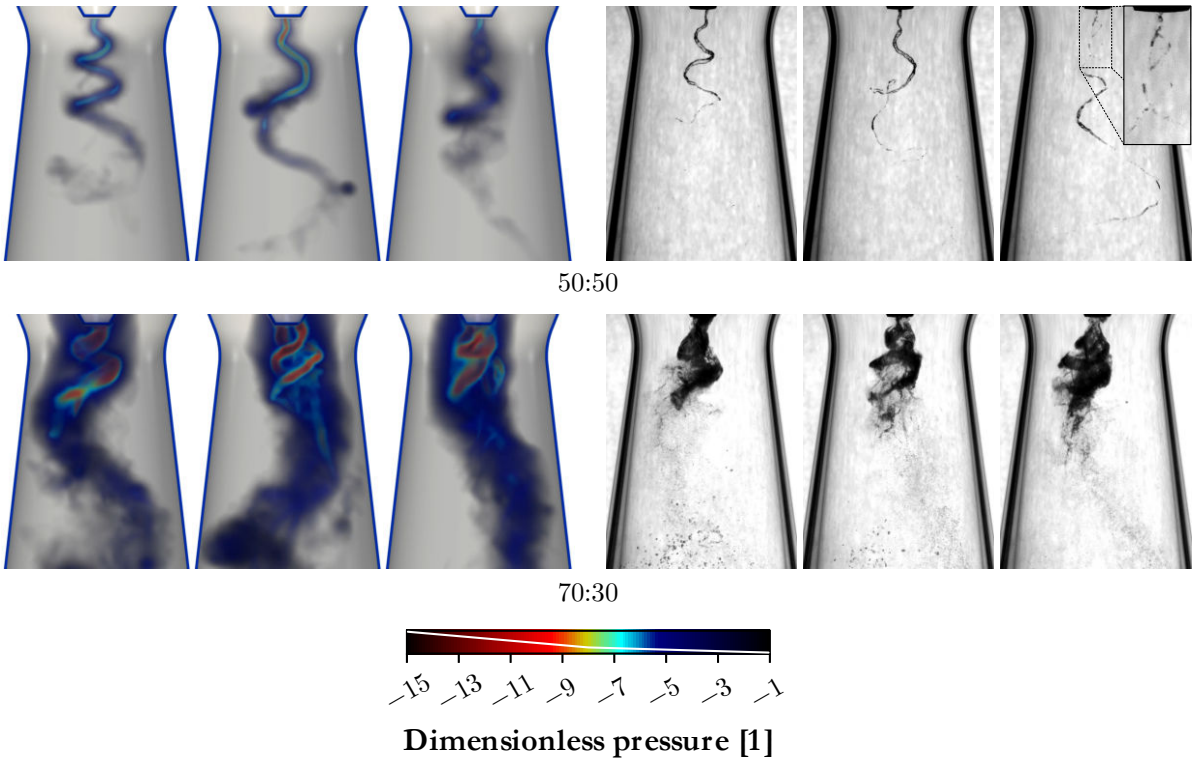

Fig. 4.24: *Results from CFD simulations with the SBES turbulence model (left) and high speed camera recordings (right). Operating points with flow rates ratios of 50:50 and 70:30.*

4.6 Results of simulations

4.6.1 Visualizations of the vortex rope for different flow rates ratios

The vortex rope is most often visualized using static pressure. This quantity is important in practice as it indicates the possibility of cavitation, and its values are typically measured by transducers on the walls to investigate the dynamical behavior of the flow. For identification and visualization of vortical structures, the modified residual vorticity is used.

Fig. 4.25 depicts volume renders of the dimensionless pressure and modified residual vorticity fields in selected time instants from both SBES simulations with transient boundary conditions. These snapshots were selected so that the flow rates ratio corresponds to the values listed below the pictures. They document the evolution of the vortex rope as the tangential flow rate increases and the axial flow rate decreases to keep the total flow rate constant. More on the dynamics of the vortex rope is to follow in further sections.

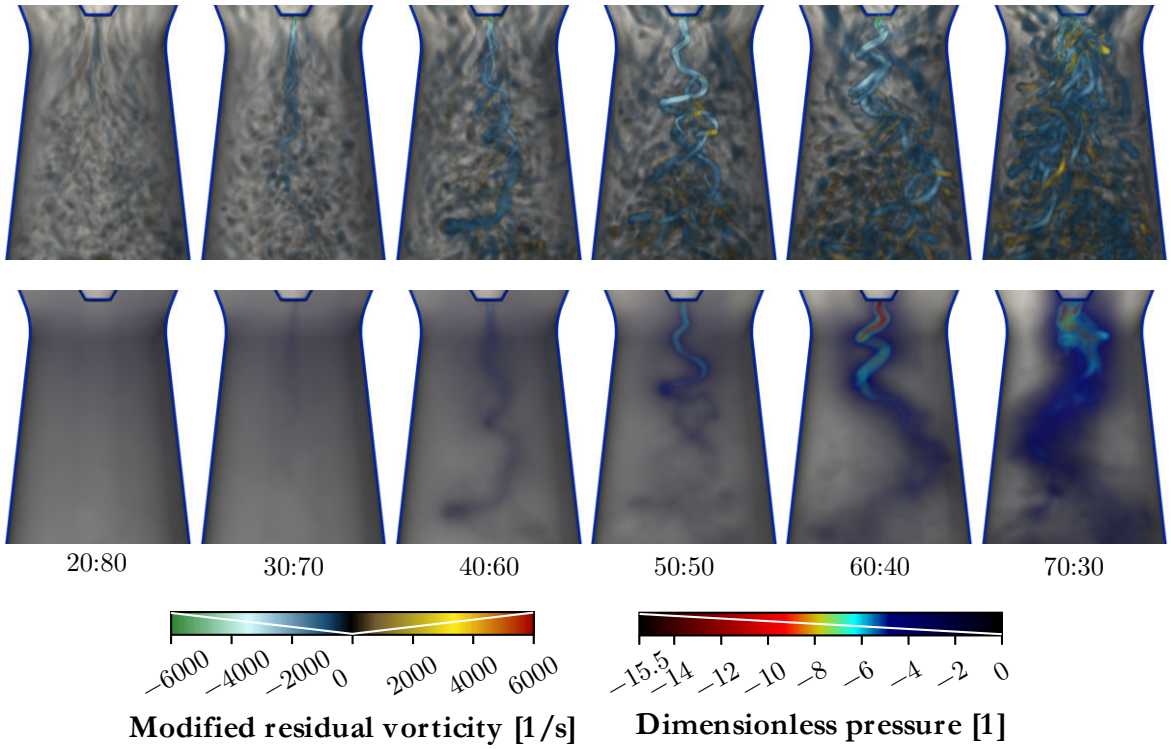

Fig. 4.25: *Evolution of the modified residual vorticity (top) and dimensionless pressure (bottom) as the boundary conditions change. The flow rates ratios are listed below each pair of pictures.*

4.6.2 Swirl number and pressure minima evolution along axis and in time

The swirl number is often used as a measure of the swirl intensity. It has been shown that different regimes of the vortex rope can be attributed to different ranges of the swirl number[21], and that the precession frequency of the vortex rope and the natural frequency of the system can be sought as a function of the swirl number only instead of separate dependencies on head and discharge[23]. There exist different definitions of the swirl number. The one used here is defined as the ratio of

the axial flux of tangential momentum to the axial flux of axial momentum (see equation (4.1)). It is therefore an integral parameter evaluated for a given cross section. In the present cases, we can consider it a function of the longitudinal coordinate and time. The resultant values for SBES simulations with transient boundary conditions are given by contour plots in Fig. 4.26.

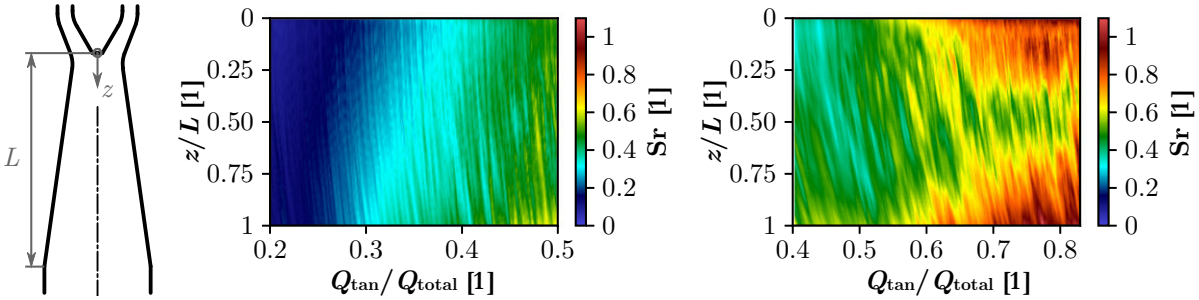

Fig. 4.26: *Dependency of the swirl number on the ratio of tangential to total flow rate (proportional to time in our case) and a dimensionless longitudinal coordinate for simulation SBES-T-2 (left) and SBES-T-1 (right).*

We see that the swirl number for lower tangential flow rates increases along the diffuser. As the tangential flow rate increases, a significant increase is observed in the upper part. It is apparently caused by the growing vortex rope. As a result, the local minimum of the swirl number evolution along the diffuser moves to around half its length. The presented contour plots show that the swirl number is just as the vortex rope form affected primarily by the flow rates ratio and only secondarily by the vortex rope strength. This supports the finding of Cheng[25] that the swirl number is not suitable for quantifying the vortex rope strength. Their V_s parameter (introduced in section 1.1) was unfortunately found numerically sensitive in this work (the results were strongly affected by the method of smoothing of the average velocity profiles). Therefore, a different approach is proposed. Parameter $\hat{p}_{(i,j)}$ is computed as follows. At first, the i% lowest dimensionless pressure values in a given cross section perpendicular to the diffuser axis are taken. From these values, the j% lowest are discarded to remove spurious peaks. Finally, an averaging procedure is applied to the remaining values, in this case weighted by the cell size. It should be noted that this simple approach works well for fairly uniform meshes. For highly nonuniform meshes, taking as many cells with the lowest pressure values as needed to cover a given percentage of the total area is suggested. The results for $\hat{p}_{(5,5)}$ in Fig. 4.27 show that the vortex rope is noticeable from $Q_{\mathrm{tan}}/Q_{\mathrm{total}} = 0.3$. From this point on, its longitudinal extent increases and pressure in its core decreases.

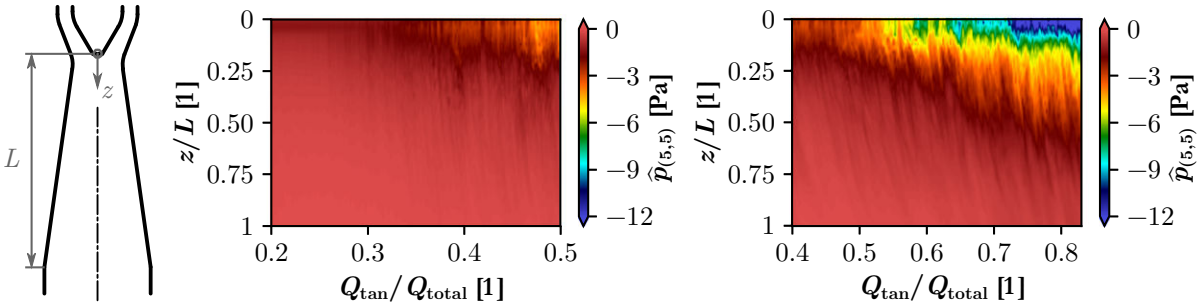

Fig. 4.27: *Dependency of $\hat{p}_{(5,5)}$ on the ratio of tangential to total flow rate (proportional to time in our case) and a dimensionless longitudinal coordinate for simulation SBES-T-2 (left) and SBES-T-1 (right).*

4.6.3 Velocity profiles

As the next step, velocity profiles in different cross sections for different operating points are investigated. The velocity profiles were computed as circumferential and temporal averages of the velocity fields. The data from SBES simulations with transient boundary conditions were used, so the temporal average was performed over a widow of $T = 0.08$ s around the operating point of interest to smooth out fluctuations to some extent. The operating point with the flow rates ratio of 50:50 was taken from simulation SBES-T-1. This window was set based on observations of the averaged fields for different values of T. It is long enough to ensure that changes in the results are minor when further widening it, and at the same time, it is short enough with respect to the unsteady boundary conditions. For simulation SBES-T-1, the component flow rates change by 2.9% of the total flow rate during time T, while for simulation SBES-T-2, it is 0.73% since the rate of change is four times smaller. The results are depicted in Fig. 4.28. We see that the axial velocity profile at the inlet persists throughout the whole range, which is given by the maintained constant flow rate. The circumferential velocity gradually increases, leading to an increase in the swirl number, as observed in Fig. 4.26.

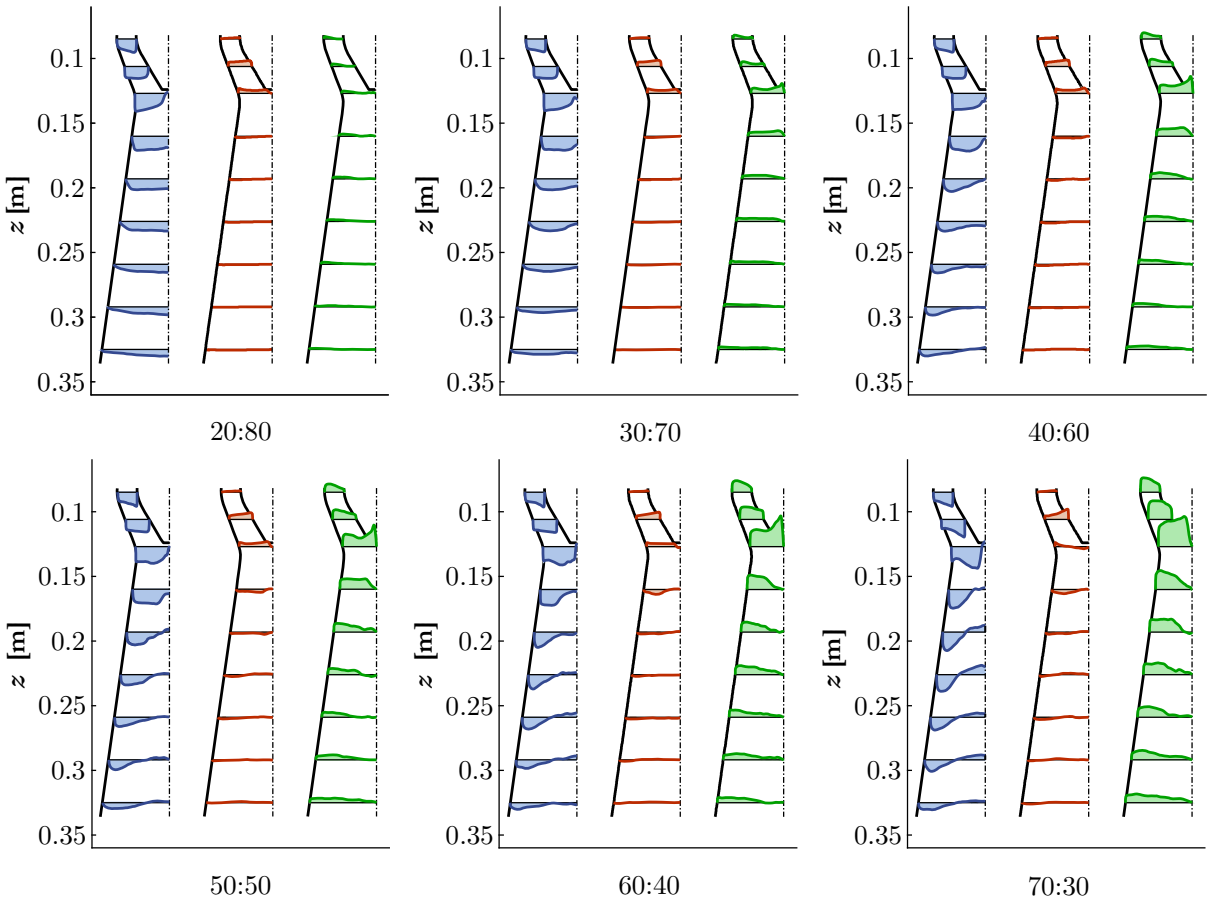

Fig. 4.28: *Velocity profiles during various phases of simulations SBES-T-2 (up to 40:60) and SBES-T-1 (from 50:50). Left: axial velocity, middle: radial velocity, right: tangential velocity. The profiles are averaged circumferentially and temporally over $T = 0.08$ s. All components are in scale. The tangential to axial flow rate ratios are listed below each picture.*

Recall that it was pointed out by Resiga et al.[76] that in swirl generators with fixed blades, there is typically an excess of axial velocity at the hub, which is exactly opposite to the turbine from the FLINDT project operating in part load with a higher axial velocity at the crown and lower at the hub. Their analysis is based on the Bernoulli equation applied to a straight device with a single inlet. Our generator, however, has two inlets, and the resulting flow incoming to the diffuser is the result of a mixing process. It is observed that the axial velocity has its maximum at the hub, similarly to the mentioned straight generators with fixed blades. The tangential velocity profile is different, with its maximum at the outer wall. As an idea for future work, it is suggested to explore possibilities of controlling the resultant velocity profiles (e.g. by different hub shapes, installations, or nonuniform velocity distributions at the inlets).

The velocity profiles in the diffuser exhibit a typical characteristic of flows with a vortex rope: axial velocity deceleration at the axis as the swirl intensity increases. It is noticeable right under the hub tip that the axial velocity close to the axis grows with the swirl number and at the last point even reaches a significant peak. This is connected with the presence of twin twisted vortices, as can be seen in Fig. 4.25.

Since the incoming flow is the result of a mixing process, we shall also investigate velocity profiles for the whole diffuser inlet cross section. The results in Fig. 4.29 were again averaged over $T = 0.08$ s. It is evident that the incoming flow is significantly nonuniform. LIC textures reveal the existence of vortical structures. They were also observed during experiments thanks to cavitation or degassing in their cores if the pressure was low enough.

Temporal fluctuations of the velocity profiles can be quantified using the standard formula for the turbulence intensity

$$I = \frac{v'}{\bar{v}}, \qquad v' = \sqrt{\frac{1}{3}\left(v_{\mathrm{x}}'^{\,2} + v_{\mathrm{y}}'^{\,2} + v_{\mathrm{z}}'^{\,2}\right)}, \qquad v_i' = v_i - \bar{v}_i \tag{4.49}$$

The results depend on the length of the time interval used for averaging. For $T = 0.08$ s, they are listed in the following table. It is evident that the turbulence intensity at first grows, then reaches its peak in the middle of the explored range, and finally decays. In other words, when either axial or tangential inflow dominates, the turbulence intensity is lower. These increased values in the middle indicate that the mixing process of the two component flows generates unsteadiness that propagates to the diffuser.

Tab. 4.4: *Turbulence intensity averaged over* $T = 0.08$ *s.*

Flow rates ratio	20:80	30:70	40:60	50:50	60:40	70:30
$\bar{I}$ **[%]**	9.6	12.4	14.6	14.5	14.2	12.5

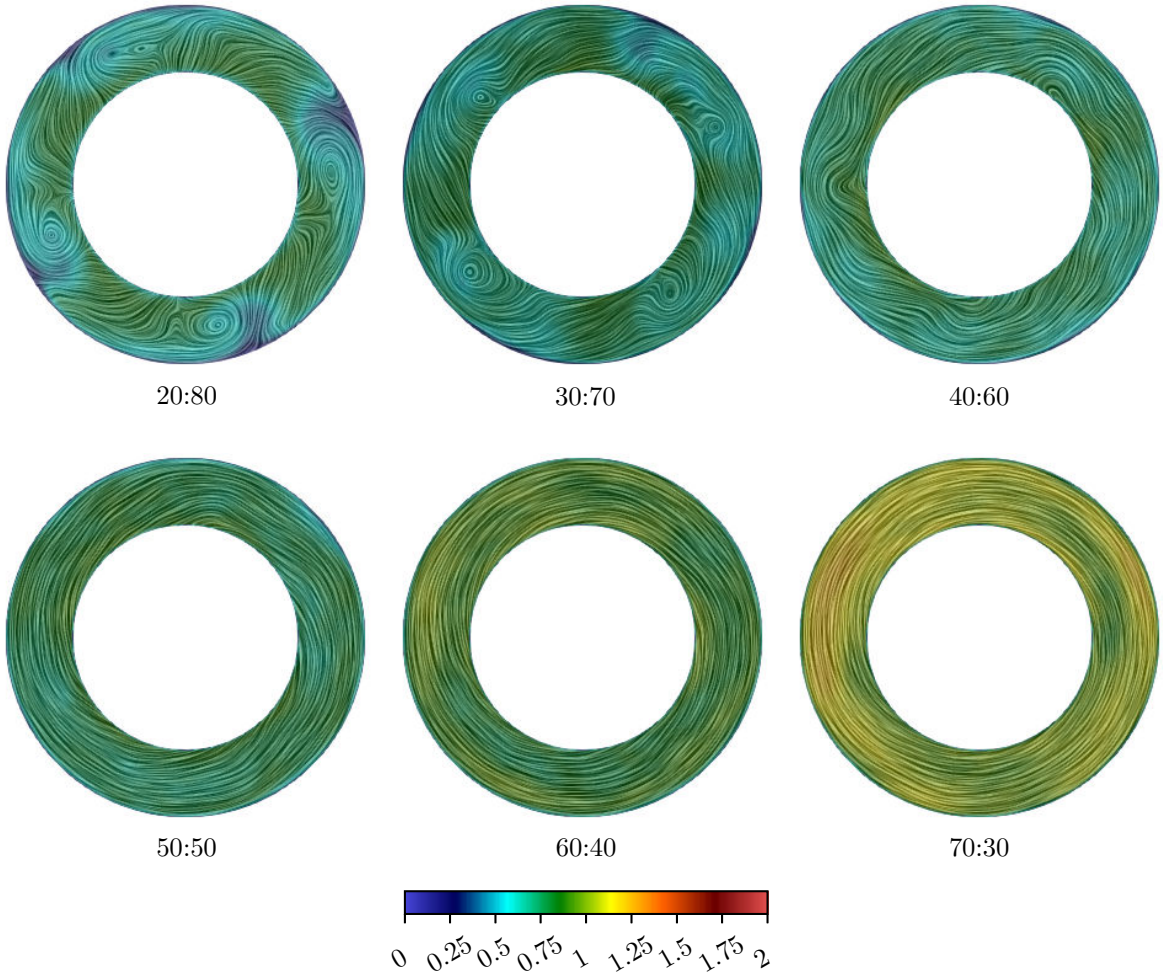

Fig. 4.29: *Velocity profiles during various phases of simulations SBES-T-1 (up to 40:60) and SBES-T-2 (from 50:50). The velocity magnitude contours are combined with an LIC texture. The profiles are temporally averaged over $T = 0.08$ s. The tangential to axial flow rate ratios are listed below each picture.*

4.6.4 Deceleration at the diffuser axis and adverse pressure gradient

The key characteristics of vortex breakdown are a stagnation point and a region of decelerated flow or even backflow further downstream. Isosurfaces of zero axial velocity are commonly used to detect backflow. In Fig. 4.28, it can be seen that the backflow (in terms of average values) at first appears at the end of the diffuser and propagates upstream as the swirl intensity increases. This is in contrast to the vortex rope, which originates at the hub tip and propagates further downstream. For this reason, the difference between the current axial velocity and the area-weighted axial velocity average is used. The dimensionless axial velocity deficit is defined as follows

$$\hat{v}_{\mathrm{z_{def}}} = \frac{\mathrm{awa}\, v_{\mathrm{z}} - v_{\mathrm{z}}}{v_{\mathrm{ref}}}, \qquad \mathrm{awa}\, v_{\mathrm{z}} = \frac{Q_{\mathrm{total}}}{S} \tag{4.50}$$

where S is the area of the cross section that is perpendicular to the diffuser axis and contains the

point of interest (in the present case, it can be expressed from the known diffuser geometry as a function of the z-coordinate). This dimensionless axial velocity deficit was evaluated for the SBES simulations with transient boundary conditions and averaged over $T = 0.08$ s.

Volume renders of this quantity are presented in Fig. 4.30, together with contours of the dimensionless axial velocity average, an LIC texture, and the contour of zero axial velocity average in a longitudinal slice. For similar visualizations of negative axial velocity average, see the bachelor's thesis of Kurková[87]. In the first picture, for the lowest tangential flow rate, we see that a significant deceleration is present only in the wake behind the hub tip. In the second picture, the contours indicate a slight deceleration at the axis, which is, nevertheless, still below the chosen visibility range of volume rendering. The wake recirculation area is now significantly reduced, especially in the center, suggesting that the emerging vortex rope dominates over the wake effects. In the following pictures, as the tangential flow rate (and hence the swirl number) is increased further on, the axial velocity deficit at the axis grows and the area of its positive values gets wider and extends downstream. It shall be noted that positive values of the axial velocity deficit are present in the boundary layer at the walls as well. Therefore, they were removed from the volume renders.

In Fig. 4.32, instantaneous fields of the dimensionless axial velocity deficit together with the modified residual vorticity fields from Fig. 4.25 are visualized to examine the relation between them. The visualizations are complemented with green streamlines illustrating the swirl intensity of the outer flow and grayscale portions of streamlines to give a notion of the 3D velocity field. It can be observed that the axial velocity deceleration and the vortex rope are related since the zone of higher axial velocity deficit values follows the inner side of the vortex rope. The values of the deficit are proportional to the vortex rope strength and related to its orientation – they are lower for parts with predominantly vertical axis and higher for bent parts with a high horizontal component of the vortex axis direction vector. This indicates that the vortex rotation is the strongest contributor to the instantaneous axial velocity deceleration.

Deceleration at the axis is also commonly encountered in actual Francis turbines. Increasing the axial momentum at the axis, e.g. by water jet injection[70], is often considered as a method to mitigate the vortex rope[2, 73, 113].

It is known that the vortex breakdown phenomenon is accelerated by an adverse pressure gradient. Diffusers are by Bernoulli's principle a source of it. In Fig. 4.31, the contours of the dimensionless axial derivative of pressure averaged over $T = 0.08$ s in a longitudinal slice are depicted. The quantity is the axial component of the dimensionless pressure gradient defined as

$$\frac{\partial \hat{p}}{\partial \hat{x}_i} = \frac{\partial p}{\partial x_i} \frac{d_{\mathrm{throat}}}{p_{\mathrm{ref}}} = \frac{\partial p}{\partial x_i} \frac{\pi^2 {d_{\mathrm{throat}}}^5}{8\rho Q^2} \tag{4.51}$$

The contours are complemented with an LIC texture of the gradient. This texture represents lines of the pressure force field, i.e. if the pressure force vectors are decomposed into forces acting tangentially and forces acting perpendicularly to the longitudinal plane, then the first mentioned are tangent to the depicted lines. Instantaneous fields are depicted in Fig. 4.33. They include the positive part of the dimensionless axial derivative of pressure visualized by volume rendering, the modified residual vorticity field visualized also by volume rendering, and portions of pressure force lines.

At the beginning (flow rates ratio 20:80), the most dominant structure observed is the centrifugal pressure forces acting toward the curvature of the wall upstream of the conical section of the diffuser. These forces bend the streamlines along the curved wall, preventing the boundary layer

separation. In the LIC texture of temporally averaged gradient values, it is apparent that the radial component of the pressure gradient changes its sign close to the diffuser axis below the hub tip. The centripetal forces present in that region hence indicate presence of swirling motion.

As the tangential flow rate increases, two distinct zones develop. At the outer walls, centripetal pressure forces prevail, which is typical of swirling flow. Around the axis, adverse axial pressure forces develop. These forces support deceleration and eventually backflow in this zone. They also act against jets injected through the hub tip in order to mitigate the vortex rope (see chapter 5). Since these forces become stronger with increasing swirl, the jet control can be expected to become increasingly costly.

From visualizations of instantaneous fields, it is evident that the decrease of pressure towards the vortex rope axis causes the most dominant pressure gradients. The axial component is positive downstream of the vortex core, which is apparent in the visualizations, and negative upstream (not visualized for the sake of lucidity). Both volume renders are more transparent, so it can be observed how the depicted pressure force lines (which were integrated against the direction of the pressure gradient) direct towards the line of local pressure minima in the vortex rope core. The derivatives of pressure in directions perpendicular to this line are zero; therefore, the pressure force lines eventually bend and continue along this line.

Assuming precessing motion of the vortex rope, it follows that at most points through which the vortex rope passes, the zones of positive and negative values of the axial pressure derivative should average to zero over time. Yet positive values of the axial derivative prevail in the area enclosed by the vortex rope. These values are so high that they are clearly not caused merely by the divergence of the diffuser. The explanation can be found in the already mentioned work by Hall[7]. He assumed a rotationally symmetric swirling flow of an ideal fluid subject to conservative external body forces in a pipe. Pressure distribution across the radius is in such cases governed by the following condition derived from Newton's second law

$$\frac{p(R)-p(0)}{\rho} = \int_0^R \frac{{v_\varphi}^2}{r}\,\mathrm{d}r \tag{4.52}$$

where v_φ is the circumferential velocity and R the radius of a particle (distance from the axis). This expresses that the pressure increases along the radius, providing centripetal pressure forces acting on particles, which is a necessary condition for swirling motion. Hall differentiated this equation with respect to z using the substantial (aslo denoted as material) derivative, i.e. we are tracking individual particles, and applied the Bernoulli equation (conservation of energy) and Kelvin's circulation theorem (conservation of angular momentum), leading to the following result

$$\frac{\mathrm{d}{v_z}^2(R)}{\mathrm{d}z} - \frac{\mathrm{d}{v_z}^2(0)}{\mathrm{d}z} = \frac{2}{\rho}\left(\frac{\mathrm{d}p(0)}{\mathrm{d}z} - \frac{\mathrm{d}p(R)}{\mathrm{d}z}\right) + 2\frac{{v_\varphi}^2(R)}{R}\frac{\mathrm{d}R}{\mathrm{d}z} = -2\int_0^R \frac{1}{r}\frac{\partial {v_\varphi}^2}{\partial z}\,\mathrm{d}r \tag{4.53}$$

Since the right-hand side is positive for decelerated swirling flow, it follows that the axial deceleration of particles, which goes hand in hand with the axial substantial derivative of pressure, is highest at the axis. Another important finding is that the variations of axial deceleration of particles and axial substantial derivative of pressure across the radius are proportional to ${v_\varphi}^2$, i.e. also to Sr^2.

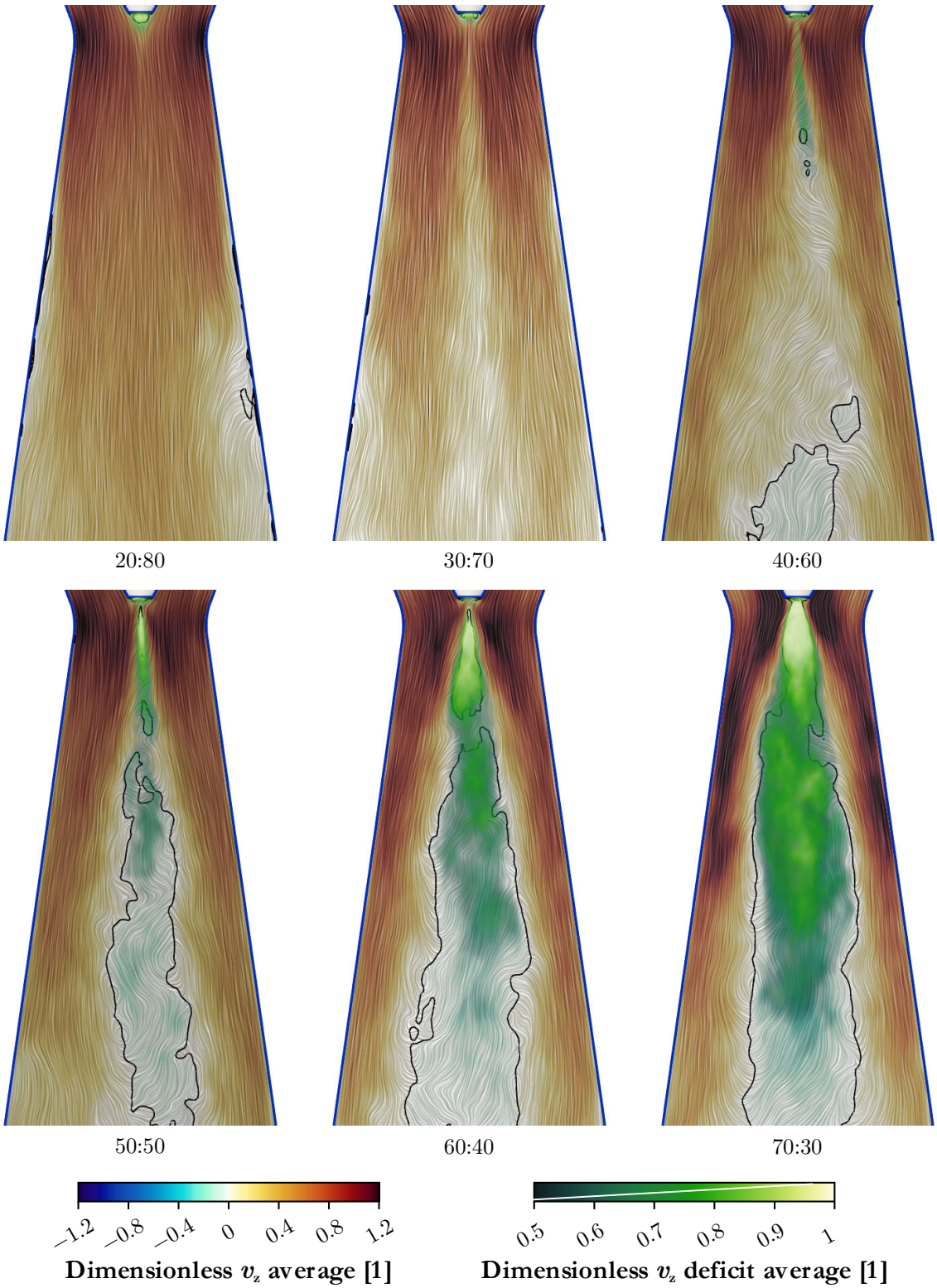

Fig. 4.30: *Volume renders of the dimensionless axial velocity deficit average complemented by contours of the dimensionless axial velocity average, an LIC texture, and the contour of zero axial velocity average (black line) in a longitudinal slice. The quantities are temporally averaged over* $T = 0.08$ *s. The tangential to axial flow rate ratios are listed below each picture.*

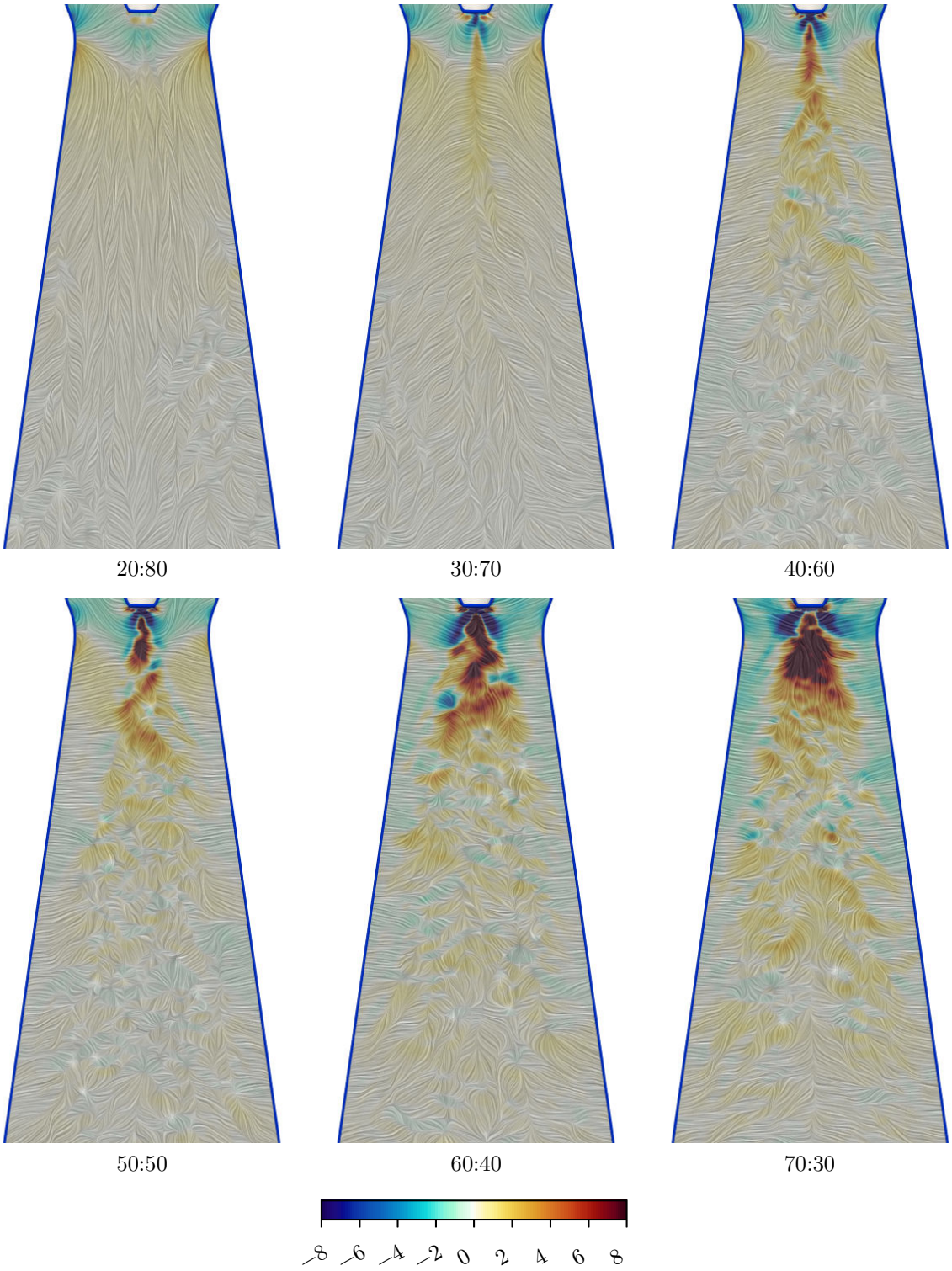

Fig. 4.31: *Contours of the dimensionless axial pressure derivative in a longitudinal slice complemented by an LIC texture of pressure force field lines. The quantities are temporally averaged over* $T = 0.08$ *s. The tangential to axial flow rate ratios are listed below each picture.*

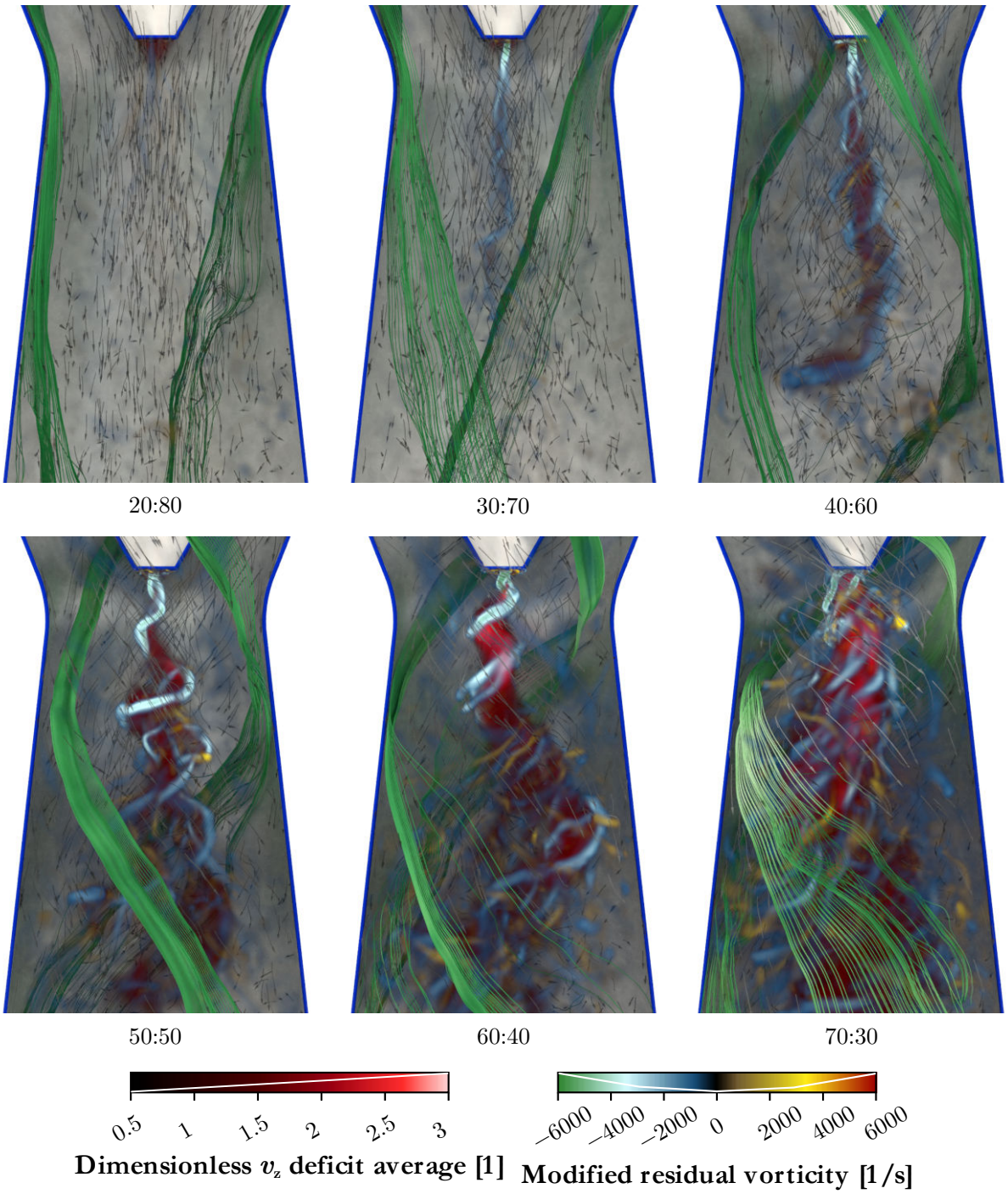

Fig. 4.32: *Volume renders of the dimensionless axial velocity deficit and the modified residual vorticity complemented by green streamlines indicating swirling at the outer walls and grayscale portions of streamlines providing a notion of the velocity field. Instantaneous snapshots, rendered in Blender.*

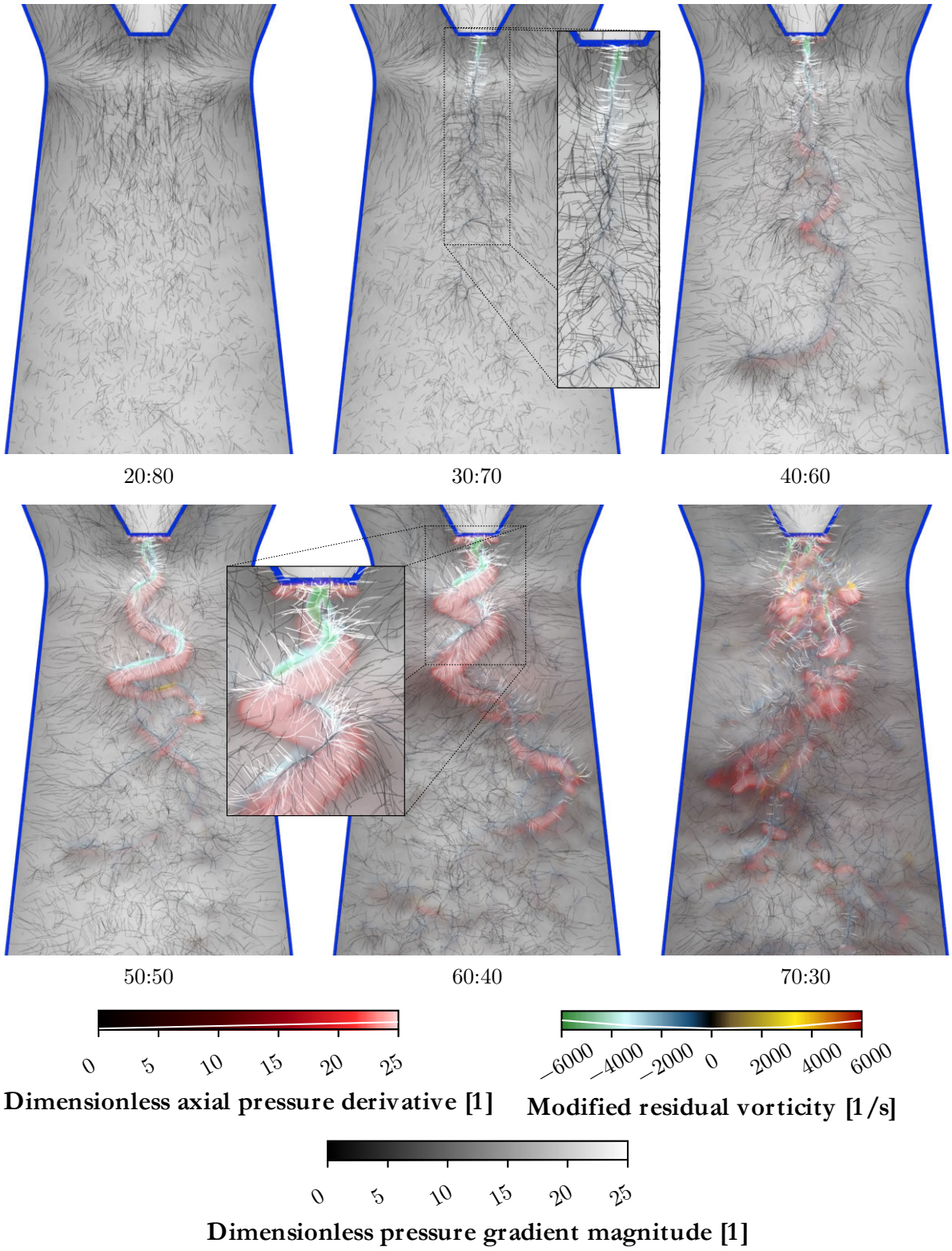

Fig. 4.33: *Volume renders of the dimensionless axial pressure derivative and the modified residual vorticity complemented by grayscale portions of pressure force lines. Instantaneous snapshots, rendered in Blender.*

4.6.5 Vortex rope behavior

So far, it has been shown how the vortex rope shape changes with the flow rates ratio and also how the temporally averaged velocity field evolves. In this section, the vortex rope dynamics will be examined more in detail based on a suitable visualization of series of instantaneous snapshots from the SBES simulations with transient boundary conditions.

In the beginning, when the axial inflow dominates and the swirl number is close to zero, the wake behind the hub tip is the most notable structure in the flow field. It is followed by a bundle of weak axial vortices, some of which rotate clockwise, while the rest rotate anticlockwise. Fig. 4.34 shows a situation from the described phase, where a clockwise-rotating vortex breaks an anticlockwise-rotating one. In the first three snapshots, we can identify a relatively strong anticlockwise rotating vortex that might possibly get stronger and develop into the well-known spiral vortex rope. However, from the fourth snapshot on, a clockwise-rotating vortex (yellow to red colors) emerges and breaks it. Shortly after that, a new anticlockwise-rotating vortex develops and becomes the strongest.

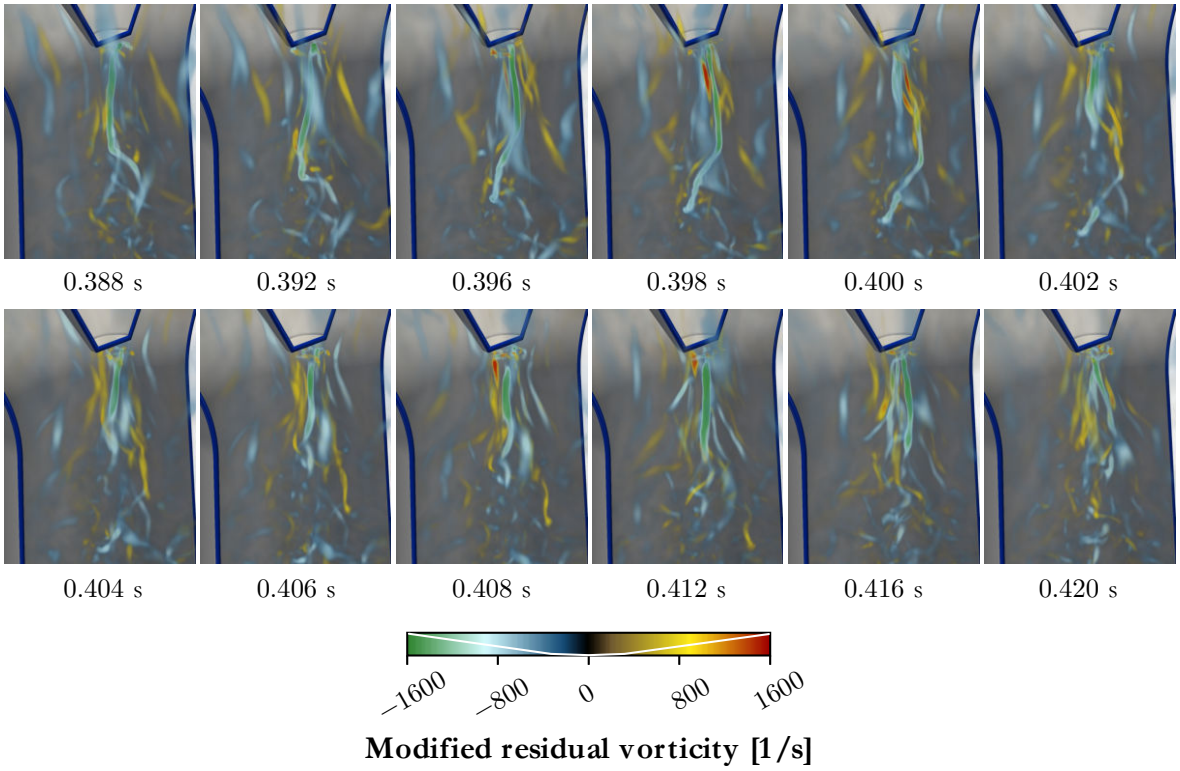

Fig. 4.34: *Interaction of vortical structures visualized by modified residual vorticity. Times are measured from the beginning of simulation SBES-T-2.*

With a further increase in swirl, a significant anticlockwise-rotating vortex develops. It corresponds to the sense of rotation of the incoming swirl, which is also anticlockwise. This vortex is at first intermittent – it often disappears and then reappears. Later on, it becomes sustained. Six snapshots from this phase are presented in Fig. 4.35. The vortex rope is straight in the upper part. The onset of a spiral shape is observed at the bottom. The most significant spiral is present in the last snapshot. Its pitch is substantially higher than that in the cases captured in the second and fourth

snapshot. We can also note that the vortex rope tends to break into two intertwined vortices. It is most notably apparent in the first snapshot.

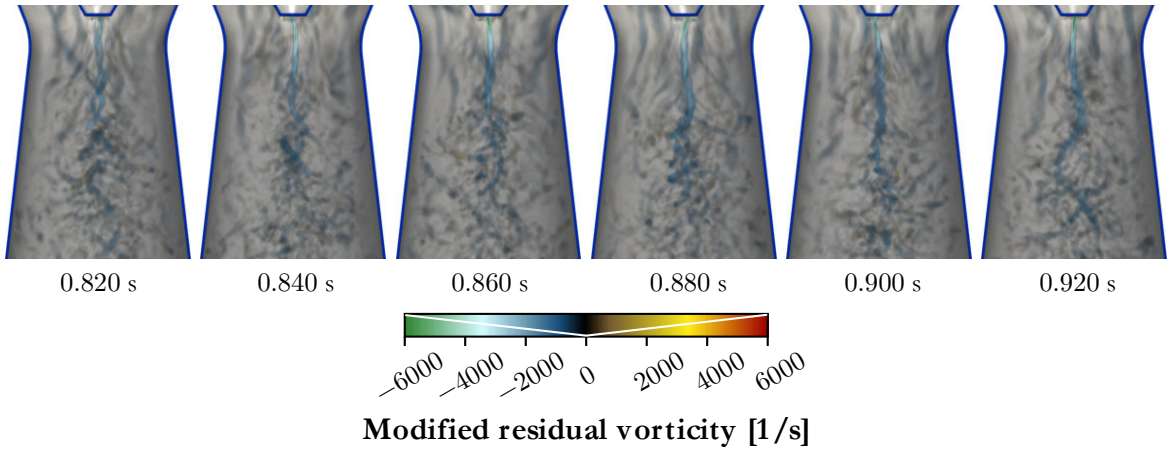

Fig. 4.35: *Snapshots from the phase where the vortex rope is already sustained. Times are measured from the beginning of simulation SBES-T-2.*

As the flow rates ratio approaches 50:50, the radial extent of the vortex rope increases. The streamwise expansion of the vortex rope surpasses that of the diffuser. This is meant in terms of mean values since the vortex rope behavior is highly unstable. There are phases where the vorticity is highly concentrated and a significant rope is observed. Sooner or later, it breaks into a bunch of disorganized smaller vortices. We can again observe the tendency of a single vortex to break into two intertwined smaller vortices. The same behavior was also observed experimentally. Although there are differences between the present CFD simulation and experiments (transient vs. fixed boundary conditions, 5 l/s vs. 10 l/s total flow rate), a comparable behavior was observed, which is presented in Fig. 4.36. The most important fact is that the tangential to axial flow rate ratio (and thus the swirl number) is the same in both cases. In the case of the CFD simulation, the change of this ratio caused by the transient boundary conditions in this short time interval is negligible.

In the first CFD snapshot, a distinct spiral vortex rope is apparent. Many small structures are present in the bottom, i.e. in the zone where the vortex rope dissipates and disintegrates. Vortices coming from the diffuser inlet as a result of the mixing process of the two flows are also notable in this representation. During the next few time steps, the top part of the vortex rope moves inconsistently with respect to the following part. At $t = 3.060$ s, the vortex rope center line is bent upward, leading to the axial vorticity sign change (switch from blue to yellow color in the picture). Then the structure tears apart. After a short time, at $t = 3.076$ s, the two separated parts reconnect. The upper part of the vortex rope at $t = 3.072$ s breaks into two intertwined vortices. After some time, the two vortices merged and at $t = 3.088$ s, the situation is similar to the initial snapshot, with a single smooth rope. Then the upper part twists again and the process again leads to the structure being torn apart, as can be clearly seen at $t = 3.100$ s. Now it takes a longer time to fully reconnect, up to $t = 3.116$ s when a single smooth vortex rope is formed. In the following snapshots, the upper part of the vortex rope gradually disintegrates into a bunch of disorganized structures. Its tail remains in this phase highly coherent and proceeds downstream out of the scope of the camera.

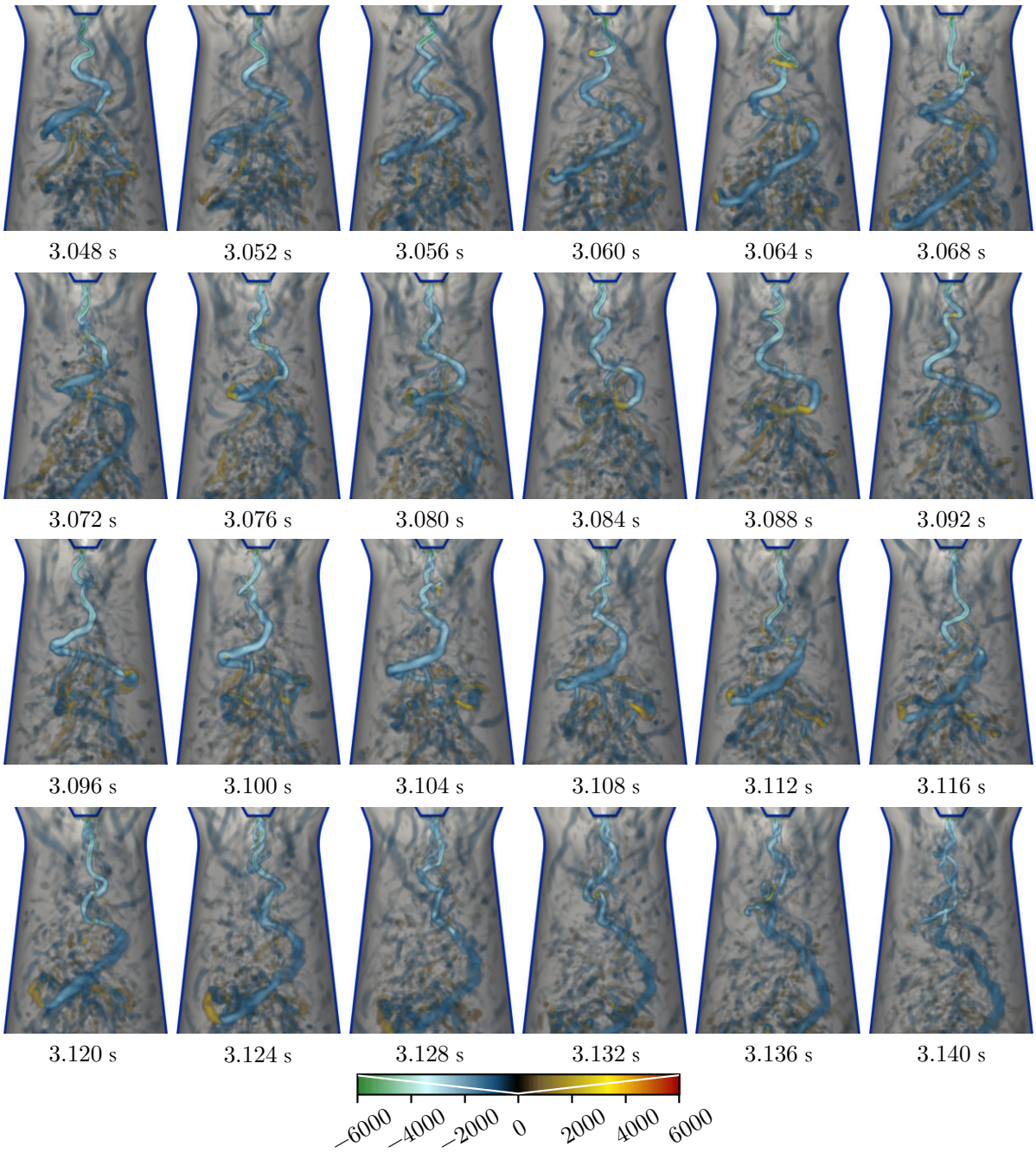

Fig. 4.36: *Top: snapshots from CFD illustrating the behavior of the vortex rope when the flow rates ratio approaches 50:50. Times are measured from the beginning of simulation SBES-T-2. Bottom: snapshots from the experiment capturing similar behavior.*

The series of six snapshots recorded by the high speed camera captures the same behavior. The twisting happens in the second snapshot. It is only a coincidence that the vortex rope looks reconnected in the third snapshot. Instead, its upper part breaks into two intertwined vortices, which is apparent in the last snapshot if looking closely.

As cavitation or degassing occurs only in areas with sufficiently low pressures, we are not able to see weaker vortices in the snapshots from the experiment. Moreover, the vortex rope was only visible in its coherent states. A further decrease in pressure to augment cavitation is not desirable for this study since it can affect the shape and behavior of the vortex rope.

It should be noted that the twisting of the vortex rope may also result in the detachment of a vortex ring. This behavior was indeed observed experimentally in the present swirl generator, and the results were published by Štefan et al.[57]

The behavior of the vortex rope for higher swirl numbers has been studied using simulation SBES-T-1. At a certain point, a qualitative change in the flow pattern was observed. This is documented in Fig. 4.37. In the first snapshot, a single vortex rope is present. Its diameter is higher than that of the vortex rope observed in the previous sequence, where the swirl number is lower. This increase in size is not accompanied by an increase in peak residual vorticity in its center – its values actually stay within the same range. On the other hand, the static pressure decreases as documented in Figs 4.25 and 4.27. We can also observe a higher density of smaller vortical structures in the center. They are affected by the motion of the vortex rope, so many interactions can be observed. Notice e.g. the bending of some vortices over the vortex rope caused by the rotation about its own center line.

The first twelve snapshots capture the motion of the vortex rope. The last six snapshots document the qualitative change in the flow pattern. The vortex rope is no longer stable and breaks into a vast amount of small vortices concentrated around a spiral center line. This complex structure as a whole rotates about the center line and around the diffuser axis. In the last snapshot, we can clearly see twin vortex ropes right under the hub tip.

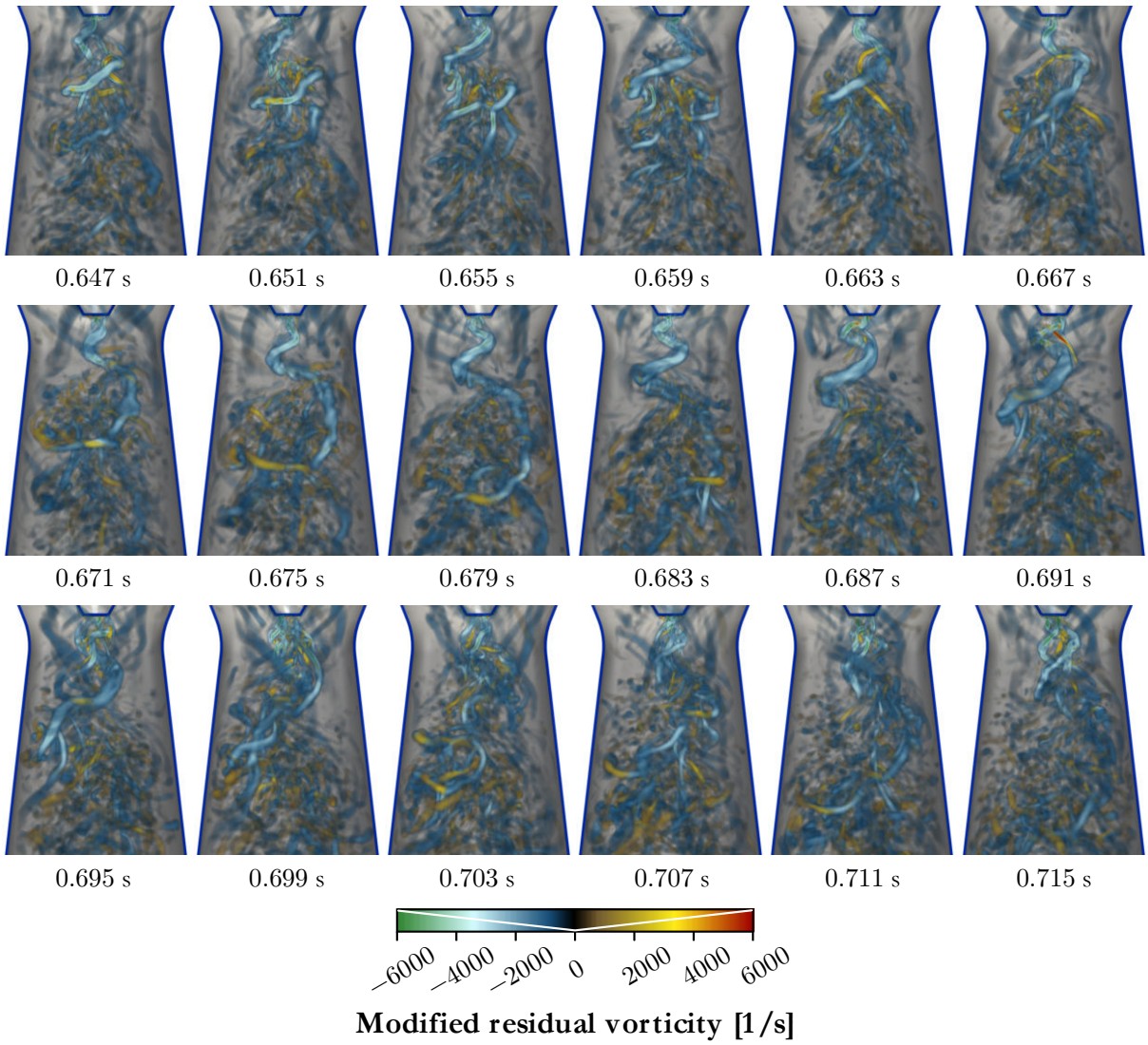

Fig. 4.37: *Snapshots from CFD illustrating the transient from a single vortex rope to twin vortex ropes. The times are measured from the beginning of simulation SBES-T-1.*

Fig. 4.38 documents the behavior of the flow after the transient. The tangential to axial flow rate ratio approaches 70:30. A center line based on the static pressure field is included in the visualizations of the CFD results (see the journal paper[85] for a description of the algorithm) to provide a notion of the vortex rope shape, which is obscured by the large number of vortices in the entire diffuser. The motion of the center line exhibits a high degree of periodicity; i.e. there is a significant peak in the frequency spectra of relevant variables. Experimental observations exhibit the same characteristics. Notice also the air bubbles that are trapped in the stagnation/backflow zone at the axis (in the bottom of the pictures). A high degree of cavitation is observed under the hub tip. In this area, twin vortex ropes are observed. These structures are highly irregular and unstable. The complexity of the flow pattern on one hand and the high degree of periodicity on the other hand together with significant asynchronous pressure pulsations caused by the rotation of the structure around the diffuser axis are the main characteristics of this regime.

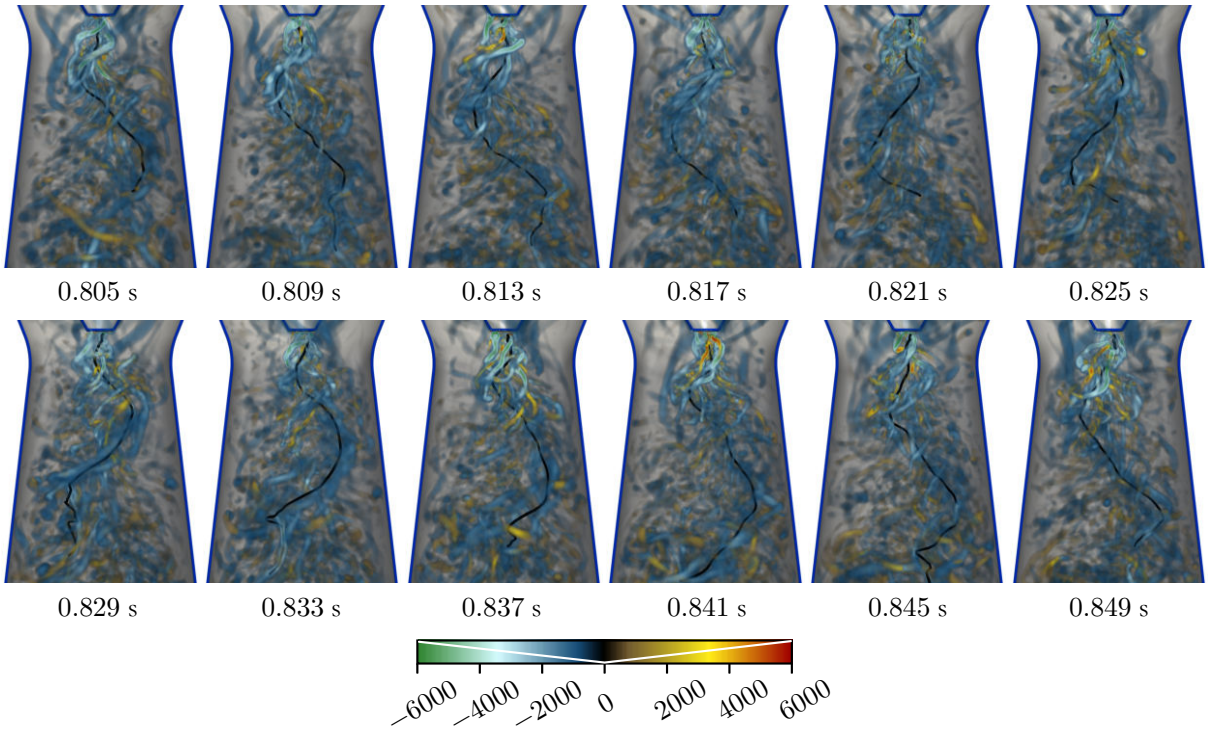

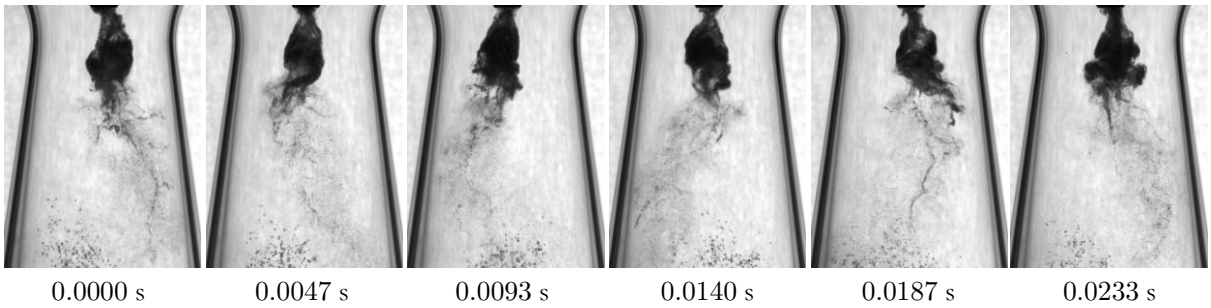

Fig. 4.38: *Top: snapshots from CFD that illustrate the behavior of the vortex rope when the tangential to axial flow rate ratio approaches 70:30. The black tube is a center line based on the static pressure field. The times are measured from the beginning of simulation SBES-T-1. Bottom: snapshots from the experiment with the same flow rates ratio.*

5 A brief study of vortex rope mitigation methods

Finding suitable methods to mitigate the vortex rope belongs to the field of flow control. Flow control is currently a significant research topic with appealing benefits (reducing cost, emissions, noise, etc.) if successfully employed in industrial applications. Finding optimal strategies is, however, hindered by the nonlinearity of the governing equations and high dimensionality if solved numerically. Moreover, the space of possible control laws is literally infinite. Indeed, the control law is realized by an actuator, and we need to select its type, number, and placement positions – with infinitely many combinations available. The author believes that the best method to tackle this challenge consists of two steps. The first step is to understand the problem. On the basis of this knowledge, the space of possible control laws should be suitably constrained. The second step is to apply machine-learning techniques to find the optimal solution in this constrained space.

An extensive review of current progress in flow control was published by Brunton and Noack[112]. They present a flow chart that illustrates the hierarchy of active control approaches. This chart (Fig. 5.1) is, according to the authors, conservative in giving preference to the most established techniques. If the task is optimization, machine-learning control may be an earlier branch. Methods for vortex rope mitigation that have been employed so far, discussed in section 1.4, belong to passive flow control (runner cone extension, fins, and other installations) and open-loop active flow control (air or water jet injection). Machine-learning control itself has been developed only recently, and employing it to find optimized ways to mitigate the vortex rope is a matter for future research.

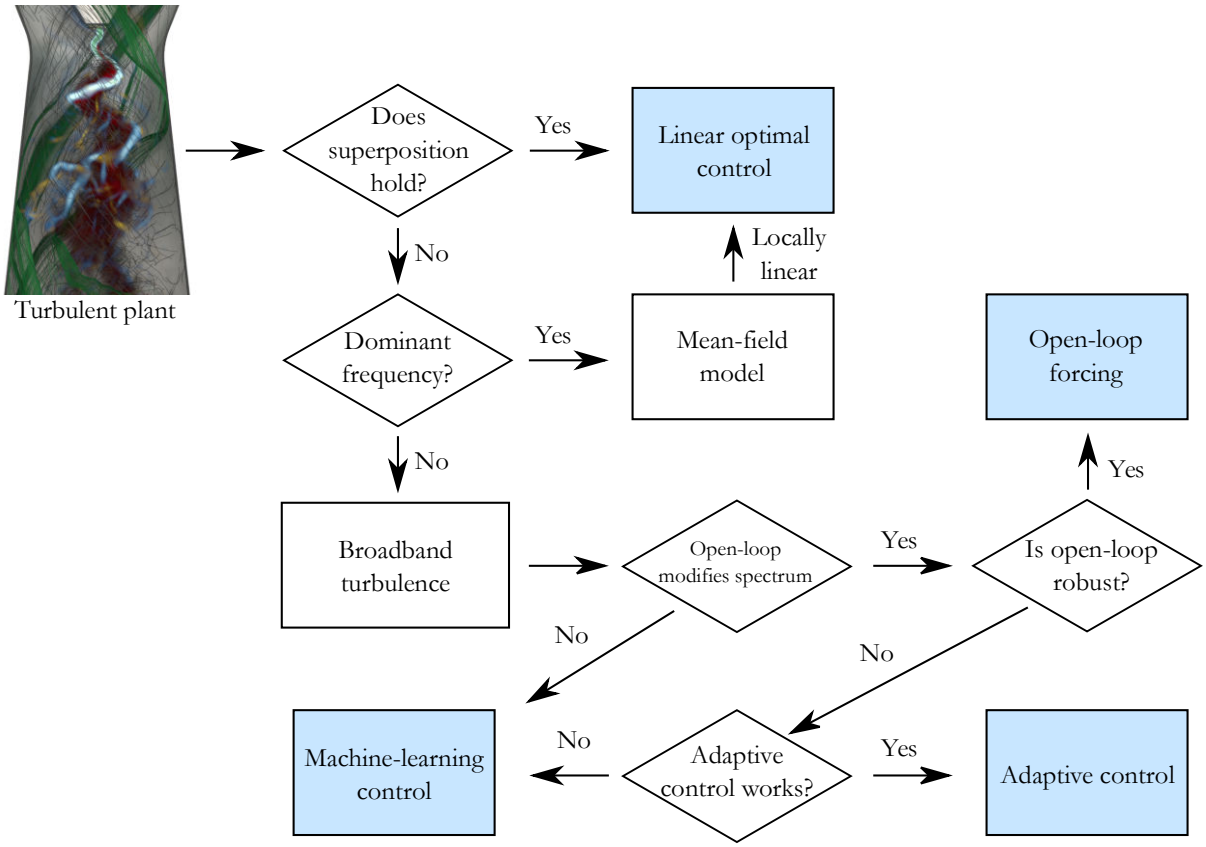

Fig. 5.1: *Flow chart that illustrates the hierarchy of active control approaches. Created according to the work of Brunton and Noack*[112].

5.1 CFD study of water jet injection through the hub tip

In this part, the water jet injection method will be tested numerically for the present swirl generator. To make things more interesting, the original straight diffuser was replaced with an elbow one. It corresponds to the draft tube used in Střekov power plant located on the Elbe river in the Czech Republic. The power plant features three Kaplan turbines and its total installed capacity is 19.5 MW[114]. The flow in this draft tube was studied numerically by Štefan within his master's thesis[115]. The reason for using an elbow diffuser is that, as was mentioned in section 1.3, synchronous pressure pulsations at the vortex rope precession frequency are not present in straight draft tubes, they were observed only in elbow draft tubes. The resultant flow is therefore expected to feature these synchronous pulsations. Moreover, elbow draft tubes are for practical reasons standardly used in water turbines, so the present case better represents the situation we can encounter in practice.

The final geometry was created as follows. The original straight diffuser was cut in the place where the diameter is equal to the distance from the throat (the narrowest cross section). Then, the elbow and downstream part of the Střekov draft tube was scaled as needed and connected to the straight section. It is noted that the original draft tube contains two fins: a vertical one to support the ceiling and a horizontal one to guide the flow in the elbow. Both these fins were removed since the first is meaningless in the present setting and the second may itself affect the vortex rope, which would render the results incomparable with the original case with a straight diffuser. The resultant geometry is depicted in Fig. 5.2.

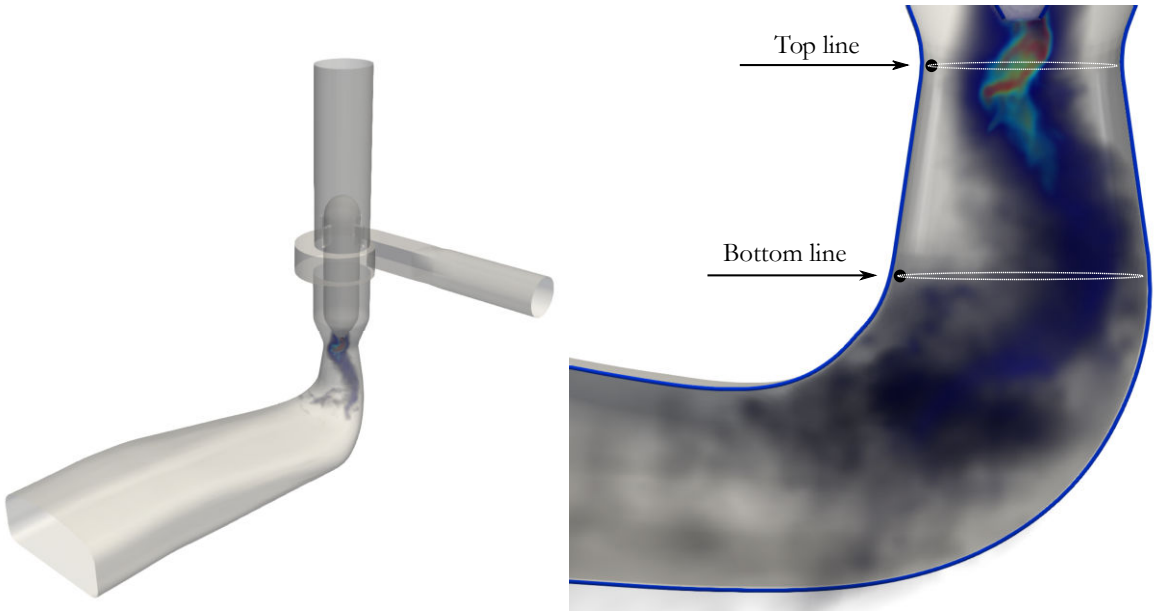

Fig. 5.2: *Left: present swirl generator with an elbow diffuser corresponding to the draft tube used in Střekov power plant. Right: a detail on the upstream part of the diffuser with designated lines where synchronous pressure pulsations were evaluated and points where the asynchronous component was computed.*

Two simulations were performed. The first is without control for flow rates ratio 70:30 as it was shown to feature a large vortex rope generating strong pressure pulsations with a dominant frequency in the Fourier spectrum. The second is for the same flow rates ratio with water jet injection through the whole hub tip surface. The water jet flow rate increases linearly in time from 0% to

20% of the flow rate coming into the diffuser (5 l/s) during 1.6 s. With the vortex rope precession frequency of 28 Hz, this time interval covers almost 45 precession periods. In both simulations, the scale-resolving SBES model was employed with the same settings as in the previously described simulations summarized in Tab. 4.2. The simulation time step was $4 \cdot 10^{-5}$ s.

To check the mentioned presence of synchronous pressure pulsations, data from two lines depicted in Fig. 5.2 were collected for both the elbow and the straight diffuser. The synchronous component is then defined as the mean value along the line and the asynchronous component as the actual value minus the synchronous component. The resultant evolutions in time and their frequency spectra are depicted in Fig. 5.3. They show that in the straight diffuser, the synchronous pulsations are weaker, and there is no significant peak in the frequency spectrum. The elbow diffuser indeed induces synchronous pulsations related to the vortex rope precessing motion as there is a significant peak for the precession frequency in the Fourier spectrum. It is also evident that synchronous pulsations are stronger at the top line. To get better understanding of synchronous pulsations, the author suggests computing circumferential average or cross-sectional average (depending on the target dimensionality) for the whole domain instead of only a single line and applying a suitable decomposition technique to find synchronous spatial mode shapes. However, this task is left for future work.

In Fig. 5.4, instantaneous snapshots from the simulation of water jet injection are presented. The corresponding ratio of the water jet flow rate to the total flow rate at the diffuser inlet is noted below each set of snapshots. From the axial velocity fields, it is evident that the jet axial velocity is well aligned with the outer flow for $Q_{\mathrm{jet}}/Q_{\mathrm{total}}$ laying somewhere between 5 and 10%. Unfortunately, the reach of the jet is rather short. The backflow region is still present farther downstream, and a spiral vortex is still observed. Increasing the jet flow rate further extends its reach, but it does not suppress the backflow; instead, the jet is deflected to the side and rotates around the backflow zone in the center. In the visualizations of the modified residual vorticity field, we can observe rather straight vortices forming in the mixing layer between the jet and the outer swirling flow. As it can be seen in Fig. 5.5, the frequency of pressure pulsations is slightly lower than at the beginning. A very undesirable effect is that the synchronous pulsations are significantly stronger. Overall, the water jet injection as it was proposed in this case actually worsened the situation.

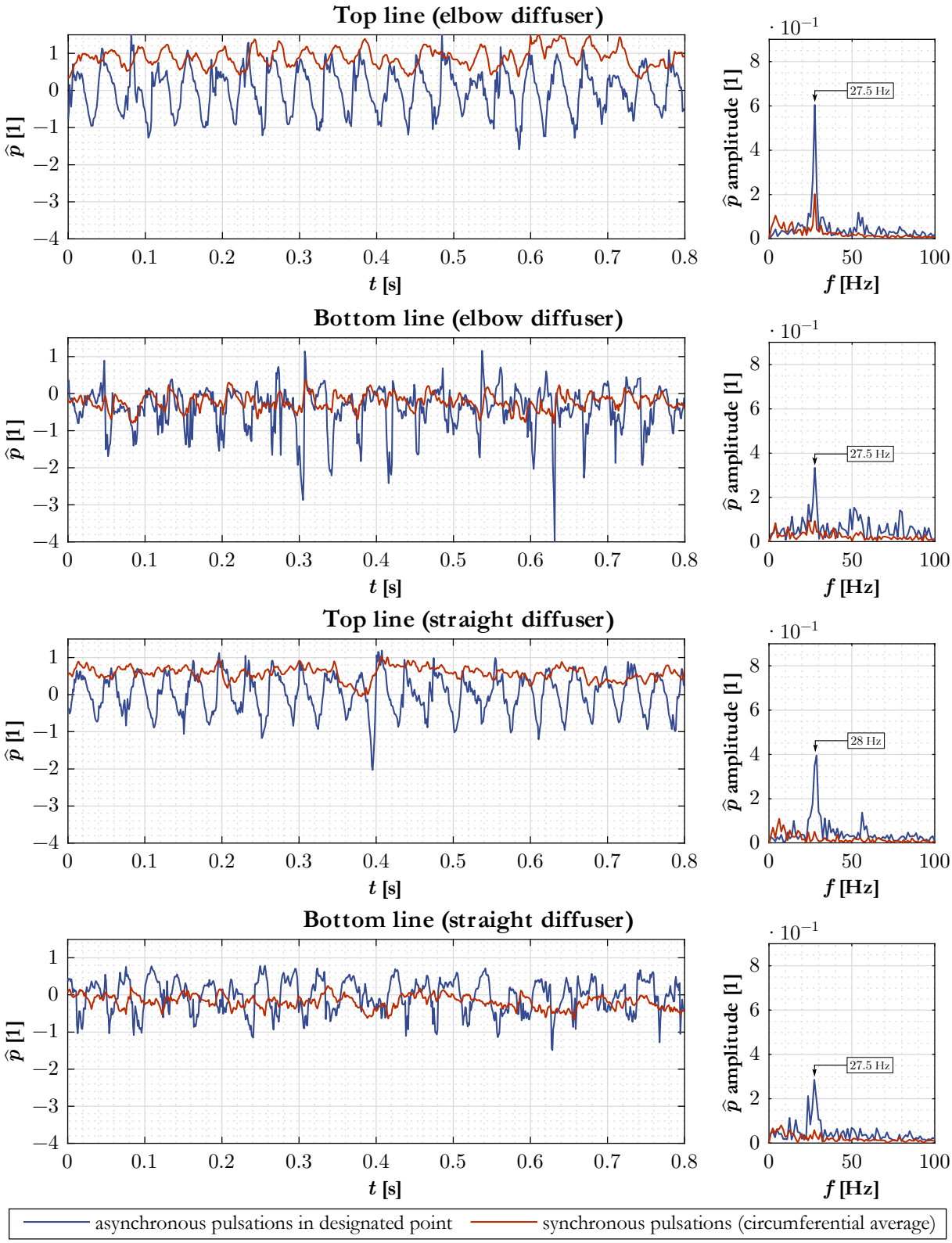

Fig. 5.3: *Dimensionless pressure evaluated in the time and frequency domain: synchronous pulsations computed by averaging along the lines designated in Fig. 5.2 and asynchronous pulsations for designated points for both the elbow and straight diffuser.*

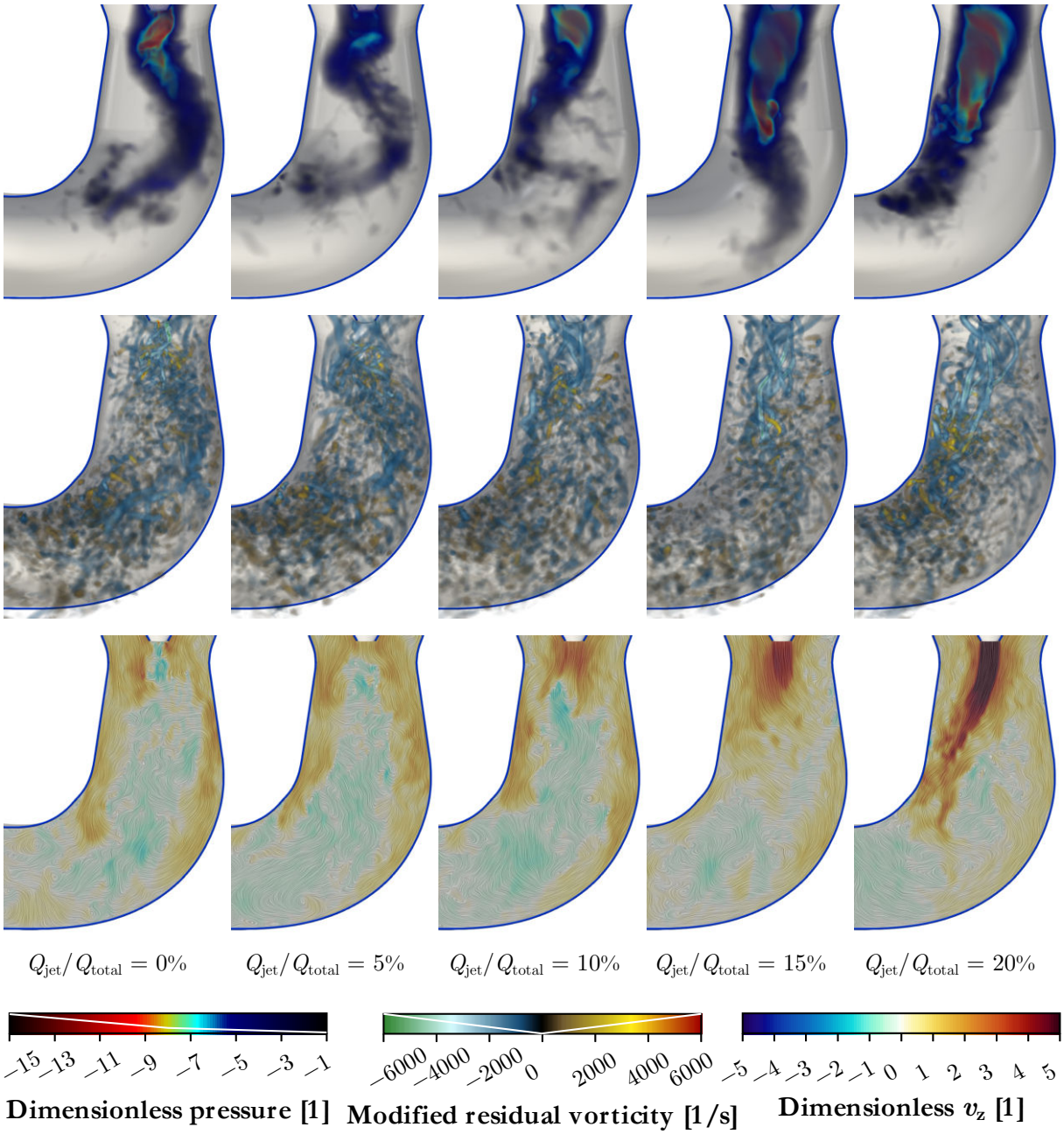

Fig. 5.4: *Instantaneous snapshots from the CFD simulation as the water jet flow rate increases.*

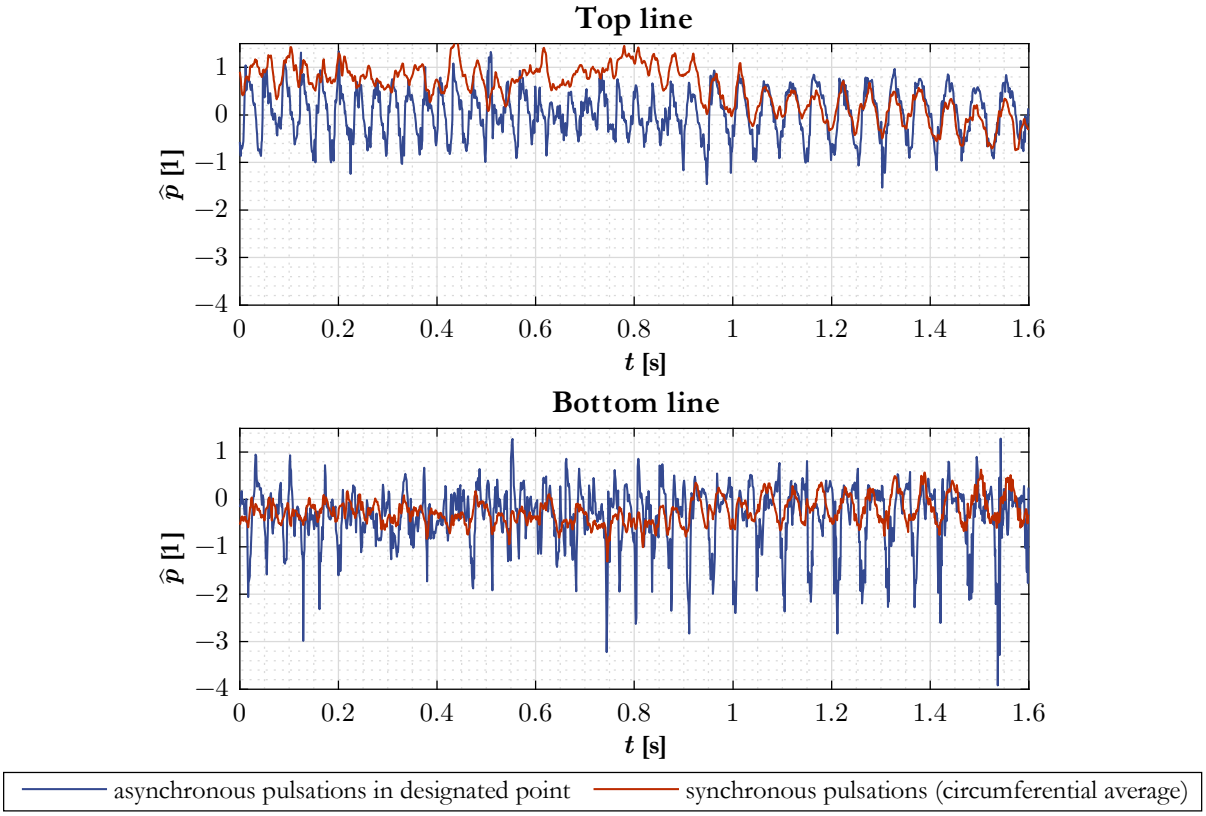

Fig. 5.5: *Dimensionless pressure evolution in time: synchronous pulsations computed by averaging along the lines designated in Fig. 5.2 and asynchronous pulsations for the designated points. Data from the CFD simulation of water jet injection with the jet flow rate increasing linearly over time from* 0% *to* 20% *of the total flow rate.*

5.2 CFD study of different active control methods

The undesirable performance of the water jet injection from the previous section led to more experimentation. It is possible that increasing the flow rate and hence the jet momentum may ultimately suppress the backflow zone, but it comes with prohibitively high energy cost for practical applications. For this reason, different configurations will be sought.

The first idea was to replace the injection from the top with suction from the bottom. No thorough hydraulic design was performed as this study is intended only as a proof of concept. A bent pipe was inserted into the diffuser. At the outlet, velocity inlet condition with outward-oriented velocity was prescribed. The pipe diameter is 15 mm, which is higher than the jet diameter of 10 mm. For comparability, the same flow rate dependence on time was prescribed, and the SBES model was used for the simulation.

The results in Figs 5.6 and 5.7 show that the situation is better in terms of suppressing the synchronous pulsations. The reason is that if the flow rate is sufficiently high, the vortex rope tail is bound to the suction tube in the center. An undesirable fact is that the pressure in the suction tube is in this case even lower than that in the vortex rope core. Another undesirable phenomenon that can be observed in LIC textures of the velocity field in Fig. 5.6 is that not only water coming from above is sucked in, but also water from the backflow zone in the bottom. However, this effect could be diminished by proper countermeasures.

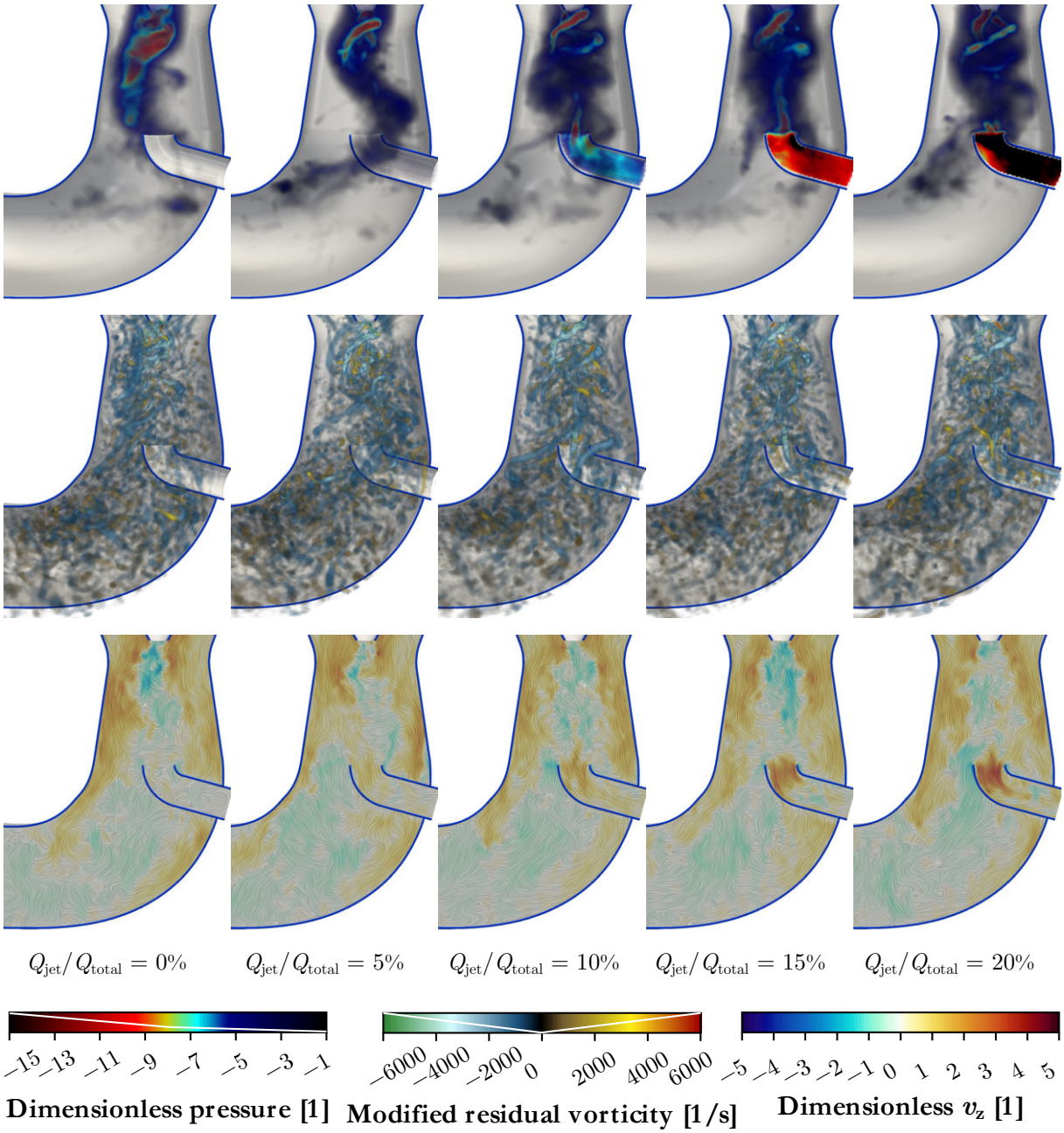

Fig. 5.6: *Instantaneous snapshots from the CFD simulation as the suction flow rate increases.*

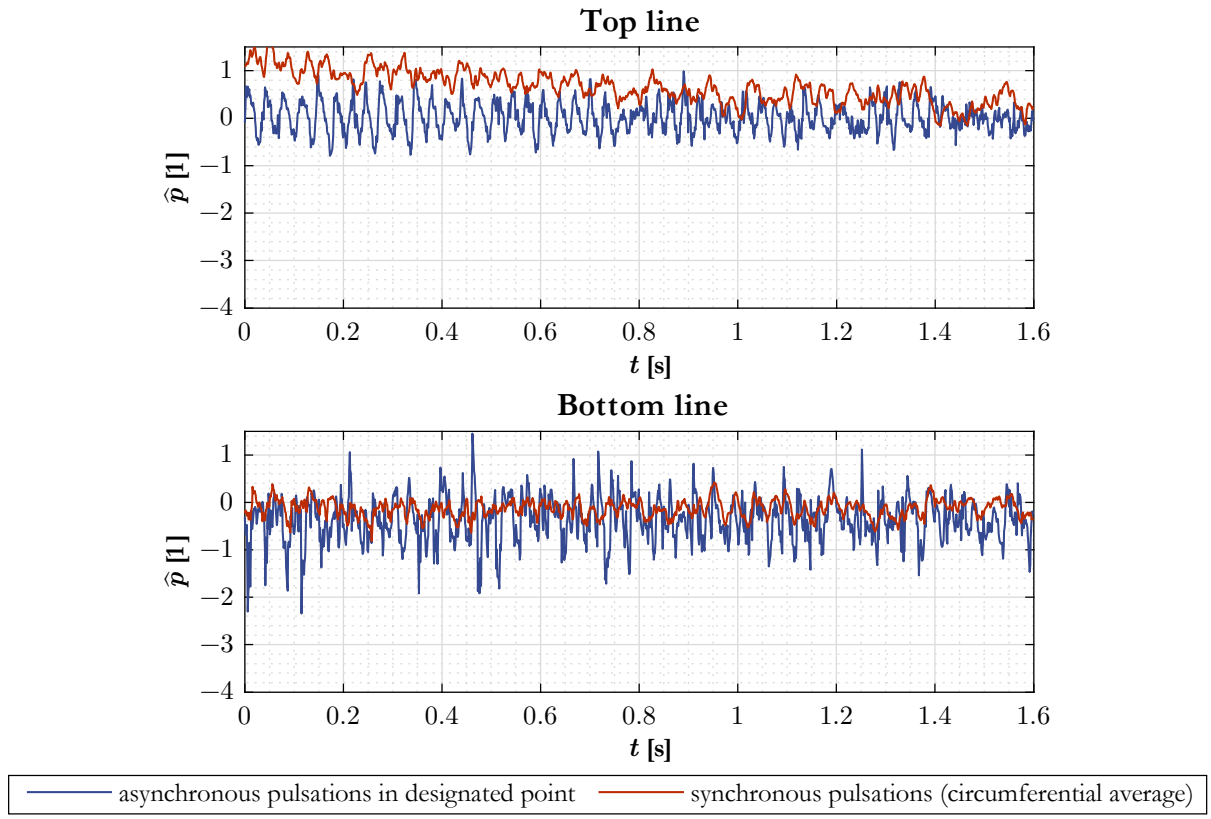

Fig. 5.7: *Dimensionless pressure evolution in time: synchronous pulsations computed by averaging along lines designated in Fig. 5.2 and asynchronous pulsations for designated points. Data from the CFD simulation of suction with the flow rate increasing linearly over time from* 0% *to* 20% *of the total flow rate.*

The last option with this configuration is to apply water jet injection and suction simultaneously. The hope was that the suction effect might stabilize the injected jet in the center and prevent its rotating motion. Pictures in Fig. 5.8 reveal that this is not true, the injected water jet motion is almost unaffected by the suction. Comparing the axial velocity fields with those from the case with water jet injection alone (depicted in Fig. 5.4) reveal that the suction effect at the final stage suppressed backflow upstream of the suction pipe, yet it is not strong enough to suppress the jet rotation. Strong synchronous pulsations develop just as in the case with water jet injection only; see Fig. 5.9.

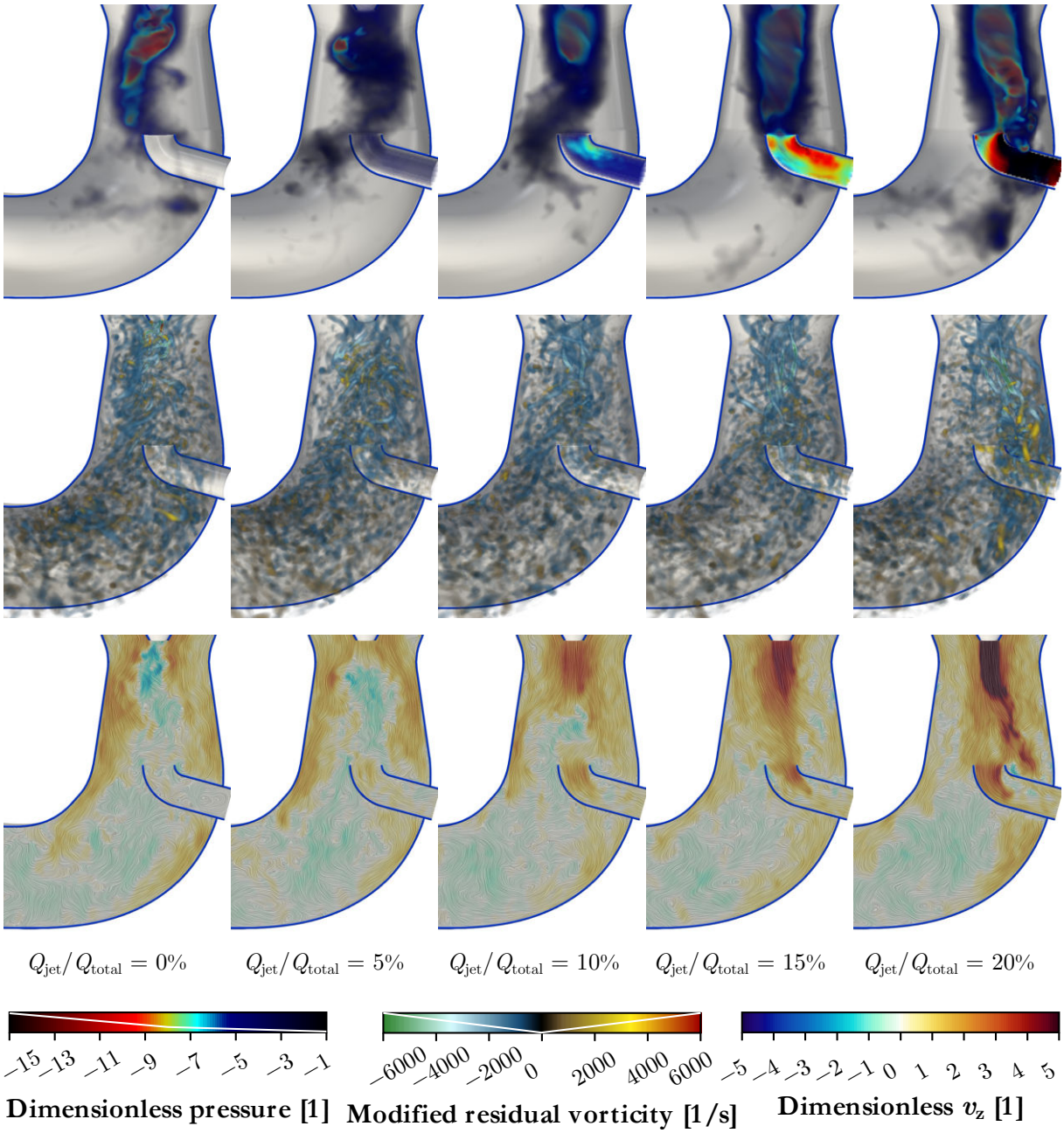

Fig. 5.8: *Instantaneous snapshots from the CFD simulation as the water jet and suction flow rate increases.*

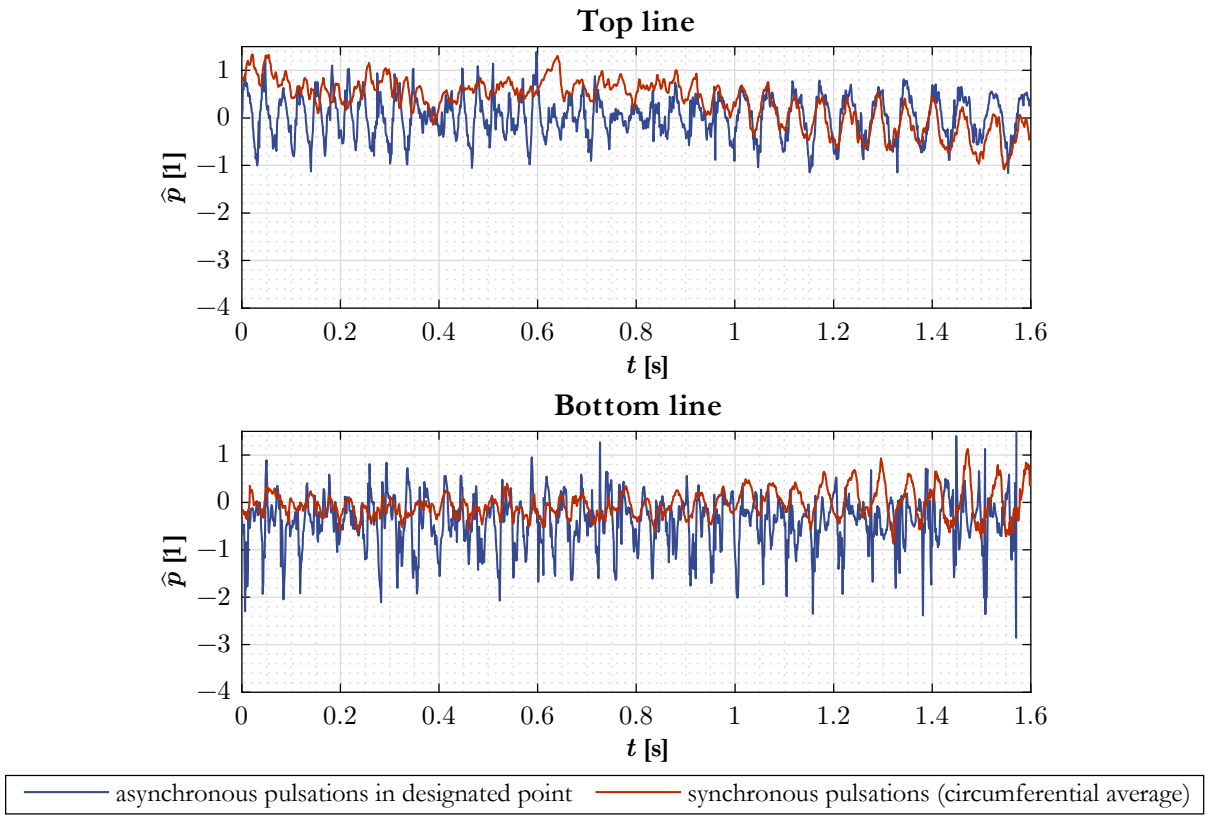

Fig. 5.9: *Dimensionless pressure evolution in time: synchronous pulsations computed by averaging along lines designated in Fig. 5.2 and asynchronous pulsations for designated points. Data from the CFD simulation of water jet injection and suction at the same time with the flow rate increasing linearly over time from* 0% *to* 20% *of the total flow rate.*

The unsatisfactory results obtained so far have led to the need to explore more configurations. For this purpose, a ring on the hub is introduced in Fig. 5.10. This ring will be used as an additional surface for water jet injection. Moreover, it was decided to use the RSM model of turbulence and consider the diffuser only. The inlet was set just behind the spiral case, and profiles of the velocity inlet boundary condition variables were computed in a separate simulation of the whole geometry. Mean values over time were used, i.e. the unsteadiness of the flow therein was neglected. These simplifications led to a substantial reduction in computational burden.

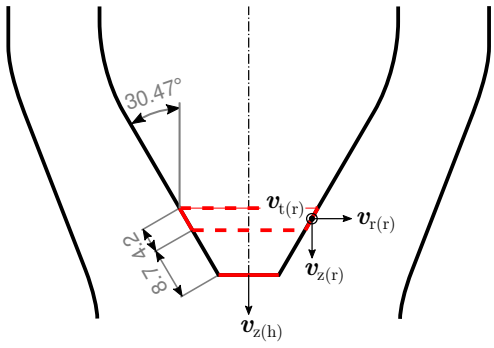

Fig. 5.10: *Geometry of a ring for additional water jet injection. The velocity components that were considered in the simulations are also designated.*

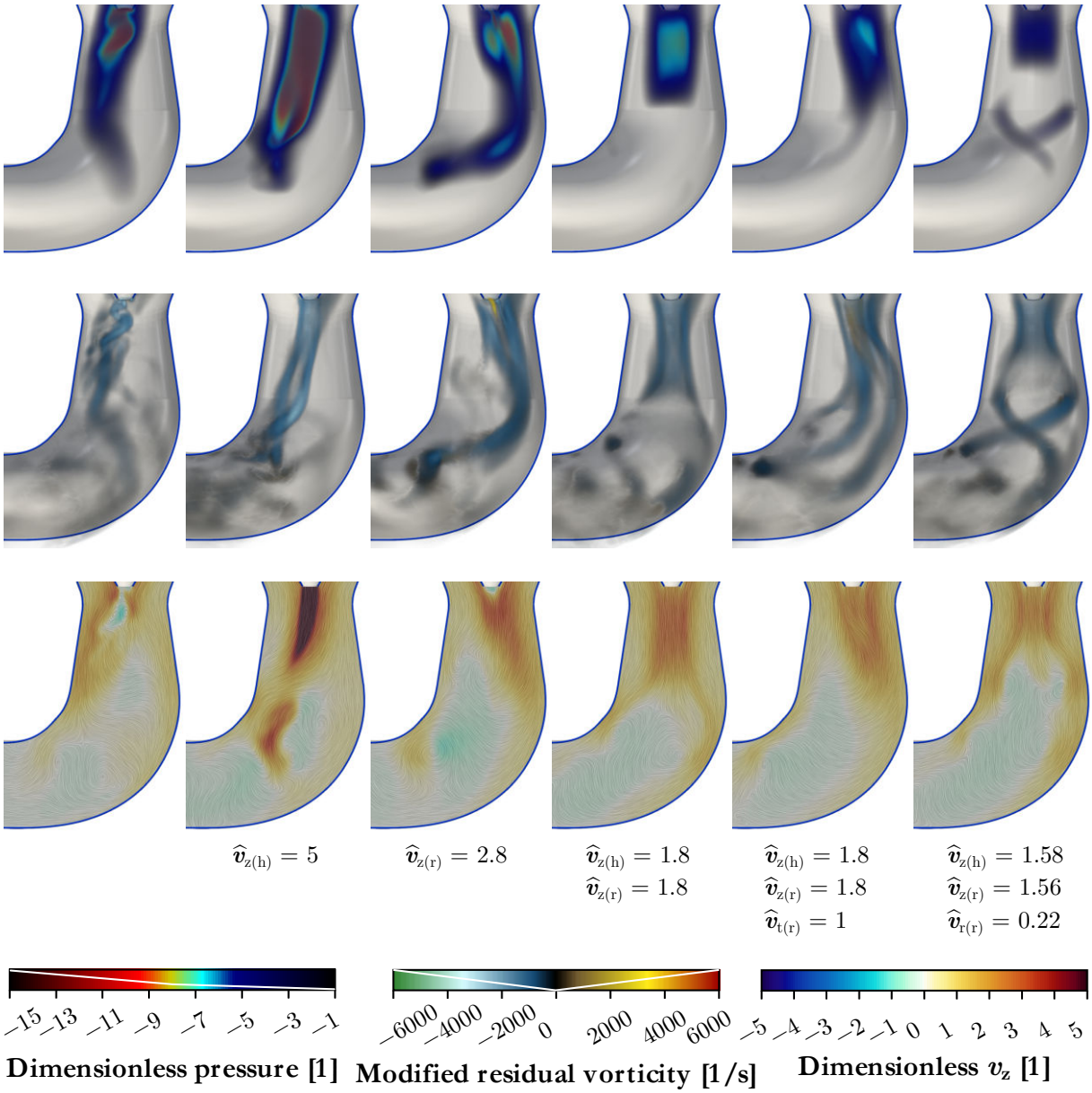

Fig. 5.11: *Instantaneous snapshots from CFD simulations with the RSM model of turbulence. The far left case is without control, the others are with active flow control by water jet injection with various parameters specified below the pictures.*

As the first step, it was necessary to ensure that the assumed simplifications do not affect the key characteristics of the flow in the diffuser. Therefore, the first two simulations considered no control and the water jet injection through the hub tip only, respectively. The water jet flow rate was fixed at 20% of the total flow rate. As soon as the initial transient faded out, the current state was saved for further postprocessing. The results in Fig. 5.11 (the first two pictures in the series) can be compared with the first and the last snapshots from the SBES simulation of the water jet injection in Fig. 5.4. It is evident that the important qualitative characteristics are retained; therefore, this setting can be used for subsequent studies of new configurations.

Four new configurations were tested. In all the cases, the water jet flow rate was fixed at 20% of the total flow rate. For this reason, the jet velocity differs among the cases since the area of the

injection surface also differs. The first case considered water jet injection through the ring only. The issue of the rotating water jet in this case remained. The second case considered water jet injection through the ring and the hub tip simultaneously. This turned out to be the best case. The water jet is wider and slower. It moved the stagnation point to the end of the straight conical part. It is likely thanks to the larger cross section of the jet that it remained straight and no deflection and rotation around the backflow zone was observed. The same conclusion has rdcently been reported by Khullar et al[116]. In the third case, counter-rotation (clockwise) was applied to the water injected through the ring. It destabilized the jet, which again undergoes a rotating motion. A clockwise-rotating vortex developed in its center. Three smaller anticlockwise-rotating vortices are present at its periphery. In the last case, the counter-rotation was replaced by radial velocity so that the angle of the jet corresponds to the angle of the diffuser. It led to the development of undesirable twin spiral vortices in the elbow.

In Fig. 5.12, the velocity component perpendicular to the depicted longitudinal slice is visualized for all the cases presented so far. This component is directly related to the circumferential velocity in cylindrical coordinates. It can be seen that the jet rotation is driven by the circumferential velocity. In cases with water jet injection through the hub tip only, the axis of rotation was deflected so that it followed the inner side of the jet. The jet deflection leads to a constriction of the flow passage, which in turn leads to an increase in the circumferential velocity visible in the pictures and, by Bernoulli's principle, to a decrease in pressure, which supports the jet deflection. This destabilizing effect of the circumferential velocity therefore needs to be taken into account when determining the parameters of the water jet injection. Some passive flow control methods to reduce the circumferential velocity will be presented in the following section.

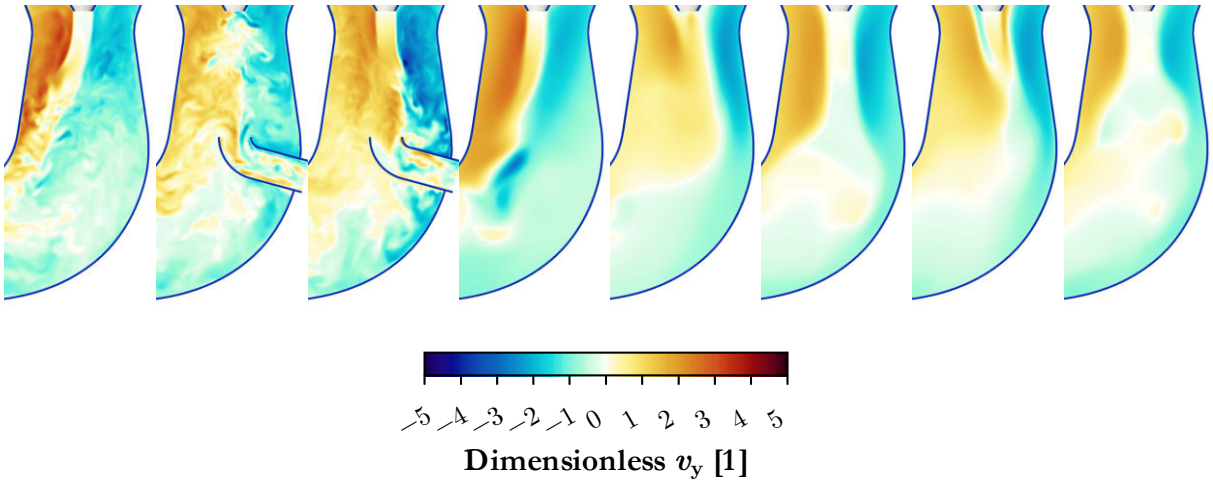

Fig. 5.12: *Instantaneous snapshots of the velocity component perpendicular to the depicted longitudinal slice for all cases presented so far. From letf to right: SBES simulations of: water jet injection, suction, both simultaneously, RSM simulations of: water jet injection from the hub tip, water jet injection from the ring depicted in Fig. 5.10, water jet injection from both, water jet injection from both with counter-rotation at the ring, water jet injection from both with radial velocity at the ring. The flow rate of the injected water is* 20% *of the total flow rate at the inlet.*

5.3 CFD study of different pasive control methods

Several passive control methods for mitigation of the vortex rope were proposed and tested. This work was carried out within a research project at the department aimed primarily at mitigation of the recirculation at the inlet of a diagonal pump. An exhaustive research report[117] has been written, in which details can be found. Only basic information regarding the test case and the most important qualitative results will be presented here.

The swirl generator designed by Štefan (see chapter 2) was used as a test case. The reason for that was that its diffuser has drilled holes for pressure transducers, allowing pressure measurements and mounting rods supporting the installations that were used to mitigate the vortex rope. The base case, i.e. without any installation, was simulated using both the RSM and SBES turbulence models. The results are presented in Figs 5.13 and 5.14. An irregular vortex rope behavior was observed. Two distinct states were detected – these are depicted in the first figure. The same behavior was observed in recordings from a high speed camera, validating the CFD results.

A total of 11 installations for mitigating the vortex rope were gradually proposed and tested. They are depicted in Fig. 5.15, and the results of CFD simulations with the RSM model of turbulence and/or experiments are presented in Figs 5.16 and 5.17.

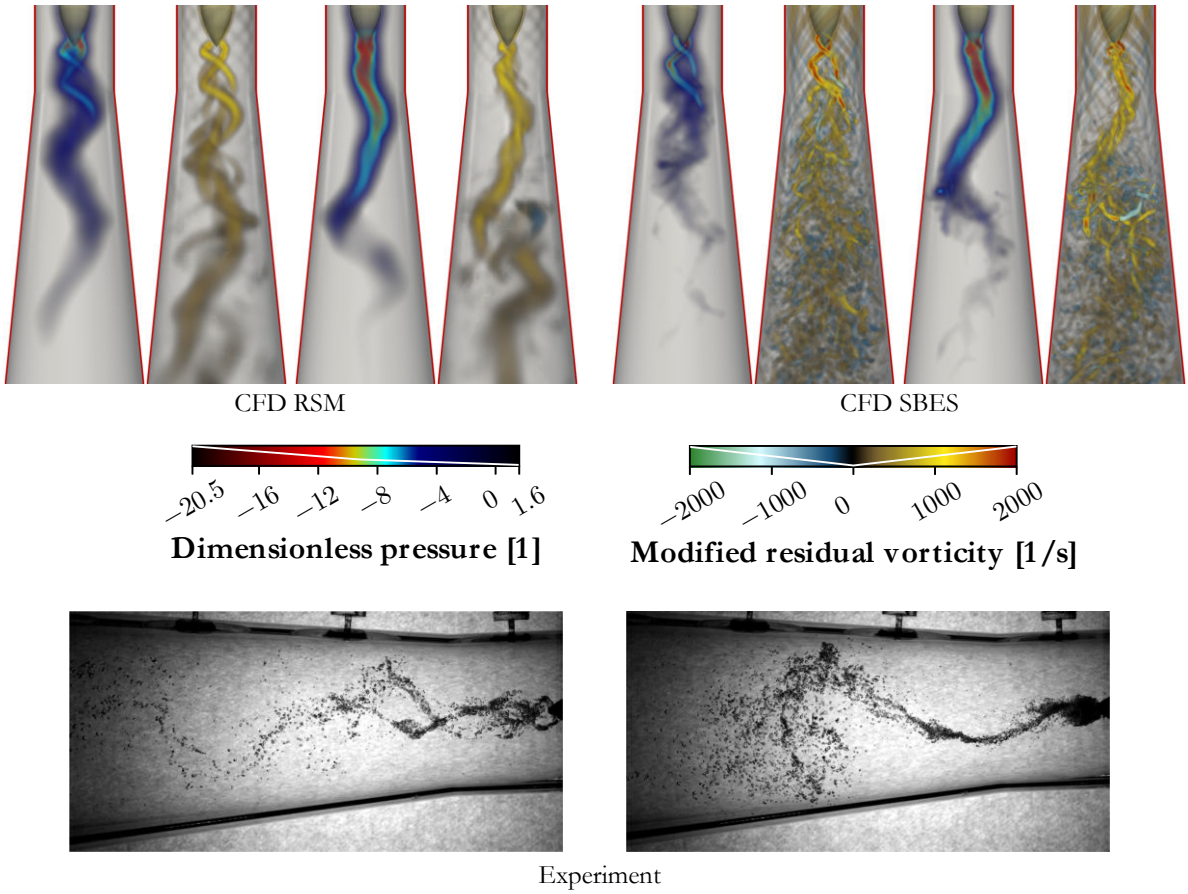

Fig. 5.13: *Volume renders of CFD data and photographs from the experiment for the base case (without any installation).*

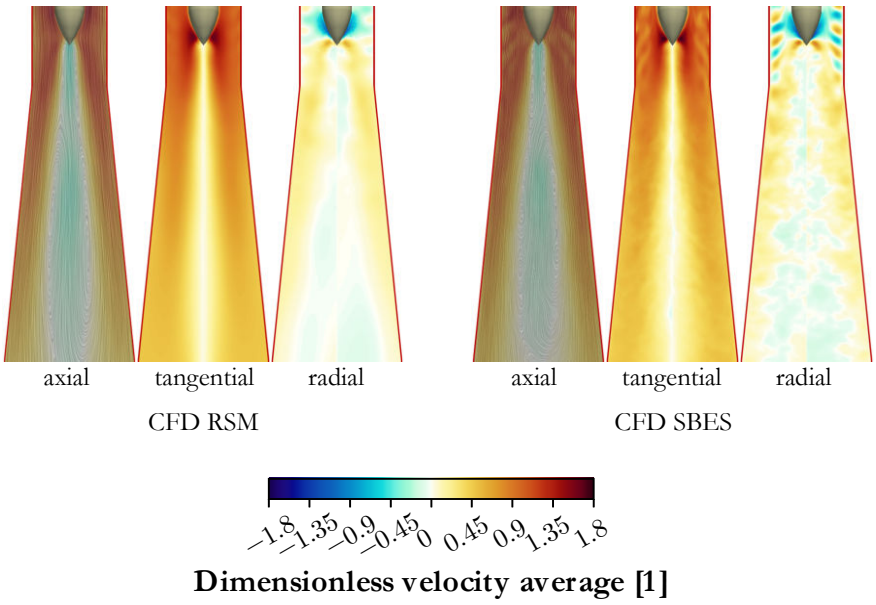

Fig. 5.14: *Dimensionless velocity average in a longitudinal slice for the base case (without any installation). The axial velocity field is complemented by an LIC texture.*

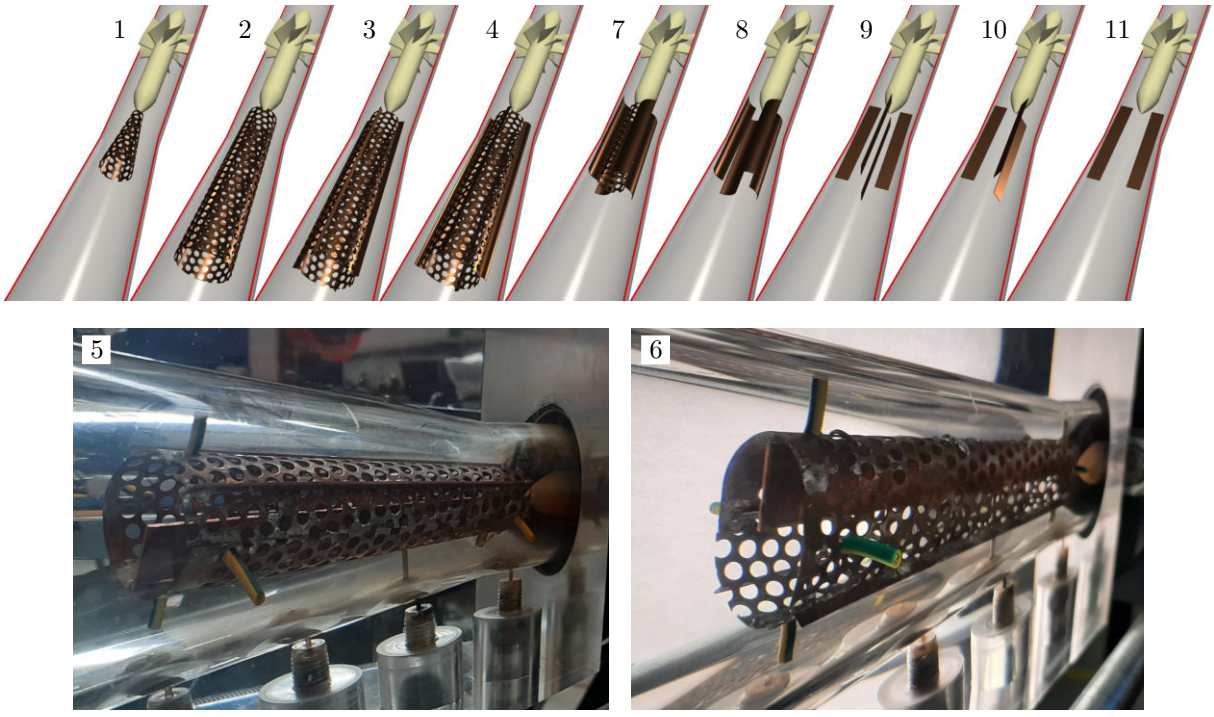

Fig. 5.15: *Renders of installations simulated by CFD and photographs of installations that were tested only experimentally.*

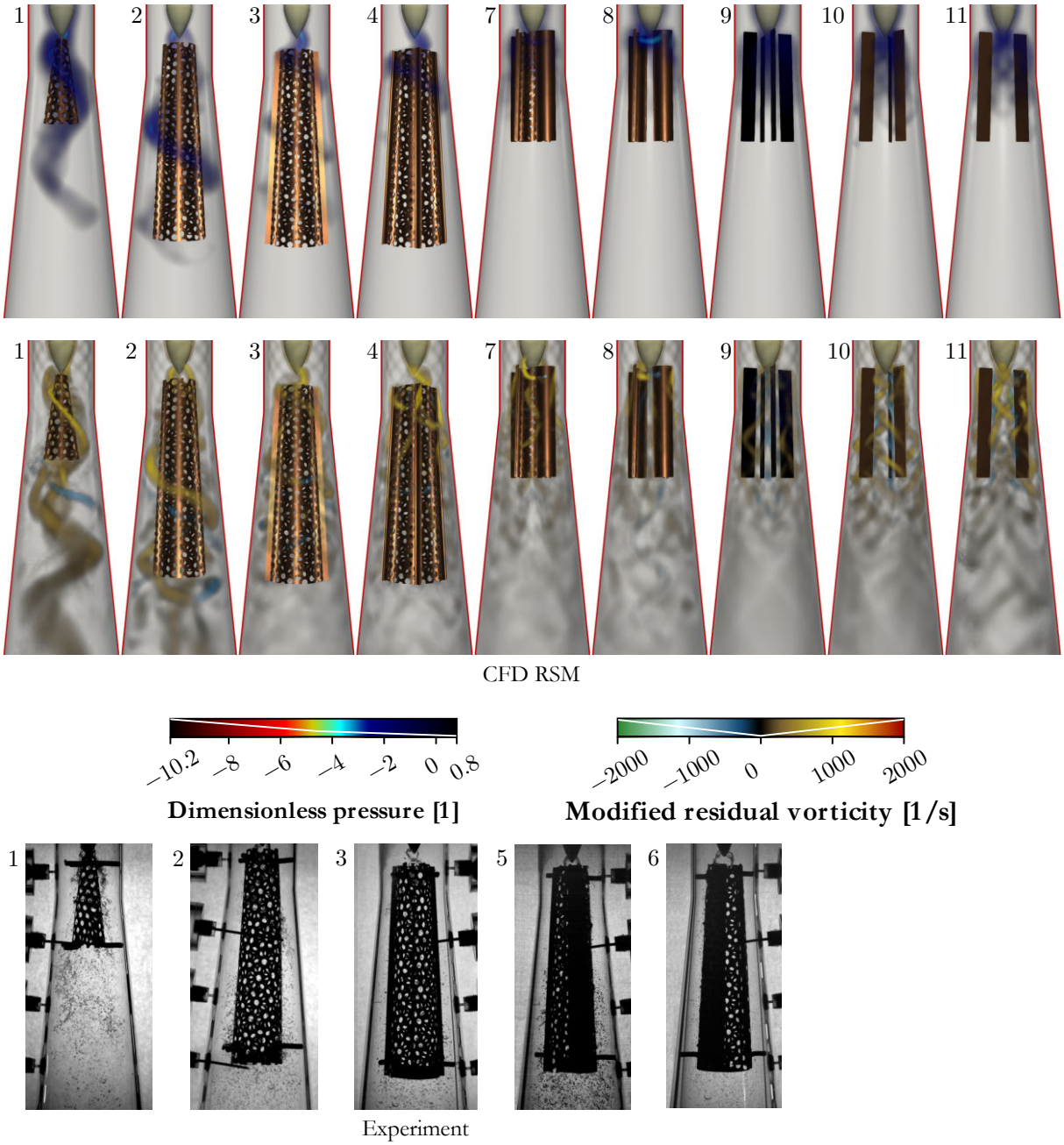

Fig. 5.16: *Volume renders of CFD data and photographs from experiments for cases with installations.*

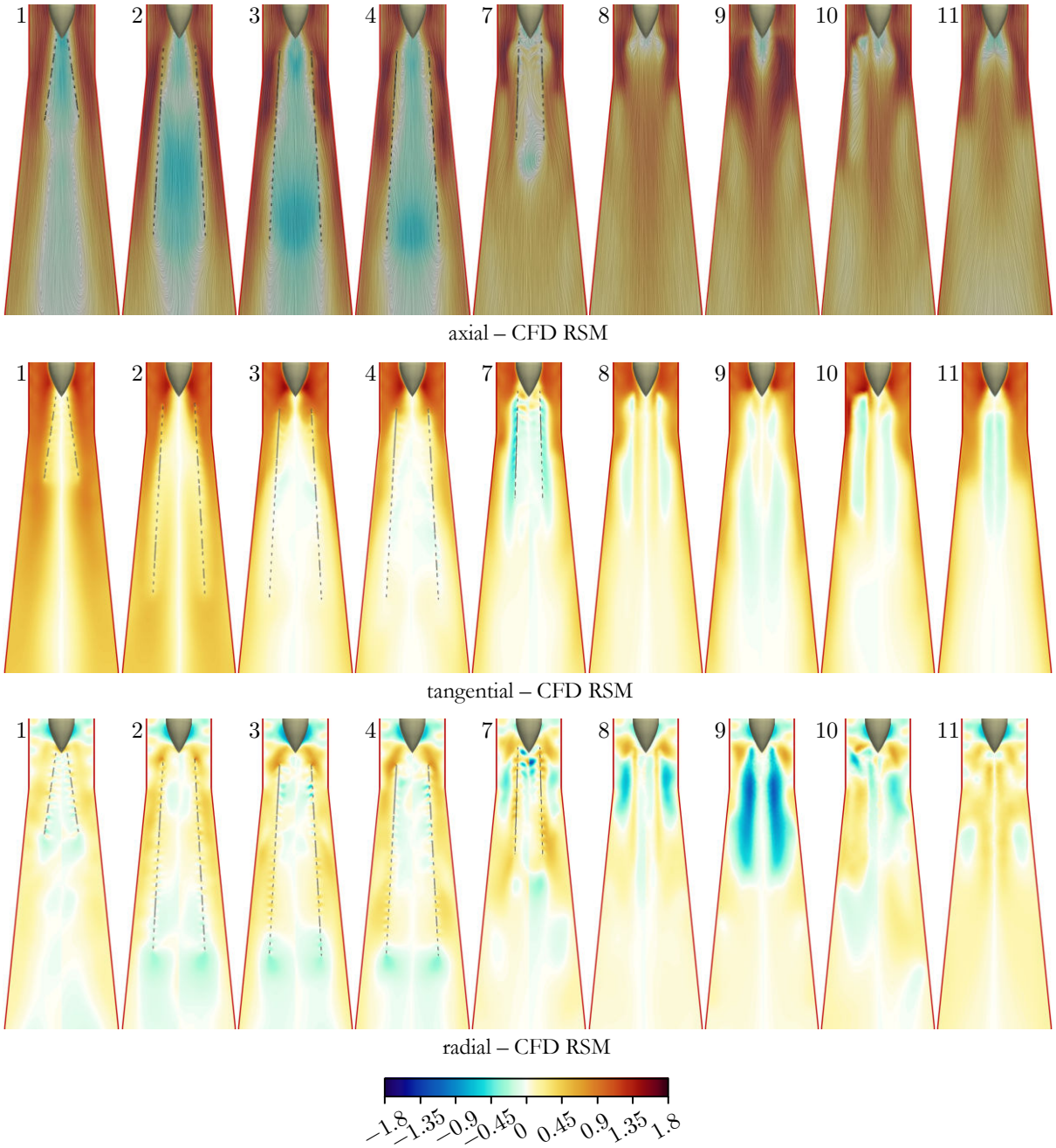

Fig. 5.17: *Dimensionless velocity average in a longitudinal slice for the cases with installations. The axial velocity field is complemented by an LIC texture.*

The first two installations are of an axisymmetric conical shape. They are made of a perforated sheet metal, and they follow the idea of professor Pochylý to induce dissipation to the flow by letting it pass through the holes. This dissipation acts only in the radial direction. Unfortunately, the flow was deflected rather than passing through the holes. The vortex rope was pushed to the space between the installation and the outer wall, and the space inside the installation was almost

completely occupied by backflow. The next two installations therefore introduce fins added perpendicularly to the outer surface of installation number 2. In case number 3, the fins are flat, whereas in case 4, the fins are curved so that they smoothly divert the tangential flow to the radial direction and therefore through the holes. The CFD results still indicate the presence of a vortex rope, but it is substantially weaker. Case 3 was also tested experimentally, and the analysis of the pressure measurements presented in the research report mentioned earlier showed that weaker pulsations caused by a precessing motion of a vortex were indeed present.

The persistent presence of a vortex rope indicates that the height of the fins needs to be increased. In case 5, two neighboring fins were replaced by a larger fin attached to the inner side of the axisymmetric part. In case 6, this installation was deformed to an elliptical shape. Both cases were tested only experimentally. It was found out that the peaks in frequency spectra related to the precessing motion of a vortex disappeared. Looking at the persistent backflow inside the installations, it was decided to reduce the diameter of the axisymmetric part and make it shorter. The installation was also moved further upstream to tackle the vortices forming at the spike. The results of CFD were significantly better. Downstream of the installation, the flow was practically steady. The only issue is that the vortices forming at the spike were pushed upstream instead of suppressed. They exert an unfavorable periodic load on the installation.

The next idea was to remove the axisymmetric perforated part. In this case, the flow deflected by the fins in the radial direction had no obstacle, leading to the complete elimination of backflow and even higher axial velocity at the axis than in the outer zone. Different numbers of flat fins were also tested with more or less similar results. Experimental validation is yet to be done.

Overall, it can be stated that the introduction of fins of proper size that deflect the tangential flow in the radial direction, which consequently leads after meeting at the axis to a deflection in the axial direction, stabilizes the flow downstream. However, vortices forming at the spike upstream persist and exert a periodic load on the fins. It may be therefore reasonable to introduce a kind of active flow control, e.g. water jet or air injection, to suppress these. In contrast to the previous section, where the water jet injection was used alone to mitigate the vortex rope and high flow rates were needed, much smaller flow rates should be sufficient since the vortices are substantially smaller.

6 Reduced-order modelling

By reduced-order modelling, we mean efforts to reduce computational complexity by decreasing the number of degrees of freedom. To achieve this, we need to find a suitable transformation of the coordinates.

The standard way of fluid flow modelling is to solve equations based on the first principles, i.e. the continuity equation and the Navier–Stokes equation. These equations feature variables defined in space and time, e.g. pressure $p(\boldsymbol{x}, t)$. The equations are discretized and solved on a spatial grid in discrete time steps. It is necessary to formulate the discretized equations for each point of the grid, ultimately leading to a set of a very high number of equations that need to be solved. Obviously, this is computationally demanding.

To reduce the number of degrees of freedom, the variables should be formulated in different coordinates, e.g. $p(\boldsymbol{\phi}(\boldsymbol{x}), \boldsymbol{a}(t))$. In this setting, $\boldsymbol{\phi}(\boldsymbol{x})$ is a vector of spatial modes and $\boldsymbol{a}(t)$ a vector of temporal functions governing their evolution. The definition of $p(\boldsymbol{\phi}(\boldsymbol{x}), \boldsymbol{a}(t))$ is then assumed as follows

$$p\big(\boldsymbol{\phi}(\boldsymbol{x}), \boldsymbol{a}(t)\big) = \sum_{i=1}^{m} \phi_i(\boldsymbol{x}) a_i(t) \tag{6.1}$$

In some special cases, a small finite number of modes m is sufficient for this equation to hold. Such cases include simple periodic flows. If the spatial modes $\phi_i(\boldsymbol{x})$ are known, it is only necessary to solve for m unknown temporal functions $a_i(t)$. In most cases, the number of modes needed to obtain the exact solution is in the discrete setting equal to $\min(M-1, N-1)$, where M is the number of snapshots and N is the number of grid points. However, many of the modes can often be neglected, which is typically true for flows that are close to periodic and not too irregular, so a very small m may be enough for a sufficient approximation. Based on the way of obtaining $\phi_i(\boldsymbol{x})$, Noack et al.[118] established three categories of modes.

Mathematical modes are a set of suitable orthonormal functions that fulfil the boundary conditions. They are derived without any relation to the governing physics. If suitably chosen, the models may be robust to different boundary conditions, such as the inflow velocity. A drawback is that the number of modes that need to be considered is typically high.

Physical modes are to some extent related to the governing equations. One example of fluid flow is the eigenmodes of the linearized Navier–Stokes equation. In successful cases, these modes provide balanced performance in terms of accuracy and robustness.

Empirical modes are computed from a reference solution (or a set of reference solutions) of the governing equations. This allows the highest reduction of the system dimension to be reached, but for the price of bad robustness away from the reference point.

In this work, models based on empirical modes will be sought. The modes can be obtained by various decomposition techniques. Some relevant methods are described in the following section.

6.1 Spatio-temporal decomposition of fluid flow data

6.1.1 Proper orthogonal decomposition

Given reference data $p(\boldsymbol{x}, t)$, the proper orthogonal decomposition (POD) aims to find spatial and temporal modes satisfying (6.1) and the following condition

$$\iint_{VT} \left(p - p_{\mathrm{POD}}^{[n]}\right)^2 \mathrm{d}V\mathrm{d}t \leq \iint_{VT} \left(p - p_{\mathrm{arb}}^{[n]}\right)^2 \mathrm{d}V\mathrm{d}t \tag{6.2}$$

Here, $p_{\mathrm{POD}}^{[n]}$ is the approximation of p obtained by summing $m = n$ most dominant POD modes in (6.1), and $p_{\mathrm{arb}}^{[n]}$ means the same for $m = n$ arbitrary modes. This condition means that there is no better decomposition than POD in terms of minimizing the square of the residual for any given number of modes. Consequently, POD has become very popular for model order reduction.

Solving the present optimization task leads to two methods of computing POD modes. The method of snapshots by Sirovich[119] will be presented in the following since it is more suitable for fluid flow data, where the spatial dimension (number of grid points N) is usually much higher than the temporal dimension (number of snapshots M). Assume the following vector (snapshot) $\boldsymbol{p}_i^{\mathrm{T}} = [p(x_1, t_i) \quad \dots \quad p(x_N, t_i)]$ and data matrix $\boldsymbol{A} = [\boldsymbol{p}_1 \quad \cdots \quad \boldsymbol{p}_M]$. Then do the following.

1) Compute the covariance matrix

$$C_{ij} = \frac{1}{M} (\boldsymbol{p}_i, \boldsymbol{p}_j)_V \tag{6.3}$$

where $(\boldsymbol{p}_i, \boldsymbol{p}_j)_V$ is an inner product defined as a numerical approximation of the following integral

$$(\boldsymbol{p}_i, \boldsymbol{p}_j)_V = \int_V p(\boldsymbol{x}, t_i) p(\boldsymbol{x}, t_j) \, \mathrm{d}V \tag{6.4}$$

2) Solve the following eigenvalue problem

$$\boldsymbol{C}\boldsymbol{e}_i = \boldsymbol{e}_i \lambda_i \tag{6.5}$$

Since the matrix $\boldsymbol{C}$ is by definition symmetric and positive-definite, the eigenvalues λ_i are real and positive and the eigenvectors are orthogonal. The eigenvectors are in the following supposed to be scaled so that $\boldsymbol{e}_i \cdot \boldsymbol{e}_i = 1$.

3) Compute the spatial modes $\boldsymbol{\phi}_i^{\mathrm{T}} = [\phi_i(x_1) \quad \dots \quad \phi_i(x_N)]$

$$\boldsymbol{\phi}_i = \frac{1}{\sqrt{M\lambda_i}} \boldsymbol{A}\boldsymbol{e}_i \tag{6.6}$$

4) Compute the temporal modes $\boldsymbol{a}_i^{\mathrm{T}} = [a_i(t_1) \quad \dots \quad a_i(t_M)]$

$$\boldsymbol{a}_i = \boldsymbol{e}_i \sqrt{M\lambda_i} \tag{6.7}$$

The following orthogonality properties hold for the POD modes

$$(\boldsymbol{\phi}_i, \boldsymbol{\phi}_j)_V = \begin{cases} 1 \text{ if } i = j \\ 0 \text{ else} \end{cases} \tag{6.8}$$

$$\frac{1}{M}\boldsymbol{a}_i \cdot \boldsymbol{a}_j = \begin{cases} \lambda_i \text{ if } i = j \\ 0 \text{ else} \end{cases} \tag{6.9}$$

It follows that the significance of each POD mode is given by its eigenvalue λ_i since, thanks to (6.8) and (6.9), it correrresponds to the L^2 norm of the POD mode. Also, due to orthogonality, the sum of the eigenvalues corresponds to the L^2 norm of the POD approximation.

$$\lambda_i = \frac{1}{M}\boldsymbol{a}_i \cdot \boldsymbol{a}_i (\boldsymbol{\phi}_i, \boldsymbol{\phi}_i)_V \cong \frac{1}{T}\iint_{VT} (\phi_i(\boldsymbol{x}) a_i(t))^2 \,\mathrm{d}V\mathrm{d}t \tag{6.10}$$

$$\sum_{i=1}^{m} \lambda_i \cong \frac{1}{T}\iint_{VT} \left(\sum_{i=1}^{m} \phi_i(\boldsymbol{x}) a_i(t)\right)^2 \mathrm{d}V\mathrm{d}t = \frac{1}{T}\iint_{VT} \left(p_{\mathrm{POD}}^{[m]}\right)^2 \mathrm{d}V\mathrm{d}t \tag{6.11}$$

Another important property follows from (6.6) if the data matrix contains velocity snapshots. The velocity components are usually stacked in a single vector, i.e. for a 3D case, $\boldsymbol{v}_i^{\mathrm{T}} = [\boldsymbol{v}_{\mathrm{x}}^{\mathrm{T}} \quad \boldsymbol{v}_{\mathrm{y}}^{\mathrm{T}} \quad \boldsymbol{v}_{\mathrm{z}}^{\mathrm{T}}]$, where $\boldsymbol{v}_{\mathrm{x}}^{\mathrm{T}} = [v_{\mathrm{x}}(x_1, t_i) \quad \ldots \quad v_{\mathrm{x}}(x_N, t_i)]$, and $\boldsymbol{v}_{\mathrm{y}}^{\mathrm{T}}$, $\boldsymbol{v}_{\mathrm{z}}^{\mathrm{T}}$ are formed analogously. The property of interest concerns the continuity equation, which is for an incompressible fluid a homogeneous linear differential equation. It is well known that any linear combination of functions that satisfy such an equation also satisfies that equation. Since the spatial modes are defined in (6.6) as a linear combination of the data snapshots, it follows that if the data snapshots satisfy the continuity equation, each spatial velocity mode satisfies it as well.

6.1.2 Discrete Fourier transform

The discrete Fourier transform (DFT) is one of the most eminent methods, with applications ranging from signal processing through data compression to solving partial differential equations. Originally proposed in the continuous form by Joseph Fourier at the beginning of the 19th century to solve the heat equation[120], the method resides in decomposing a function of a given variable into the Fourier series of sines and cosines. In the present setting with spatio-temporal data, the discrete Fourier transform is applied on the data from each grid point, one by one. The modes come in pairs that share the same frequency. In the following formulation in the domain of real numbers, the frequencies are defined as

$$f_i = \frac{i}{M\Delta t}, \qquad i = 0 \ldots \mathrm{ceil}\frac{M}{2} \tag{6.12}$$

where Δt is the time step between the snapshots (uniform sampling is assumed). The temporal and spatial modes are then defined as

$$\boldsymbol{a}_{i(\sin)}^{\mathrm{T}} = [\sin(2\pi f_i t_1) \quad \dots \quad \sin(2\pi f_i t_M)] \tag{6.13}$$

$$\boldsymbol{a}_{i(\cos)}^{\mathrm{T}} = [\cos(2\pi f_i t_1) \quad \dots \quad \cos(2\pi f_i t_M)] \tag{6.14}$$

$$\boldsymbol{\phi}_{i(\sin)} = \frac{2}{M}\boldsymbol{A}\boldsymbol{a}_{i(\sin)} \tag{6.15}$$

$$\boldsymbol{\phi}_{i(\cos)} = \frac{2}{M}\boldsymbol{A}\boldsymbol{a}_{i(\cos)} \tag{6.16}$$

In practice, it is not efficient to use this definition for the computation of modes. Instead, the fast Fourier transform (FFT) algorithms should be used. They exploit the symmetries observed in a matrix formulation of the discrete Fourier transform to reduce the computational complexity from $\mathcal{O}(M^2)$ to $\mathcal{O}(M \log M)$. Note that the Fourier transform is usually formulated in the domain of complex numbers, in which case the real part corresponds to the cosine mode and the imaginary part corresponds to the sine mode. The results also need to be multiplied by $\frac{2}{M}$ to obtain the same results as in (6.15) and (6.16). The advantage of the discrete Fourier transform is that the temporal modes are given in a closed form, allowing extrapolation into the future. However, there is an assumption that the data are periodic; i.e. the pattern we obtain on the covered time interval simply repeats itself in time. The modes are interpretable since they represent pure harmonic oscillations. The disadvantage is that in more complex cases, it performs significantly worse than POD in terms of model order reduction, i.e. it is needed to include many more modes in the model for the same accuracy.

6.1.3 Spectral proper orthogonal decomposition

The previously described two methods can be considered as two antipoles with the Fourier transform aimed at spectral purity on one side and the proper orthogonal decomposition aimed at optimal model order reduction properties on the other side. The spectral purity of the Fourier transform comes handy with respect to interpretability, but in more complex cases, it might be beneficial to relax the constant-amplitude and frequency constraint to some extent. The proper orthogonal decomposition may be found to be unsuitable if the data are corrupted by inaccuracies and/or noise since due to the optimality property, it might be overfitting. It is analogous to curve fitting to noisy data, where a smooth approximation is preferred over interpolation. Sieber et al.[122] bridge the two methods using a method they called the spectral proper orthogonal decomposition (SPOD). It comes from the observation that the covariance matrix of POD typically exhibits similar values on diagonals. Considering that if the covariance matrix is circulant, the eigenvectors correspond to the Fourier modes $\boldsymbol{a}_{i(\sin)}$ and $\boldsymbol{a}_{i(\cos)}$, it follows that bridging POD and the discrete Fourier transform can be obtained by finding a method of transforming the POD covariance matrix smoothly depending on a chosen parameter into a circulant matrix. To clarify, a circulant matrix is a matrix where all the rows are composed of the same elements in the same order with the first element of the i-th row corresponding to the last element of the $i-1$st row, i.e., it has the following structure

$$\boldsymbol{C} = \begin{bmatrix} c_0 & c_1 & \cdots & c_{M-2} & c_{M-1} \\ c_{M-1} & c_0 & c_1 & & c_{M-2} \\ c_{M-2} & c_{M-1} & c_0 & \ddots & \vdots \\ \vdots & \ddots & \ddots & \ddots & c_1 \\ c_1 & \cdots & c_{M-2} & c_{M-1} & c_0 \end{bmatrix} \tag{6.17}$$

As a method of transition between the POD covariance matrix and a circulant matrix, Sieber et al. suggest using convolution along the diagonals that share the same value in the circulant matrix. It can be written as

$$C_{ij}^{\mathrm{SPOD}} = \sum_{k=-N_\mathrm{f}}^{N_\mathrm{f}} g_k C_{i+k,j+k}^{\mathrm{POD}} \tag{6.18}$$

Here, the indices of the POD covariance matrix can exceed its extent. In that case, if an index is below one, M is added, and if an index is above M, M is subtracted. The convolution kernel g_k can be chosen arbitrarily as long as it acts as a low-pass filter in the frequency domain. Since the Fourier transform of a convolution of two functions in a time domain equals to the multiplication of their Fourier transforms (convolution theorem), it follows that the Fourier transform of such a kernel should be decaying towards higher frequencies. One of such kernels is the boxcar function that gives a moving average as its output, i.e. $g_k = \frac{1}{N_\mathrm{f}}$. However, the Fourier transform of this function is a sinc function, which is decaying towards higher frequencies in an oscillatory manner. Therefore, the authors prefer a Gaussian function since its Fourier transform is another Gaussian that is monotonically decaying towards higher frequencies. The convolution kernel that uses one of its standard forms reads

$$g_k = \frac{1}{\sigma\sqrt{2\pi}} \exp\left(-\frac{k^2}{2\sigma^2}\right) \tag{6.19}$$

Since the Gaussian function is nonzero along the whole axis of real numbers, the length N_f of the convolution kernel should generally be infinite to cover its whole extent. In practice, N_f is determined so that the values of the Gaussian for $k > N_\mathrm{f}$ and $k < -N_\mathrm{f}$ are below a chosen limit. In this setting, POD is obtained for $\sigma \to 0$ and DFT is obtained for $\sigma \to \infty$.

After the filtered covariance matrix is obtained, the spatial and temporal modes are computed using the same procedure as in POD. It should be mentioned that the spatial modes $\boldsymbol{\phi}_i$ are no longer orthogonal. Nevertheless, the temporal functions $\boldsymbol{a}_i$ are still orthogonal since the symmetry of the covariance matrix is preserved. Also, the eigenvalues can no longer be used to measure the significance of modes. Instead, it is necessary to compute the respective norm of each mode directly.

6.2 Application of POD to the present case, effect of SPOD

The methods described so far will now be applied to the present case with a vortex rope, and their performance will be compared. Namely, the dimensionless pressure $\hat{p}$ fields from different SBES simulations were considered.

As the first step, POD was performed since it has become the standard in cases with strong coherent structures. It was introduced for these purposes in 1967 by Lumley[121]. In Figs 6.1 and 6.2, results for SBES simulations with fixed boundary conditions are presented. They include the mean field, 19 most dominant spatial modes, frequency spectra of selected temporal modes, and a cumulative accuracy of the POD approximation as the modes are added. The plotted cumulative accuracy is defined as follows

$$\lambda_{\mathrm{c}}(m) = \frac{\sum_{i=1}^{m} \lambda_i}{\sum_{i=1}^{M} \lambda_i} = \frac{\sum_{i=1}^{m} \boldsymbol{a}_i \cdot \boldsymbol{a}_i(\boldsymbol{\phi}_i, \boldsymbol{\phi}_i)_V}{\sum_{i=1}^{M} \boldsymbol{a}_i \cdot \boldsymbol{a}_i(\boldsymbol{\phi}_i, \boldsymbol{\phi}_i)_V} = \frac{\sum_{i=1}^{m} \boldsymbol{a}_i \cdot \boldsymbol{a}_i(\boldsymbol{\phi}_i, \boldsymbol{\phi}_i)_V}{\sum_{i=1}^{M} (\hat{\boldsymbol{p}}'_i, \hat{\boldsymbol{p}}'_i)_V} \tag{6.20}$$

where m is the number of considered modes, M is the total number of modes, and $\hat{\boldsymbol{p}}'_i$ is a vector containing the values of the fluctuations $\hat{p}'$ in the grid points. Values of λ for individual modes are noted below pictures of spatial modes. It is important to note that the temporal mean was subtracted, so POD was applied to fluctuations only. This is a standard procedure since it leads to beneficial properties. If a boundary with constant boundary conditions (e.g. constant inlet velocity) is part of the domain, then the boundary conditions are contained in the subtracted mean, and POD modes do not affect them. This preserving property is beneficial in reduced-order models for temporal functions $a_i(t)$ since erroneous changes of boundary conditions are avoided by construction. Another property is that eigenvalues λ_i can be interpreted as variances.

Looking at the pictures of spatial modes, it can be seen that relatively simple patterns exist. Modes 1 and 2 exhibit the same pattern of two spiral structures (positive and negative) in all the presented cases, covering the range of flow rates ratios from 50:50 to 70:30. It represents the mean shape of the vortex rope tail. One can notice that these structures move upstream and become larger as the swirl increases. There are also modes related to vortices forming at the hub tip (4 and 5 for 50:50, 3 and 4 for 60:40, and more modes for 70:30 due to more regimes – recall Fig. 4.24). The axial extent of these modes decreases as the swirl increases. This behavior is likely related to the behavior of the general vortex breakdown phenomenon in tubes that moves upstream as the swirl increases[4]. In this case, it is greatly influenced by the presence of the central hub, which acts as a boundary, preventing further upstream movement. There is also a pair of modes related to the first superharmonics (18 and 19 for 50:50, 8 and 9 for 60:40, 3 and 4 for 70:30). The spatial modes feature two positive and two negative spirals, and the dominant frequency of the temporal modes is (at least for the last two operating points) two times the dominant frequency of the leading mode pair (1 and 2). In the last case (with the elbow diffuser), the second superharmonics are also present (mode pair 8 and 9). The spatial modes exhibit three positive and three negative spirals located in the bottom part, indicating that oscillations therein are of a more complex shape. Last kind of modes that can be observed are those of low-frequency pulsations (e.g. 3 for 50:50, 5–7 for 60:40, 5 and 6 for 70:30). Especially mode 3 of the 50:50 regime exhibit a high degree of rotational symmetry, meaning that it is strongly related to synchronous pressure pulsations. It is also evident that these pulsations propagate upstream since the whole upper part of the spatial mode exhibits non-zero values.

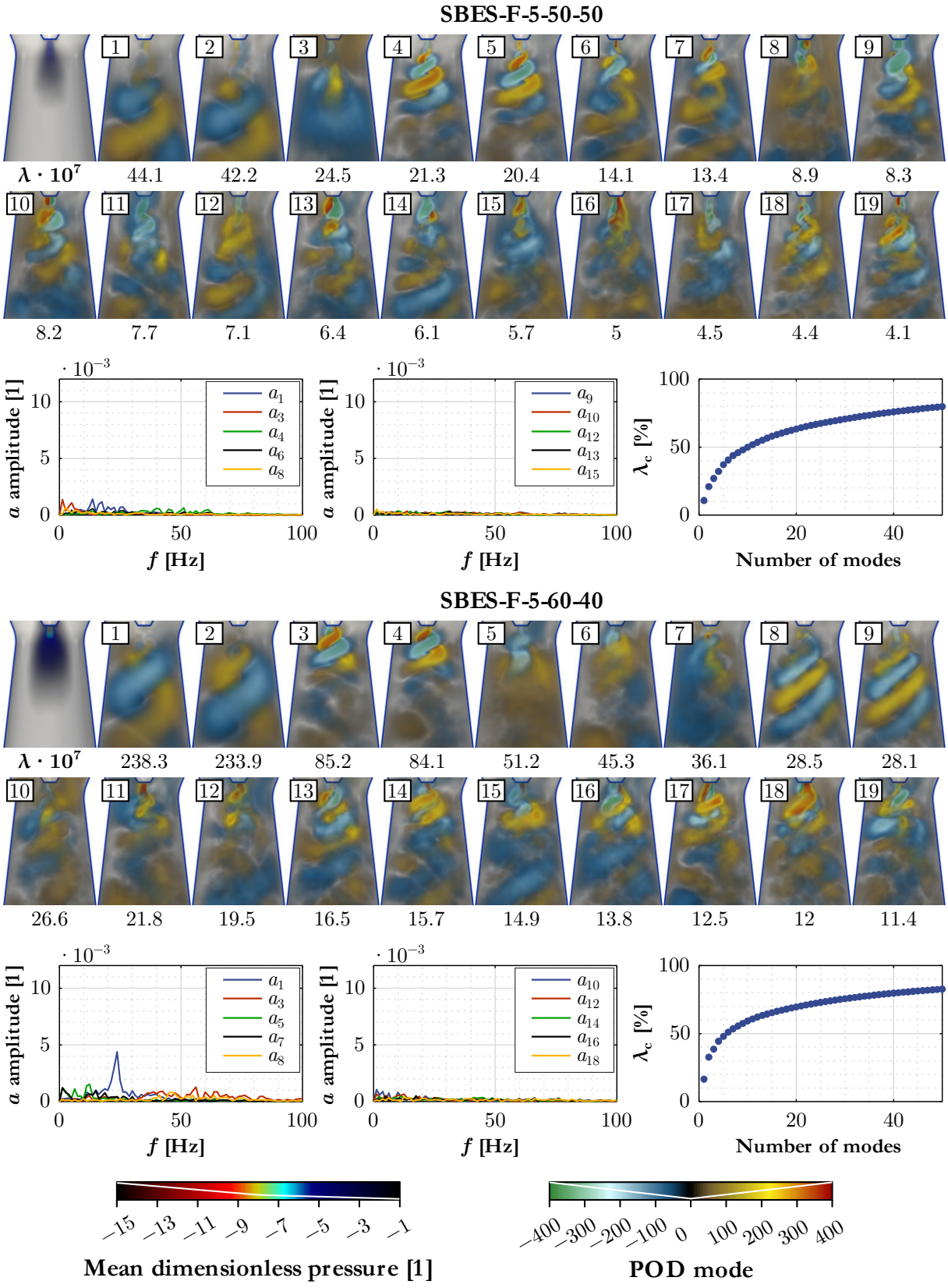

Fig. 6.1: *Results of POD applied to the data from simulations SBES-F-5-50-50 and SBES-F-5-60-40.*

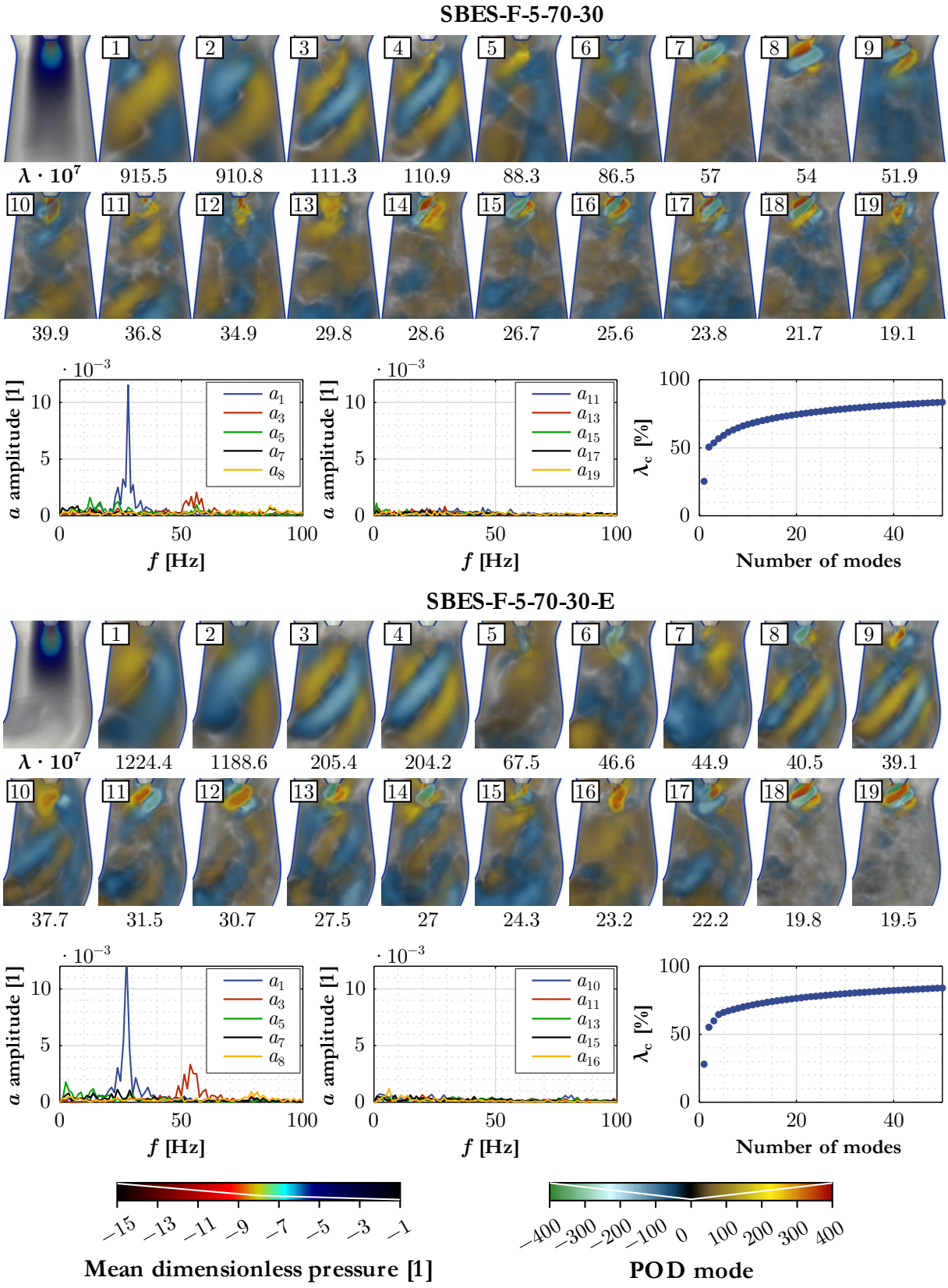

Fig. 6.2: *Results of POD applied to the data from simulations SBES-F-7-70-30 and SBES-F-5-70-30-E (elbow diffuser).*

Next, POD will be applied to the data from simulation SBES-T-1, i.e. the simulation with transient boundary conditions covering a range of operating conditions with a well-developed vortex rope. The algorithm will be modified so that it takes into account some characteristic aspects of this transient. The first thing to keep in mind is related to the mean field. In the cases with fixed boundary conditions, a decomposition into the temporal mean and fluctuations was taken as the first step. After that, POD was applied to the fluctuations. In the previous figures, it can be seen that the mean field changes with the operating point. Therefore, if the standard POD procedure is applied to the transient case, there will be a mode that covers this slow dynamics. Another aspect is caused by the fact that the vortex rope becomes stronger as the swirl number increases during the transient simulations. The POD optimality condition then causes that the accuracy of reconstructions is significantly biased towards the latter phase with much stronger fluctuations. To obtain a balanced performance, a suitable scaling needs to be employed.

The following algorithm was proposed in this work to address the aforementioned aspects.

1) Compute the temporal mean, subtract it from the data, and apply POD the standard way to the obtained fluctuations.
2) Find the POD mode related to the mean field evolution in time. The temporal function of this mode can exhibit a certain level of fluctuations superimposed on a smooth, slowly evolving function. In that case, it may be reasonable to approximate the trend by a suitable function, e.g. by a polynomial or exponential, and disregard the fluctuations.
3) Subtract the mean field and its evolution mode found in the previous step from the original data to obtain only fluctuations related to the vortex rope.
4) Normalize each snapshot as follows

$$\hat{\boldsymbol{p}}'_{i\,\mathrm{norm}} = \frac{\hat{\boldsymbol{p}}'_i}{\sqrt{(\hat{\boldsymbol{p}}'_i, \hat{\boldsymbol{p}}'_i)_V}} \tag{6.21}$$

   The result of this step is that the values on the main diagonal of the covariance matrix are the same; therefore, all snapshots have equal weight in the POD optimality condition.
5) Perform POD of the normalized data set to obtain the spatial modes $\boldsymbol{\phi}_i$.
6) Giving the data of the fluctuations before normalization $\hat{\boldsymbol{p}}'_i$, compute the temporal modes as follows

$$a_i(t_j) = (\boldsymbol{\phi}_i, \hat{\boldsymbol{p}}'_j)_V \tag{6.22}$$

During execution of this procedure, it was found out that the mean-field evolution mode is the most dominant mode. Its temporal function was well approximated by a quadratic function. The final results are presented in Fig. 6.3. Mode number 1 is the mean-field variation mode. Values of λ and $\lambda_c(m)$ were computed only for the following modes so that only the fast dynamics related to the vortex rope motion are considered. Moreover, values of $\lambda_c(m)$ were computed not only for the entire time interval, but also for its thirds. This reveals the cumulative accuracy of the decomposition in various phases of the vortex rope evolution. The values of λ denoted under spatial modes (evaluated for the whole time interval) are not descending monotonically towards higher modes. This is one of the consequencies of the balancing procedure. Note that $\lambda_c(m)$ for the whole time interval is indeed significantly biased towards the values for the last third of that interval.

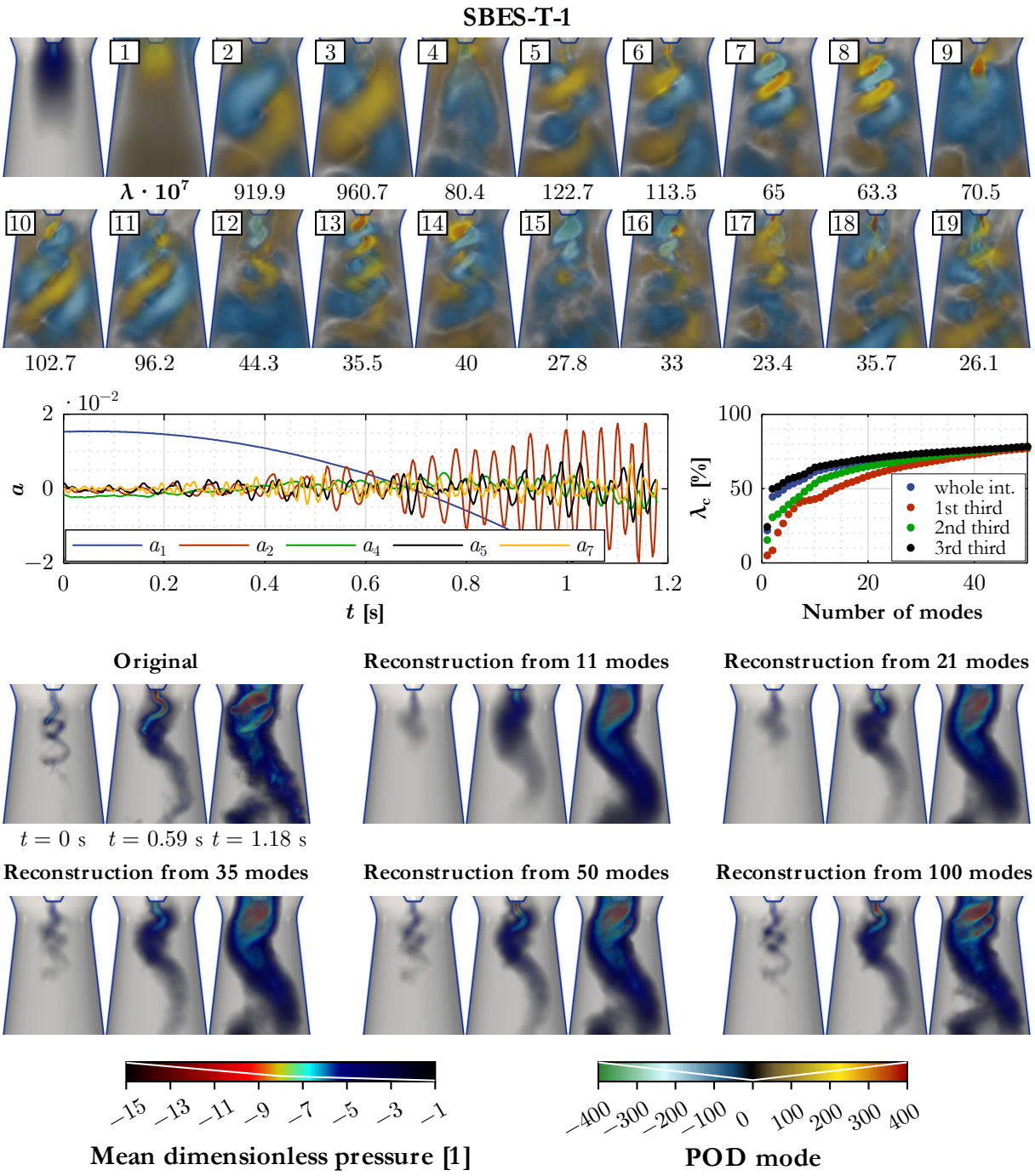

Fig. 6.3: *Results of POD applied to the data from simulation SBES-T-1. Values of λ_c presented in the chart assume only modes from number 2 on, i.e. only the dynamics related to the vortex rope motion. The time interval was divided into thirds to assess the performance of POD in different phases, not just in the whole interval.*

Modes 2 and 3 are of the same pattern as modes 1 and 2 obtained by POD of the 70:30 regime. This is why they bring most of their contribution at the end of the simulation. Mode 4 is to some extent related to the mentioned slow dynamics. At the beginning of the simulation, its temporal function is almost constant. In the end, when a strong vortex rope has developed, it also exhibits

oscillations on the same frequency as the previous two modes that capture the precession of the vortex rope tail. The next four modes are important in the initial phase. The first two of them modify structures in modes 2 and 3 similarly as mode 1 evolves the mean field. They move the two spiral structures downstream to obtain patterns that were observed in modes 1 and 2 of the 50:50 regime. Modes 7 and 8 are related to the vortex forming below the hub tip, similarly to modes 4 and 5 of the 50:50 regime. Mode 9 is of a highly symmetric pattern; thus, it is related to synchronous pressure pulsations. Modes 10 and 11 represent the first superharmonics. Higher modes exhibit less organized and less regular structures. The evolutions of the cumulative accuracy indicate that they contribute comparably to each of the subintervals and increase the accuracy only slowly. It can be observed that the accuracy initially grows faster for the later phases of the simulation, which is consistent with what was observed for the simulations with fixed boundary conditions. When the first 50 modes are taken, the accuracies of the subintervals meet and continue to increase evenly. Looking at the pictures of three chosen snapshots and their reconstructions from different number of POD modes, we see that the first eleven modes provide a fairly good approximation of the last snapshot, where a large strong vortex rope is present. Obviously, the smaller structures of which the whole structure is formed are missing, but its shape and pressure decrease toward the center are well captured. In the first two snapshots, we see that the tail of the vortex rope looks very blurred. A total of 35 modes need to be taken to obtain the correct shape and many more to achieve the correct pressure values at the centerline. This fact underlines its irregular behavior.

6.2.1 Effect of SPOD

The effect of SPOD is studied on data from simulation SBES-F-5-70-30. As previously described, this regime features a strong vortex rope. The frequency spectra of the axial velocity (that was compared with the PIV measurements in Fig. 4.23) and the most dominant POD modes exhibit a significant peak related to the precessing motion of the structure. SPOD is in this case based on the Gaussian filter (6.19). Different σ values were tested. Filter length $N_\mathrm{f} = 3\sigma$ was used in all cases since $g_{3\sigma} \cong 0.01 g_0$, which is considered small enough so that $k > 3\sigma$ and $k < -3\sigma$ can be neglected.

Fig. 6.4 presents various charts relevant for comparison. The first shows the values on the main diagonal of the covariance matrix to illustrate how SPOD flattens the evolution towards the constant values of the circulant matrix leading to DFT. The second reveals the impact on the accuracy of the approximation when considering up to 40 most dominant modes. The last chart shows the frequency spectra of five chosen modes. As the modes often come in pairs (in the case of DFT, the modes are paired by definition), five most dominant even modes were chosen.

In the POD frequency spectra, it is evident that modes 2 and 4 contain the most dominant peaks, but they are also corrupted by a certain level of noise. To this end, SPOD with $\frac{\sigma}{M} = 1/64$ and $\frac{\sigma}{M} = 1/32$ perform well in terms of filtering the noise. In both cases, frequencies away from the peaks are diminished. Also, none of the five modes contains frequencies above the first superharmonic peak. SPOD with $\frac{\sigma}{M} = 5/32$ seems overbiased to DFT. The cumulative accuracy chart shows that the first mode pair itself represents 50% of the L^2 norm of pressure fluctuations. POD and the first two SPODs fully capture it, i.e. not only the dominant frequency, but also the surrounding frequencies that are related to frequency and/or amplitude fluctuations. DFT extracts the most dominant frequency only. In all cases, higher modes are much less significant, leading to only

slow improvements as new modes are added to the approximation. It requires hundreds of modes to reach a negligible residual, underlining the complex and irregular behavior of the observed vortex rope.

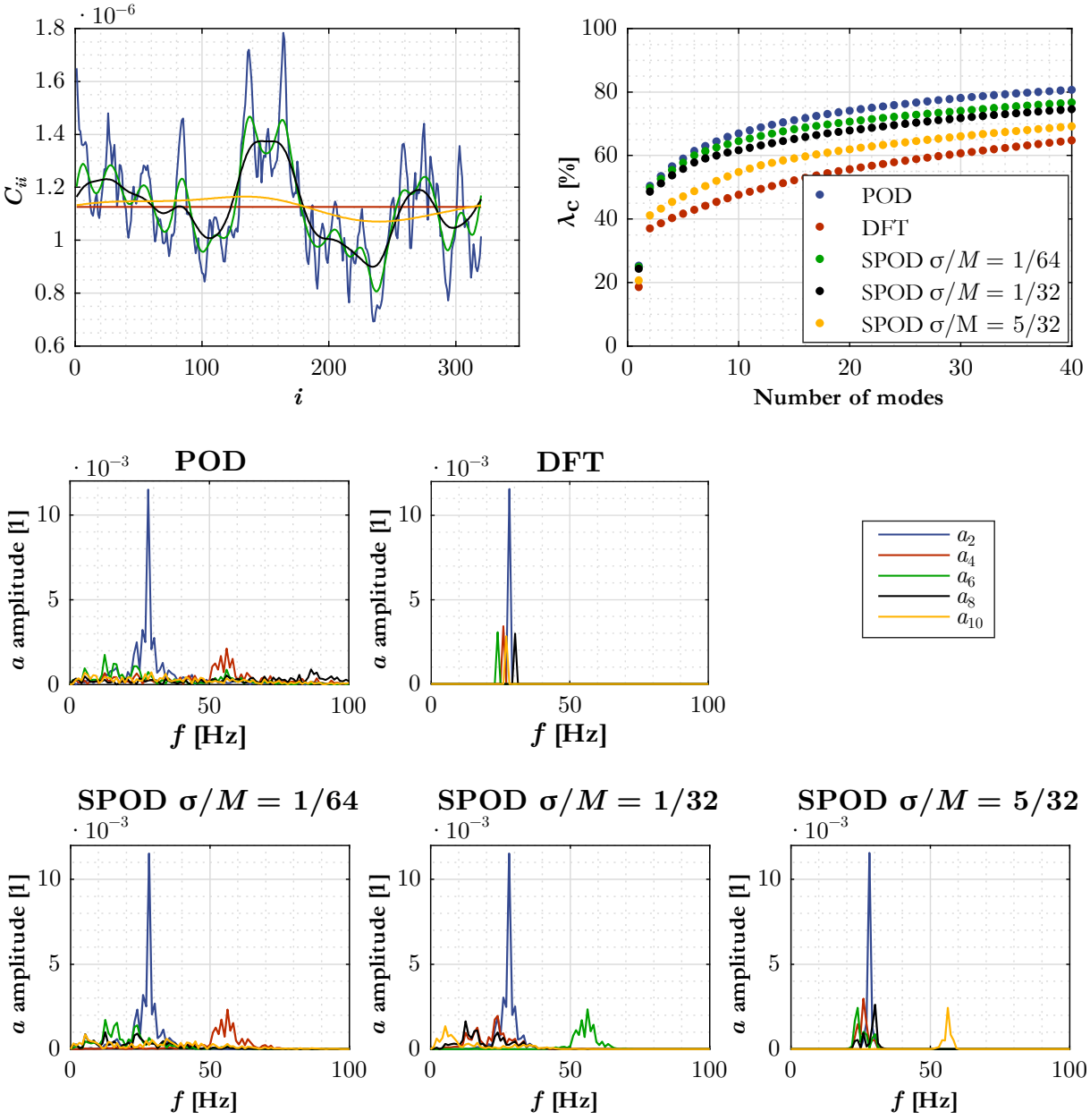

Fig. 6.4: *Comparison of POD, DFT, and SPOD with different Gaussian kernels applied to the dimensionless pressure data from simulation SBES-F-5-70-30. Top left: main diagonal of the covariance matrix, top right: cumulative accuracy of the approximation, bottom: frequency spectra of chosen temporal functions.*

6.3 Machine learning for dimensionality reduction

If more specific decompositions than those presented so far are desired, i.e. decompositions with more complex objective functions and/or constraints, different machine learning algorithms come into play. To clarify, machine learning is a term that encompasses a wide range of techniques from simple linear regression through optimization methods to training deep neural networks. These techniques can be categorized into supervised, unsupervised, and semi-supervised learning. Dimensionality reduction techniques, in general, belong to unsupervised learning[123]. In this section, more advanced methods will be discussed. The key characteristic is that there is no closed-form solution, the modes are learned by suitable optimization techniques so that they minimize a given loss function while satisfying given bounds.

Learning decompositions with a high number of unknown parameters has recently been enabled thanks to advances in neural networks. As the computing power is still growing according to Moore's law, it is now possible to realize ideas that were impossible at the time they were formulated. An ordinary laptop nowadays provides sufficient power to train deep neural networks with hundreds of thousands of unknown weights. Myriad appealing applications across different fields including beating expert humans in various games, image recognition, speech recognition, targeted advertising, and performance evaluation from sensor data (e.g. failure detection), to name a few, have led to an enormous interest in deep learning. Thanks to that, specialized hardware including massively parallel GPUs and TPUs has been developed, enabling processing of unprecedented amounts of data. Moreover, powerful open-source softwares are available (Tensorflow, PyTorch).

6.3.1 Autoencoders

A standard method for more advanced dimensionality reduction is training a specific neural network called an autoencoder. A neural network can be understood as a composition of functions called layers with unknown parameters to be trained called weights. These weights are usually trained using algorithms based on the gradient descent method, where the gradient is computed using the backpropagation method. The input of an autoencoder is a data snapshot, and its output is an approximation of this snapshot.

The simplest case, a linear shallow autoencoder (Fig. 6.5 left), has one so-called hidden layer called encoder. It is a dense layer (each neuron is connected to all the input neurons), where the number of neurons in this layer must be lower than the snapshot size. This layer serves as a bottleneck. What follows is another dense layer called decoder. Its size is the same as the input size, and its output is supposed to be an approximation of the input. To clarify, a general dense layer with input $\boldsymbol{x}$ performs the following operation

$$\boldsymbol{y} = f\big(g(\boldsymbol{x})\big), \qquad g(\boldsymbol{x}) = \boldsymbol{W}\boldsymbol{x} + \boldsymbol{b} \tag{6.23}$$

where $\boldsymbol{W}$ is a matrix of weights called kernel, $\boldsymbol{b}$ is a vector of weights called bias, and $f\big(g(\boldsymbol{x})\big)$ is an activation function. In case of a linear layer, $f\big(g(\boldsymbol{x})\big) = g(\boldsymbol{x})$. However, autoencoder layers are assumed to be without bias, i.e. $\boldsymbol{b} = \boldsymbol{0}$. The shallow linear autoencoder therefore uses the encoder layer to compute the so-called latent variables $\boldsymbol{z}$ for each snapshot. The vectors containing the values of individual neurons z_i for all the data snapshots correspond to the temporal modes $\boldsymbol{a}_i$. Knowing the latent variable $\boldsymbol{z}$, an approximation of the input variable can be obtained by the decoder layer. The weights of this layer acting on neuron z_i correspond to the spatial mode $\boldsymbol{\phi}_i$. With

the structure of the neural network set, the last thing to do is to specify a loss function to be minimized by the gradient descent. It represents a metric that quantifies the difference between the output approximation $\tilde{\boldsymbol{x}}$ and the input snapshot $\boldsymbol{x}$. The most prominent loss functions are the mean squared error $\mathcal{L}(\boldsymbol{x}, \tilde{\boldsymbol{x}}) = \frac{1}{N}(\tilde{\boldsymbol{x}} - \boldsymbol{x})^2$ and the mean absolute error $\mathcal{L}(\boldsymbol{x}, \tilde{\boldsymbol{x}}) = \frac{1}{N}\sum_i |\tilde{x}_i - x_i|$, where N is the dimension of the two vectors. Using $\mathcal{L}(\boldsymbol{x}, \tilde{\boldsymbol{x}}) = (\tilde{\boldsymbol{x}} - \boldsymbol{x}, \tilde{\boldsymbol{x}} - \boldsymbol{x})_V$ and training the modes one by one, i.e. the hidden layer has only one neuron, leads to POD. Obviously, it is more efficient to compute the POD modes the direct way than training an autoencoder.

Using more than one encoding layer and more than one decoding layer leads to a deep autoencoder (Fig. 6.5 right). In addition, nonlinear activation functions are typically used. With this setting, the output approximation can no longer be expressed by relation (6.1). It is instead represented by a more complex function given by the structure of the decoder. It follows that this more complex function enables more efficient decomposition (less modes are needed for the same accuracy); however, the interpretability may be worse.

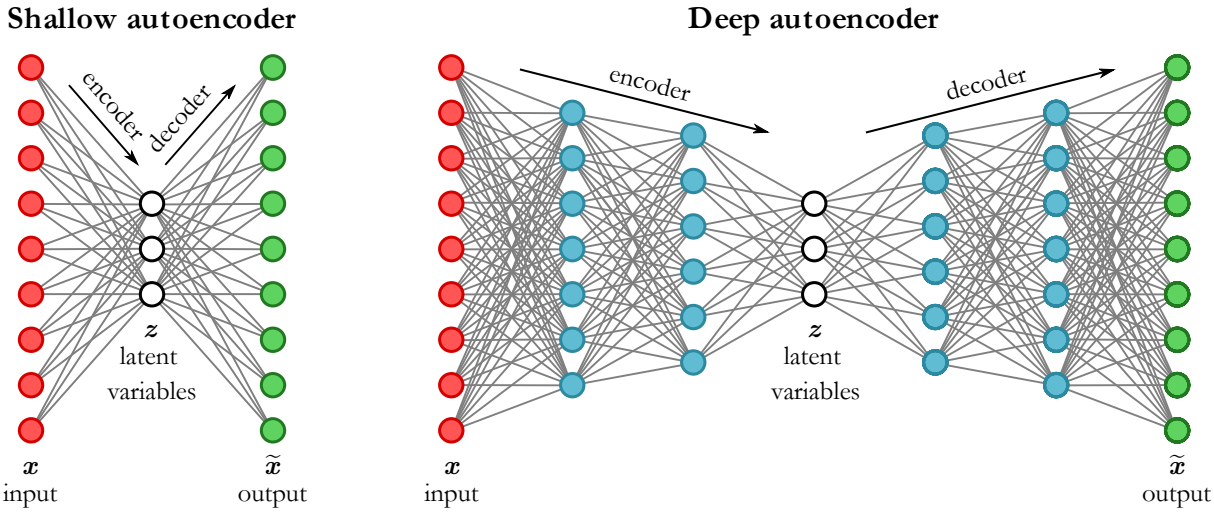

Fig. 6.5: *A sketch of the structure of a shallow autoencoder (left) and a deep autoencoder (right). Both autoencoders are composed of dense layers. These layers are associated with a matrix of weights. This matrix of weights is multiplied by the layer input vector to obtain the layer output vector. In the drawing, which is a common way of depicting neural networks composed of dense layers, columns of circles (neurons) represent vectors, and each connection designated by a gray line represents multiplication of the neuron on the left side by a weight. The value of each neuron is obtained by summing the results of all connections connected from the left and applying an activation function.*

Fukami et al.[124] developed an autoencoder based on convolutional layers instead of dense layers. More importantly, they used a hierarchical architecture that orders the modes in descending order based on their contribution to the output approximation. It tackles the drawback of the basic architecture in Fig. 6.5 that it provides no such information – it needs to be computed after the training by direct computation of a given norm of each mode. Moreover, the hierarchical architecture in fact optimizes each mode one by one, similarly to POD. In contrast, the basic architecture works only with the output approximation. There is no control over the distribution of the input data content among the modes. The authors performed POD of the modes of their convolutional hierarchical autoencoder and showed that a single autoencoder mode represents the content of more than one POD mode.

Another drawback of the basic autoencoder architecture is that since the results are expressed as a function of the data snapshots, it is not possible to directly extrapolate into the future. This is also true for POD and SPOD. DFT allows for extrapolation since the temporal functions are sines and cosines, but, as was already mentioned, it suffers from the periodicity assumption. Obviously, finding models for prediction of the quantities of interest is the most crucial part of reduced-order modelling, whether it is extrapolation into the future, interpolation between states with different boundary conditions, or in general, finding the results for combinations of parameters that are not covered by the input data. There are two ways to do that.

6.3.2 Methods for predicting unknown states

Intrusive modelling

Intrusive modelling relies on knowledge of the governing equations. A standard method in POD-based reduced-order modelling is to project the spatial modes onto the governing partial differential equation using the Galerkin projection to obtain a set of ordinary differential equations for temporal modes that can be written as $\dot{\boldsymbol{a}} = f(\boldsymbol{a})$. Lee and Carlberg have recently proposed a generalization of this method for nonlinear modes that can be obtained using a deep autoencoder[125]. However, Noack et al.[118] showed that the standard Galerkin system is often structurally unstable. They showed that for the laminar Kármán vortex street (periodic vortex shedding behind a cylinder) close to the onset point, it can be stabilized by incorporating a mode they called the shift mode. This mode is defined as the difference between the temporal mean and the unstable steady solution. The resultant model can predict the development of the instability, i.e. how the flow transitions from the unstable steady solution to the periodic vortex shedding. Another difficulty comes into play when the residual of the low-dimensional approximation is not negligible. In that case, the effect of neglected modes needs to be modelled, which is analogous to the closure problem of RANS and LES turbulence modelling[126].

Nonintrusive modelling

Nonintrusive modelling is based purely on the input data. Simply put, the task is to find patterns and capture trends in observations of the system. There are cases for which the data are available, but the governing equations are not known or only partially known, e.g. spreading of diseases or brain activity monitoring. In that situation, nonintrusive modelling is essential. Due to the above-mentioned difficulties with intrusive modelling, nonintrusive modelling is often utilized also in cases with known governing equations. Thanks to the renewed interest in machine learning in recent years, new techniques have started to emerge.

Champion et al.[127] proposed simultaneous training of an autoencoder and a SINDy model for the latent variables $\boldsymbol{z}$. SINDy (Sparse Identification of Nonlinear Dynamics) is a technique proposed by Brunton et al.[128] that resides in finding a set of ODEs in form $\dot{\boldsymbol{z}} = f(\boldsymbol{z})$, where a library of candidate functions is used to express $f(\boldsymbol{z})$ and, most importantly, sparsity is promoted in the objective function, meaning that $f(\boldsymbol{z})$ is expressed by superposition of as few candidate functions as possible.

There are also architectures built on the theory of the Koopman operator[129]. Simply put, they take the current state vector, e.g. $\boldsymbol{z}(t_i)$, and return the future state vector $\boldsymbol{z}(t_{i+1})$. Many approaches revolve around predicting the future evolution of the temporal POD modes $\boldsymbol{a}_i$ or autoencoder

latent variables $\boldsymbol{z}$. When it comes to solving various forecasting problems or series processing in general by neural networks, recurrent architectures are typically used. The most prominent of them, the LSTM (Long Short-Term Memory) network, was used by Hasegawa et al.[130] in combination with a convolutional autoencoder to predict the dynamics of a 2D Kármán vortex street. They trained the autoencoder on data for various Reynolds numbers falling into the laminar regime. After obtaining the latent variables $\boldsymbol{z}$, they used an LSTM network to predict their future behavior. The Reynolds number was included as input, giving the possibility of predicting the behavior for values other than those included in the training set. Performance was various – it depended on how much the patterns changed between the training operating points. Under favorable conditions, the model provided very accurate predictions.

San et al.[131] proposed an architecture of a dense network to advance temporal POD modes over time. They used the values from the previous step, time, and the Reynolds number (their case was dependent on the Reynolds number) as input. Other architectures were proposed by Pawar et al.[132] They used a vector of several latest values of a temporal function as input to predict the output. Two types of output were considered: the next value of the temporal function, and a numerical slope in the present time that can be used to compute the next value. A better performance was reported for the latter output. They also found out that their nonintrusive model substantially outperformed a corresponding intrusive Galerkin model. One of the test cases was the chatotic Lorenz system. Even though the predictions quickly deviated from the ground truth, it was found out that the attractor is preserved. In other words, the mutual relations between the three Lorenz system variables and their statistics are preserved. This behavior is, in fact, nothing more than a manifestation of the inherent sensitivity of chaotic systems to the initial conditions.

6.4 Proposal of methods for quasiperiodic systems

Although all the methods presented so far are applicable to the present case, a different approach will be pursued. It is targeted at the quasiperiodic nature of the most dominant modes. The term quasiperiodicity is defined only loosely. For the purposes of this work, it means that evolution can be described by a periodic function with parameters that may vary in time to some extent. The following expression is assumed

$$g(t) = (a_0 + a'(t))[\sin(2\pi f_0(t + t'(t)) + \varphi_0)] \tag{6.24}$$

This is in fact a sine function with initial phase φ_0, amplitude $a(t) = a_0 + a'(t)$ varying in time, and frequency varying in time as well, which is modelled by admitting fluctuations of time $t'(t)$. If the frequency evolution in time $f(t) = f_0 + f'(t)$ is known, the following relation for $t'(t)$ can be derived

$$t'(t) = \frac{1}{f_0} \int_0^t f'(t)\,\mathrm{d}t \tag{6.25}$$

Now note that the sensitivity of periodic functions to frequency is proportional to time, e.g.

$$\frac{\partial(\sin(2\pi f_0 t))}{\partial f_0} = 2\pi t \cos(2\pi f_0 t) \tag{6.26}$$

Indeed, a little different frequency initially causes only a small distortion, but as the phase shift grows in time, so does the difference between the evolutions. This is especially important when fitting such functions to data. Consider data presenting a sine function with an unknown frequency that shall be found. Assume the following error function

$$\varepsilon(\mathrm{d}f, t) = \frac{1}{t}\int_0^t |\tilde{g}(\mathrm{d}f, t) - g(t)|\mathrm{d}t \tag{6.27}$$

where

$$g(t) = \sin(2\pi f_0 t)\,, \qquad \tilde{g}(\mathrm{d}f, t) = \sin(2\pi(f_0 + \mathrm{d}f)t) \tag{6.28}$$

Here, $\mathrm{d}f$ is the difference between the correct and estimated frequency. The error function for this problem is plotted below in Fig. 6.6, where $T_0 = 1/f_0$ is the period. It is evident that the error function for an infinitesimally small $\mathrm{d}f$ grows monotonically with the integration time. For higher values of $\mathrm{d}f$, it initially grows rapidly and later starts oscillating. These oscillations generate valleys of local minima throughout the domain. Now consider data covering a given time range t/T_0 and an unknown frequency that shall be found. It is evident that the longer the time range, the more accurate the initial guess of the frequency needs to be if fast algorithms based on gradient descent are to be used. Otherwise, they would get stuck in the closest of many local minima along the path towards the correct frequency. Fortunately, for short enough t/T_0, the error function decreases monotonically, meaning that the gradient descent will succeed. Exploiting this fact is the core idea of the algorithm proposed further on.

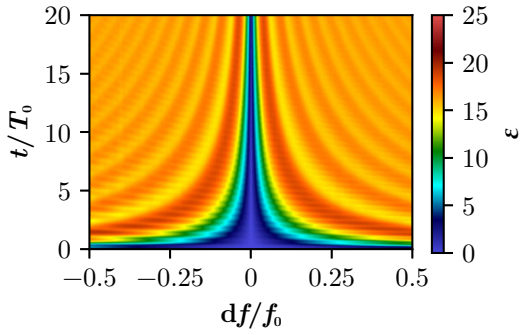

Fig. 6.6: *A plot of the error function defined above.*

6.4.1 A regression method for quasiperiodic functions

In this section, an algorithm for regression of quasiperiodic functions defined above will be proposed. It will be explained by an example. Consider a function in the form (6.24), where $a_0 = 1$, $f_0 = 20$, $\varphi_0 = \pi/4$, and

$$a'(t) = \sum_{i=1}^{3} a_{i(\mathrm{a}')} \sin(2\pi f_{i(\mathrm{a}')} t + \varphi_{i(\mathrm{a}')}) \tag{6.29}$$

$$t'(t) = \sum_{i=1}^{3} a_{i(t')} \sin\left(2\pi f_{i(t')} t + \varphi_{i(t')}\right) \tag{6.30}$$

The values of the remaining constants are given in the table below.

Tab 6.1: *Values of the constants in the function introduced above.*

i	$a_{i(\mathrm{a}')}$	$f_{i(\mathrm{a}')}$	$\varphi_{i(\mathrm{a}')}$	$a_{i(t')}$	$f_{i(t')}$	$\varphi_{i(t')}$
1	0.01	0.8	0	0.015	1	0
2	0.004	0.5	$\pi/2$	0.005	0.5	0
3	0.002	1.8	$\pi/2$	0.002	2	0

Fluctuations of amplitude and time are therefore expressed as a Fourier series with three components. The constants were chosen so that a moderate modulation of the carrier sine function is obtained. The function in the time domain as well as its frequency spectrum for signal length $T = 5$ is plotted below in Fig. 6.7. It turns out that the Fourier transform is misleading in this case since the most dominant peak belongs to $f = 19.2$, while $f_0 = 20$. There are also many other frequencies with nonzero amplitudes on both sides of the most dominant peak. This is caused by the frequency and amplitude modulations since both frequency and amplitude modulation of a carrier signal of frequency f_0 with a modulation signal of frequency f_m result in presence of peaks spaced by f_m on both sides of the carrier frequency f_0.

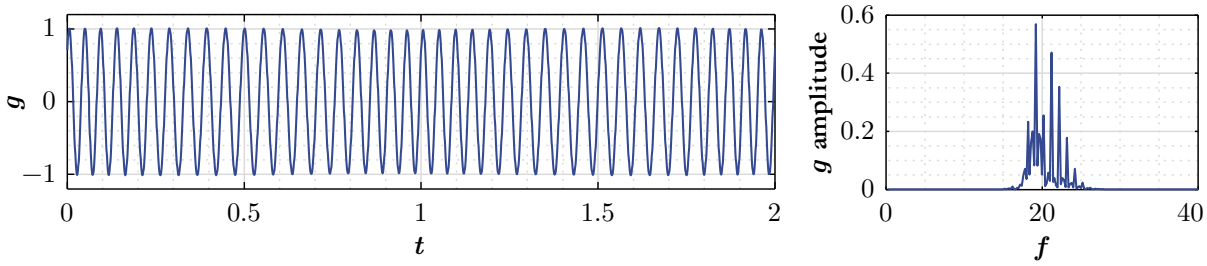

Fig. 6.7: *A plot of the function defined above and its frequency spectrum for signal length* $T = 5$.

A similar situation was observed in the frequency spectra of flow in the present swirl generator. There is no single-frequency peak, but rather a certain range of frequencies with higher amplitudes around a dominant frequency, indicating the presence of frequency and amplitude fluctuations. Identification of these fluctuations is therefore of interest.

Consider a discrete data set covering the given function $g(t)$ from $t = 0$ to $t = 5$. Assume that the data can be expressed in the form given by (6.24), (6.29), (6.30), which is in this case obviously true. The task is to find the constants in the expressions so that the best fit is obtained. As was explained and illustrated in Fig. 6.6, fitting the constants directly by a gradient method requires a very precise initial condition. The following method is proposed to obtain it.

The first step is to perform the discrete Fourier transform of the whole signal to detect the dominant frequency, which is in this case $f = 19.2$. This corresponds to a period of $T = 1/f \cong 0.052$. Then, data covering the first period T only are taken and the best fit of the following sine function is sought

$$\tilde{g}(a, f, \varphi, t) = a \sin(2\pi f t + \varphi) \tag{6.31}$$

where a, f, and φ need to be determined by minimizing a chosen loss function measuring the difference between the original and the fitted signal, e.g. the sum of the squares of the residual. Many minimization methods have been developed, and they are available in common computational packages. In this case, the BFGS algorithm (Boyden-Fletcher-Goldfarb-Shanno algorithm) implemented within the SciPy package for Python was used. As the initial values of a, f, and φ, the values obtained from the Fourier transform were used. As soon as the best-fit values are obtained, a new value of the period is computed from the best-fitting frequency, and then the subsequent period is extracted. The process is repeated until all the data is processed. The reason for learning period by period is that the time range needs to be short enough to ensure convergence of gradient-based methods as was shown in Fig. 6.6. At the same time, it needs to be long enough for the problem to be well posed. One period is to this end considered a suitable choice.

After fitting, the initial values of f_0 and a_0 are computed as the temporal mean of f and a, respectively. The initial phase φ_0 is the phase of the first period. Then, the fluctuating parts $f'(t)$ and $a'(t)$ are computed. By converting $f'(t)$ to $t'(t)$ using (6.25) and applying the Fourier transform to it and $a'(t)$, we can determine the initial values of the constants in (6.29), (6.30). Since the sampling is generally nonuniform and the time steps are rather high, it is reasonable to resample the data beforehand to a finer uniform sampling by a suitable method. In this case, a method based on cubic spline interpolation was used. The results of learning after resampling are plotted in Fig. 6.8. The learned evolutions agree with the true evolution almost perfectly. Also, the error in the mean values f_0 and a_0 is negligible.

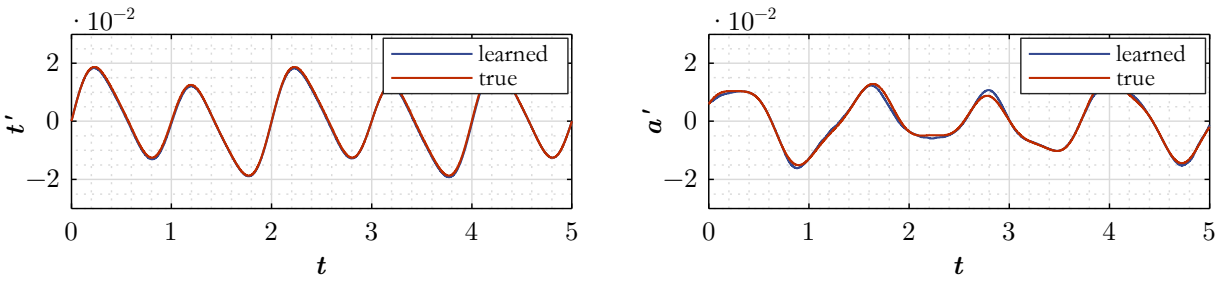

Fig. 6.8: *Plots of the true and learned fluctuations of time and amplitude.*

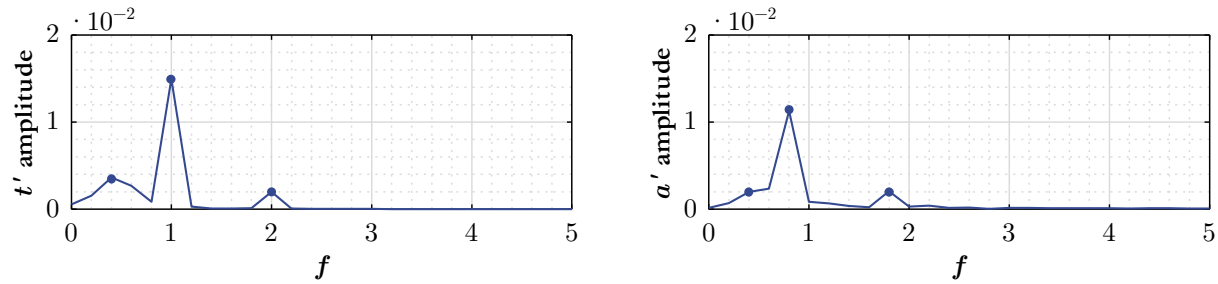

Fig. 6.9: *Plots of the frequency spectra of the learned fluctuations in time and amplitude. The designated points will be used as the initial condition in subsequent learning.*

The results of the Fourier transform are presented in Fig. 6.9. Three most significant points will be used as the initial values of the constants in (6.29), (6.30). The algorithm resides in seeking the maximal amplitude and checking if the detected point is not too close to an already chosen point. In this case, points adjacent to already chosen points were disqualified in order to avoid unpleasant consequences of the spectral leakage problem. The resulting points are designated in the graphs.

By comparing them with the true values in Tab. 6.1, we see that the values for $i = 1$ and 3 agree almost perfectly, whereas the last point, where the true $f = 0.5$ for both time and amplitude fluctuations, is subject to the spectral leakage problem. As a consequence, the initial frequency is different (0.4), the initial amplitude is lower, and the initial phase is very different. It is noted that these initial values can be improved by machine learning at the cost of a longer computing time. Knowing the initial values of all the constants, it is possible to evaluate the initial condition for the final regression of (6.24), (6.29), and (6.30). It is plotted against the true evolution in Fig. 6.10 (left). Only a slight frequency shift is visible.

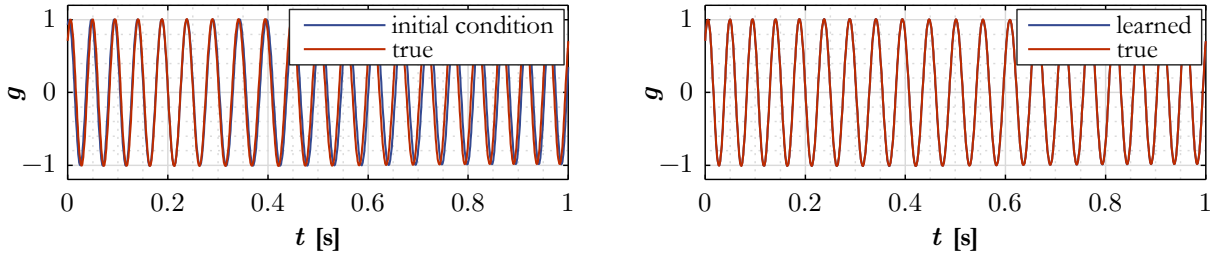

Fig. 6.10: *Left: initial condition for the final fitting in comparison with the true evolution, right: the final result in comparison with the true evolution.*

After the final regression, the evolution obtained agrees with the ground truth almost perfectly. By comparing the constants with the true values, it was found out that only one of the less significant components of $a'(t)$ is different (namely that with $f = 0.5$, where the learned value is 0.424, the amplitude is slightly lower, and the phase is different). The error in the remaining constants is within the desired precision. It is possible that exact results can be obtained with a different minimization algorithm. However, reaching exact results is beyond the scope of this work. For the present purpose, the results obtained are considered satisfactory.

6.4.2 NN architecture for spatio-temporal decomposition of quasiperiodic systems

In this section, a neural network architecture for spatio-temporal decomposition suitable for quasiperiodic systems will be proposed. The decomposition is assumed in linear form (6.1), and the temporal functions are by construction in the following form

$$a_{\sin}(t) = (a_{0(\sin)} + a'(t)) \sin\big(2\pi f_0 (t + t'(t))\big) \tag{6.32}$$

$$a_{\cos}(t) = (a_{0(\cos)} + a'(t)) \cos\big(2\pi f_0 (t + t'(t))\big) \tag{6.33}$$

$$a'(t) = \sum_{i=1}^{m} a_{i(\mathrm{a}')} \sin\big(2\pi f_{i(\mathrm{a}')} t + \varphi_{i(\mathrm{a}')}\big) \tag{6.34}$$

$$t'(t) = \sum_{i=1}^{m} a_{i(t')} \sin\big(2\pi f_{i(t')} t + \varphi_{i(t')}\big) \tag{6.35}$$

The architecture is sketched in Fig. 6.11. Its input is time. Two dense layers are connected to the input. Their kernels corresponds to $2\pi f_{i(t')}$ and $2\pi f_{i(a')}$, and their biases correspond to $\varphi_{i(t')}$ and $\varphi_{i(a')}$. Sine is used as the activation function. The outputs are clearly harmonic functions with

different frequencies and phase shifts. An alternative way is to use sine and cosine functions with the same frequency and different amplitudes instead of phase shifts. In the subsequent layers, only kernels are trainable; biases are set to zero. Thanks to that, the kernels act as $a_{i(t')}$ and $a_{i(a')}$, and the layers perform summation of the harmonic components so that $t'(t)$ and $a'(t)$ are obtained at the output. A dense layer with a single neuron, where the kernel is set to one and the bias is set to zero, is then applied to t and $t'(t)$ in order to obtain their sum. Similarly, another dense layer with a single neuron, where the kernel is set to one and the bias is trainable and corresponds to $a_{0(\sin)}$, is applied to $a'(t)$ to obtain $a_{0(\sin)} + a'(t)$. Another layer with the same setting produces $a_{0(\cos)} + a'(t)$. Two more dense layers in the same fashion follow, leading to the final form of the sine and cosine temporal modes. The output dense layer produces an approximation of the snapshot from time t. Its kernel weights correspond to the spatial modes $\boldsymbol{\phi}_{i(\sin)}$ and $\boldsymbol{\phi}_{i(\cos)}$, bias is set to zero.

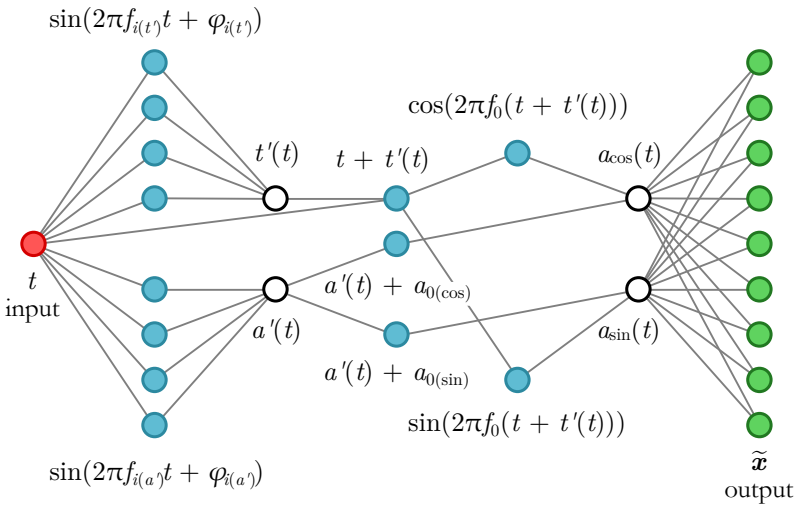

Fig. 6.11: *The proposed neural network architecture for finding quasiperiodic modes.*

Note that only dense layers were used in the network. The reason for that is that setting up this network in software is in this case easy since dense layers are commonly available. Obviously, the architecture could be simplified by introducing custom layers programmed for this purpose.

Initial values of $a_{0(\sin)}$, $a_{0(\cos)}$, f_0, $\boldsymbol{\phi}_{i(\sin)}$, and $\boldsymbol{\phi}_{i(\cos)}$ can be determined by the discrete Fourier transform described in section 6.1.2. Initial frequencies of the components of time and amplitude fluctuations should cover the desired range uniformly. Amplitudes and phases can be initialized randomly, provided that the values are not too large. Determining a suitable number of components (m) is another task that needs to be solved, the so-called hyperparameter optimization. It requires some experimentation to find a suitable setting.

It should be noted that using architectures of neural networks based on the Fourier series is not a new idea. Lange et al.[133] proposed a similar architecture. However, their method is restricted to periodic time series. The neural network presented herein is more complex. It produces a pair of modes with a quasiperiodic temporal function, and it is meant to address the disadvantage of SPOD that there is no closed form of the temporal modes. The architecture allows straightforward extrapolation into the future, i.e. it is itself a nonintrusive reduced-order model. As soon as the first pair of modes is trained, it is subtracted from the data, and the second pair of modes can be trained from the residual. This procedure is repeated until the residual is sufficiently reduced. In the end,

we obtain a hierarchical set of mode pairs. A test was performed on the present CFD data to check the viability of this method. However, a more thorough study is still needed. It should address questions regarding the dependence of the results on initial conditions and required parameters for successful training (sampling in time, batch size). This is left for future work.

6.5 Reduced-order model of the present flow with a vortex rope

The method presented in section 6.4.1 will now be applied to the present case with a vortex rope. The idea is to use the spatial POD modes from the simulation with transient boundary conditions covering a range of operating conditions with a well-developed vortex rope (SBES-T-1, Fig. 6.3). By projecting these modes onto the data from simulations with fixed boundary conditions (SBES-F-5-50-50, SBES-F-5-60-40, SBES-F-5-70-30), we obtain temporal functions valid for each regime. The final step is the application of the proposed method to obtain closed-form expressions of these temporal functions. These expressions can be readily extrapolated in time up to infinity. Moreover, by interpolating the dependence of the parameters on the operating point, we obtain a reduced-order model for a wider range of operating conditions.

Let's now walk through the procedure. The projection step reads for $i \geq 2$

$$a_i(t_j) = (\boldsymbol{\phi}_i, \hat{\boldsymbol{p}}_j - \boldsymbol{\phi}_0 - \boldsymbol{\phi}_1(\boldsymbol{\phi}_1, \hat{\boldsymbol{p}}_j - \boldsymbol{\phi}_0)_V)_V \tag{6.36}$$

where $\boldsymbol{\phi}_i$ is the i-th POD mode from the simulation with transient boundary conditions, $\hat{\boldsymbol{p}}_j$ is the j-th snapshot of the dimensionless pressure from the respective simulation with fixed boundary conditions, $\boldsymbol{\phi}_0$ is the mean field from the simulation with transient boundary conditions, $\boldsymbol{\phi}_1$ is the first mode (the slow dynamics), and $(\boldsymbol{\phi}_1, \hat{\boldsymbol{p}}_j - \boldsymbol{\phi}_0)_V$ is in fact $a_1(t_j)$. Note that the mean-field and slow dynamics are subtracted from the data snapshot. This is because these modes are not orthogonal; the orthogonality property (6.8) holds only for modes with $i \geq 2$.

As soon as all the temporal functions were obtained, the method for identification of quasiperiodic functions was applied to modes with $i \geq 2$. A total of five Fourier components were considered for the fluctuations of amplitude and time given by (6.29), (6.30). The temporal function of the first mode (a_1) was assumed constant. It is defined as the mean value of the discrete values $\boldsymbol{a}_1$. The following constraints and measures were considered for the remaining modes.

- For the paired modes (2 and 3, 5 and 6, 7 and 8, 10 and 11), the difference between the values of the initial phase shift φ_0 has to be either $\pi/2$ or $-\pi/2$. This comes from the observation of the POD temporal functions. The paired modes together model a travelling wave (the precessing motion of the vortex rope), and maintaining proper phase shift is therefore essential. Moreover, all the frequencies and phase shifts in the expressions of the fluctuations of time and amplitude (6.29), (6.30) are shared, and all the amplitudes of the second mode are enforced to be multiples of the amplitudes of the first mode.
- For the mode pair 2 and 3 and its first superharmonic pair 10 and 11, it was enforced that the base frequency f_0 of the latter pair is twice the frequency of the first pair.
- The loss function for the final fitting was defined as

$$\mathcal{L} = \frac{\sum_{j=1}^{M} \left(\tilde{a}_i(t_j) - a_i(t_j)\right)^2}{\sum_{j=1}^{M} a_i(t_j)^2} + \frac{\sum \left(\mathcal{F}\left(\tilde{a}_i(t \in \langle t_{10M}, t_{11M}\rangle)\right) - \mathcal{F}(a_i)\right)^2}{\sum \mathcal{F}(a_i)^2} \tag{6.37}$$

where $\tilde{a}_i(t_j)$ is the prediction of $a_i(t_j)$ found by machine learning, $\mathcal{F}$ denotes the Fourier transform, and $\tilde{a}_i(t \in \langle t_{10M}, t_{11M}\rangle)$ is the prediction evaluated for the denoted time interval. This condition in fact states that the predicted evolution must fit the training data well, and at the same time the Fourier transform of the predicted evolution on an interval far beyond the reach of the training data must agree with the Fourier transform of the training data. For comparability, the length of the time interval and the sampling step must agree. The purpose of the Fourier part is to prevent overfitting. Without it, it was observed that the model overfits the training data, and the evolution beyond the training interval quickly deteriorated if the evolution of the training data was rather complex. In the present case, this measure provided satisfactory results.

- The base amplitude a_0 was set untrainable for the final fitting, i.e. the initial value determined in the first phase was retained. This is also to prevent overfitting since for more complex evolutions, it was observed that the model tended to decrease a_0 significantly and fit the evolutions by excessive fluctuations.
- In the initial phase, when the signal is processed period by period and the best fitting sine function is sought, problems were encountered for more complex evolutions. Therefore, if the frequency of the fitted function for the current period differed significantly from the value for the previous period, the new values were ignored and the values from the previous period were assigned instead. The limit difference was set to 30% of the original value. It shall be noted that the mentioned more complex evolutions were far beyond what can be considered a reasonable quasiperiodic evolution amenable to the present method. Various other measures can be proposed to treat these situations.
- The evolutions of the fluctuations of time identified in the first phase had generally a nonzero mean. Therefore, the mean was subtracted and translated into a phase shift

$$\Delta\varphi_0 = \overline{t'} 2\pi f_0 \tag{6.38}$$

where $\overline{t'}$ is the mean value for the training interval. This phase shift was subsequently added to the initial value of φ_0. Without this measure, zero frequency was often identified by the Fourier transform as the most dominant, which consequently led in the final phase to incorrect low frequencies with a high amplitude that caused significant distortions outside the training interval.

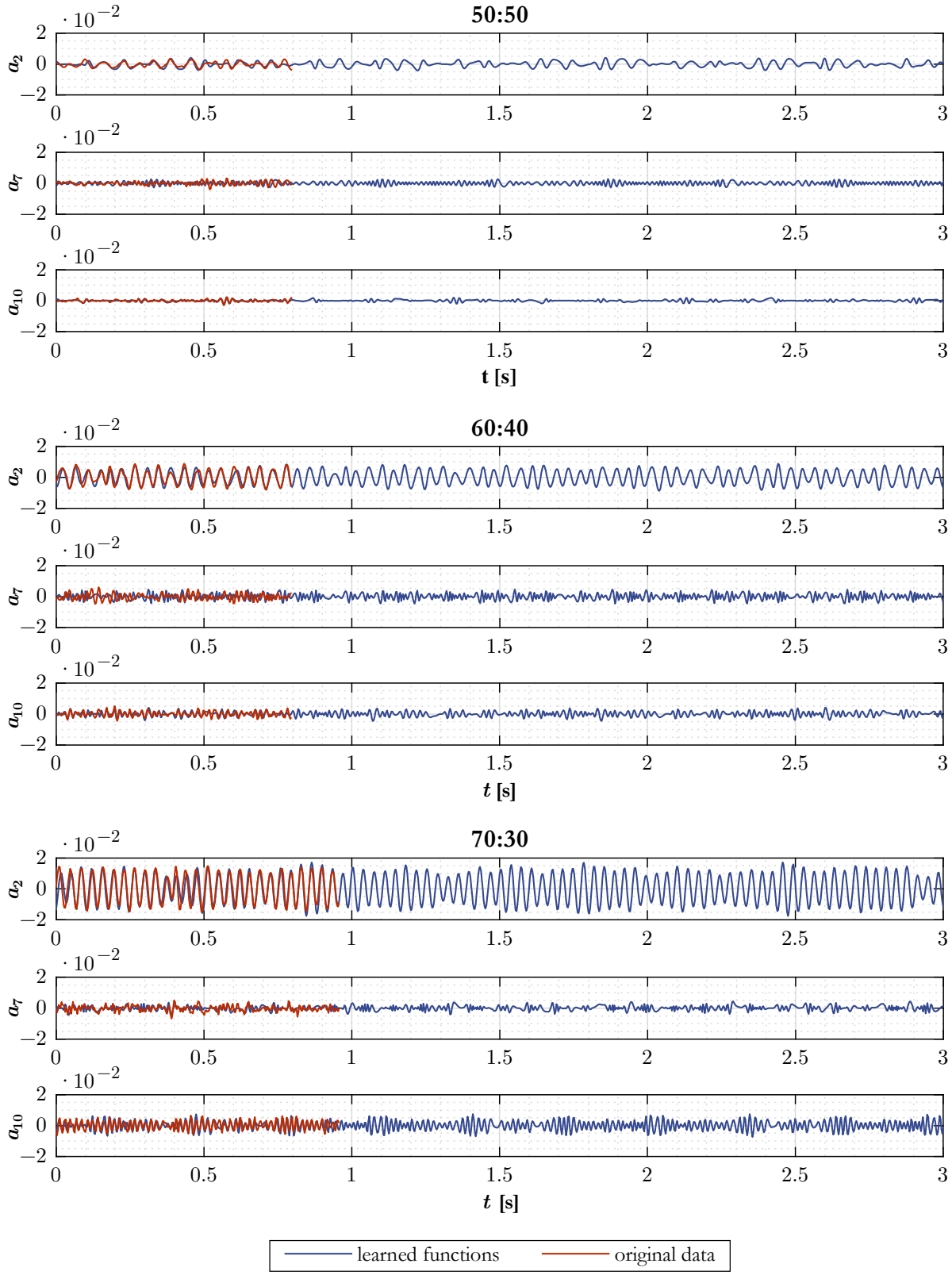

Fig. 6.12: *Original data and learned evolutions of chosen temporal modes of the dimensionless pressure for different operating points.*

The resultant temporal functions a_2, a_7, and a_{10} are plotted for $t \in \langle 0,3 \rangle$ in Fig. 6.12. It can be observed that the best results were achieved for modes a_2 and a_{10} for the last two regimes, where the quasiperiodicity assumption is justified. On the contrary, mode a_7 has complicated evolutions that are far from periodic. There is a significant discrepancy between the model and the training data; however, the model has learned some of the patterns that can be seen in the training data and repeats them along the way.

Reconstructions of the dimensionless pressure field are presented in Fig. 6.13. Three snapshots from the training range are compared against the original data, and three predictions of future states are also given to check whether the vortex rope shapes look reasonably. It turned out that most of the reconstructions look credible. Only the snapshots for $t = 0.6$ s and $t = 3$ s for the flow rates ratio of 60:40 exhibit certain phase mismatch between the modes modelling the tail and the upper vortex. Uncoupled nature is therefore the weakest aspect of the present model.

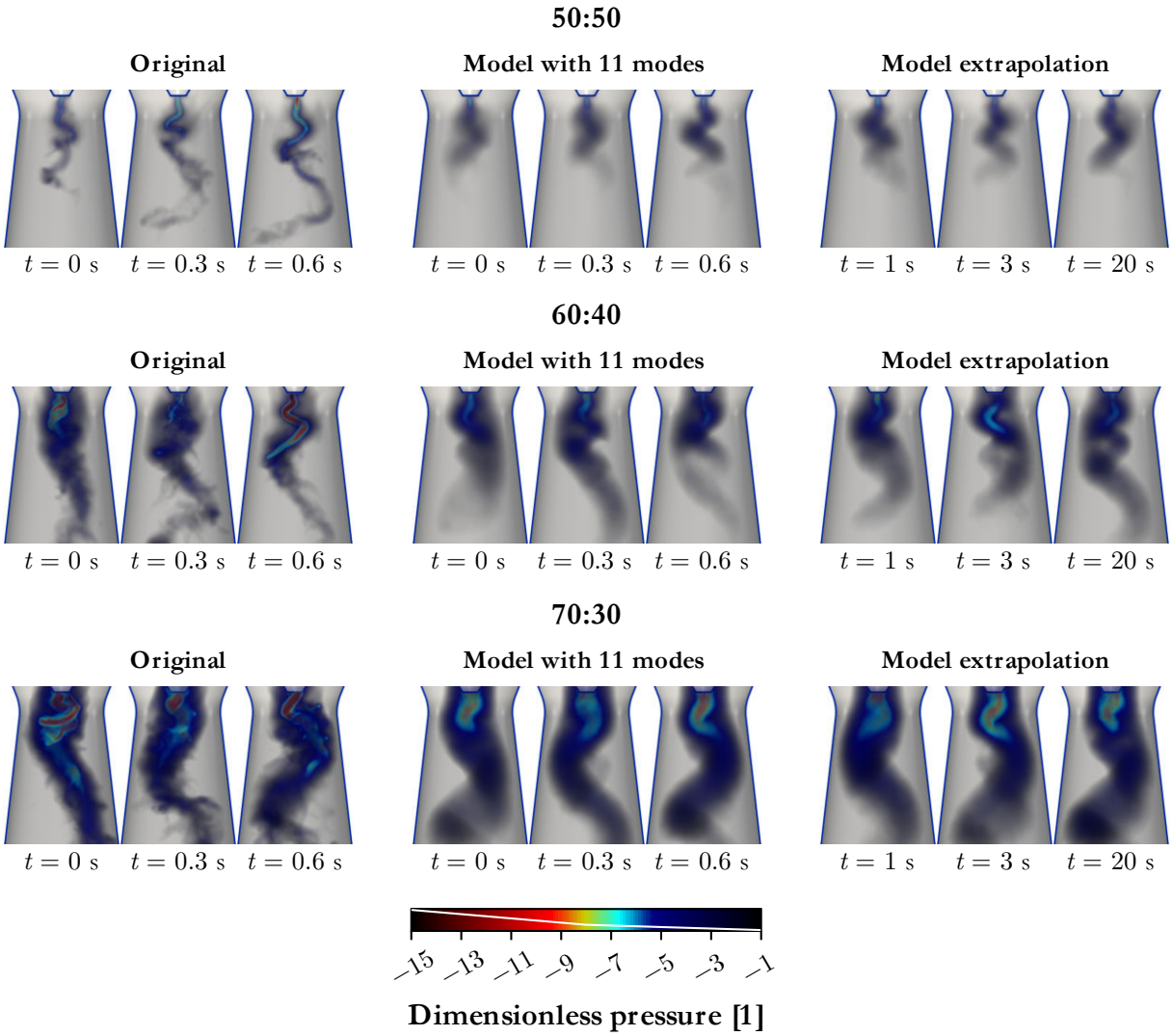

Fig. 6.13: *Three original snapshots, their approximations from* 11 *modes identified by machine learning, and extrapolations of the model to the future.*

It is also no surprise that these issues are pronounced for the flow rates ratio of 60:40. It lies on the border between different vortex rope regimes – the thin vortex rope observed for lower swirl intensity, and the large structure with mostly twin vortex ropes under the hub tip observed for higher swirl intensity. Irregular switching between these regimes was observed, which explains why all the modes are similarly important and bring a comparable contribution to the overall accuracy as can be observed in Fig. 6.3. It may be summarized that the predictions are credible if the vortex rope shape is well established.

One of the main outcomes of the model is the identification of the evolution of frequency in time. Since fluctuations of time were considered in the model, the frequency must be computed as follows

$$f(t) = f_0 \left(1 + \frac{\mathrm{d}t'(t)}{\mathrm{d}t}\right) \tag{6.39}$$

The results for the most dominant precession mode (a_2) are plotted in Fig. 6.14. It is evident that significant fluctuations were identified for the flow rates ratio of 50:50. As the swirl intensity increases, it can be seen in Fig. 6.12 that the amplitude increases and the shape of the function gets closer to sinusoidal. We can now observe that this goes hand in hand with a decrease in frequency fluctuations. However, they cannot be neglected even in the last regime, when their peak values reach 8% of the base frequency f_0.

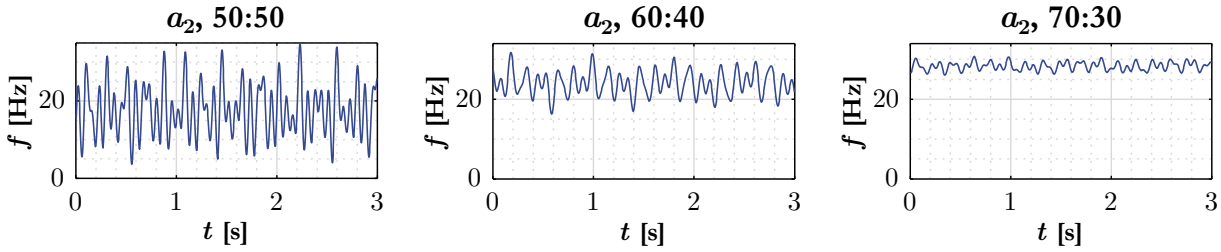

Fig. 6.14: *Dependence of frequency on time and the flow rates ratio for mode* a_2.

The last step in the development of the reduced-order model is interpolating or approximating the dependence of the parameters on the operating points. Since only three points were available in this case, an interpolation by a quadratic function was performed. The evolutions of the base frequencies and amplitudes are depicted in Fig. 6.15. Knowing the dependence of the parameters on the operating point, it was possible to perform reconstructions of the dimensionless pressure fields for operating points covering the range of the flow rates ratio from 50:50 to 70:30. The results are depicted in Fig. 6.16. The value of time t was set to 1 s. It can be seen that the transition is not monotonous. Various forms can be observed on the way from the small weak vortex rope at the beginning to the large strong vortex rope at the end, which agrees with the observations of the transient process in the results of the simulation with transient boundary conditions (SBES-T-1).

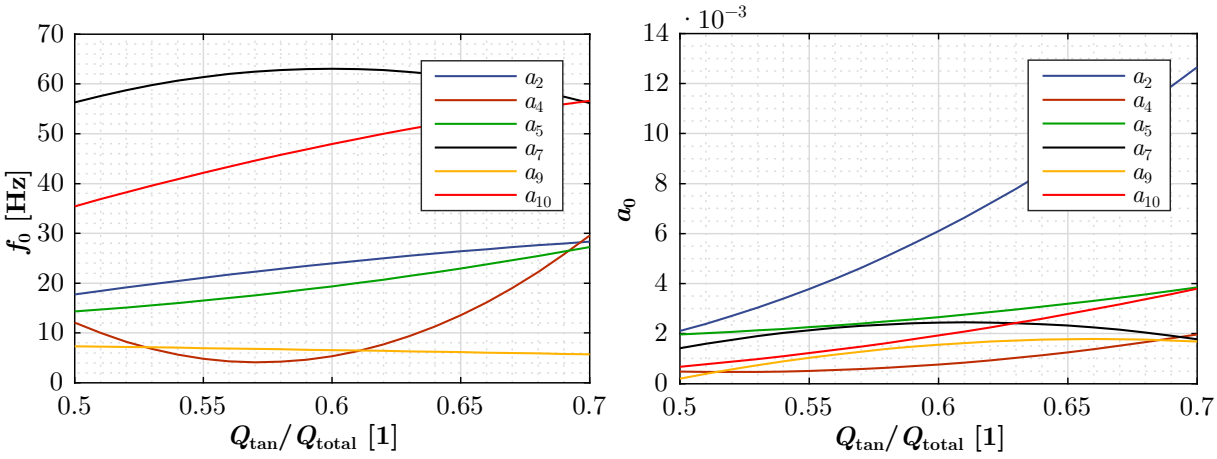

Fig. 6.15: *Dependence of the base frequency f_0 and amplitude a_0 of POD modes on the flow rates ratio obtained by interpolating the three known values by a quadratic function.*

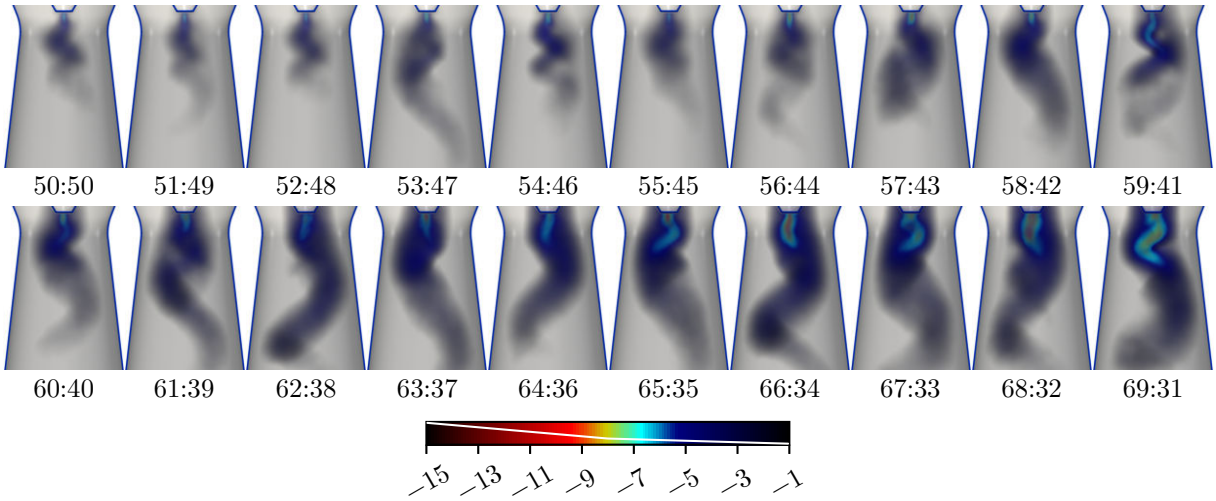

Fig. 6.16: *Reconstructions of the dimensionless pressure field for the same time instant and various flow rates ratios listed below each picture.*

Conclusions and suggestions for future research

The present work dealt with the vortex rope phenomenon. It is a comprehensive study that describes the whole process from designing a new swirl generator through CFD study of the flow to proposing reduced-ordel modelling methods. It resulted in many findings, which will now be summarized. Also, several ideas were given but not elaborated within this work. They are therefore left as suggestions for future research.

The newly designed swirl generator fills the gap between precise but expensive devices and cheap devices without any regulation of the swirl intensity. It is based on mixing two inflows. It brings a drawback of nonuniform unsteady velocity profiles at the diffuser inlet, which complicates analyses of the resultant flow. On the other hand, it presents a good challenge to propose flow control methods to mitigate the vortex rope since only methods robust to these imperfections can succeed. The insertion of a blade ring into the spiral case to improve the conditions at the diffuser inlet is considered for future work.

Many CFD simulations with the SBES model of turbulence have been performed. This model uses RANS equations in both inlet pipes and LES equations in the spiral case and further downstream. The CFD results were verified by comparison with the PIV measurements. The evolution of the vortex rope with increasing swirl intensity was thoroughly studied. For this purpose, visualization methods based on volume rendering have been devised, and many criteria for the detection of vortical structures have been tested. Some less common methods were also included. Applications of these methods in the field of hydraulic machinery are lacking. Two of the methods, the M_Z vortex criterion and the Finite-time Lyapunov exponent, are related to the flow field topology and could be beneficial in theoretical studies of the flow field. The last method, the residual vorticity, was found to provide the best results in vortex identification and therefore became the method of choice in this work.

A brief study of both active and passive methods to mitigate the vortex rope has also been carried out. A cautionary outcome is that if water jet injection through the hub tip is applied, the jet may start rotating around the diffuser axis due to the circumferential velocity of the outer swirling flow, eventually causing stronger pressure pulsations than uncontrolled vortex rope itself. Better results were obtained when the water jet injection was replaced by suction at the bottom, yet they are not very satisfactory. A combination of these methods also did not perform well. The best results were achieved for water jet injection through a greater cross section. It suggests that a sufficiently high diameter of the jet is needed to prevent the mentioned undesired behavior. Unfortunately, the method is still energetically costly. Several passive methods were studied using a different swirl generator. It turned out that fins of proper size and position may stabilize the flow downstream. However, vortical structures persist upstream and exert an unsteady load on the fins. Therefore, it may be reasonable to use an active flow control method to suppress these vortices. The required power is expected to be lower since these vortices are weaker than the entire uncontrolled vortex rope. Finding an optimized flow control method is generally a very challenging task since it depends on many parameters. It is even more difficult if closed-loop control is pursued (the present methods are all open-loop – no feedback is involved). To this end, methods based on reinforcement learning seem promising. An appealing application to a Kármán vortex street has recently been published by Rabault[134].

The last part was dedicated to reduced-order modelling. Three decomposition techniques were considered, abbreviated POD, DFT, and SPOD. These techniques provide spatial mode shapes and corresponding temporal functions for the time range covered by the data from simulations.

The task of reduced-order modelling is to find models that enable extrapolation in time and interpolation between the operating points. In this work, a nonintrusive technique aimed at the identification of quasiperiodic patterns in the temporal functions has been proposed. It resides in choosing a suitable expression for the temporal functions and finding the parameters by machine learning. This task is complicated by the fact that the loss function is oscillatory; therefore, fast algorithms based on gradient descent need a good initial condition in order to avoid getting stuck in an unfavorable local minimum. Therefore, a method for determining a good initial condition has been proposed. It works well for functions satisfying the quasiperiodicity assumptions. For more complex functions, the performance is obviously poorer, and the model gets prone to overfitting.

In the present case, it turned out that the quasiperiodicity assumptions hold well for the most dominant mode pair at operating points with a higher swirl intensity. This mode pair is related to the precessing motion of the vortex rope tail. In fact, the spatial modes correspond to its mean shape. The model can be used to quantify variations in frequency and amplitude of pressure pulsations caused by this leading-mode pair. Interpolation between operating points led to credible results, i.e. the model is able to capture the trend.

The temporal functions of other modes were far from the quasiperiodicity assumptions. Several measures for aiding the model generalizability were used, including matching the frequency spectra after extrapolation to the future with those of the training data within the loss function and enforcing known phase shifts for the paired modes. Still, the model works more as a generator of functions that satisfy these constraints rather than reliably identifying trends in the data. Nevertheless, reconstructions of the pressure field look good. The patterns observed in the training data are preserved; only sometimes a phase mismatch can be observed between parts of the vortex rope. Improvements might be achieved by considering a nonlinear decomposition instead of a linear one. The goal is to find a representation for which the dynamics are simpler. The mutual relations between the modes should also be taken into account. This task has become the subject of many research efforts, especially in fields where no governing equations are available and finding trends in the data is the only way of predicting yet unknown states.

Reduced-order models of the vortex rope like the present one may be applied, for example, in connection with 1D models to predict propagation of pressure pulsations throughout the whole hydraulic conduit. For the cases with a higher swirl intensity where a strong vortex rope occurs, it was shown that the whole most dominant peak in the frequency spectrum can be expressed as a single mode pair. Its superharmonics are another mode pairs. The main advantage of the reduced-order model is that it runs orders of magnitude faster than full-order CFD simulations, thereby significantly speeding up computations where applicable. For these purposes, future work should be aimed at decomposing the pulsations into synchronous and asynchronous parts. The reason for this is that the synchronous part corresponds to pulsations that occur for the whole circumference or cross section (depending on the target dimensionality), not only locally. It is these pulsations that propagate further on through the conduit. For axisymmetric geometries, the synchronous part can be obtained by taking the circumferential average, leading to a 2D field, or by taking the cross-sectional average, leading to a 1D field. Further decomposition (e.g. by POD) should then be applied to these parts separately.

Another possible application of reduced-order models is in the field of digital twins. For water turbines, such reduced-order models can provide a real-time estimate of quantities that cannot be measured directly during operation. For example, the history of the load acting on various parts may be helpful in determining the date of the next maintenance.

References

[1] GOYAL, R., M. J. CERVANTES, and B. K. GANDHI. Vortex Rope Formation in a High Head Model Francis Turbine. *Journal of Fluids Engineering*. 2017, **139**(4), 041102. DOI: 10.1115/1.4035224. ISSN 0098-2202.

[2] SUSAN-RESIGA, R. and S. MUNTEAN. Decelerated Swirling Flow Control in the Discharge Cone of Francis Turbines. *Fluid Machinery and Fluid Mechanics*. Berlin: Springer, 2009, 89–96. DOI: 10.1007/978-3-540-89749-1_12. ISBN 978-3-540-89748-4.

[3] ESCUDIER, M. Vortex breakdown: Observations and explanations. *Progress in Aerospace Sciences*. 1988, **25**(2), 189–229. DOI: 10.1016/0376-0421(88)90007-3. ISSN 0376-0421.

[4] LUCCA-NEGRO, O. and T. O'DOHERTY. Vortex breakdown: a review. *Progress in Energy and Combustion Science*. 2001, **27**(4), 431–481. DOI: 10.1016/S0360-1285(00)00022-8. ISSN 0360-1285.

[5] HALL, M. G. Vortex Breakdown. *Annual Review of Fluid Mechanics*. 1972, **4**(1), 195–218. DOI: 10.1146/annurev.fl.04.010172.001211. ISSN 0066-4189.

[6] LUNDA, F. *Rozpad víru*. Brno, 2019. Bachelor's thesis. Brno University of Technology. Supervisor O. Urban.

[7] HALL, M. G. The structure of concentrated vortex cores. *Progress in Aerospace Sciences*. 1966, **7**, 53–110. DOI: 10.1016/0376-0421(66)90006-6. ISSN 0376-0421.

[8] SQUIRE, H. B. Analysis of the vortex breakdown phenomenon: Part 1. London, 1960. Research report. Imperial College of Science and Technology.

[9] BENJAMIN, T. B. Theory of the vortex breakdown phenomenon. *Journal of Fluid Mechanics*. 1962, **14**(04), 593–629. DOI: 10.1017/S0022112062001482. ISSN 0022-1120.

[10] SUSAN-RESIGA, R., G. D. CIOCAN, I. ANTON, and F. AVELLAN. Analysis of the Swirling Flow Downstream a Francis Turbine Runner. *Journal of Fluids Engineering*. 2006, **128**(1), 177–189. DOI: 10.1115/1.2137341. ISSN 0098-2202.

[11] XUNGANG, S. and S. XIAOWEN. Relation between the quasi-cylindrical approximation and the critical classification for swirling flow. *Acta Mechanica Sinica*. 1987, **3**(4), 304–314. DOI: 10.1007/BF02486816. ISSN 0567-7718.

[12] PASCHE, S., F. AVELLAN, and F. GALLAIRE. Part Load Vortex Rope as a Global Unstable Mode. *Journal of Fluids Engineering*. 2017, **139**(5), 051102. DOI: 10.1115/1.4035640. ISSN 0098-2202.

[13] NISHI, M and S LIU. An Outlook on the Draft-Tube-Surge Study. *International Journal of Fluid Machinery and Systems*. 2013, **6**(1), 33–48. DOI: 10.5293/IJFMS.2013.6.1.033. ISSN 1882-9554.

[14] NISHI, M., T. KUBOTA, S. MATSUNAGA, and Y. SENOO. Study on Swirl Flow and Surge in an Elbow Type Draft Tube. *IAHR/AIRH 10th Symposium 10E, Hydraulic Machinery and Equipment Associated with Energy Systems in the New Decade of the 1980's*. Tokio, 1980.

[15] FOROUTAN, H. and S. YAVUZKURT. Analysis and Prevention of Vortex Rope Formation in the Draft Tube Cone of a Hydraulic Turbine. *ASME 2012 International Mechanical Engineering Congress and Exposition*. 2012, **7**, 2167–2177. DOI: 10.1115/IMECE2012-86224. ISBN 978-0-7918-4523-3.

[16] NISHI, M., S. MATSUNAGA, T. KUBOTA, and Y. SENOO. Flow Regimes in an Elbow-Type Draft Tube. *Proceedings of 11th IAHR Symposium on Hydraulic Machinery and Systems*. Amsterdam, 1982.

[17] NISHI, M., S. MATSUNAGA, Y. SENOO, and T. KUBOTA. Effect of Draft Tube Shape on the Characteristics of Pressure Surge and Swirl Flow. *Proceedings of 13th IAHR Symposium on Hydraulic Machinery and Systems*. Montreal, 1986.

[18] JACOB, T. *Evaluation on a scale model and prediction of the stability of operation of Francis turbines*. Laussane, 1993. Doctoral thesis. EPFL Laussane. Supervisor P. Henry.

[19] RHEINGANS, W. J. Power swings in hydroelectric power plants. *Transactions of the ASME*. 1940, **62**, 171–184.

[20] SKOTÁK, A. *Vírové struktury v savce vodní turbíny*. Brno, 2004. Doctoral thesis. Brno University of Technology. Supervisor F. Pochylý

[21] WAHL, T. L. Draft Tube Surging Times Two: The Twin Vortex Phenomenon. *HydroReview*. 1994, **13**, 60–69. ISSN 0884-0385.

[22] CASSIDY, J. J. and H. T. FALVEY. Observations of unsteady flow arising after vortex breakdown. *Journal of Fluid Mechanics*. 1970, **41**(4), 727–736. DOI: 10.1017/S0022112070000873. ISSN 0022-1120.

[23] FAVREL, A., J. G. PEREIRA JUNIOR, C. LANDRY, A. MÜLLER, C. NICOLET, and F. AVELLAN. New insight in Francis turbine cavitation vortex rope: role of the runner outlet flow swirl number. *Journal of Hydraulic Research*. 2017, **56**(3), 367–379. DOI: 10.1080/00221686.2017.1356758. ISSN 0022-1686.

[24] CALA, C. E., E. C. FERNANDES, M. V. HEITOR, and S. I. SHTORK. Coherent structures in unsteady swirling jet flow. *Experiments in Fluids*. 2006, **40**(2), 267–276. DOI: 10.1007/s00348-005-0066-9. ISSN 0723-4864.

[25] CHENG, H., L. ZHOU, Q. LIANG, Z. GUAN, D. LIU, Z. WANG, and W KANG. A method of evaluating the vortex rope strength in draft tube of Francis turbine. *Renewable Energy*. 2020, **152**, 770–780. DOI: 10.1016/j.renene.2020.01.020. ISSN 0960-1481.

[26] HOUDE, S., M. S. ILIESCU, R. FRASER, S. LEMAY, G. D. CIOCAN, and C. DESCHÊNES. Experimental and Numerical Analysis of the Cavitating Part Load Vortex Dynamics of Low-Head Hydraulic Turbines. *ASME-JSME-KSME 2011 Joint Fluids Engineering Conference: Volume 2, Fora*. ASMEDC, 2011, 171–182. DOI: 10.1115/AJK2011-33006. ISBN 978-0-7918-4441-0.

[27] DÖRFLER, P. K., M. SICK, and A. COUTU. *Flow-Induced Pulsation and Vibration in Hydroelectric Machinery: Engineer's Guidebook for Planning, Design and Troubleshooting*. London: Springer, 2013. ISBN 978-1-4471-4251-5.

[28] JOŠT, D and A. LIPEJ. Numerical prediction of the vortex rope in the draft tube. *3rd IAHR International Meeting of the Workgroup on Cavitation and Dynamic Problems in Hydraulic Machinery and Systems*. Brno, 2009.

[29] ZHANG, R. K., F. MAO, J. Z. WU, S. Y. CHEN, Y. L. WU, and S. H. LIU. Characteristics and Control of the Draft-Tube Flow in Part-Load Francis Turbine. *Journal of Fluids Engineering*. 2009, **131**(2), 021101. DOI: 10.1115/1.3002318. ISSN 0098-2202.

[30] RUPRECHT, A., T. HELMRICH, T. ASCHENBRENNER, and T. SCHERER. Simulation of pressure surge in a hydro power plant caused by an elbow draft tube. *10th International Meeting of the Work Group on The Behaviour of Hydraulic Machinery Under Steady Oscillatory Conditions*. Trondheim, 2001.

[31] RUPRECHT, A. Numerical prediction of vortex instabilities in turbomachinery. *Advances in High Performance Computing and Computational Sciences*. Springer, 2006, 211–224. Notes on Numerical Fluid Mechanics and Multidisciplinary Design (NNFM). DOI: 10.1007/978-3-540-33844-4_17. ISBN 978-3-540-33864-2.

[32] AVELLAN, F. Flow Investigation in a Francis Draft Tube: the Flindt Project. *Proceedings of 20th IAHR Symposium on Hydraulic Machinery and Systems*. Charlotte, 2000.

[33] CIOCAN, G. D., M. S. ILIESCU, T. C. VU, B. NENNEMANN, and F. AVELLAN. Experimental Study and Numerical Simulation of the FLINDT Draft Tube Rotating Vortex. *Journal of Fluids Engineering*. 2007, **129**(2), 146–158. DOI: 10.1115/1.2409332. ISSN 0098-2202.

[34] VU, T. C., C. DEVALS, Y. ZHANG, B. NENNEMANN, and F. GUIBAULT. Steady and unsteady flow computation in an elbow draft tube with experimental validation. *International Journal of Fluid Machinery and Systems*. 2011, **4**(1), 85–96. DOI: 10.5293/IJFMS.2011.4.1.085. ISSN 1882-9554.

[35] FOROUTAN, H. and S. YAVUZKURT. Simulation of flow in a simplified draft tube: turbulence closure considerations. *IOP Conference Series: Earth and Environmental Science*. 2012, **15**(2). DOI: 10.1088/1755-1315/15/2/022020. ISSN 1755-1307.

[36] MATHEY, F., D. COKLJAT, J. P. BERTOGLIO, and E. SERGENT. Assessment of the vortex method for Large Eddy Simulation inlet conditions. *Progress in Computational Fluid Dynamics, An International Journal*. 2006, **6**(1/2/3). DOI: 10.1504/PCFD.2006.009483. ISSN 1468-4349.

[37] RAJAN, G. K. and J. M. CIMBALA. Computational and Theoretical Analyses of the Precessing Vortex Rope in a Simplified Draft Tube of a Scaled Model of a Francis Turbine. *Journal of Fluids Engineering*. 2017, **139**(2), 021102. DOI: 10.1115/1.4034693. ISSN 0098-2202.

[38] CERVANTES, M. J., U. ANDERSSON, and H. M. LÖVGREN. Turbine-99 unsteady simulations – Validation. *IOP Conference Series: Earth and Environmental Science*. 2010, **12**. DOI: 10.1088/1755-1315/12/1/012014. ISSN 1755-1315.

[39] *Francis-99* [online]. Norwegian Hydropower Centre [accessed 2020-07-23]. Available at: https://www.ntnu.edu/nvks/francis-99

[40] MINAKOV, A., A. SENTYABOV, and D. PLATONOV. Numerical investigation of flow structure and pressure pulsation in the Francis-99 turbine during startup. *Journal of Physics: Conference Series*. 2017, **782**. DOI: 10.1088/1742-6596/782/1/012004. ISSN 1742-6588.

[41] MINAKOV, A., D. PLATONOV, A. SENTYABOV, and A. GAVRILOV. Francis-99 turbine numerical flow simulation of steady state operation using RANS and RANS/LES turbulence model. *Journal of Physics: Conference Series*. 2017, **782**. DOI: 10.1088/1742-6596/782/1/012005. ISSN 1742-6588.

[42] CHENG, H., L. J. ZHOU, and Y. Z. ZHAO. Very large eddy simulation of the vortex rope in the draft tube of Francis turbine. *IOP Conference Series: Earth and Environmental Science*. 2019, **240**. DOI: 10.1088/1755-1315/240/2/022001. ISSN 1755-1315.

[43] KRAPPEL, T. and S. RIEDELBAUCH. Scale Resolving Flow Simulations of a Francis Turbine Using Highly Parallel CFD Simulations. *High Performance Computing in Science and Engineering ´16*. Cham: Springer, 2016, 499–510. DOI: 10.1007/978-3-319-47066-5_34. ISBN 978-3-319-47065-8.

[44] JUNGINGER, B. and S. RIEDELBAUCH. Analysis of a full load operating point of a propeller turbine using scale-resolving turbulence models. *WASSERWIRTSCHAFT*. 2019, **109**(S1), 124–129. DOI: 10.1007/s35147-019-0248-7. ISSN 0043-0978.

[45] NICOLET, C., A. ZOBEIRI, P. MARUZEWSKI, and F. AVELLAN. Experimental Investigations on Upper Part Load Vortex Rope Pressure Fluctuations in Francis Turbine Draft Tube. *International Journal of Fluid Machinery and Systems*. 2011, **4**(1), 179–190. DOI: 10.5293/IJFMS.2011.4.1.179. ISSN 1882-9554.

[46] NISHI, M., T: KUBOTA, S. MATSUNAGA, and Y. SENOO. Surging Characteristics of Conical and Elbow-Type Draft Tubes. *Proceedings of 12th IAHR Symposium on Hydraulic Machinery and Systems*. Stirling, 1984.

[47] BRENNEN, C. The unsteady, dynamic characterization of hydraulic systems with emphasis on cavitation and turbomachines. *Joint ASME/ASCE/IAHR Symposium*. Fort Collins, 1978.

[48] DÖRFLER, P. K. Cavitation Compliance in 1D Part-load Vortex Models. *International Journal of Fluid Machinery and Systems*. 2017, **10**(3), 197–208. DOI: 10.5293/IJFMS.2017.10.3.197. ISSN 1882-9554.

[49] STUPARU, A. and R. SUSAN-RESIGA. The Origin of the Plunging Pressure Fluctuations for a Swirling Flow With Precessing Vortex Rope in a Straight Diffuser. *6th IAHR Meeting of the Working Group Cavitation and Dynamic Problems*. Ljubljana, 2015.

[50] KOUTNÍK, J., K. KRÜGER, F. POCHYLÝ, P. RUDOLF, and V. HABÁN. On cavitating vortex rope form stability during Francis turbine part load operation. *IAHR International Meeting of the Work Group on Cavitation and Dynamic Problems in Hydraulic Machinery and Systems*. Barcelona, 2006.

[51] KIRSCHNER, O., A. RUPRECHT, E. GÖDE, and S. RIEDELBAUCH. Experimental investigation of pressure fluctuations caused by a vortex rope in a draft tube. *IOP Conference Series: Earth and Environmental Science*. 2012, **15**(6). DOI: 10.1088/1755-1315/15/6/062059. ISSN 1755-1307.

[52] RUDOLF, P., V. HABÁN, F. POCHYLÝ, J: KOUTNÍK, and K. KRÜGER. Collapse of Cylindrical Cavitating Region and Conditions for Existence of Elliptical Form of Cavitating Vortex Rope. *Proceedings of the 2nd IAHR International Meeting of the Workgroup on Cavitation and Dynamic Problems in Hydraulic Machinery and Systems*. Timisoara, 2007. DOI: 10.13140/2.1.3527.8084.

[53] DÖRFLER, P. K. On the High-partial-load Pulsation in Francis Turbines. *International Journal of Fluid Machinery and Systems*. 2019, **12**(3), 200–216. DOI: 10.5293/IJFMS.2019.12.3.200. ISSN 1882-9554.

[54] DÖRFLER, P. K. Observation of pressure pulsations at high partial load on a Francis model turbine with high specific speed. *6th Meeting of the IAHR Work Group on the Behavior of Hydraulic Machinery Under Steady Oscillatory Conditions*. Lausanne, 1993.

[55] PLATONOV, D., A. MINAKOV, D. DEKTEREV, and A. MASLENNIKOVA. An Experimental Investigation of the Air Injection Effect on the Vortex Structure and Pulsation Characteristics in the Francis Turbine. *International Journal of Fluid Machinery and Systems*. 2020, **13**(1), 103–113. DOI: 10.5293/IJFMS.2020.13.1.103. ISSN 1882-9554.

[56] SKRIPKIN, S. G., M. A. TSOY, P. A. KUIBIN, and S. I. SHTORK. Study of Pressure Shock Caused by a Vortex Ring Separated From a Vortex Rope in a Draft Tube Model. *Journal of Fluids Engineering*. 2017, **139**(8), 081103. DOI: 10.1115/1.4036264. ISSN 0098-2202.

[57] ŠTEFAN, D., P. RUDOLF, M. HUDEC, V. URUBA, P. PROCHÁZKA, and O. URBAN. Experimental investigation of vortex ring formation as a consequence of spiral vortex re-connection. *IOP Conference Series: Earth and Environmental Science*. 2019, **405**. DOI: 10.1088/1755-1315/405/1/012033. ISSN 1755-1315.

[58] NISHI, M., X. M. WANG, K. YOSHIDA, T. TAKAHASHI, and T. TSUKAMOTO. An Experimental Study on Fins, Their Role in Control of the Draft Tube Surging. *Hydraulic Machinery and Cavitation*. Dordrecht: Springer, 1996, 905–914. DOI: 10.1007/978-94-010-9385-9_92. ISBN 978-94-010-9387-3.

[59] PŮLPITEL, L., SKOTÁK, A., and J. KOUTNÍK. Natural Air Admission of a Deep Submerged Pump Turbine. *Hydrovision'98*. Reno, 1998.

[60] KIM, S. J., Y. S. CHOI, Y. CHO, J. W. CHOI, J. J. HYUN, W. G. JOO, and J. H. KIM. Effect of Fins on the Internal Flow Characteristics in the Draft Tube of a Francis Turbine Model. *Energies*. 2020, **13**(11). DOI: 10.3390/en13112806. ISSN 1996-1073.

[61] GOGSTAD, P. J. and O. G. DAHLHAUG. Evaluation of runner cone extension to dampen pressure pulsations in a Francis model turbine. *IOP Conference Series: Earth and Environmental Science*. 2016, **49**. DOI: 10.1088/1755-1315/49/8/082019. ISSN 1755-1307.

[62] VEKVE, T. *An experimental investigation of draft tube flow*. Trondheim, 2004. Doctoral thesis. NTNU Trondheim.

[63] NAKANISHI, K. and T. UEDA. Air supply into draft tube of Francis turbine. *Fuji Electric Review*. 1964, **10**(3), 81–91.

[64] DÖRFLER, P. K. Design criteria for air admission systems in Francis turbines. *13th Symposium of IAHR Section for Hydraulic Machinery, Equipment and Cavitation*. Montreal, 1986.

[65] DASKIRAN, C., B. ATTIYA, M. ALTIMEMY, I. H. LIU, and A. OZTEKIN. Oxygen dissolution via pump-turbine – Application to wastewater treatment. *International Journal of Heat and Mass Transfer*. 2019, **131**, 1052–1063. DOI: 10.1016/j.ijheatmasstransfer.2018.11.130. ISSN 0017-9310.

[66] CHIRKOV, D. V., P. K. SHCHERBAKOV, S. G. CHERNY, V. A. SKOROSPELOV, and P. A. TURUK. Numerical investigation of the air injection effect on the cavitating flow in Francis hydro turbine. *Thermophysics and Aeromechanics*. 2017, **24**(5), 691–703. DOI: 10.1134/S0869864317050055. ISSN 0869-8643.

[67] UNTERLUGGAUER, J., A. MALY, and E. DOUJAK. Investigation on the Impact of Air Admission in a Prototype Francis Turbine at Low-Load Operation. *Energies*. 2019, **12**(15). DOI: 10.3390/en12152893. ISSN 1996-1073.

[68] MUNTEAN, S., R. SUSAN-RESIGA, V. C. CÂMPIAN, C. DUMBRAVA, and C. ADRIAN. In situ unsteady pressure measurements on the draft tube cone of the Francis turbine with air injection over an extended operating range. *6th International Conference on Energy and Environment*. Bucharest, 2013.

[69] KOUTNÍK, J. Analysis of Pressure Oscillations Measured in the Twin-Penstock of PSPP Stechovice. *Proceedings of 20th IAHR Symposium on Hydraulic Machinery and Systems*. Charlotte, 2000.

[70] SUSAN-RESIGA, R., T. C. VU, S. MUNTEAN, G. D. CIOCAN, and B. NENNEMANN. Jet Control of the Draft Tube Vortex Rope in Francis Turbines at Partial Discharge. *23rd IAHR Symposium on Hydraulic Machinery and Systems*. Yokohama, 2006.

[71] SUSAN-RESIGA, R., S. MUNTEAN, V. HASMATUCHI, I. ANTON, and F. AVELLAN. Analysis and Prevention of Vortex Breakdown in the Simplified Discharge Cone of a Francis Turbine. *Journal of Fluids Engineering*. 2010, **132**(5), 051102. DOI: 10.1115/1.4001486. ISSN 0098-2202.

[72] TĂNASĂ, C., R. SUSAN-RESIGA, S. MUNTEAN, and A. I. BOSIOC. Flow-Feedback Method for Mitigating the Vortex Rope in Decelerated Swirling Flows. *Journal of Fluids Engineering*. 2013, **135**(6), 061304. DOI: 10.1115/1.4023946. ISSN 0098-2202.

[73] ALTIMEMY, M., B. ATTIYA, C. DASKIRAN, I. H. LIU, and A. OZTEKIN. Mitigation of flow-induced pressure fluctuations in a Francis turbine operating at the design and partial load regimes—LES simulations. *International Journal of Heat and Fluid Flow*. 2019, **79**, 108444. DOI: 10.1016/j.ijheatfluidflow.2019.108444. ISSN 0142-727X.

[74] BLOMMAERT, G., F. AVELLAN, J. E. PRENAT, and A. BOYER. Active control of Francis turbine operation stability. *3rd ASME/JSME Joint Fluids Engineering Conference*. San Francisco, 1999.

[75] FENG, J. J., W. F. LI, H. WU, J. L. LU, W. L. LIAO, and X. Q. LUO. Investigation on pressure fluctuation in a Francis turbine with improvement measures. *IOP Conference Series: Earth and Environmental Science*. 2014, **22**(3). DOI: 10.1088/1755-1315/22/3/032006. ISSN 1755-1307.

[76] SUSAN-RESIGA, R., S. MUNTEAN, and C. TĂNASĂ. Hydrodynamic Design and Analysis of a Swirling Flow Generator. *4th German – Romanian Workshop on Turbomachinery Hydrodynamics*. Stuttgart, 2008.

[77] BOSIOC, A. I., S. MUNTEAN, C. TĂNASĂ, R. SUSAN-RESIGA, and L. VÉKÁS. Unsteady pressure measurements of decelerated swirling flow in a discharge cone at lower runner speeds. *IOP Conference Series: Earth and Environmental Science*. 2014, **22**(3). DOI: 10.1088/1755-1315/22/3/032008. ISSN 1755-1307.

[78] JAVADI, A., A. I. BOSIOC, H. NILSSON, S. MUNTEAN, and R. SUSAN-RESIGA. Experimental and Numerical Investigation of the Precessing Helical Vortex in a Conical Diffuser, With Rotor–Stator Interaction. *Journal of Fluids Engineering*. 2016, **138**(8), 081106. DOI: 10.1115/1.4033416. ISSN 0098-2202.

[79] SKRIPKIN, S. G., M. A. TSOY, P. A. KUIBIN, and S. I. SHTORK. Swirling flow in a hydraulic turbine discharge cone at different speeds and discharge conditions. *Experimental Thermal and Fluid Science*. 2019, **100**, 349–359. DOI: 10.1016/j.expthermflusci.2018.09.015. ISSN 0894-1777.

[80] RUDOLF, P., M. HUDEC, P. ZUBÍK, and D. ŠTEFAN. Experimental measurement and numerical modeling of cavitating flow in converging-diverging nozzle. *EPJ Web of Conferences*. 2012, **25**. DOI: 10.1051/epjconf/20122501081. ISSN 2100-014X.

[81] ŠTEFAN, D. *Study of the dissipation in spiraling vortical structures*. Brno, 2015. Doctoral thesis. Brno University of Technology. Supervisor P. Rudolf

[82] ŠTEFAN, D., P. RUDOLF, S. MUNTEAN, and R. SUSAN-RESIGA. Structure of flow fields downstream of two different swirl generators. *Engineering Mechanics*. 2013, **20**(5), 339–353. ISSN 1802-1484.

[83] CHIGIER, N. A. and J. M. BEÉR. Velocity and Static-Pressure Distributions in Swirling Air Jets Issuing From Annular and Divergent Nozzles. *Journal of Basic Engineering*. 1964, **86**(4), 788–796. DOI: 10.1115/1.3655954. ISSN 0021-9223.

[84] SHEEN, H. J., W. J. CHEN, S. Y. JENG, and T. L. HUANG. Correlation of swirl number for a radial-type swirl generator. *Experimental Thermal and Fluid Science*. 1996, **12**(4), 444–451. DOI: 10.1016/0894-1777(95)00135-2. ISSN 08941777.

[85] URBAN, O., M. KURKOVÁ, and P. RUDOLF. Application of Computer Graphics Flow Visualization Methods in Vortex Rope Investigations. *Energies*. 2021, **14**(3), 623. DOI: 10.3390/en14030623. ISSN: 1996-1073.

[86] ČASTULÍKOVÁ, V. *Metody počítačové vizualizace proudění*. Brno, 2019. Bachelor's thesis. Brno University of Technology. Supervisor O. Urban.

[87] KURKOVÁ, M. *Studium vírových struktur vznikajících ve vírovém generátoru*. Brno, 2020. Bachelor's thesis. Brno University of Technology. Supervisor O. Urban.

[88] FUCHS, R. *The Visible Vortex—Interactive Analysis and Extraction of Vortices in Large Time-Dependent Flow Data Sets*. Vienna, 2008. Doctoral Thesis. Vienna University of Technology. Supervisor H. Hauser.

[89] SADLO, F., R. PEIKERT, and M. SICK. Visualization Tools for Vorticity Transport Analysis in Incompressible Flow. *IEEE Transactions on Visualization and Computer Graphics*. 2006, **12**(5), 949–956. DOI: 10.1109/TVCG.2006.199. ISSN: 1077-2626.

[90] KAUFMAN, A., K. HÖHNE, W. KRÜGER, L: ROSENBLUM, and P. SCHRÖDER. Research issues in volume visualization. *IEEE Computer Graphics and Applications*. 1994, **14**(2), 63–67. DOI: 10.1109/38.267473. ISSN: 0272-1716.

[91] ROSENBLUM, L. J. Research issues in scientific visualization. *IEEE Computer Graphics and Applications*. 1994, **14**(2), 61–63. DOI: 10.1109/38.267472. ISSN: 0272-1716.

[92] AYACHIT, U. *The ParaView Guide*. New York: Kitware, 2017 [accessed 2021-7-26]. Available at: https://docs.paraview.org/en/latest/

[93] KOLÁŘ, V. Vortex identification: New requirements and limitations. *International Journal of Heat and Fluid Flow*. 2007, **28**(4), 638–652. DOI: 10.1016/j.ijheatfluidflow.2007.03.004. ISSN 0142-727X.

[94] ZHANG, Y., K. LIU, H. XIAN, and X. DU. A review of methods for vortex identification in hydroturbines. *Renewable and Sustainable Energy Reviews*. 2018, **81**(2), 1269–1285. DOI: 10.1016/j.rser.2017.05.058. ISSN 1364-0321.

[95] HUNT, J. C. R., A. A. WRAY, and P. MOIN. Eddies, streams, and convergence zones in turbulent flows. *Center for turbulence research report CTR-S88*. 1988, 193–208.

[96] HALLER, G. An objective definition of a vortex. *Journal of Fluid Mechanics*. 1999, **525**, 1–26. DOI: 10.1017/S0022112004002526. ISSN 0022-1120.

[97] CHONG, M. S., A. E. PERRY, and B. J. CANTWELL. A general classification of three-dimensional flow fields. *Physics of Fluids A: Fluid Dynamics*. American Institute of Physics, 1990, **2**(5), 765–777. DOI: 10.1063/1.857730. ISSN 0899-8213.

[98] ZHOU, J., R. J. ADRIAN, S. BALACHANDAR, and T. M. KENDALL. Mechanisms for generating coherent packets of hairpin vortices in channel flow. *Journal of Fluid Mechanics*. 1999, **387**, 353–396. DOI: 10.1017/S002211209900467X. ISSN 0022-1120.

[99] JEONG, J. and F. HUSSAIN. On the identification of a vortex. *Journal of Fluid Mechanics*. 1995, **285**, 69–94. DOI: 10.1017/S0022112095000462. ISSN 0022-1120.

[100] HALLER, G. Defining coherent vortices objectively from the vorticity. *Journal of Fluid Mechanics*. 2016, **795**, 136–173. DOI: 10.1017/jfm.2016.151. ISSN 0022-1120.

[101] HALLER, G. Lagrangian Coherent Structures. *Annual Review of Fluid Mechanics*. 2015, **47**, 137–162. DOI: 10.1146/annurev-fluid-010313-141322. ISSN 0066-4189.

[102] GREEN, M. A., C. W. ROWLEY, and HALLER, G. Detection of Lagrangian coherent structures in three-dimensional turbulence. *Journal of Fluid Mechanics*. 2007, **572**, 111–120. DOI: 10.1017/S002211200600364. ISSN 0022-1120.

[103] LIPINSKI, D., B. CARDWELL., and K. A. MOHSENI. A Lagrangian analysis of a two-dimensional airfoil with vortex shedding. *Journal of Physics A: Mathematical and Theoretical*. 2008, **41**, 344011. DOI: 10.1088/1751-8113/41/34/344011. ISSN 1751-8113.

[104] PENG, J. and J. O. DABIRI. The 'upstream wake' of swimming and flying animals and its correlation with propulsive efficiency. *Journal of Experimental Biology*. 2008, **211**(16), 2669–2677. DOI: 10.1242/jeb.015883. ISSN 0022-0949.

[105] WILSON, M. M., J. PENG, J. O. DABIRI, and J. D. ELDREDGE. Lagrangian coherent structures in low Reynolds number swimming. *Journal of Physics: Condensed Matter*. 2009, **21**, 204105. DOI: 10.1088/0953-8984/21/20/204105. ISSN 0953-8984.

[106] BERON-VERA, F. J., M. J. OLASCOAGA, and G. J. GONI. Oceanic mesoscale eddies as revealed by Lagrangian coherent structures. *Geophysical Research Letters*. 2008, **35**(12), L12603. DOI: 10.1029/2008GL033957. ISSN 0094-8276.

[107] SHADDEN, S. C., F. LEKIEN, and J. E. MARDSEN. Definition and properties of Lagrangian coherent structures from finite-time Lyapunov exponents in two-dimensional aperiodic flows. *Physica D: Nonlinear Phenomena*. 2005, **212**(3–4), 271–304. DOI: 10.1016/j.physd.2005.10.007. ISSN 0167-2789.

[108] HALLER, G. Lagrangian coherent structures from approximate velocity data. *Physics of Fluids*. 2002, **14**(6), 1851–1861. DOI: 10.1063/1.1477449. ISSN 1070-6631.

[109] BRUNTON, S. L. and C. W. ROWLEY. Fast computation of finite-time Lyapunov exponent fields for unsteady flows. *Chaos: An Interdisciplinary Journal of Nonlinear Science*. 2010, **20**(1), 017503. DOI: 10.1063/1.3270044. ISSN 1054-1500.

[110] CELIK, I., U. GHIA, P. ROACHE, C. FREITAS, H. COLEMAN, and P. RAAD. Procedure for Estimation and Reporting of Uncertainty Due to Discretization in CFD Applications. *Journal of Fluids Engineering*. 2008, **130**(7), 078001. DOI: 10.1115/1.2960953. ISSN 0098-2202.

[111] MENTER, F. Stress-Blended Eddy Simulation (SBES)—A New Paradigm in Hybrid RANS-LES Modeling. *Progress in Hybrid RANS-LES Modelling*. Cham: Springer, 2016, pp. 27–37. ISBN 978-3-319-70030-4.

[112] BRUNTON, S. L. and B. R. NOACK. Closed-Loop Turbulence Control: Progress and Challenges. *Applied Mechanics Reviews*. 2015, **67**(5), 050801. DOI: 10.1115/1.4031175. ISSN 0003-6900.

[113] GOYAL, R., B. K. GANDHI, and M. J. CERVANTES. Experimental study of mitigation of a spiral vortex breakdown at high Reynolds number under an adverse pressure gradient. *Physics of Fluids*. 2017, **29**(10), 104104. DOI: 10.1063/1.4999123. ISSN 1070-6631.

[114] *The Střekov Hydro Power Station* [online]. CEZ Group [accessed 2021-10-29]. Available at: https://www.cez.cz/en/energy-generation/hydroelectric-power-plants/cez-hydroelectric-power-plants/czech-republic/the-strekov-hydro-power-station

[115] ŠTEFAN, D. *Struktura proudění a energetické přeměny v kolenové sací troubě*. Brno, 2011. Master's thesis. Brno University of Technology. Supervisor P. Rudolf

[116] KHULLAR, S,. K. M. SINGH, M. J. CERVANTES, and B. K. GANDHI. Influence of runner cone profile and axial water jet injection in a low head Francis turbine at part load. *Sustainable Energy Technologies and Assessments*. 2022, **50**, 101810. DOI: 10.1016/j.seta.2021.101810. ISSN 2213-1388.

[117] URBAN, O., M. KURKOVÁ, and F. POCHYLÝ. *Analytický rozbor recirkulace na vstupu do oběžného kola odstředivého čerpadla, posouzení opatření pro její omezení*. Brno, 2021. Research report. Brno University of Technology.

[118] NOACK, B. R., K: AFANASIEV, M. MORZYŃSKI, G. TADMOR, and F. THIELE. A hierarchy of low-dimensional models for the transient and post-transient cylinder wake. *Journal of Fluid Mechanics*. 2003, **497**, 335–363. DOI: 10.1017/S0022112003006694. ISSN 0022-1120.

[119] SIROVICH, Lawrence. Turbulence and the dynamics of coherent structures. Part I: Coherent structures. *Quarterly of Applied Mathematics*. 1987, **45**(3), 561–571. DOI: 10.1090/qam/910462. ISSN 1552-4485.

[120] FOURIER, J. B. J. *The Analytical Theory of Heat*. Cambridge: Cambridge University Press, 2009. ISBN 978-1108001786.

[121] LUMLEY, J. L. *Atmospheric Turbulence and Radio Wave Propagation*. Moscow: Nauka, 1967. ISBN 978-1108001786.

[122] SIEBER, M., C. O. PASCHEREIT, and K. OBERLEITHNER. Spectral proper orthogonal decomposition. *Journal of Fluid Mechanics*. 2016, **792**, 798–828. DOI: 10.1017/jfm.2016.103. ISSN 0022-1120.

[123] BRUNTON, S. L., B. R. NOACK, and P: KOMOUTSAKOS. Machine Learning for Fluid Mechanics. *Annual Review of Fluid Mechanics*. 2020, **52**, 477–508. DOI: 10.1146/annurev-fluid-010719-060214. ISSN 0066-4189.

[124] FUKAMI, K., NAKAMURA, T., and K. FUKAGATA. Convolutional neural network based hierarchical autoencoder for nonlinear mode decomposition of fluid field data. *Physics of Fluids*. 2020, **32**, 095110. DOI: 10.1063/5.0020721. ISSN 1070-6631.

[125] LEE, K. and K. T. CARLBERG. Model reduction of dynamical systems on nonlinear manifolds using deep convolutional autoencoders. *Journal of Computational Physics*. 2020, **404**, 108973. DOI: 10.1016/j.jcp.2019.108973. ISSN 0021-9991.

[126] WANG, Z., I: AKHTAR, J. BORGGAARD, and T. ILIESCU. Proper orthogonal decomposition closure models for turbulent flows: A numerical comparison. *Computer Methods in Applied Mechanics and Engineering*. 2012, **237–240**, 10–26. DOI: 10.1016/j.cma.2012.04.015. ISSN 0045-7825.

[127] CHAMPION, K., B: LUSCH, J. N. KUTZ, and S. L. BRUNTON. Data-driven discovery of coordinates and governing equations. *Proceedings of the National Academy of Sciences*. 2019, **116**(45), 22445-22451. DOI: 10.1073/pnas.1906995116. ISSN 0027-8424.

[128] BRUNTON, S. L., J. L. PROCTOR, and J. N. KUTZ. Discovering governing equations from data by sparse identification of nonlinear dynamics. *Proceedings of the National Academy of Sciences*. 2016, **113**(15), 3932–3937. DOI: 10.1073/pnas.1517384113. ISSN 0027-8424.

[129] BRUNTON, S. L., M. BUDIŠIĆ, E. KAISER, and J. N. KUTZ. Modern Koopman Theory for Dynamical Systems. *arXiv*. 2021, 2102.12086v2. Available at: https://arxiv.org/abs/2102.12086v2

[130] HASEGAWA, K., K. FUKAMI, T. MURATA, and K. FUKAGATA. CNN-LSTM based reduced order modeling of two-dimensional unsteady flows around a circular cylinder at different Reynolds numbers. *Fluid Dynamics Research*. 2020, **52**(6), 065501. DOI: 10.1088/1873-7005/abb91d. ISSN 1873-7005.

[131] SAN, O., R. MAULIK, and M. AHMED. An artifical neural network framework for reduced order modeling of transient flows. *Communications in Nonlinear Science and Numerical Simulation*. 2019, **77**, 271–287. DOI: 10.1016/j.cnsns.2019.04.025. ISSN 1007-5704.

[132] PAWAR, S., S. M. RAHMAN, H. VADDIREDDY, O. SAN, A. RASHEED, and P. VEDULA. A deep learning enabler for nonintrusive reduced order modeling of fluid flows. *Physics of Fluids*. 2019, **31**, 085101. DOI: 10.1063/1.5113494. ISSN 1070-6631.

[133] LANGE, H., S. L. BRUNTON, and J. N. KUTZ. From Fourier to Koopman: Spectral Methods for Long-term Time Series Prediction. *Journal of Machine Learning Research*. 2021, **22**(41), 1–38. ISSN 1533-7928.

[134] RABAULT, J., M. KUCHTA, A. JENSEN, U. RÉGLADE, and N. CERARDI. Artificial neural networks trained through deep reinforcement learning discover control strategies for active flow control. *Journal of Fluid Mechanics*. 2019, **865**, 281–302. DOI: 10.1017/jfm.2019.62. ISSN 0022-1120.

[135] *Using Image Sequence of Medical Scans as Volume Data in Cycles* [online]. [accessed 2021-1-9]. Available at: https://blender.stackexchange.com/questions/62110/using-image-sequence-of-medical-scans-as-volume-data-in-cycles/

Nomenclature

Operators and constants

Note: although common notation is used throughout this work, some of the operators and constants are listed below if needed.

Operator	Description
awa	area-weighted average
$\cos$	cosine
$\det$	determinant of a matrix
$\exp$	exponential function
i	imaginary unit
$\ln$	natural logarithm
sgn	sign function
$\sin$	sine
tr	trace of a matrix
$\dfrac{\mathrm{d}(1)}{\mathrm{d}(2)}$	total derivative of quantity (1) with respect to quantity (2)
$\dfrac{\mathrm{D}(1)}{\mathrm{D}(2)}$	material derivative of quantity (1) with respect to quantity (2)
$\dfrac{\partial(1)}{\partial(2)}$	partial derivative of quantity (1) with respect to quantity (2)
$\int (1)\,\mathrm{d}(2)$	integral of quantity (1) with respect to quantity (2)
Δ	Laplace operator
Δ	difference operator
π	Ludolphine π number ($= 3.141592653589793\ldots$)
∇	nabla (del) operator
$\mathcal{F}$	Fourier transform
$\mathcal{O}$	Bachmann–Landau (big O) notation
$(\cdot)^{\mathrm{T}}$	matrix transpose
$(\cdot)'$	fluctuating part of a quantity
$\overline{(\cdot)}$	mean value of a quantity
$\lvert(\cdot)\rvert$	absolute value
$\lVert(\cdot)\rVert$	norm of a matrix or vector
$(\mathbf{1},\mathbf{2})_V$	inner product of vectors $\mathbf{1}$ and $\mathbf{2}$ containing values of functions (1) and (2) in grid points covering spatial domain V, defined as an approximation of $\int_V (1)(2)\,\mathrm{d}V$

Symbols

Note 1: less important symbols used less frequently may not be listed here. In that case, they shall be clarified in the text.

Note 2: scalars are denoted by regular letters, vectors and matrices are denoted by bold letters. Vector magnitude, vector elemenents, and matrix elements are denoted by regular letters since they are scalars. Example: $\boldsymbol{v}$ is the velocity vector, v_x is its x-axis element and v is the velocity magnitude.

Symbol	Unit	Description
a	–	amplitude
$a(t)$	–	temporal mode
$\boldsymbol{a}_i$	–	vector containing i-th temporal mode values in discrete time instants
$\boldsymbol{b}$	–	bias vector of a dense layer in a neural network
$\boldsymbol{C}$	–	covariance matrix
c_p	[1]	pressure recovery coefficient
d	[m]	diameter
D	–	discriminant
D	[m]	diameter
$\boldsymbol{D}$	[1]	Cauchy–Green deformation tensor
D_h	[m]	hydraulic diameter
$\boldsymbol{e}_i$	–	i-th eigenvector
f	[s^{-1}]	frequency
f_s	[1]	shielding function
Fr	[1]	Froude number
$\boldsymbol{g}$	[1]	convolution kernel in SPOD formulation
$G(r)$	–	function on which the V_s parameter is based on
H	[m]	head
I	[1]	turbulence intensity
$I_{1–3}$	–	invariants of the velocity gradient tensor
k	[J/kg]	turbulence kinetic energy
L	[m]	characteristic length
$m(\alpha)$	–	function for determination of indefiniteness of $\boldsymbol{M}$
$\boldsymbol{M}$	[$1/\mathrm{s}^2$]	strain acceleration tensor (Cotter–Livlin derivative of $\boldsymbol{S}$)
$\boldsymbol{M}_\mathrm{z}$	[1]	$\boldsymbol{M}_\mathrm{z}$-criterion for vortex identification
n	[1/s]	rotational speed
$\boldsymbol{n}$	[1]	unit outer normal vector
N_f	[1]	convolution kernel length in SPOD formulation
p	[Pa]	pressure
$p_{(i,j)}$	[Pa]	parametr based on p for quantification of the vortex rope strength
$\boldsymbol{P}$	[m]	position vector of a probe
Q	[$1/\mathrm{s}^2$]	Q-criterion for vortex identification

Q	[m^3/s]	flow rate
$\boldsymbol{Q}$	[1]	rotation matrix
r	[m]	radial coordinate
$\boldsymbol{r}$	[m]	position vector
R	[1/s^3]	third invariant of the velocity gradient tensor (I_3)
R	[m]	radius
$\boldsymbol{R}$	[1/s]	rotation tensor (antisymmetric part of the velocity gradient tensor)
s_{1-3}	[1/s]	eigenvalues of the strain-rate tensor
S	[m^2]	surface area
$\boldsymbol{S}$	[1/s]	strain-rate tensor (symmetric part of the velocity gradient tensor)
Sr	[1]	swirl number
t	[s]	time
T	[s]	period, time interval
$\boldsymbol{u}$	[m/s]	blade circumferential velocity vector
$\boldsymbol{v}$	[m/s]	absolute velocity vector
v_m	[m/s]	meridional velocity
v_u	[m/s]	circumferential (tangential) component of absolute velocity
v_z	[m/s]	axial velocity
$v_{\mathrm{z}_\mathrm{def}}$	[m/s]	axial velocity deficit with respect to the mean cross-sectional axial velocity
v_φ	[m/s]	circumferential (tangential) velocity
V	[m^3]	volume
V_s	[1/s]	integral parameter quantifying swirl intensity by Cheng et al.
$\boldsymbol{w}$	[m/s]	relative velocity vector
$\boldsymbol{W}$	–	matrix of weights (kernel) of a dense layer in a neural network
$\boldsymbol{x}$	[m]	position vector
y^+	[1]	dimensionless wall distance
Y	[J/kg]	specific energy
Z	–	elliptic cone (part of $\boldsymbol{M}_\mathrm{z}$-criterion definition)
β_2	[1]	trailing edge angle
Δ	[m]	length scale
Δ	[1/s^6]	Δ-criterion for vortex identification
Δt	[s]	time step
ε	[J/(kg·s)]	turbulence dissipation rate
η_{1-3}	[m]	coordinates in the basis of the strain-rate tensor eigenvectors
$\lambda_\mathrm{c}(m)$	–	cumulative accuracy of a decomposition, m is the number of modes
λ_i	–	i-th eigenvalue
λ_2	[1/s^2]	λ_2-criterion for vortex identification
μ	[Pa·s]	dynamic viscosity
μ_t	[Pa·s]	dynamic eddy viscosity
ν	[m^2/s]	kinematic viscosity
ν_t	[m^2/s]	kinematic eddy viscosity

$\boldsymbol{\xi}$	[m]	vector of the difference of the positions of two particles
ρ	[kg/m^3]	density
σ	[1/s]	finite-time Lyapunov exponent
σ	–	standard deviation
φ	[1]	flow coefficient
φ	[1]	phase shift
$\varphi_{t_0}^{t}(\boldsymbol{x}_0)$	–	flow map
$\phi(\boldsymbol{x})$	–	spatial mode
$\boldsymbol{\phi}_i$	–	vector containing i-th spatial mode values in grid points
ψ	[1]	head coefficient
ω	[1/s]	angular velocity
ω	[1/s]	specific turbulence dissipation rate
$\boldsymbol{\Omega}$	[1/s]	vorticity vector
Ω_z	[1/s]	axial component of vorticity
Ω_φ	[1/s]	circumferential (tangential) component of vorticity
$\widetilde{\Omega}$	[1/s]	modified vorticity
$\mathcal{L}(\cdot)$	–	loss function of a machine learning model
$\mathcal{V}$	[m^2/s]	Lyapunov function
$\nabla \boldsymbol{v}$	[1/s]	velocity gradient tensor

Abbreviations

Abbreviation	Meaning
BEP	Best Efficiency Point
BFGS	Boyden-Fletcher-Goldfarb-Shanno algorithm
BRF	Best Reference Frame
BUT	Brno University of Technology
CFD	Computational Fluid Dynamics
DDES	Delayed Detached Eddy Simulation
DES	Detached Eddy Simulation
DFT	Discrete Fourier Transform
FFT	Fast Fourier Transform
FLINDT	FLow INvestigation in a Francis Draft Tube
FTLE	Finite-Time Lyapunov Exponent
GCI	Grid Convergence Index
GPU	Graphics Processing Unit
LDA	Laser Doppler Anemometry
LES	Large Eddy Simulation
LIC	Line Integral Convolution
LSTM	Long Short-Term Memory
NN	Neural Network
ODE	Ordinary Differential Equation
PISO	Pressure-Implicit with Splitting of Operators
PIV	Particle Image Velocimetry
POD	Proper Orthogonal Decomposition
PRESTO!	PREssure STaggering Option
QUICK	Quadratic Upstream Interpolation for Convective Kinematics
RANS	Reynolds-Averaged Navier–Stokes equations
RMS	Root Mean Square
RRF	Rotated Reference Frame
RSM	Reynolds Stress equation Model
SAS	Scale-Adaptive Simulation
SBES	Stress-Blended Eddy Simulation
SINDy	Sparse Identification of Nonlinear Dynamics
SPOD	Spectral Proper Orthogonal Decomposition
SST	Shear Stress Transport
TPU	Tensor Processing Unit
UPT	Universitatea Politehnica Timişoara
URANS	Unsteady Reynolds-Averaged Navier–Stokes equations
VLES	Very Large Eddy Simulation
VTK	Visualization ToolKit
WALE	Wall-Adapting Local Eddy viscosity model
X3D	eXtensible 3D

Appendix

A Volume rendering of data from ParaView in Blender

In this appendix, the procedure of transfering data for volume rendering from ParaView (version 5.8.0) to Blender (version 2.82a) and the settings therein are described. The reason for doing this is that there are things that can be easily done in Blender, while in ParaView, they are cumbersome or even impossible, e.g. properly combining multiple volume renderings in a single picture or setting transparency according to one variable and colors according to another one. The price of this is the time needed for preparations and the rendering itself.

The first step comprises the preparation of the volume rendering in ParaView. Once the data are loaded, apply "Resample To Image" filter on them. It resamples the data to a structured grid of a given size, making the rendering much faster, allowing for quick explorations and experimentation with color and transparency settings. The disadvantage is that curved boundaries will be jagged and selective refinements will be lost, which is fortunately not a problem in our case. Once the results look as desired, they can be saved in TIFF (Tagged Image File Format) format as a series of images. Before that, it is needed to adjust the data so that the range on the colorbar is from 0 to 255. For example, if one has prepared a volume rendering of the static pressure and the colorbar range is from -10 to 1, it is needed to subtract 1 and multiply the result by $-\frac{255}{11}$. The areas with the lowest pressures (which are of interest) will then correspond to the brightest pixels in the images. This can be done in ParaView using the "Calculator" function. The "Result Array Type" setting needs to be set to float or unsigned character. The volume rendering is in this case given by a series of slices along the z-axis, with each slice represented as a raster graphics image. The advantage of TIFF is that it allows saving all the images to a single file. This file is then adjusted to be usable in Blender as the source for its volume shaders. For the approach used in this work[135], it is required to gather all images from the TIFF file and convert them into a single image with the component images stacked one by one next to each other. The resultant image is typically very wide. Part of such an image is presented in Fig. A.1.

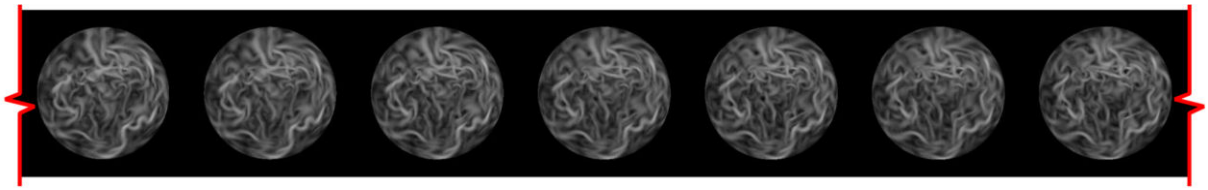

Fig. A.1: *A part of the image ready to be imported into Blender as the source texture for volume rendering. It shows* 7 *slices out of* 640 *distributed uniformly along the diffuser. This particular image was used for volume renderings with forward FTLE fields (the case with the lower* Sr*) in Fig. 4.7. Higher values are brighter.*

This image was obtained using the following MATLAB code.

```
input = 'D:\CFD\generator2017\FTLE\image.tiff';          % input image
output = 'D:\CFD\generator2017\FTLE\final_image.png';  % output image, png
format

numimgs = size(imfinfo(input),1);       % number of images in the file
```

```
I = imread(input,1);                    % load the first image
s = size(I);                            % find its size
pic = uint8(zeros(s(1),numimgs*s(2))); % predefine the matrix for the re-
sultant image
pic(:,1:s(2)) = I;                      % insert the first image
pos = s(2) + 1;                         % move the position pointer

% Insert other images using a for loop
for i = 2:numimgs
      I = imread(fullfile(cesta,soubor),i);
      pic(:,pos:(pos + s(2) - 1)) = I;
      pos = pos + s(2);
end

% Write resultant image
imwrite(pic,output);
```

The resultant image is ready to be loaded into Blender as part of the following volume rendering procedure. It is based on the rendering of a cube (which is one of the basic objects in Blender) using a volume shader. The dimensions and position of the cube must be adjusted to match the actual dimensions and position of the structured grid in ParaView. The color and transparency level for each point of the cube is determined from the image. This requires a procedure that finds the corresponding pixel in the image. This process is given by the network of nodes created in Blender "Shader Editor" depicted in Fig. A.2. The first part (at the top of the figure) finds the pixel in the image corresponding to the given position within the cube. As we have a finite number of slices along the z-axis, we need to interpolate between the two closest slices to obtain a smooth representation. This is why there are two similar procedures, with the only difference in the rounding operation: floor is used in the top branch, leading to the closest plane with a lower z-value, whereas ceil is used in the bottom branch, leading to the closest plane with a higher z-value. The image is imported within the orange box ("Image Texture" node, bottom of Fig. A.2). The interpolation is processed by the yellow "MixRGB" node. Two "Color Ramp" nodes follow to assign colors and transparency to each point. They should be set according to the colorbar and opacity transfer function prepared in ParaView if the same appearance is required. Shader "Principled Volume", which combines scattering, absorption, and emission, is used. Here, scattering and emission were used at the same time. The two "Multiply" nodes are used to control the intensities of these two effects. Note that for extremely small scales, the volume rendering may not be visible. In such cases, it is necessary to properly rescale the objects.

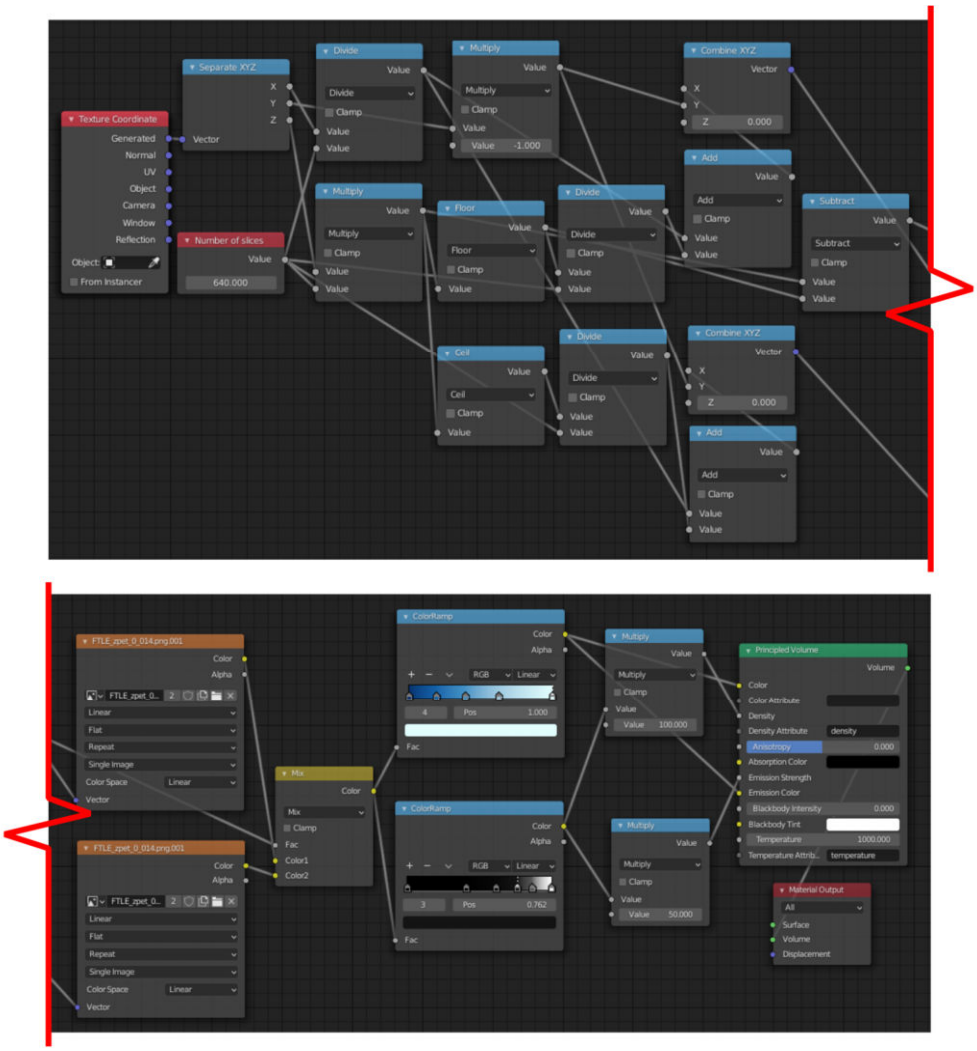

Fig. A.2: *The network of operations used in Blender "Shader Editor" cut into two parts. Red lines mark the cut.*

B Vortex rope in CFD and experiments

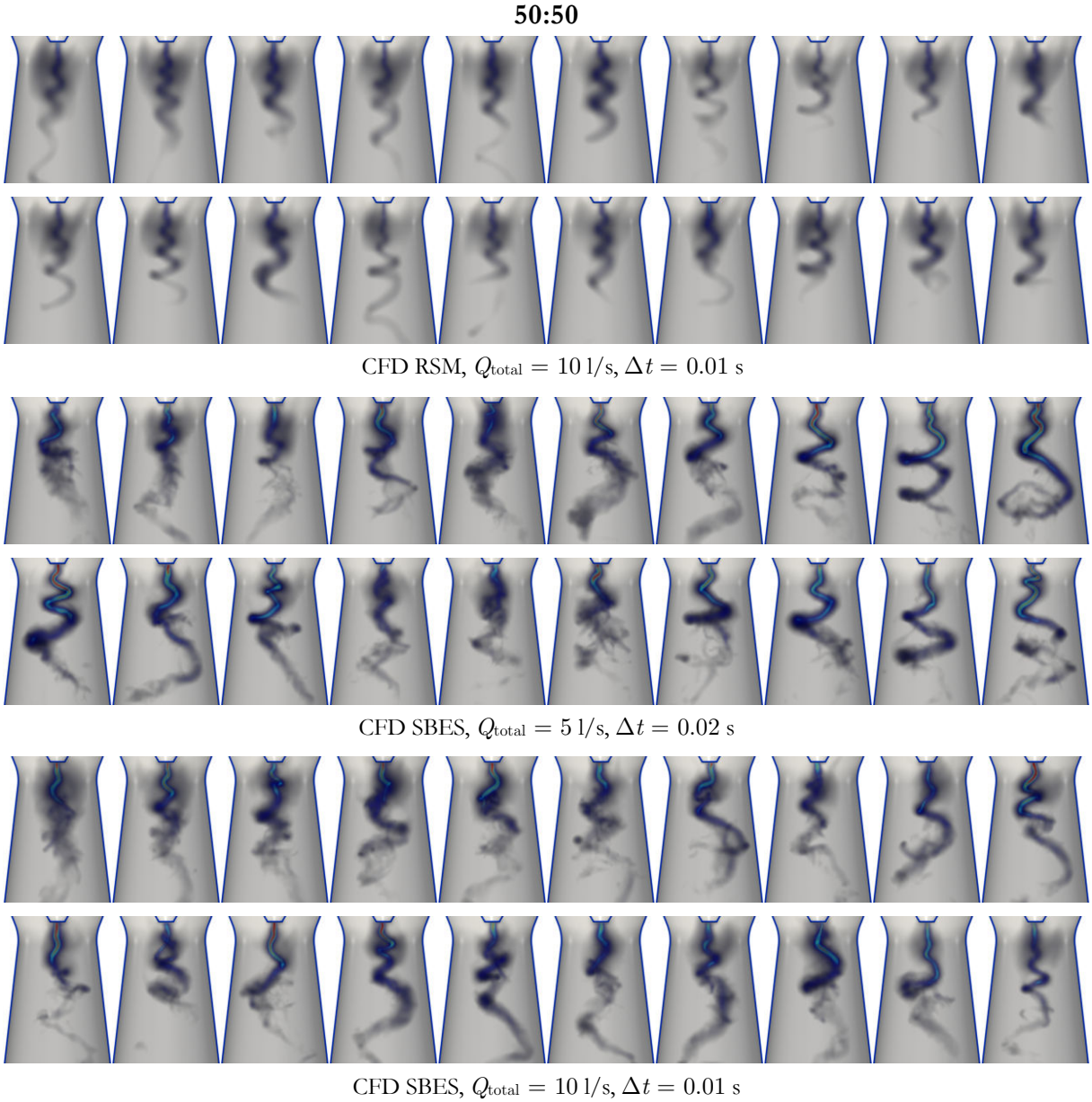

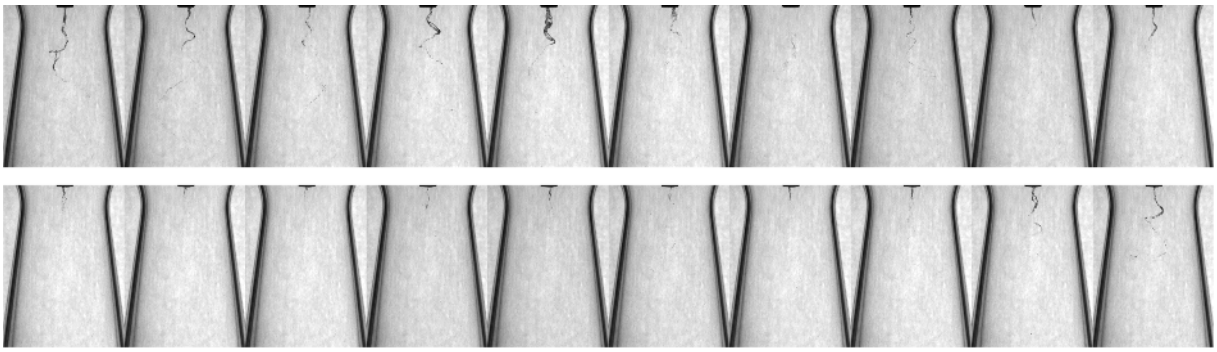

Experiment, $Q_{\text{total}} = 10\ \text{l/s}, \Delta t = 0.01\ \text{s}$

60:40

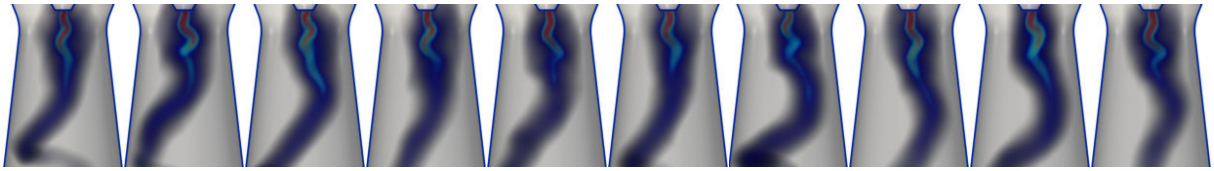

CFD RSM, $Q_{\text{total}} = 10\ \text{l/s}, \Delta t = 0.03\ \text{s}$

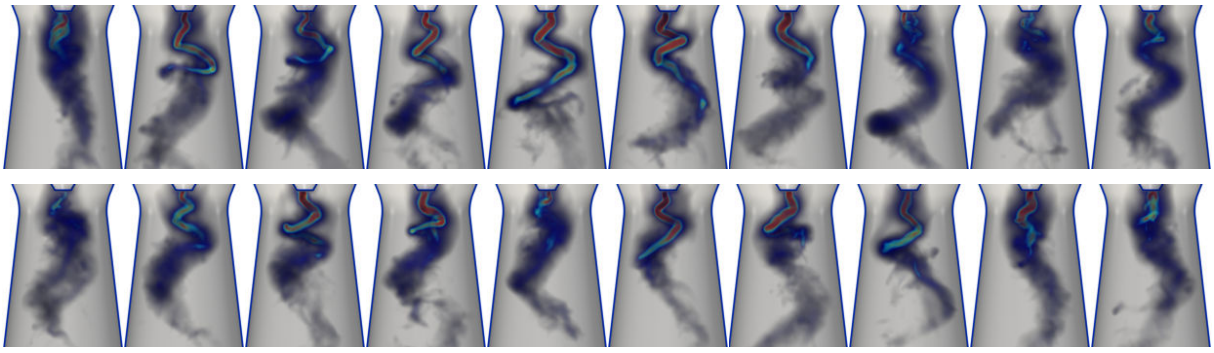

CFD SBES, $Q_{\text{total}} = 5\ \text{l/s}, \Delta t = 0.04\ \text{s}$

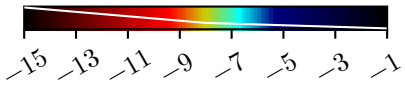

Dimensionless pressure [1]

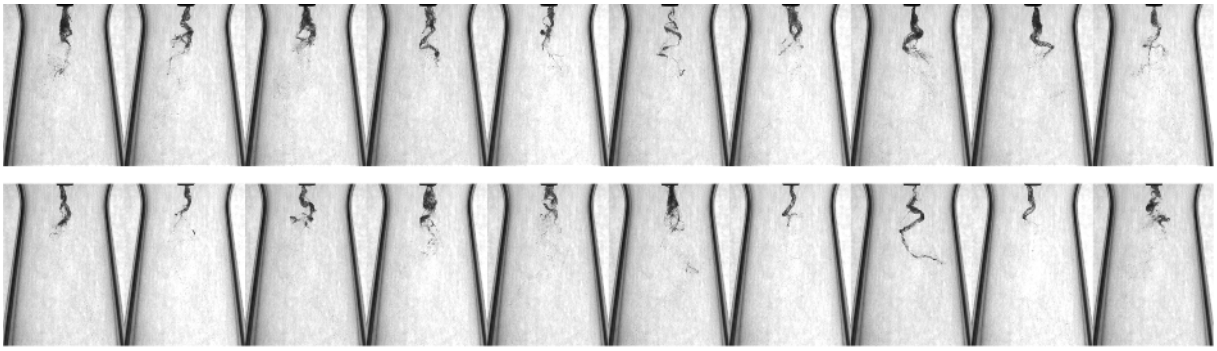

Experiment, $Q_{\text{total}} = 10\ \text{l/s}, \Delta t = 0.03\ \text{s}$

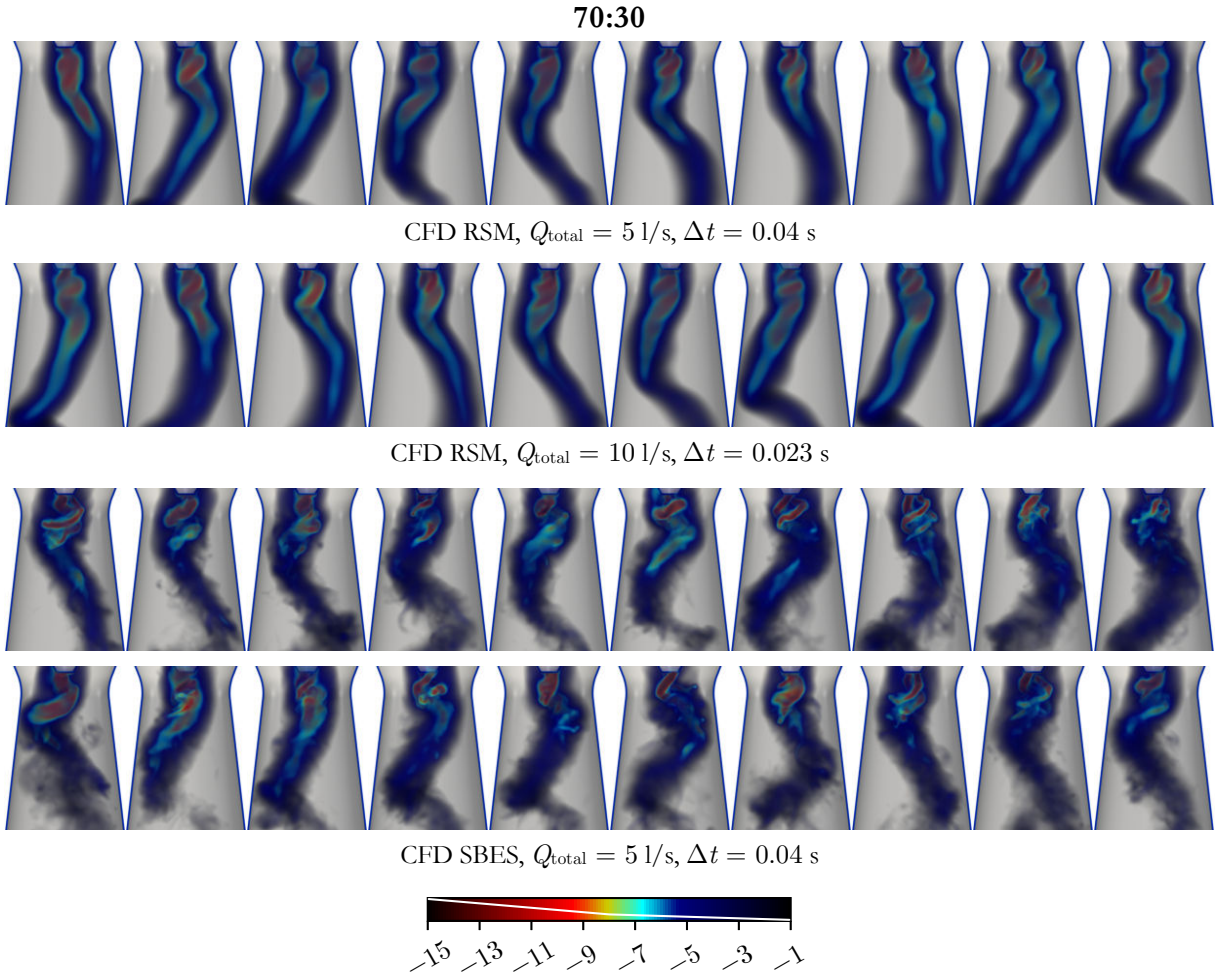

Fig.B.1: *Visualizations of the vortex rope from CFD simulations with fixed boundary conditions using the dimensionless pressure and from experiments thanks to cavitation in its core.*